Non-Cartesian Sparkling encoding for High spatio-temporal resolution functional Magnetic Resonance Imaging (fMRI) at 7 Tesla and beyond

Zaineb Amor

▶ **To cite this version:**

Zaineb Amor. Non-Cartesian Sparkling encoding for High spatio-temporal resolution functional Magnetic Resonance Imaging (fMRI) at 7 Tesla and beyond. Medical Imaging. Université Paris-Saclay, 2024. English. NNT : 2024UPAST032 . tel-04573047

HAL Id: tel-04573047
https://theses.hal.science/tel-04573047

Submitted on 13 May 2024

HAL is a multi-disciplinary open access archive for the deposit and dissemination of scientific research documents, whether they are published or not. The documents may come from teaching and research institutions in France or abroad, or from public or private research centers.

L'archive ouverte pluridisciplinaire **HAL**, est destinée au dépôt et à la diffusion de documents scientifiques de niveau recherche, publiés ou non, émanant des établissements d'enseignement et de recherche français ou étrangers, des laboratoires publics ou privés.

université PARIS-SACLAY

Non-Cartesian SPARKLING encoding for High spatio-temporal resolution functional Magnetic Resonance Imaging (fMRI) at 7 Tesla and beyond

Encodage non-cartésien SPARKLING pour l'Imagerie par Résonance Magnétique fonctionnelle (IRMf) à haute résolution spatio-temporelle à 7 Tesla et au-delà

Thèse de doctorat de l'université Paris-Saclay

École doctorale n° 575, Electrical, Optical, Bio : physics and Engineering (EOBE)
Spécialité de doctorat : Physique et imagerie médicale
Graduate School : Sciences de l'ingénierie et des systèmes
Référent : Faculté des sciences d'Orsay

Thèse préparée dans l'unité de recherche **NeuroSpin** (Université Paris-Saclay, CEA), sous la direction de **Alexandre Vignaud**, Directeur de recherche et la co-direction de **Philippe Ciuciu**, Directeur de recherche

Thèse soutenue à Paris-Saclay, le 9 avril 2024, par

Zaineb Amor

Composition du jury

Membres du jury avec voix délibérative

Luisa Ciobanu Directrice de recherche, CEA	Présidente
Benedikt A. Poser Professor, Maastricht University	Rapporteur & Examinateur
Johanna S. Vannesjö Associate professor, Norwegian University of Science and Technology	Rapportrice & Examinatrice
Michel Dojat Directeur de recherche, Inserm	Examinateur
Jean-Philippe Ranjeva Professeur, Université Aix-Marseille	Examinateur

THESE DE DOCTORAT
NNT : 2024UPAST032

université PARIS-SACLAY

ÉCOLE DOCTORALE
Physique et ingénierie : Electrons, Photons, Sciences du vivant (EOBE)

Title : Non-Cartesian SPARKLING encoding for High spatio-temporal resolution functional Magnetic Resonance Imaging (fMRI) at 7 Tesla and beyond

Keywords : Non-Cartesian imaging ; compressed-sensing fMRI ; ultra-high field ; off-resonance correction ; magnetic field monitoring ; sliding-window fMR image reconstruction.

Abstract : Functional MRI (fMRI) is currently one of the most commonly used functional neuroimaging techniques to probe brain activity non-invasively through the blood oxygen level-dependent (BOLD) contrast that reflects neurovascular coupling. It offers an interesting trade-off between spatial and temporal resolution in order to study the whole brain as an aggregation of intrinsic functional systems. The quest for higher spatial and/or temporal resolution in fMRI while preserving a sufficient temporal signal-to-noise ratio (tSNR) has generated a tremendous amount of methodological contributions in the last decade ranging from Cartesian vs. non-Cartesian readouts, 2D vs. 3D acquisition strategies, parallel imaging and/or compressed sensing (CS) accelerations and simultaneous multi-slice acquisitions to cite a few. In this work, we focus on the use of CS in fMRI ; more specifically, we consider Spreading Projection Algorithm for Rapid K-space sampLING (SPARKLING) encoding scheme.

The main focus and goal of this thesis involves the evaluation of 3D-SPARKLING as a viable acquisition scheme for high-resolution whole-brain fMRI. In this regard, we initially compared its capabilities with state-of-the-art 3D-EPI. After observing higher sensitivity to static and dynamic magnetic field imperfections in 3D-SPARKLING data, we established an experimental protocol to correct them. Finally, we studied the capabilities and limitations of employing a sliding-window reconstruction in combination with the SPARKLING encoding scheme to enhance temporal resolution during image reconstruction in fMRI retrospectively. A simulation study where the ground truth is controlled was conducted and demonstrated the possibility of detecting high-frequency oscillations in the BOLD signal and separating physiological noise from neural activity.

Titre : Encodage non-cartésien Sparkling pour l'Imagerie par Résonance Magnétique fonctionnelle (IRMf) à haute résolution spatio-temporelle à 7 Tesla et au-delà

Mots clés : Imagerie non cartésienne ; IRMf à échantillonnage compressif ; ultra haut champ ; correction d'effet hors-resonance ; mesure du champ magnétique ; reconstruction d'images IRMf à fenêtre glissante.

Résumé : L'IRM fonctionnelle (IRMf) est actuellement l'une des techniques de neuroimagerie fonctionnelle les plus utilisées pour sonder l'activité cérébrale de manière non invasive grâce au contraste dépendant du niveau d'oxygène dans le sang (BOLD) qui reflète le couplage neurovasculaire. Elle offre un compromis intéressant entre la résolution spatiale et temporelle afin d'étudier le cerveau entier en tant qu'agrégation de systèmes fonctionnels intrinsèques. La recherche d'une résolution spatiale et/ou temporelle plus élevée en IRMf tout en préservant un rapport signal/bruit temporel suffisant (tSNR) a généré une quantité considérable de contributions méthodologiques au cours de la dernière décennie, allant des methodes d'encodage cartésiennes ou non cartésiennes, des stratégies d'acquisition 2D ou 3D, de l'imagerie parallèle et/ou de échantillonnage compressif (CS) et des acquisitions multibandes, pour n'en citer que quelques-unes. Dans ce travail, nous nous concentrons sur l'utilisation du CS dans l'IRMf, plus spécifiquement, nous considérons le schéma d'encodage SPARKLING.

L'objectif principal de cette thèse est d'évaluer 3D-SPARKLING en tant que schéma d'acquisition viable pour l'IRMf à haute résolution et pour cerveau entier. À cet égard, nous avons d'abord comparé ses performances avec l'état de l'art en la matière : 3D-EPI. Après avoir observé une plus grande sensibilité aux imperfections statiques et dynamiques du champ magnétique dans les données 3D-SPARKLING, nous avons établi un protocole expérimental pour les corriger. Enfin, nous avons étudié les possibilités et les limites de l'utilisation d'une reconstruction par fenêtre glissante en combinaison avec le schéma d'encodage SPARKLING pour améliorer rétrospectivement la résolution temporelle pendant la reconstruction des images IRMf. Une étude de simulation dans laquelle la vérité terrain est contrôlée a été menée et a démontré la possibilité de détecter les oscillations à haute fréquence dans le signal BOLD et de séparer le bruit physiologique de l'activité neuronale.

لا دور لي في حياتي
سوي أَنني،
عندما عَـلَمْتني تراتيلها،
قلتُ : هل من مزيد ؟
وأَوقدتُ قنديلها
ثم حاولتُ تعديلها
ـ محمود درويش، لاعب النرد

I have no role in my life,
Except that,
When it taught me its melodies,
I said : Is there more ?
And I lit its lantern
Then I tried to tweak it

- Mahmoud Darwish, The dice player

© Zaineb Amor 2024

Acknowledgements

I extend my sincere gratitude to the individuals whose contributions have been invaluable in completing this thesis. Your support, guidance, and expertise have made this journey possible.

My deepest appreciation to my dedicated supervisors, Alexandre Vignaud and Philippe Ciuciu, whose insightful feedback and constructive criticism greatly enriched the quality of this work.

Special thanks go to the PIs of the METRIC and MIND teams, in particular Nicolas Boulant, Caroline Le Ster, Frank Mauconduit, Alexis Amadon, and Bertrand Thirion, for their help throughout my thesis. I thank the radiographers at NeuroSpin as well. I am also grateful to Christian Mirkes from Skope Magnetic Resonance Technologies AG for his valuable expertise on the Skope field camera system.

To the reviewers and members of the jury, your time and expertise are deeply appreciated.

I extend my thanks to my fellow current and former PhD students from the METRIC and MIND teams, who have shared this academic journey with me. Special mention to Chaithya GR, Pierre-Antoine Comby, Guillaume Daval-Frérot, Redouane Jamil, Renata Baptista, and Paul-François Gapais for their camaraderie and collaborative spirit.

Lastly, I want to dedicate this work to my parents, Dorra Rassaa and Hatem Amor, and extend my appreciation to my brother Mahmoud Amor, as well as my friend Yasmin Kalboussi.

* * *
* *
*

Contents

General introduction

Context & Motivations

FUNCTIONAL Magnetic Resonance Imaging (fMRI) stands today as a powerful non-invasive neuroimaging tool. It offers distinct advantages over other non-invasive techniques such as Electroencephalography (EEG) and Magnetoencephalography (MEG). While EEG and MEG offer direct measurements of neural activity with excellent temporal resolution, these modalities are limited in terms of spatial localization. In contrast, one key strength of fMRI lies in its ability to provide improved spatial resolution and reduced uncertainty in the localization of brain activity despite its moderate temporal precision. In fact, fMRI captures hemodynamic and metabolic changes resulting from neural activity, offering an indirect (and slower) yet insightful measurement of brain function.

Understanding the origin of the phenomenon, we can trace it back to 1880 when A. Musso introduced what he called the "Human circulation balance" method. The idea was to infer the change in blood flow in the brain following increased brain activity. The experimental setup involved the participants lying on a balance table and being presented with stimuli or asked to perform some cognitive task. Musso observed that the balance would tip toward the head of the participants as they performed the task. That said, the late 20th century witnessed the most crucial milestones for fMRI.

In 1990, S. Ogawa's groundbreaking discovery of Blood Oxygenation Level-Dependent (BOLD) contrast [Oga+90] in rodents marked a pivotal moment in fMRI history. His first aim was to image the rodent brain with high contrast to see whether it is possible to detect physiological changes. During his experiments on anesthetized mice, he noticed intra-cortical black lines on the magnetic resonance (MR) images that disappeared when he switched the breathing air to pure oxygen (O_2). Further investigations revealed a similar disappearance of black lines when imaging a mouse brain while it is being euthanized with carbon monoxide (CO). The common denominator in both experiments was a chemical-induced alteration in oxyhemoglobin and deoxyhemoglobin concentrations in the blood. The presence or absence of black lines was explained by local changes in susceptibility-induced field variations around blood vessels: The BOLD contrast was born.

Going forward, in 1992, the first papers reporting endogenous (without any external contrast agent) BOLD fMRI experiments were published by P. Bandettini [Ban+92], S. Ogawa [Oga+92] and K. K. Kwong [Kwo+92]. Motor and/or visual stimulations were implemented, and signal changes correlating to the tasks were reported, revealing activations in the motor and/or visual cortex: BOLD fMRI was born.

Since its inception, fMRI has undergone significant progress in terms of MR methodology, data processing, and statistical analysis tools, and it has been used on non-human animals and humans alike. Regarding MR methodology, advancements were pursued in hardware, including high magnetic field strengths and coil and gradients design, alongside software developments focusing on enhancing fMRI data acquisition and image reconstruction strategies. The goal was to enhance sensitivity and specificity, i.e., detecting the lowest BOLD effect with the highest spatial accuracy (by improving the resolution) and expanding the range of contrasts beyond the traditional BOLD contrast, which continues to be the predominant choice even today. Preprocessing and statistical analysis tools have evolved from conventional approaches rooted in image processing and standard regression analysis to more challenging encoding and decoding models of brain activity. Moreover, fMRI applications have also

advanced from studying sensory-motor functions to more complex cognitive functions such as language, mathematics, learning, and decision-making. On the downside, reproducibility remains a persistent issue despite the availability of numerous open-source fMRI datasets and the standardization of many processing pipelines. Additionally, achieving clinical applications for fMRI remains a goal that is currently, for the most part, out of reach. More broadly, across all the mentioned sub-domains (MR methodology, processing and analysis tools, applications in cognitive and clinical neuroscience), researchers persist in their efforts to enhance spatiotemporal resolution, analysis robustness, and the relevance of applications. This is driven by a strong belief that these collective endeavors will eventually converge, yielding a highly reliable and efficient modality for studying the healthy and pathological brain.

In this specific Ph.D. endeavor, our focus was on the MR methodology aspect. More specifically, our focus centers on addressing the acquisition and image reconstruction aspects, conveniently adapting them to achieve high spatiotemporal resolution fMRI. The quest for higher spatial and/or temporal resolution in fMRI while preserving a sufficient temporal signal-to-noise ratio (tSNR) and without sacrificing brain coverage has generated a tremendous amount of methodological contributions in the last decade. These developments range from Cartesian [Pos+10] vs. non-Cartesian [Glo12] readouts and 2D vs. 3D acquisition strategies to parallel imaging and/or compressed sensing (CS) [LDP07] accelerations and simultaneous multi-slice acquisitions [Moe+10] to cite a few. CS allows for almost exact reconstruction of signals from highly undersampled measurements using pseudo-random sampling schemes and nonlinear reconstruction methods, as long as the original signals admit a sparse representation in an appropriate transform. In CS-MRI, pseudo-random under-sampling operates in k-space with a variable density that densely samples the center of k-space and sparsely samples its periphery to recover MR images with a low-level of noise-like artifacts and good imaging contrast. The sparsity of MR images is typically enforced on a spatial wavelet basis. CS has been applied to MRI both in the Cartesian and non-Cartesian acquisition setting [BUF07; Lus+08; Fen+14; Cha+14b]. However, today, the use of CS in fMRI remains limited and confined to spiral readouts. Nonetheless, P. Ciuciu and collaborators have recently developed SPARKLING (Spreading Projection Algorithm for Rapid K-space sampLING) to accelerate MR imaging using CS-based principles. SPARKLING implements variable density sampling (VDS) while complying with the hardware gradient constraints. This encoding scheme has been first validated for 2D T_2^*-w MR anatomical imaging [Laz+19] and then extended to 3D imaging [Laz+20; Cha+22] under the name 3D-SPARKLING. 3D-SPARKLING shows promise in addressing the challenge of improving spatiotemporal resolution in fMRI without compromising brain coverage, and it will be the central focus of this work. That being said, when targeting high-resolution fMRI for large or full brain coverage, even with efficient undersampling techniques, BOLD sensitivity is significantly compromised due to smaller voxels (meaning there is less BOLD signal available voxel-wise), increased noise, and higher sensitivity to physiological noise. This is why moving to higher field strength is utilized as a BOLD sensitivity booster in such a case. This, to a large extent, justifies the push for higher field strengths, as seen with the 11.7T Iseult MR scanner [Ved+14; Que+23] and the envisioned 14T scanner by the DYNAMIC consortium set to be located in Nijmegen [Bat+23]. However, collecting data at higher magnetic fields also introduces new challenges: Static and dynamic magnetic field imperfections become more prominent at higher fields and ought to be compensated for or corrected if need be. This will also be a pivotal issue in this work.

Thesis Outline

This manuscript is divided into two main parts: The first presents the background and the basic concepts necessary to understanding the challenge of high-resolution fMRI at ultra-high magnetic fields. The second presents the contributions of this work. We start by describing the first part.

Chapter 1: *Unraveling brain function by subjecting nuclear spins to magnetic fields* provides an overview of the fundamental principles governing Magnetic Resonance Imaging (MRI) and its application in fMRI. We introduce the physics of MRI, elucidating Nuclear Magnetic Resonance (NMR) principles, how MR images are formed, and some practical considerations in MRI technology today. Then, we focus on the principles specific to fMRI, including neurovascular coupling, BOLD contrast, and the Hemodynamic Response Function (HRF). We further cover T2 and T*2-weighted fMRI scanning methodologies, encompassing Gradient-Recalled-Echo (GRE) and Spin-Echo (SE) sequences. This chapter very briefly addresses practical aspects of task-based BOLD fMRI, such as experimental design, preprocessing, and statistical analysis. Finally, it discusses contemporary challenges in BOLD fMRI, such as the sensitivity vs. specificity trade-off, magnetic field inhomogeneities, and the impact of motion and physiological noise.

Chapter 2: *Achieving higher spatiotemporal resolution in fMRI through k-space undersampling* is dedicated to the exploration of various strategies and methodologies aimed at accelerating fMRI acquisitions. First, in the Cartesian framework, we discuss how to accelerate fMRI acquisitions using accelerated echo planar imaging (EPI) and parallel imaging (PI) to achieve higher resolution. Second, we explore the potential of non-Cartesian readouts in accelerating fMRI acquisitions. Finally, a significant focus is placed on the application of CS to fMRI, covering the principles of sparsity and nonlinear reconstructions. The innovative 3D-SPARKLING technique, a key aspect of this work, is introduced, and its theoretical underpinnings are discussed.

Chapter 3: *Ultra High Field (UHF) fMRI* motivates the rationale for Ultra High Field (UHF) fMRI, providing a discussion of its advantages while also addressing the associated challenges. A special emphasis is put on magnetic field imperfections and the different solutions to overcome them. More specifically, aspects of using a field monitoring camera for this purpose are explored.

We then shift our focus to the three main contributions of this thesis, which constitute the second part of this manuscript. In Chapter 4: *Experimental setup for non-Cartesian CS-based 3D-SPARKLING high spatial resolution fMRI*, we introduce the different steps of the experimental protocol we opted for, in the rest of this work, to collect high-resolution *in vivo* fMRI data with 3D-SPARKLING.

First contribution: In Chapter 5: *Evaluation of 3D-SPARKLING fMRI against the state-of-the-art 3D-EPI*, we investigate the use of a finely tuned version of the CS-based 3D-SPARKLING and compare it to state-of-the-art Cartesian 3D-EPI during both a retinotopic mapping paradigm and resting-state acquisitions at 1mm^3 (isotropic spatial resolution) and a temporal resolution of 2.4s for whole-brain fMRI at 7T. This study involves six healthy volunteers, and both acquisition sequences were run on each individual in a balanced order across subjects. The performances of both acquisition techniques are compared to one another in regard to tSNR, sensitivity to the BOLD effect, and spatial specificity.

Second contribution: In Chapter 6: *Impact of $\mathbf{B}_0$ field imperfections correction on BOLD sensitivity in 3D-SPARKLING fMRI data*, we adapt the experimental protocol to enable the use of Skope's Clip-on field camera 3D-SPARKLING fMRI challenging its long TR_{probe} constraint (by using an external spoiling gradient) and evaluate it for 1mm^3 3D-SPARKLING retinotopic mapping and resting-state fMRI acquisitions. We demonstrate the feasibility of our experimental protocol and study the impact of static and dynamic $\mathbf{B}_0$ field imperfections correction during image reconstruction on fMRI data in terms of image quality, tSNR, sensitivity to the BOLD contrast, and quality of the retinotopic maps. The study is conducted on three different healthy volunteers.

Third contribution: In Chapter 7: *Sliding-window reconstruction for improved temporal resolution in SPARKLING fMRI*, we explore the potential benefit of combining the sliding-window image reconstruction with the SPARKLING encoding scheme, taking advantage of its intrinsic properties, to increase the temporal resolution of fMRI sequence of images. A simulation study with a controlled ground truth is conducted. This study serves as a demonstration designed to showcase to which extent it is possible to detect high-frequency oscillations in the BOLD signal and disentangle physiological noise, such as breathing, from neural activity using a sliding-window reconstruction. To maintain computational simplicity and clear demonstration, BOLD fMRI simulation data was generated in 2D using 2D-SPARKLING. The extension of the implementation of such a technique in 3D is straightforward. However, the findings need to be validated in 3D and *in vivo*.

Finally, in Chapter 8: *General conclusions and perspectives* we summarize the contributions of this thesis and discuss the future directions and perspectives.

In Appendix A: *Evaluation of 3D-SPARKLING fMRI against the state-of-the-art 3D-EPI* and Appendix B: *Impact of $\mathbf{B}_0$ field imperfections correction on BOLD sensitivity in 3D-SPARKLING fMRI data* we present some additional results to complete Chapter 5 and Chapter 6 respectively.

In Appendix C: *Preliminary in vivo validation of the sliding-window image reconstruction technique for 3D-SPARKLING fMRI data*, we briefly present preliminary results to test the sliding-window approach in 3D-SPARKLING fMRI data acquired *in vivo*. We discuss its validity and limitations.

* * *
* *
*

Résumé en Français

Contexte & Motivations

L'IMAGERIE par résonance magnétique fonctionelle (IRMf) est, aujourd'hui, l'une des techniques d'imagerie non-invasive les plus puissantes utilisées en neuroimagerie. Cette technique offre des avantages qui lui sont particuliers en comparison avec d'autre methodes non-invasives telles que l'électroencéphalographie (EEG) et la magnétoencéphalographie (MEG). Alors que l'EEG et la MEG fournissent des mesures directes de l'activité neuronale avec une résolution temporelle excellente, ces modalités d'imagerie sont limitées en terme de localisation spatiale. En revanche, l'un des principaux atouts de l'IRMf réside dans le fait qu'il est possible d'obtenir de meilleures résolutions spatiales et de réduire l'incertitude de la localisation de l'activité du cerveau malgré une précision temporelle modérée. En effet, l'IRMf capture des changements hémodynamiques et métaboliques qui résultent de l'activité neuronale, et fournit ainsi des mesures indirectes (et lentes) mais néanmoins éclairantes, des fonctions cérébrales.

Pour comprendre l'origine du phénomène, il faut remonter à 1880, lorsque A. Musso a introduit ce qu'il a appelé la méthode de "Human circulation balance". L'idée était de déduire le changement du flux sanguin dans le cerveau suite à une augmentation de l'activité cérébrale. Le dispositif expérimental consistait à allonger les participants sur une balance sous forme de table et à leur présenter des stimuli ou à leur demander d'effectuer une tâche cognitive. Musso a observé que la balance basculait vers la tête des participants lorsqu'ils effectuaient la tâche. Cela dit, c'est à la fin du 20e siècle que les étapes clés les plus cruciales de l'IRMf ont eu lieu.

En 1990, la découverte révolutionnaire de S. Ogawa du contraste "Blood Oxygenation Level-Dependent" (BOLD) [Oga+90] chez les rongeurs a marqué un tournant dans l'histoire de l'IRMf. Son premier objectif était d'imager le cerveau des rongeurs avec un contraste élevé pour voir s'il était possible de détecter des changements physiologiques. Au cours de ses expériences sur des souris anesthésiées, il a remarqué des lignes noires intra-corticales sur des images acquises par résonance magnétique (RM) qui disparaissaient lorsqu'il remplaçait l'air respiré par les rongeurs par de l'oxygène pur (O_2). Des experiences supplémentaires ont révélé une disparition similaire des lignes noires lors de l'acquisition d'images du cerveau d'une souris euthanasiée au monoxyde de carbone (CO). Le dénominateur commun à ces deux expériences était une altération, déclenchée de manière chimique, des concentrations d'oxyhémoglobine et de désoxyhémoglobine dans le sang. La présence ou l'absence de lignes noires s'expliquait par des changements locaux du champ magnétique induites par des variations de la susceptibilité magnétique autour des vaisseaux sanguins : Le contraste BOLD était né.

En 1992, les premiers articles faisant état d'expériences d'IRMf BOLD endogène (sans agent de contraste externe) ont été publiés par P. Bandettini [Ban+92], S. Ogawa [Oga+92] et K. K. Kwong [Kwo+92]. Des stimulations motrices et/ou visuelles ont été mises en œuvre et des changements de signaux en corrélation avec les tâches ont été observés, révélant des activations dans le cortex moteur et/ou visuel : L'IRMf BOLD était née.

Depuis sa création, l'IRMf a connu des progrès significatifs en termes de méthodologie de l'IRM, de pré-traitement des données et d'outils d'analyse statistique, et cette méthode a été utilisée sur des animaux non-humains comme sur des humains. En ce qui concerne la méthodologie de l'IRM, des progrès ont été réalisés au niveau du matériel (hardware), y compris le developement d'aimants générant des champs magnétiques avec des intensités de

plus en plus élevées. et une conception de plus en plus efficace des gradients d'encodage et des antennes de transmission et de réception. Parallèlement, des développements logiciels (software) axés sur l'amélioration de l'acquisition des données IRMf et des stratégies de reconstruction d'images ont aussi été entrepris. L'objectif est d'améliorer la sensibilité et la spécificité, c'est-à-dire la capacité à détecter l'effet BOLD le plus faible avec la plus grande précision spatiale (en améliorant la résolution) et d'élargir la gamme des contrastes utiles au-delà du, traditionnel, contraste BOLD, qui reste encore aujourd'hui le choix prédominant. Les outils de prétraitement et d'analyse statistique ont aussi évolué, passant d'approches conventionnelles fondées sur le traitement des images et l'analyse de régression standard à des modèles d'encodage et de décodage de l'activité cérébrale plus complexes.

En outre, les applications de l'IRMf sont passées de l'étude des fonctions sensorimotrices à des fonctions cognitives plus complexes telles que le langage, les mathématiques, l'apprentissage et la prise de décision. En revanche, la reproductibilité reste un problème persistant malgré la disponibilité de nombreux jeux (sets) de données d'IRMf publiques et en libre accès (open-source) et l'homogénéisation de nombreuses pipelines de pré-traitement. Ceci étant dit, la robustesse de cette méthode pour des applications cliniques reste un objectif qui est actuellement, pour la plupart, hors de portée.

Plus généralement, dans tous les sous-domaines mentionnés (méthodologie de l'IRM, outils de pré-traitement et d'analyse, applications en neurosciences cognitives et cliniques), les chercheurs poursuivent leurs efforts pour améliorer la résolution spatio-temporelle, la robustesse de l'analyse et la pertinence des applications. Ils sont convaincus que ces efforts collectifs finiront par converger et donneront naissance à une méthode de neuroimagerie extrêmement fiable et efficace pour l'étude du cerveau sain et pathologique.

Dans le cadre de ce projet de doctorat, nous nous sommes concentrés sur l'aspect méthodologique de l'IRM. Plus précisément, nous nous sommes concentrés sur des aspects relatifs à l'acquisition et la reconstruction d'images acquises par résonance magnétique, en les adaptant de manière pratique pour acquérir et reconstruire des données d'IRMf à haute résolution spatio-temporelle. La recherche d'une résolution spatiale et/ou temporelle plus élevée en IRMf tout en préservant un rapport signal/bruit temporel (tSNR) suffisamment élevé et sans sacrifier la couverture du cerveau en entier a généré un nombre considérable de contributions méthodologiques au cours des dernières décennies. Ces développements vont des méthodes cartésiennes [Pos+10] vs. non-cartésiennes [Glo12] aux stratégies d'acquisition 2D vs. 3D pour l'imagerie parallèle et/ou les méthodes d'accélération basées sur l'échantillonnage compressif (CS) [LDP07], en passant par les acquisitions multicoupes simultanées [Moe+10] pour n'en citer que quelques-uns. L'échantillonnage compressif permet une reconstruction presque exacte des signaux à partir de mesures fortement sous-échantillonnées à l'aide de schémas d'échantillonnage pseudo-aléatoires et de méthodes de reconstruction non linéaires, pour autant que les signaux originaux admettent une représentation parcimonieuses dans un domaine (via une transformation mathématique) approprié. En IRM basé sur l'échantillonnage compressif, le sous-échantillonnage pseudo-aléatoire opère dans l'espace k (k-space), qui correspond à la transformée de Fourier de l'image IRM, avec une densité variable qui échantillonne densément le centre de l'espace k et de manière parcimonieuse sa périphérie pour récupérer des images IRM avec des artefacts de bas-niveau qui ressemblent à du bruit blanc et un bon contraste d'imagerie. La parcimonie des images IRM est généralement appliquée dans une base d'ondelettes (wavelets) spatiales. L'échantillonnage compressif a été appliquée à l'IRM dans le cadre des méthodes d'acquisition cartésiennes et non cartésiennes [BUF07; Lus+08; Fen+14; Cha+14b]. Cependant, aujourd'hui, l'utilisation de l'échantillonnage compressif dans l'IRMf reste limitée et se cantonne aux méthodes basée sur des schémas d'échantillonnage en spirale.

Néanmoins, P. Ciuciu et ses collaborateurs ont récemment développé SPARKLING (Spreading Projection Algorithm for Rapid K-space sampLING) pour accélérer l'imagerie IRM en utilisant des principes basés sur la théorie de l'échantillonnage compressif. SPARKLING met en œuvre l'échantillonnage à densité variable (VDS) tout en respectant les contraintes physiques et matérielles du système de gradient. Ce schéma d'encodage a été validé pour la première fois pour l'imagerie IRM anatomique en 2D T_2^*-w [Laz+19] puis étendu en 3D [Laz+20; Cha+22] sous le nom de 3D-SPARKLING. 3D-SPARKLING est favorable pour

relever le défi de l'amélioration de la résolution spatio-temporelle de l'IRMf sans compromettre la couverture du cerveau en entier, et cette méthode sera au centre de ce travail. Ceci étant dit, lorsque l'on cible l'IRMf à haute résolution pour une couverture large ou complète du cerveau, même avec des techniques de sous-échantillonnage efficaces, la sensibilité au signal BOLD est considérablement compromise en raison de voxels plus petits (ce qui signifie qu'il y a moins de signal BOLD disponible par voxel), d'un bruit thermique accru et d'une plus grande sensibilité au bruit physiologique. C'est pourquoi le passage à une intensité de champ plus élevée est utilisé pour augmenter la sensibilité au signal BOLD dans un tel cas. C'est ce qui justifie dans une large mesure les efforts en recherche pour atteindre des intensités de champ plus élevées, comme c'est le cas avec le scanner IRM Iseult 11,7T [Ved+14; Que+23] et le scanner 14T envisagé par le consortium DYNAMIC, qui devrait être situé à Nijmegen [Bat+23]. Cependant, la collecte de données à des champs magnétiques plus élevés pose également de nouveaux défis : Les imperfections statiques et dynamiques du champ magnétique deviennent plus importantes à des champs plus élevés et doivent être compensées ou corrigées si nécessaire. Il s'agit là d'une question essentielle dans le cadre de ce travail.

Thesis Outline

Ce manuscrit est divisé en deux parties principales : La première présente le contexte et les concepts de base nécessaires pour comprendre le défi que représente l'IRMf à haute résolution à des champs magnétiques ultra-élevés. La seconde présente les contributions de ce travail. Nous commençons par décrire la première partie.

Chapter 1: *Unraveling brain function by subjecting nuclear spins to magnetic fields* fournit une vue d'ensemble des principes fondamentaux régissant l'imagerie par résonance magnétique (IRM) et son application à l'IRMf. Nous présentons la physique de l'IRM, en élucidant les principes de la résonance magnétique nucléaire (RMN), la façon dont les images sont formées en IRM et certaines considérations pratiques de la technologie IRM d'aujourd'hui. Nous nous concentrons ensuite sur les principes propres à l'IRMf, notamment le couplage neurovasculaire, le contraste BOLD et la fonction de réponse hémodynamique (HRF). Nous couvrons également les méthodologies d'acquisition IRMf pondérées T_2 et T^*_2, y compris les séquences Gradient-Recalled-Echo (GRE) et Spin-Echo (SE). Ce chapitre aborde très brièvement les aspects pratiques de l'IRMf BOLD basée sur une tâche (task-based), tels que la conception expérimentale, le pré-traitement et l'analyse statistique. Enfin, il aborde les défis contemporains de l'IRMf BOLD, tels que le compromis sensibilité/spécificité, les inhomogénéités du champ magnétique et l'impact du mouvement et du bruit physiologique.

Chapter 2: *Achieving higher spatiotemporal resolution in fMRI through k-space undersampling* est consacré à l'exploration de diverses stratégies et méthodologies d'acquisition visant à accélérer les acquisitions d'IRMf. Tout d'abord, dans le cadre cartésien, nous examinons comment accélérer les acquisitions d'IRMf en utilisant l'imagerie écho planaire accélérée (EPI) et l'imagerie parallèle (PI) pour obtenir une plus grande résolution. Ensuite, nous explorons le potentiel des méthodes non cartésiennes pour accélérer les acquisitions d'IRMf. Enfin, l'accent est mis sur l'application de l'échantillonnage compressif à l'IRMf, couvrant les principes de parcimonie et les reconstructions non linéaires. La technique innovante 3D-SPARKLING, un aspect clé de ce travail, est présentée et ses fondements théoriques sont discutés.

Chapter 3: *Ultra High Field (UHF) fMRI* motive la raison d'être de l'IRMf à ultra-haut champ (UHF), en discutant de ses avantages tout en abordant les défis qui y sont associés. L'accent est mis sur les imperfections du champ magnétique et les différentes solutions pour les surmonter. Plus précisément, les aspects de l'utilisation d'une caméra de contrôle de champ à cette fin sont explorés.

Nous nous concentrons ensuite sur les trois principales contributions de cette thèse, qui constituent la deuxième partie de ce manuscrit. Dans Chapter 4: *Experimental setup for non-Cartesian CS-based 3D-SPARKLING high spatial resolution fMRI*, nous présentons les différentes étapes du protocole expérimental que nous avons choisi, dans la suite de ce travail, pour recueillir des données IRMf haute résolution *in vivo* avec 3D-SPARKLING.

Première contribution: Dans Chapter 5: *Evaluation of 3D-SPARKLING fMRI against the state-of-the-art 3D-EPI*, nous étudions l'utilisation d'une version affinée du 3D-SPARKLING et nous le comparons à l'état de l'art cartésien 3D-EPI sur un paradigme de cartographie rétinotopique et des acquisitions de l'état de repos à 1mm^3 (résolution spatiale isotropique) et une résolution temporelle de 2,4s pour l'IRMf du cerveau entier à 7T. Cette étude porte sur six volontaires sains, et les deux séquences d'acquisition ont été exécutées sur chaque individu dans un ordre équilibré entre les sujets. Les performances des deux techniques d'acquisition sont comparées l'une à l'autre en ce qui concerne le tSNR, la sensibilité à l'effet BOLD et la spécificité spatiale.

Tout d'abord, en ce qui concerne les données d'IRMf au repos, nous montrons que 3D-EPI produit une meilleure qualité d'image que 3D-SPARKLING. D'autre part, 3D-SPARKLING produit un tSNR plus élevé chez tous les participants sur l'ensemble du cerveau, mais surtout dans le lobe occipital. Sur les données IRMf liées à la tâche, nous avons vérifié la validité des données IRMf rétinotopique, c'est-à-dire la capacité à détecter une activité cérébrale évoquée dans le cortex visuel à 7T pour l'ensemble des paramètres d'acquisition que nous avons pris en compte, notamment la résolution spatio-temporelle et les deux schémas d'encodage. Malgré la qualité modérée des cartes de phase BOLD produites par les données collectées, il est possible de récupérer une cartographie modérément fiable des aires visuelles sur la surface corticale. Deuxièmement, nous avons démontré que 3D-SPARKLING a une meilleure sensibilité à l'effet BOLD dans la matière grise et une meilleure spécificité spatiale. Comparé à 3D-EPI, 3D-SPARKLING produit, en moyenne, 7% de voxels activés en plus dans la matière grise par rapport au nombre total de voxels activés. Cela dit, nous avons observé que 3D-SPARKLING est pénalisé par sa grande sensibilité aux imperfections du champ B_0, et que la simple correction du terme statique apporte des améliorations limitées. Il convient de noter qu'à l'instar de l'implémentation 3D-EPI que nous avons utilisée, d'autres techniques récentes d'IRMf telles que [Kas+22] et [GMC22] effectuent des corrections des fluctuation dynamiques du champ dynamique dans l'imagerie non cartésienne au niveau de l'étape de reconstruction des images. Pour ce faire, ils ont utilisé soit des estimations externes provenant d'une caméra de champ, soit leur séquence d'une manière auto-navigatée. Notre objectif suivant était d'étudier comment ce type de correction affecte positivement les données IRMf 3D-SPARKLING.

Deuxième contribution: Dans Chapter 6: *Impact of $\mathbf{B}_0$ field imperfections correction on BOLD sensitivity in 3D-SPARKLING fMRI data*, nous adaptons le protocole expérimental pour permettre l'utilisation de la caméra de champ de Skope pour l'IRMf 3D-SPARKLING en défiant sa contrainte de TR_{probe} long (en utilisant un gradient de spoiling externe) et nous l'évaluons pour la cartographie rétinotopique 3D-SPARKLING de 1mm^3 et les acquisitions d'IRMf à l'état de repos. Nous démontrons la faisabilité de notre protocole expérimental et étudions l'impact de la correction statique et dynamique des imperfections du champ $\mathbf{B}_0$ pendant la reconstruction de l'image sur les données d'IRMf en termes de qualité d'image, de tSNR, de sensibilité au contraste BOLD et de qualité des cartes rétinotopiques. L'étude est menée sur trois volontaires sains différents.

La correction des imperfections de B_0 a amélioré la qualité de l'image et a entraîné une augmentation de 20 à 30% du rapport signal/bruit temporel médian (tSNR). En utilisant les données d'IRMf recueillies au cours d'une expérience de cartographie rétinotopique, nous avons démontré une augmentation significative de la sensibilité au contraste BOLD et une amélioration de la précision des cartes de phase BOLD : 44% (resp., 159%) de voxels activés en plus ont été récupérés lors de l'utilisation d'un niveau de contrôle de signification basé sur

une valeur p de 0,001 sans correction pour les comparaisons multiples (resp., 0,05 avec une correction du taux de fausse découverte (FDR)).

Le prochain et dernier objectif de ce travail est d'explorer la possibilité d'améliorer rétrospectivement la résolution temporelle par une approche de fenêtre glissante, en particulier dans le contexte des acquisitions SPARKLING, dans le but de découvrir sa viabilité, ses capacités et ses limites.

Troisième contribution: Dans Chapter 7: *Sliding-window reconstruction for improved temporal resolution in SPARKLING fMRI*, nous explorons les avantages potentiels de la combinaison de la reconstruction d'images par fenêtre glissante avec le schéma d'encodage SPARKLING, en tirant parti de ses propriétés intrinsèques, pour augmenter la résolution temporelle d'une séquence d'images d'IRMf. Une étude de simulation avec une vérité terrain contrôlée est réalisée. Cette étude sert de démonstration pour montrer dans quelle mesure il est possible de détecter les oscillations à haute fréquence dans le signal BOLD et de séparer le bruit physiologique, tel que la respiration, de l'activité neuronale à l'aide d'une reconstruction par fenêtre glissante. Afin de préserver la simplicité du calcul et la clarté de la démonstration, les données de simulation IRMf BOLD ont été générées en 2D à l'aide de 2D-SPARKLING.

Sur des données de simulation de d'IRMf 2D, nous avons démontré qu'une méthode de reconstruction à fenêtre glissante permet de suivre les oscillations BOLD au-delà de 0,2Hz (et même jusqu'à 0,5Hz) et de démêler le bruit physiologique de l'activité neuronale à des SNR/tSNR réalistes. L'extension de la mise en œuvre d'une telle technique en 3D est simple. Toutefois, les résultats doivent être validés en 3D et *in vivo*.

Finalement, dans Chapter 8: *General conclusions and perspectives* nous résumons les contributions de cette thèse et discutons des orientations et perspectives futures.

Dans Appendix A: *Evaluation of 3D-SPARKLING fMRI against the state-of-the-art 3D-EPI* et Appendix B: *Impact of $\mathbf{B}_0$ field imperfections correction on BOLD sensitivity in 3D-SPARKLING fMRI data* nous présentons quelques résultats supplémentaires pour compléter le chapitre 5 et le chapitre 6 respectivement.

Dans Appendix C: *Preliminary in vivo validation of the sliding-window image reconstruction technique for 3D-SPARKLING fMRI data*, nous présentons brièvement les résultats préliminaires obtenus pour tester l'approche de la fenêtre coulissante dans les données IRMf 3D-SPARKLING acquises *in vivo*. Nous discutons de sa validité et de ses limites.

* * *
* *
*

Publications

Accepted articles in Peer-Reviewed Journals

- **Z. Amor**, C. Le Ster, G. Chaithya, G. Daval-Frérot, N. Boulant, F. Mauconduit, B. Thirion, P. Ciuciu and A. Vignaud. "Impact of B_0 field imperfections correction on BOLD sensitivity in 3D-SPARKLING fMRI data". In: *Magnetic Resonance in Medicine* 91.4 (2024), pp. 1434–1448
- **Z. Amor**, P. Ciuciu, G. Chaithya, G. Daval-Frérot, F. Mauconduit, B. Thirion and A. Vignaud. "Non-Cartesian 3D-SPARKLING vs Cartesian 3D-EPI encoding schemes for functional Magnetic Resonance Imaging at 7 Tesla". In: *PLoS One, Accepted* (2024)

Accepted papers in Peer-reviewed Conferences

- **Z. Amor**, C. Le Ster, P.-A. Comby, A. Vignaud and P. Ciuciu. "Non-Cartesian non-Fourier fMRI imaging for high-resolution retinotopic mapping at 7 Tesla". In: *9th IEEE International Workshop on Computational Adavnces in Multi-Sensor Adaptive Processing (CAMSAP)*. Los Suenos, Costa Rica, 2023
- P.-A. Comby, **Z. Amor**, A. Vignaud and P. Ciuciu. "Denoising of fMRI volumes using local low rank methods". In: *20th IEEE International Symposium on Biomedical Imaging (ISBI)*. Cartagena de Indias, Colombia, 2023

Abstracts in Peer-reviewed Conferences

- **Z. Amor**, G. R. Chaithya, C. Le Ster, G. Daval-Frérot, N. Boulant, F. Mauconduit, C. Mirkes, P. Ciuciu and A. Vignaud. "B_0 field distortions monitoring and correction for 3D non-Cartesian fMRI acquisitions using a field camera: Application to 3D-SPARKLING at 7T". in: *ISMRM Annual Meeting*. London, UK, 2022
- **Z. Amor**, G. R. Chaithya, G. Daval-Frérot, B. Thirion, F. Mauconduit, C. Mirkes, P. Ciuciu and A. Vignaud. "Prospects of non-Cartesian 3D-SPARKLING encoding for functional MRI: A preliminary case study for retinotopic mapping". In: *ISMRM Annual Meeting*. London, UK, 2022
- **Z. Amor**, G. R. Chaithya, G. Daval-Frérot, B. Thirion, F. Mauconduit, P. Ciuciu and A. Vignaud. "3D-SPARKLING for functional MRI: A pilot study for retinotopic mapping at 7T". in: *OHBM*. Glasgow, Scotland, UK, 2022
- **Z. Amor**, C. Le Ster, G. R. Chaithya, G. Daval-Frérot, B. Thirion, N. Boulant, F. Mauconduit, C. Mirkes, P. Ciuciu and A. Vignaud. "Impact of ΔB_0 imperfections correction on BOLD sensitivity in 3D-SPARKING fMRI data". In: *ISMRM Annual Meeting*. Toronto, ON, Canada, 2023
- **Z. Amor**, P.-A. Comby, P. Ciuciu and A. Vignaud. "Achieving high temporal resolution using a sliding-window approach for SPARKLING fMRI data: A simulation study". In: *ISMRM Annual Meeting, (in press)*. Singapore, 2024

Part I

Background

Chapter 1

Unraveling brain function by subjecting nuclear spins to magnetic fields

This chapter is a comprehensive overview of Magnetic Resonance Imaging (MRI) as a pivotal tool in studying the structures and functions of the human body, specifically the brain, non-invasively. The first section of this chapter elucidates the fundamental physics of MRI, from the fundamental principles of Nuclear Magnetic Resonance (NMR) to the practicalities of MRI technology and signal acquisition. The second section focuses on functional MRI (fMRI) as a revolutionary technology at the intersection of neuroscience and medical imaging. A brief review of neurovascular coupling and the Blood Oxygenation Level-Dependent (BOLD) contrast sheds light on how neural activity translates into measurable signals. This is followed by discussing practical aspects such as scanning methodologies and experimental designs. This section concludes with a reflection on contemporary challenges in fMRI.

This chapter draws inspiration from the following books:

- Scott H. Faro and Feroze B. Mohamed, Functional MRI: Basic Principles and Clinical Applications [FHM06].
- Kamil Uludag and Kamil Ugurbil, fMRI: From Nuclear Spins to Brain Functions [UUB15].
- Massimo Filippi, fMRI Techniques and Protocols [Fil16].
- Hélène Ratiney and Olivier Beuf, Les enjeux de l'IRM - Techniques et méthodes quantitatives pour la santé [RB23].

1.1 Physics of MRI

1.1.1 NMR principles

First demonstrated by I. I. Rabi's team (1938) [Rab+38] using a molecular beam of lithium chloride (LiCl) that is placed in a vacuum and then further elucidated simultaneously and independently by F. Bloch's and E. M. Purcell's teams (1946) [Blo46; PTP46] in condensed matter, NMR studies chemicals through their interactions with magnetic fields.

Similarly to a rotating object that possesses an angular moment according to classical physics[1], nuclei are characterized by an intrinsic quantum property, the so-called nuclear spins denoted $\hbar I$, where $\hbar$ is Planck's constant divided by 2π, and I is the spin number. When the nucleus mass number $A = Z + N$, where Z (respectively, N) is the number of protons (respectively, neutrons), is odd, then the spin number I takes on values of either integers or half an integer, resulting in a non-zero $\hbar I$. Such a nucleus[2] exhibits a nuclear magnetic moment equal to $\gamma\hbar I$, where γ is called the gyromagnetic ratio, and will behave as a magnetic dipole. In the following, we illustrate the NMR phenomenon for ^{1}H, commonly referred to as a proton, a nucleus of particular interest, as it is abundant in human tissues. For ^{1}H, $I = \frac{1}{2}$ leading to two possible magnetic spin numbers $m_s = \pm\frac{1}{2}$.

Magnetization

Let us consider a sample of nuclei characterized by their non-zero spins. If placed in an external magnetic field $\mathbf{B}_0 = |\mathbf{B}_0|\mathbf{z}$, each of these individual nuclei will align with it either according to the same direction or the opposite one depending on the sign of their m_s. Moreover, individual nuclei will precess around $\mathbf{B}_0$ at a frequency that is proportional to $|\mathbf{B}_0|$, the so-called Larmor frequency $\omega_0 = \gamma|\mathbf{B}_0|$, inducing this way, at the level of the sample and at thermal equilibrium, an average macroscopic angular momentum denoted $\mathbf{M}_0$ and aligned with $\mathbf{B}_0$. $\mathbf{M}_0$ is defined in Eq.(1.1), where N_p is the number of protons in the sample, k Boltzmann's constant, γ is called the proton gyromagnetic ratio[3], and T_s the temperature of the sample in Kelvin:

$$\mathbf{M}_0 = \frac{N_p\gamma^2\hbar^2\mathbf{B}_0}{4kT_s}. \tag{1.1}$$

An alternative expression is $\mathbf{M}_0 = \chi_0\mathbf{B}_0$, where $\chi_0 = \frac{N_p\gamma^2\hbar^2}{4kT_s}$ is referred to as nuclear magnetic susceptibility. Considering the typical scale of χ_0, $\mathbf{M}_0$ is significantly weaker than $\mathbf{B}_0$: In [Abr61], $|\mathbf{M}_0|$ is quantified as 4.8pA/m for 1mm^3 of water, $|\mathbf{B}_0| = 1.5$ Tesla, and $T_s = 300$ Kelvin.

Excitation

As $\mathbf{M}_0$ is enveloped by the larger $\mathbf{B}_0$, it is challenging to perform a direct measurement of $\mathbf{M}_0$. An indirect measurement can be implemented through the application of an oscillating

[1] Although this analogy is useful to conceptualize this phenomenon visually, one needs to keep in mind that spins are quantum properties that describe the intrinsic nuclear angular momentum of nuclei and not a rotation as traditionally considered in classical physics.

[2] Such nuclei are for instance ^{1}H, ^{31}P, ^{23}Na, ^{19}F.

[3] 42.57MHz/T.

electromagnetic field pulse called $\mathbf{B}_1$. $\mathbf{B}_1$ needs to be perpendicular to $\mathbf{B}_0$, and if its oscillation frequency is equal to ω_0 then nuclear magnetic resonance is enabled (the nuclear spins absorb the energy delivered by $\mathbf{B}_1$): The net magnetization $\mathbf{M}_0$ is flipped by an angle α (known as flip angle) into the transverse plane, and can then be decomposed into a transverse component $\mathbf{M}_{xy}$ or $\mathbf{M}_T$ and a longitudinal component $\mathbf{M}_z$ or $\mathbf{M}_L$. The module of $\mathbf{B}_1$ and its duration denoted T_{B_1} characterizes the flip angle since $\alpha = \omega_1 \int_0^{T_{B_1}} |\mathbf{B}_1(t)|dt$.

Relaxation

Tipping $\mathbf{M}_0$ disrupts the spins system from its equilibrium state, and similarly to any physical system, it will tend to regain equilibrium by reverting to its initial state and, therefore, dispersing the absorbed energy away. We refer to this process as relaxation. It results from two major processes:

- Spin-spin relaxation: This refers to the energy exchange between the spins of the same system (considered confined). It describes how the spins that were, after excitation, initially coherent experience dephasing. In Fig. 1.1, we consider the particular case of $\alpha = 90°$: As the spins are dephased, the magnitude of the transversal component exponentially decreases over time according to a relaxation time denoted T_2, therefore $\mathbf{M}_T$ varies in time. We will then denote it $\mathbf{M}_T(t)$.

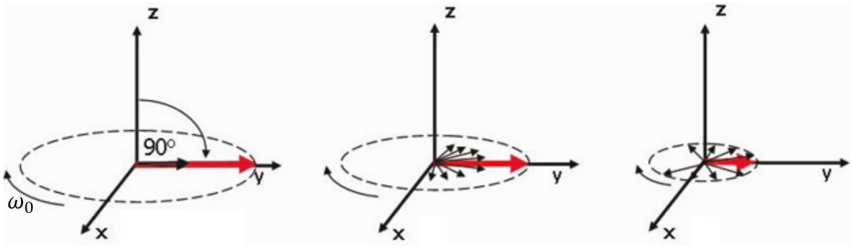

Figure 1.1: Spin-spin relaxation: As spins dephase, the transversal component's magnitude exponentially decreases over time, governed by the relaxation time T_2. $\alpha = 90°$ is considered here. In this illustration, a rotating frame at ω_0 is considered. (This figure is a modified version of that shown in [Rid10].)

- Spin-lattice relaxation: This refers to the transfer of energy from the excited spin system to the neighboring atoms (i.e., the lattice) and describes the exponential regrowth of the longitudinal component of magnetization ($\mathbf{M}_L(t)$) according to a relaxation time denoted T_1 as illustrated in Fig. 1.2

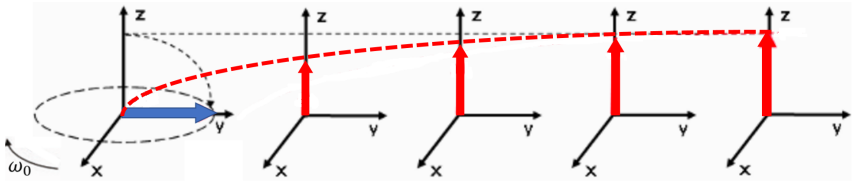

Figure 1.2: Spin-lattice relaxation: As energy is transferred from the excited spin system to the surrounding lattice, the longitudinal magnetization component ($\mathbf{M}_L(t)$) experiences an exponential regrowth over time, governed by a relaxation time denoted as T_1. In this illustration, a rotating frame at ω_0 is considered. (This figure is a modified version of that shown in [Rid10].)

In Fig. 1.1 and Fig. 1.2, we opted to position the spins system in the rotating (at the Larmor frequency ω_0) reference frame where the precession movement is no longer visible. However, in reality, it persists: Fig. 1.3 shows the trajectory of the tip of $\mathbf{M}(t) = \mathbf{M}_T(t) + \mathbf{M}_L(t)$ throughout the relaxation process for the specific case of $\alpha = 90°$. With that in mind, adopting

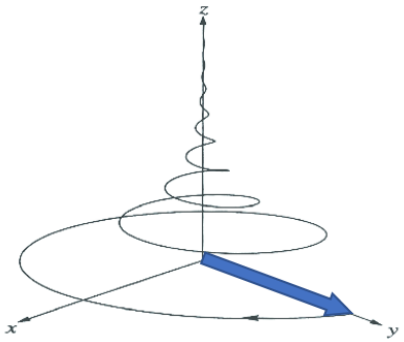

Figure 1.3: Trajectory of the tip of $\mathbf{M}(t) = \mathbf{M}_T(t) + \mathbf{M}_L(t)$ during relaxation in the non-rotating frame, also called laboratory frame. (This figure is an adapted version of that shown in [LL00]).

the rotating frame proves to be a convenient simplification hypothesis. Consequently, we will continue to consider this rotating frame hereafter. We will also consider the more general case of an arbitrary α. The evolution of $\mathbf{M}_T(t)$ and $\mathbf{M}_L(t)$ in time can be expressed according to the following Bloch equations:

$$\frac{d\mathbf{M}_T}{dt} = -\frac{\mathbf{M}_T}{T_2} \tag{1.2}$$

$$\frac{d\mathbf{M}_L}{dt} = \frac{\mathbf{M}_0 - \mathbf{M}_L}{T_1} \tag{1.3}$$

Eq. (1.2) and Eq. (1.3) develop into the hereafter formulas describing the so-called free induction decay (FID) signal.

$$\mathbf{M}_T(t) = \mathbf{M}_T(0)e^{\frac{-t}{T_2}} \tag{1.4}$$

$$\mathbf{M}_L(t) = \mathbf{M}_L(0)e^{\frac{-t}{T_1}} + \mathbf{M}_0(1 - e^{\frac{-t}{T_1}}) \tag{1.5}$$

T_2 (respectively, T_1), mentioned earlier, is called transversal (respectively, longitudinal) relaxation time. In reality, T_2 is accompanied by a second relaxation time denoted $T_2^{'}$ and due to local inhomogeneities in $\mathbf{B}_0$, denoted ΔB_0. These inhomogeneities accelerate spin dephasing and accentuate signal loss due to the loss of coherence between the spins. While T_2 acts at the microscopic level of the spins, $T_2^{'}$ indicates local differences in $\mathbf{B}_0$ at the mesoscopic and macroscopic scales. Globally, a T_2^* relaxation time is defined as $\frac{1}{T_2^*} = \frac{1}{T_2} + \frac{1}{T_2^{'}}$. Building on these relaxation times, we can express the relaxation rates as $R_1 = \frac{1}{T_1}$, $R_2 = \frac{1}{T_2}$, and $R_2^* = \frac{1}{T_2^*}$.

1.1.2 MRI

The FID signal described in the previous section is global information that is agnostic to the local spatial differences. Fortunately, almost 30 years after the discovery of the NMR phenomenon (i.e., one generation later), P. Lauterbur [Lau73a] and Sir P. Mansfield [MM77] succeeded in obtaining spatially-localized information from this signal (Fig. 1.4). Both used varying magnetic fields on top of the homogeneous and constant $\mathbf{B}_0$. The idea behind this was that if the precession frequency is proportional to the magnetic field, applying gradient magnetic fields ($\mathbf{G} = (G_x, G_y, G_z)$) means that ω becomes $\omega(t, x, y, z) = \gamma(|\mathbf{B}_0| + G_x(t)x + G_y(t)y + G_z(t)z)$. This spatial dependency of the precession frequency is useful to localize the transverse component of the FID signal in space.

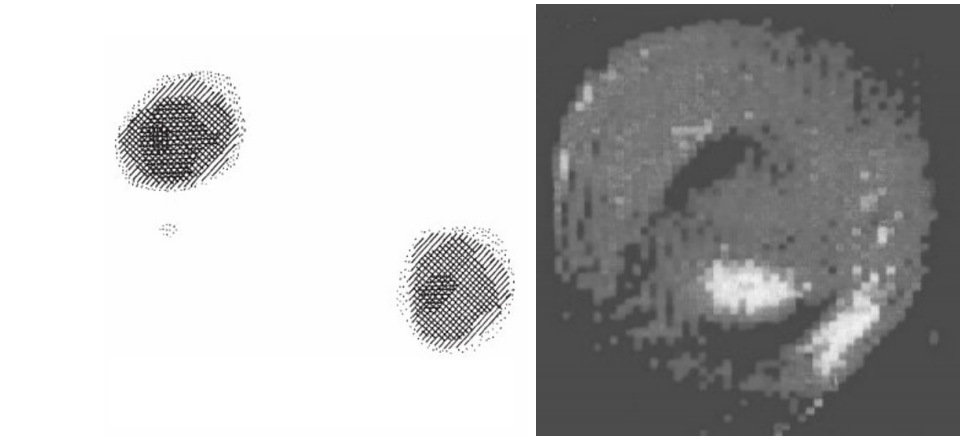

Figure 1.4: Left: MR image acquired by P. Lauterbur and taken from [Lau73a]. MR image, performed at 1.4T, of two water tubes, 1-mm-diameter each - Right: MR image acquired by Sir P. Mansfield and taken from [MM77]. MR image of the transversal plane of a human finger performed at 0.35T.

Image formation

In Eq.(1.2), $\mathbf{M}_T(t)$ has two components $\mathbf{M}_x(t) = |\mathbf{M}_T(t)|cos(\omega t)$ and $\mathbf{M}_y(t) = |\mathbf{M}_T(t)|sin(\omega t)$. Therefore, we can rewrite it, while ignoring $e^{\frac{-t}{T_2}}$ and considering a specific spatial location (x, y, z), as $\mathbf{M}_T(t, x, y, z) = |\mathbf{M}_T(t, x, y, z)|e^{-i\omega(t,x,y,z)t}$. The MR signal denoted $S(t)$ measured at time t is the summation of $\mathbf{M}_T(t, x, y, z)$ over the acquisition field-of-view (FOV) and is expressed as the following,

$$S(t) = \int_{FOV} \overbrace{|\mathbf{M}_T(t=0,x,y,z)|e^{-i\gamma|\mathbf{B}_0|t}}^{M(t=0,x,y,z)} \overbrace{e^{-i\gamma \int_0^t G_x(t')x + G_y(t')y + G_z(t')zdt'}}^{e^{-2i\pi(k_x(t)x+k_y(t)y+k_z(t)z)}} dxdydz \tag{1.6}$$

where $\mathbf{k}(t) = (k_x(t), k_y(t), k_z(t))$ describes the spatial frequencies (also called, k-space locations) for which the MR signal is encoded.

$$k_i(t) = \frac{\gamma}{2\pi} \int_0^t G_i(t')dt', \text{ where } i = x, y, z \tag{1.7}$$

In practice, $M(t = 0, x, y, z)$ represents the image domain, and the domain in which the MR signal is captured is called k-space. Eq. (1.6) and Eq. (1.8) demonstrate that a Fourier transform binds the complex signal acquired during an MRI acquisition to the corresponding (also complex) image (I) through the so-called k-space locations $\mathbf{k}$.

$$I(x, y, z) = M(t = 0, x, y, z) = \int_0^t S(t')e^{2i\pi(k_x(t')x+k_y(t')y+k_z(t')z)}dt' \tag{1.8}$$

We can define $K = [\mathbf{k}(0), ..., \mathbf{k}(t)]$ as the set of k-space locations considered, and it usually constitutes a continuous trajectory. Since I and S are linked by a Fourier transform, it is crucial to meet the Nyquist-Shannon theorem in order to produce images without aliasing artifacts, specifically:

- The k-space samples need to be spaced by $\Delta k_i = \frac{1}{FOV_i}$, where $i = x, y, z$.
- The furthest k-space location from the center of k-space $k_{i,max} \geq \frac{1}{2\Delta i}$, where $\Delta i,\ i = x, y, z$ are the voxels dimensions.

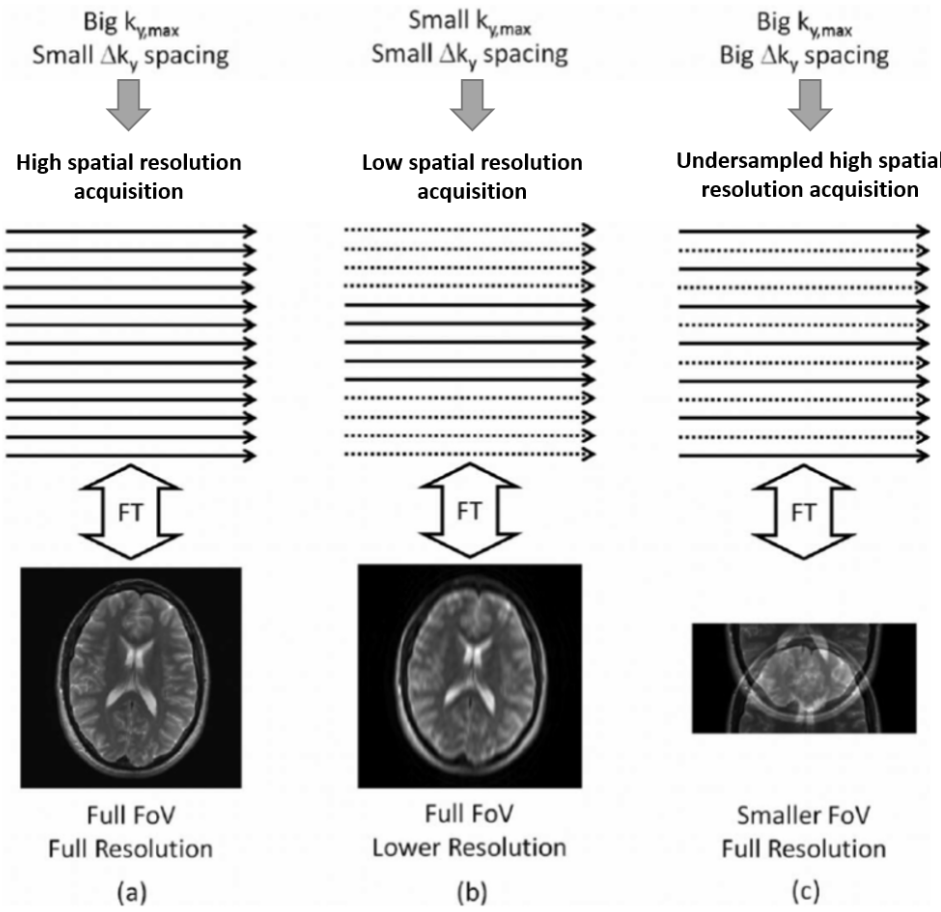

Figure 1.5: Nyquist-Shannon Criterion in MRI acquisition: (a) Nyquist-Shannon criterion is respected for high and (b) low spatial resolution MR imaging. (c) An aliased high spatial resolution MR image acquired by undersampling the k-space below the Nyquist-Shannon criterion. (This figure is an adapted version of that shown in [Des+12]).

The most typical and easiest-to-implement trajectory (K) is a line on a Cartesian grid as shown in Fig. 1.5 (a), and an MR image (respectively, volume) is acquired by sampling the entire 2D (respectively, 3D) k-space grid line by line. According to the Nyquist-Shannon criterion, when considering a constant FOV_i, it follows that the higher the spatial resolution increases (Δi decreases), the k-space grid that needs to be sampled becomes larger ($k_{i,max}$ increases). Consequently, the duration needed for the complete sampling process is elongated. This means that a compromise between the spatial resolution and MR image/volume acquisition time needs to be found. Conversely, if the objective is to diminish the acquisition time while maintaining a consistent field of view (i.e., the same Δk_i), it becomes necessary to decrease $k_{i,max}$. This, in turn, results in a reduction in resolution (cf. Fig. 1.5 (b)). Attempting to reduce the acquisition time by increasing Δk_i (i.e., undersampling the k-space below the Nyquist-Shannon criterion) while concurrently maintaining the same spatial resolution (and therefore $k_{i,max}$) gives rise to aliasing artifacts (cf. Fig. 1.5 (b)). This characteristic is a key factor contributing to the inherently slow nature of MRI as an imaging modality.

MRI in practice

The initial developments in the spatial encoding of NMR signals laid the foundation for the present field of MRI technology and its diverse applications.

Hardware:

- In practice, the creation of $\mathbf{B}_0$ relies on magnets, usually superconducting and ensuring a strong magnetic field (from 1.5 Tesla up to 11.7 Tesla[4], and maybe more in the future). Scanners using low fields (around 0.5T and lower) are also used for specific applications. It's noteworthy that the higher the magnetic field, the higher the signal quality (in terms of signal-to-noise ratio (SNR)). Nevertheless, this benefit comes at the expense of bigger challenges related to 1) the threshold in the critical field (about 12 Tesla) for niobium-titanium (NbTi) typically employed as superconducting material for the magnet [Bat+23] and 2) imperfections and inhomogeneities in $\mathbf{B}_0$. A more in-depth discussion of the aspects related to 2) will be provided later in Chapter 3.

- Radio frequency (RF) coils integrating both transmit and receive elements are employed to excite the spins and then collect the FID signal due to the relaxation process. The transmission and reception elements may comprise single or multiple channels/sensors. When multiple receive channels are involved, a set of techniques coined as parallel imaging (PI) comes into action. We will discuss this topic further in Chapter 2. In practice $\mathbf{B}_1$ has two components: The first, $\mathbf{B}_1^+$ is in-phase with $\mathbf{B}_0$ (oscillates in the same direction than nuclear precession) and causes the magnetization to tip into the transverse plane. The second, $\mathbf{B}_1^-$ is out-of-phase with $\mathbf{B}_0$ and is unwanted. Ideally, $\mathbf{B}_1^-$ is null and $\mathbf{B}_1 = \mathbf{B}_1^+$. However, the fulfillment of this condition may vary depending on the design of the RF coils.

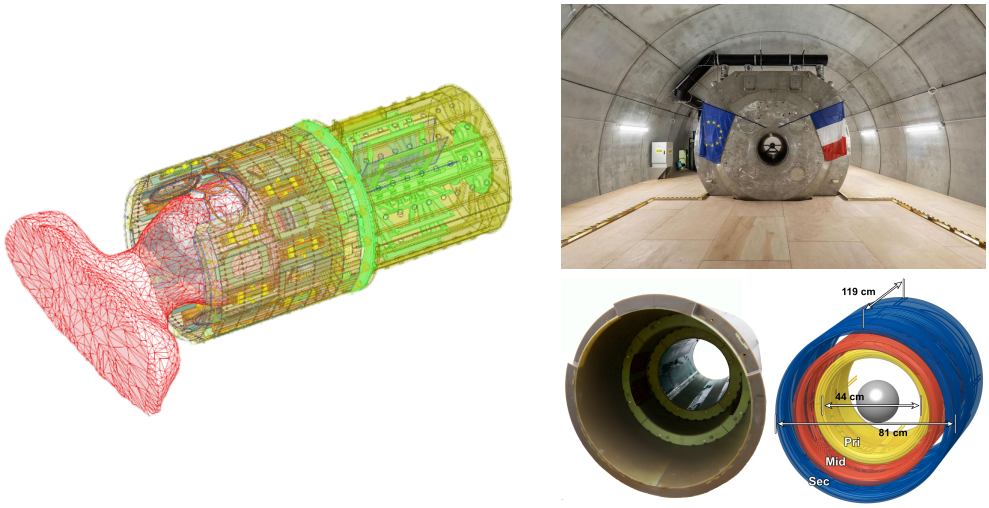

Figure 1.6: Left: Multi transmit and receive-channels head coil commissioned especially for the 11.7T Iseult MRI scanner - Upper right: Iseult's 11.7 magnet [Ved+14; Que+23]: Strongest clinical MRI magnet today - Bottom right: The impulse head gradient characterized by its high G_{max} = 200 mT/m and S_{max}=900T/m/s) [Fei+23].

- Spatial encoding of the FID signal and, therefore, image formation is ensured through the use of field gradients along the 3 axes ($\mathbf{k}_x$,$\mathbf{k}_y$,$\mathbf{k}_z$) that introduce small local field variations over space and time. Their effectiveness is characterized by their ability to induce these variations rapidly and quantified by two criteria known as the maximum gradient magnitude (G_{max}) and maximum slew rate (S_{max}). These parameters

[4]https://www.cea.fr/english/Pages/News/voyage-aimant-IRM-projet-iseult.aspx

translate, respectively, the first and second-time derivatives of the trajectories K (cf. Eq. (1.7)).

In order to coordinate the operations of these hardware elements, a software known as pulse sequence is implemented.

Pulse sequences: A pulse sequence, as shown in Fig. 1.7, defines a series of timed RF pulses and gradients, their scheduling, and eventual delays. The set of events is usually repeated (each TR, also called Repetition Time) a few times to acquire a full MR image/volume. The echo time (TE) and readout duration specify, respectively, the time at which the center of k-space is traversed to give the imaging contrast and the duration during which the MR signal is actively collected. The choice of TR and TE is crucial in determining the imaging contrast. It influences the predominant effects that impact how tissues appear in the image domain (the relative intensity of their corresponding voxels), be it T_1, T_2, or spin density (the concentration of spins in the tissue) effects. Typically, a long TR minimizes the T_1 effect, while a short TE minimizes the T_2 effect. We can also refer to this phenomenon as the MR image weighting (cf examples in Fig.1.8). These parameters should be chosen carefully according to the application. Eventually, the ultimate contrast of MR images/volumes depends on a variety of factors, including the type of the sequence.

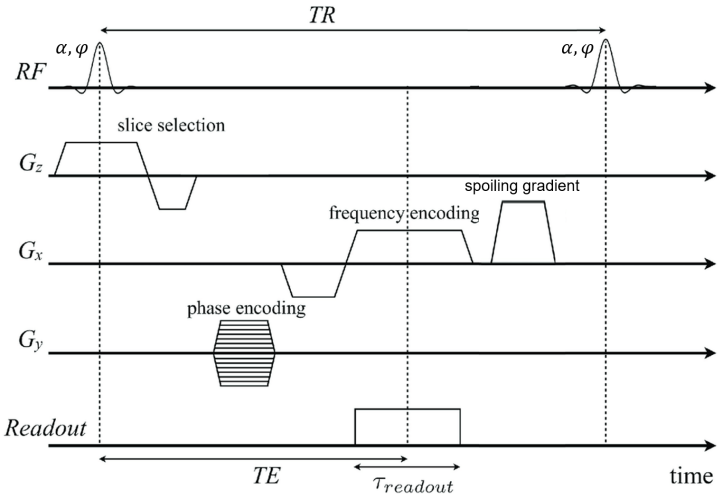

Figure 1.7: Example of a simplified pulse sequence diagram: A 2D Cartesian Gradient-Recalled-Echo (GRE) sequence. The gradient waveforms over G_x, G_y, and G_z serve to selectively excite a specific portion of the object being imaged and spatially encode the recorded NMR signal. Additionally, gradient and RF spoiling are illustrated through an additional gradient after the readout (G_x), and the relative phase of the RF flip angle (denoted φ) applied in addition to the targeted flip angle (denoted α). (This figure is an adapted version of that shown in [Pui+21]).

Fig. 1.7 illustrates an example of a pulse sequence diagram for 2D imaging, namely a conventional 2D gradient-recalled-echo (GRE) sequence (the concept of a GRE sequence will be explained in the next section). The profiles of G_x, G_y depict a specific type of spatial encoding that samples the different k-space points over a Cartesian grid in linewise fashion: G_x samples the k-space data points on a given line during the readout duration (i.e. the actual duration when the k-space samples are collected). This is why it can also be called a readout gradient. G_y serves to move from one line to the next (to be positioned at the correct k-space line) before the readout gradient is played and is called the phase encoding gradient. Furthermore, this diagram illustrates the concurrent application of a slice selection gradient played on G_z along with the RF excitation pulse: The goal of such a gradient is to selectively target and excite a specific portion or slice within the 3D object being imaged. In fact, if we revisit ω's variation with respect to $\mathbf{G}$ and focus on the $\mathbf{z}$ component, we can

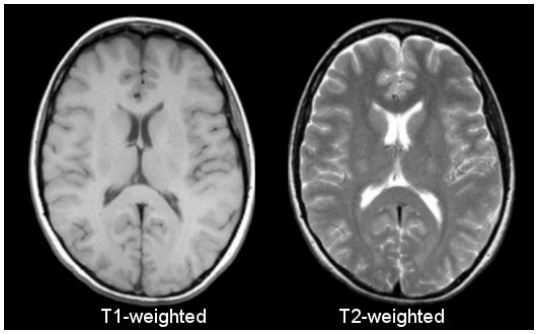

Figure 1.8: T_1 and T_2-weighted brain MR images: Short TR and TE are commonly used to obtain T_1-weighted imaging whereas both long TR and TE are employed in T_2-weighted applications. (This figure is an adapted version to that shown in [Naz+20]).

express this relationship as $\omega(t, z) = \gamma(|\mathbf{B}_0| + G_z(t)z)$. When considering two different z positions and assuming a constant $G_z(t)$ during the plateau ($G_z(t) = G_z$), we obtain:

$$\omega(z_1) = \omega_1 = \gamma(|\mathbf{B}_0| + G_z z_1) \tag{1.9}$$

$$\omega(z_2) = \omega_2 = \gamma(|\mathbf{B}_0| + G_z z_2) \tag{1.10}$$

And consequently,

$$\omega_2 - \omega_1 = \Delta\omega = \gamma G_z(z_2 - z_1) = \gamma G_z(\Delta z). \tag{1.11}$$

Thus, through the judicious application of the appropriate G_z, one can precisely excite the desired frequency range $\Delta\omega$ and consequently select only the corresponding segment or slice of the 3D object denoted as Δz: The gradient strength (G_z) conditions the thickness of the acquired slice, whether it's a straightforward thin 2D slice, a series of slices forming a slab that partially or entirely covers the object. In addition to the factors mentioned earlier, the choice between exciting a single slice or a volumetric slab also influences the overall contrast of the MR image.

Moreover, an additional gradient, known as the spoiling gradient, is applied along G_x: Ideally, before the application of each RF pulse, the magnetization should exclusively have a longitudinal component devoid of any transverse component. However, in practical terms, ensuring this condition would require waiting approximately 5 times the tissue's T_2 before applying the next RF pulse (i.e., $TR \approx 5 \times T_2$). Otherwise, the image contrasts will be degraded. Nonetheless, waiting for such an extended period of time isn't necessary to fully acquire a single line of k-space, leading to inefficient use of time. The purpose of the spoiling gradient is to eradicate any residual transverse magnetization that persists after the acquisition of each k-space line. The spoiling gradient can be applied along one or more gradient directions. However, it must possess a sufficiently strong momentum (the product of the gradient's magnitude and its duration). Therefore, a compromise between its magnitude and duration must be found to ensure that the gradient system's capabilities and available time within the pulse sequence are used efficiently. RF spoiling is also typically included in a GRE pulse sequence. It involves adding RF pulses with varying flip angles (denoted φ in Fig. 1.7) to reduce the residual transverse magnetization.

In the most general case, 3D imaging can be performed, and the profiles of G_x, G_y, and G_z can be arbitrary as long as they define a continuous trajectory and respect the G_{max} and S_{max} constraints.

MRI safety: While MRI is a non-invasive and non-ionizing imaging technique, certain safety measures must still be met. The two most crucial ones are:

- Specific Absorption Rate (SAR): RF pulses with high flip angles are notably energetic, leading to a substantial deposition of energy into the patient's tissues. Maximum

SAR depicts the maximum rate at which the tissues absorb energy that should not be exceeded in order to prevent excessive heating. As the field strength increases, the SAR limits become increasingly restrictive.

- Peripheral Nerve Stimulation (PNS): The rapid switching of magnetic gradients induces electric fields in the patient's tissues. These electric fields can stimulate peripheral nerves, resulting in muscle twitching. PNS limits are generally less restrictive than those associated with SAR, yet they should still be met to ensure the comfort of the patient.

A pulse sequence (beyond the example illustrated above, various types exist and can be implemented) can be employed to collect a single image/volume or repeated several times to gather a series of consecutive images/volumes, leading to what is known as dynamic MRI. In what follows, we highlight how a specific variant of this approach, called functional MRI (fMRI), can be instrumental in understanding brain function and cognition.

1.2 Principles of fMRI

1.2.1 Neurovascular coupling and blood oxygenation dependent-level (BOLD) contrast

The neurovascular coupling describes a rather complex interplay between the hemodynamic responses and metabolic changes that follow neural activity, as illustrated in Fig. 1.9. In fact, neural events trigger an increase in the metabolic rate of oxygen consumption ($CMRO_2$), leading to a decrease in the concentration of oxyhemoglobin[5] (denoted OHb), which is diamagnetic relative to that of deoxyhemoglobin[6] (denoted DHb), which is paramagnetic. These metabolic changes are accompanied by hemodynamic alterations, namely the increased cerebral blood flow (CBF) and volume (CBV), which, conversely, result in an increase in the concentration of oxyhemoglobin relative to that of deoxyhemoglobin ($\frac{OHb}{DHb}$). As the contribution of CBF/CBV is larger than that of $CMRO_2$ [FR86], overall blood oxygenation ($\frac{OHb}{DHb}$) increases.
Unlike diamagnetic oxyhemoglobin, paramagnetic deoxyhemoglobin locally distorts $\mathbf{B}_0$, leading to a reduction in the T_2 and/or T_2^* relaxation time and, consequently, in the T_2 and/or T_2^*-weighted MR signal. Therefore, an increase in $\frac{OHb}{DHb}$ will locally increase the T_2 and/or T_2^*-weighted MR signal and vice versa.
Local changes in magnetic susceptibility due to the neurovascular coupling (and therefore an increase of $\frac{OHb}{DHb}$) can be tracked in a series of T_2 and/or T_2^*-weighted MR images. This is recognized as the blood oxygenation level-dependent (BOLD) contrast [Oga+90]. In summary, near the activated brain regions, the following occurs:

- When $CMRO_2$ increases, $\frac{OHb}{DHb}$ decreases and therefore, the BOLD signal as well.
- As CBF rises, so does $\frac{OHb}{DHb}$, and hence, the BOLD signal is boosted. In parallel, an increase in CBF also impacts the T_1-weighted signal.
- CBV, while being distinct from CBF, is correlated to it. It also impacts the BOLD and T_1-weighted MR signal.

Due to CBF/CBV uplift in larger proportion than the $CMRO_2$, this chain of reactions leads to an overall increase in the BOLD signal locally. A more in-depth discussion can be found in [UUB15] (Chapter 8). The superposition of these sources of signal evolution, which may happen at different paces and vary from one brain region to another, defines the Hemodynamic Response Function (HRF).

[5] hemoglobin bound to oxygen
[6] hemoglobin that has released its oxygen

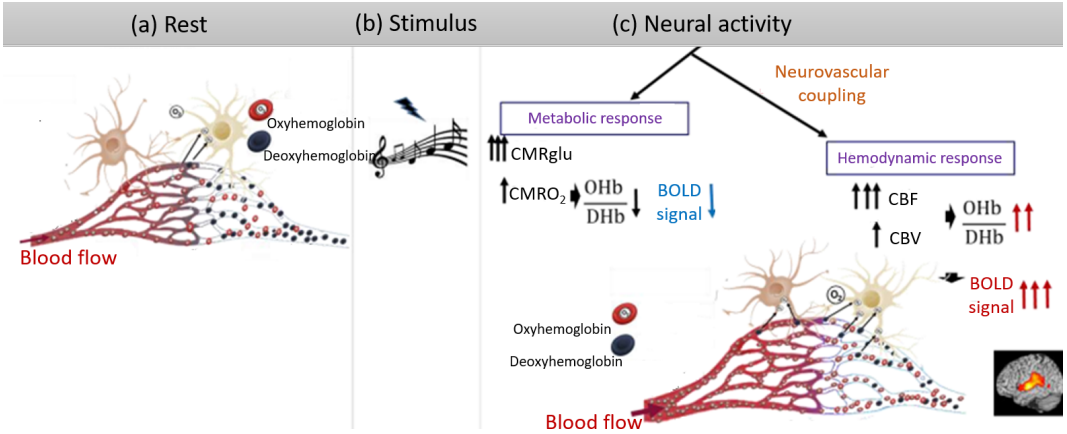

Figure 1.9: Neurovascular coupling and BOLD mechanism. Metabolic and hemodynamic responses following neural activity lead to an overall increase in the blood oxygenation locally near the activated brain regions and, therefore, a local increase in the BOLD signal. (This figure is an adapted version to that shown in [RB23]).

Hemodynamic Response Function

The HRF is the transfer function that binds, under the hypothesis that the system is linear, the neural events to the hemodynamic changes and, consequently, to the BOLD signal evolution. For humans, its canonical model [Fri+95] has a sluggish temporal profile and is characterized by an onset lag, reaches its peak after 5 to 6 seconds, and vanishes through a post-stimulus undershoot. The inherent slowness and delays of the HRF set limits to the temporal resolution of the BOLD signal. Nevertheless, some relatively rapid transient events have been observed in the HRF, such as the initial dip. Moreover, the effective temporal precision and linearity of the HRF is still a subject of debate and an active research topic [Ciu+03; STC13; Lew+16; PL21]. Furthermore, the profile of the HRF depends on the species, the nature of cognitive tasks/processes, and the brain regions and their vascular structures. Therefore, while being distinct from its spatial dependencies, the HRF's temporal resolution remains intricately interconnected with it.

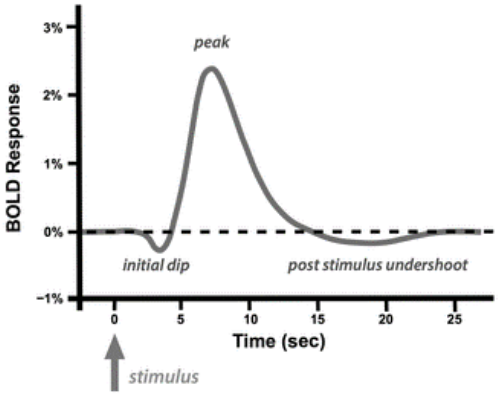

Figure 1.10: HRF profile: In humans, the canonical HRF model has a slow temporal profile, featuring an onset lag, peaking after 5 to 6 seconds, and exhibiting a post-stimulus undershoot. (This figure is taken from the mriquestions website[7]).

Intrinsic spatial resolution

The intrinsic spatial specificity of the signal changes due to the neurovascular coupling is in the sub-millimeter scale, as demonstrated by optical imaging. In hemodynamic-based

fMRI, the spatial specificity depends on the sources contributing to the signal changes. For instance, the CBV contributions are known to be very specific compared to the global BOLD contributions. When focusing on the BOLD contrast, marked by a higher sensitivity when compared to CBV-only-based contrasts such as vascular space occupancy (VASO)[8], we refer to its intrinsic specificity as the BOLD Point Spread Function (PSF). In BOLD fMRI, we commonly account for both intravascular and extravascular contributions. The former is related to hemodynamic and metabolic changes within the vessels. The latter refers to changes occurring in the surrounding tissues in closer contact with neurons. This extravascular contribution is particularly relevant to neuronal events, providing more specific insight into the neural activity associated with the observed BOLD signal. The apparent spatial specificity of BOLD (i.e., discernable in the fMRI data) depends not only on the underlying physiological processes and vascular architecture but also on the imaging parameters. For instance, for a typical GRE sequence, as illustrated in Section 1.1.2, the spatial specificity is about 2mm^3. However, with recent developments, the spatial resolution (and, therefore, spatial specificity) has been pushed around 1mm^3 and even to the sub-millimeter scale, with the recent rise of layer fMRI [Sha+19; Kas+18; BHF21; Uğu21]: Typically 0.8mm^3 is used, but up to around 0.4mm^3 was obtained on partial brain coverage [Viz+22]. Improving spatial resolution accentuates extravascular contributions relative to intravascular ones, thereby enhancing the specificity of BOLD as an indirect measure of neuronal activity.

BOLD sensitivity

BOLD fMRI captures a change in T_2 and/or T_2^*, hence in R_2 and/or R_2^*. BOLD sensitivity describes the ability to detect small changes in the BOLD signal in the order of magnitude of $\frac{\Delta S}{S_0} \approx TE\Delta R_2$ or $\frac{\Delta S}{S_0} \approx TE\Delta R_2^*$, and it depends on several factors, including:

- The field strength: The BOLD signal accounts for some percentages of signal variation in an fMRI time series. However, as the field strength $|\mathbf{B}_0|$ increases, so does the BOLD signal [Rob+93]. This is because the difference in magnetic susceptibility between deoxyhemoglobin and oxyhemoglobin is amplified with $|\mathbf{B}_0|$.

- The voxel size: When the voxel size increases, a larger amount of BOLD signal is accumulated, and therefore, the sensitivity is enhanced. Nevertheless, this improvement comes at the cost of reduced specificity.

- The type of sequences used and their parameterization: Beyond the voxel size, other imaging parameters impact the sensitivity of BOLD, such as the type of sequence (typically, we speak of GRE versus Spin-Echo (SE) sequences) or the bandwidth (denoted BW and translating how fast the MR signal is sampled).

- The predominant (T_2 or T_2^*) contrast: Whether predominantly T_2 or T_2^*, the contrast in BOLD fMRI is contingent on some of the already mentioned factors, such as field strength, the selection of TE (preferably close to the T_2 or T_2^* values of gray matter), and the specific pulse sequence employed.

Hereafter, we will briefly explain the two main types of MR sequences that reveal BOLD contrast.

1.2.2 T_2 and T_2^*-weighted fMRI generic scanning methodology

Two main sequences are used for BOLD fMRI, namely, GRE, and SE. Hereafter, we will focus on the mechanism of echo formation for these two sequences without diving into the spatial encoding for now.

[8] Overview about research endeavors in VASO-weighted fMRI: https://layerfmri.com/2020/01/02/vasoworldwide/

Gradient-Recalled Echo sequences

In a GRE sequence, the FID is manipulated by means of a) a dephasing gradient with a specified polarity, accelerating the dephasing of the spins after the RF excitation, and b) a rephasing gradient in the opposite polarity (also called readout gradient), resulting in the formation of an echo. The signal peak within this echo occurs in the middle of the rephasing gradient (at the TE). The RF excitation is typically applied for the Ernst angle defined as $\alpha_{Ernst} = cos^{-1}(e^{\frac{-TR}{T_1}})$, where T_1 is related to the gray matter. α_{Enrst} ensures an optimal MR signal. GRE sequences are sensitive to B_0 inhomogeneities and, consequently, provide a predominant T_2^*-weighted contrast and a high sensitivity to BOLD.

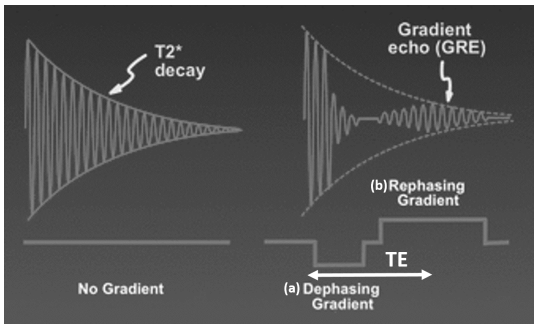

Figure 1.11: Echo formation in GRE sequence: A readout (rephasing) gradient is used to generate the echo whose signal peak occurs at the TE). (This figure is adapted from the mriquestions website).

Spin-Echo sequences

In SE sequences, two consecutive RF pulses, one for $\alpha = 90°$ followed by another for $\alpha = 180°$, are employed to produce the echo. SE sequences are known for their lower sensitivity to B_0 inhomogeneities as compared to GRE sequences, and therefore, they provide a predominant T_2-weighted contrast. Their sensitivity to BOLD is lower than that of GRE. However, they provide a better spatial specificity. In [UMU09], the authors demonstrated through simulations that SE sequences become particularly relevant with increasing field strength due to enhanced sensitivity, and the T_2-weighted signal becoming more associated with extravascular effects, rendering it more specific. However, increased field strength presents a challenge for SE sequences because of the high flip angles used, leading to SAR becoming a substantial limitation that essentially hinders the efficient implementation of this strategy.

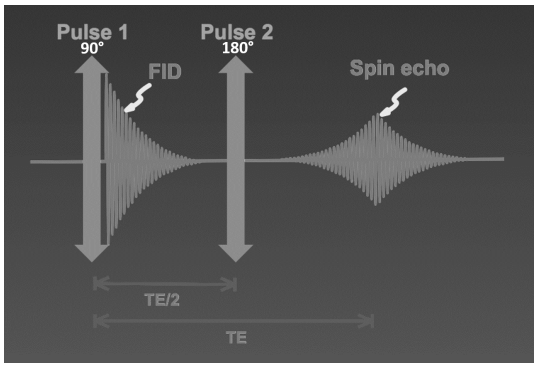

Figure 1.12: Echo formation in SE sequence: Two RF pulses, the first corresponding to $\alpha = 90°$, and the second to $\alpha = 180°$, are employed to generate the echo. (This figure is adapted from the mriquestions website).

Whether employing a GRE or SE sequence, the spatial encoding can be accomplished using a variety of gradient waveforms/trajectories. In the next chapter, particular emphasis

will be given to the major alternatives while focusing on GRE sequences because they are faster than SE sequences and provide a higher BOLD sensitivity with reduced SAR limitations.

Functional MRI experiments involve using a pulse sequence to acquire MR images/volumes over time while a participant is inside the scanner engaged in a task or still at rest. There are two primary categories of fMRI tasks:

- Resting-state fMRI, where the participant does "nothing." It provides insight into spontaneous neural activity and reveals the intrinsic functional brain networks [LSS12].
- Task-based fMRI, where controlled sensory-motor or cognitive (e.g., working memory) tasks are used.

In the following, we will focus on task-based fMRI.

1.2.3 Task-based BOLD fMRI: Experimental design, preprocessing and statistical analysis

Task-based fMRI can be sensory-motor, such as audio, visual, motor, or cognitive. These tasks can be implemented through block-based or event-based paradigms or a combination of both. While block-based designs guarantee a higher BOLD signal by capturing sustained neural activity over a period typically around 20s or more, event-based designs enable a finer definition of responses to specific stimuli. Preprocessing usually includes:

- Realignment: The heads of participants usually move inside the scanner. Even though the movement is usually slight, it is important to correct the consequent displacement of the voxels in the fMRI time series. This stage estimates motion parameters considering a rigid body movement scenario.
- Distortions correction: The above-mentioned $\mathbf{B}_0$ inhomogeneities produce deformations in the individual fMRI images/volumes that should be corrected.
- Registration: Usually, the fMRI images/volumes are co-registered with a high spatial resolution T_1-weighted anatomical scan. This is performed to facilitate the localization of the activation patterns along the cortical ribbon.
- Filtering and smoothing: Low-pass filtering and spatial smoothing can also be applied.

Statistical inference is typically performed using a general linear model (GLM) voxel-wise modeling that can be expressed as written in Eq. (1.12), where $\mathbf{Y}$, $\mathbf{X}$, $\boldsymbol{\beta}$ and $\boldsymbol{\epsilon}$ are, respectively, the data, the regressors (defining the task), scaling parameters, and residual errors.

$$\mathbf{Y} = \mathbf{X}\boldsymbol{\beta} + \boldsymbol{\epsilon} \tag{1.12}$$

The goal is to estimate $\boldsymbol{\beta}$ by fitting $\mathbf{X}$ to $\mathbf{Y}$. The statistical significance of $\boldsymbol{\beta}$ is then assessed to decide whether a voxel is activated by the task or not. The analysis typically assumes that the observations at consecutive temporal points are independent from one another and the residual errors are normally distributed. However, in practice, the fMRI signal exhibits temporal correlation. This is why prewhitening is performed: Auto-regressive modeling of the autocorrelation structure of the fMRI signal can be implemented, for instance [Ols+19].

1.2.4 Challenges in BOLD fMRI today

In the last three decades following its inception, fMRI has significantly progressed. However, major challenges persist. Some of these challenges belong to the realm of methods and physics of fMRI, while others fall within the realm of (fundamental and clinical) neuroscience and physiology.

In the following, we delve into selected issues that hold paramount significance within the scope of this work.

Sensitivity vs. specificity trade-off

One of the persistent challenges in fMRI is the trade-off between the ability to detect the signal and to localize it finely. Achieving a finer spatial localization involves moving to smaller voxel sizes. In fact, smaller voxel sizes effectively reduce the contributions of large vessels and draining veins, which exhibit large but poorly localized responses, in BOLD contrast. However, this comes at the expense of decreased SNR since (in 3D) $SNR \propto \Delta x \Delta y \Delta z \sqrt{N_y N_z N_{avg} BW}$, where $\Delta x \Delta y \Delta z$ is the voxel size and N_y and N_z the sampling matrix size ($N_i = FOV_i / \Delta i$). N_{ave} usually equals 1 in fMRI. Furthermore, a finer spatial resolution for a constant FOV implies a larger sampling matrix size. As a result, the data acquisition period for a single volume is extended. When considering a sequence of fMRI volumes, this leads to lower statistical power and degraded temporal resolution. While a low temporal resolution might not pose significant issues in controlled block-design fMRI experiments, it becomes a constraint when studying complex cognitive functions under ecologically viable (i.e., realistic) conditions and investigating the underlying neurovascular coupling mechanisms.

In broad terms, there is a four-way trade-off between spatial resolution, temporal resolution, coverage, and SNR. In Chapter 2, we will explore strategies aimed at more effectively tuning these compromises by adapting the data acquisition methods.

B_0 Field inhomogeneities

With the rise of layer fMRI, which aims to characterize neural responses across the different laminar and columnar structures of the cortical depth, the quest for sub-millimeter spatial resolution intensifies. Even when diminishing the FOV and adapting the temporal resolution, this pursuit remains challenging. This is what justifies today the ongoing race towards higher field strengths since $SNR \propto |\mathbf{B}_0|^\alpha$ [PSS16; Ste+22] (The quantification of α has varied across different studies; however, in all instances, it satisfies the condition $\alpha \geq 1.5$). In practical terms, what holds significance in fMRI is temporal SNR (tSNR), which reflects the temporal stability of the data and is defined on a voxel-wise basis as $tSNR(\nu) = \frac{\bar{\mu}(\nu)}{\sigma(\nu)}$. $\bar{\mu}(\nu)$ represents the temporal mean of the intensities of voxel ν, while $\sigma(\nu)$ corresponds to the temporal standard deviation of the intensities of voxel ν after detrending. In [TRW11], the authors demonstrated that in the thermal noise regime (when noise is predominantly derived from the MRI system itself rather than the physiology of the participant), the SNR and tSNR are linearly linked. Therefore, an increase in SNR leads to a better tSNR. Furthermore, the contrast-to-noise ratio (CNR) also increases at higher fields. Yet, with the increase of field strengths, issues related to $\mathbf{B}_0$ inhomogeneities and imperfections also amplify. In Chapter 3, we will discuss the sources of these issues, their impact on the data, and the strategies to overcome these challenges.

Motion and physiological noise

The subject's motion and physiological noise, such as breathing or heartbeat, also degrade the quality of the fMRI data. As spatial resolution improves, these issues become increasingly pronounced, manifesting in observable voxel displacement, blurring, or signal loss. Furthermore, processes like breathing and heartbeat can induce unwanted signal variations and impact the correctness and efficiency of the statistical analysis. Motion and physiological noise correction is one of the most active research and methods development topics in the field today.

In conclusion, this chapter has provided an overview of MRI and its extension to fMRI. As we navigate the details of fMRI, three key pillars emerge: Achieving high resolution, both spatially and temporally, ensuring large enough (or even full) brain coverage, and the significance of field strength in fMRI. The pursuit of these objectives constitutes the essence of the next chapters. Chapter 2 will explore the methodologies and strategies to attain high resolution without sacrificing brain coverage. Following that, Chapter 3 will investigate the

advantages and challenges associated with performing fMRI at high magnetic field strength, offering insights into the benefits and inconveniences while proposing effective solutions.

* * *
* *
*

Chapter 2

Achieving higher spatiotemporal resolution in fMRI through k-space undersampling

In the previous chapter, we discussed the fundamental principles of MRI and fMRI. Our discussion highlighted three crucial pillars: The pursuit of higher resolution (spatial, temporal, or spatiotemporal), brain coverage, and high-field fMRI. In this chapter, our attention shifts towards addressing the first two objectives: Achieve higher resolution without compromising brain coverage. We will discuss the main strategies for achieving higher spatiotemporal resolution in fMRI. Traditionally, fMRI acquisitions in the Cartesian framework have been accelerated using Echo Planar Imaging (EPI) and Parallel Imaging (PI) techniques. The principles of these traditional approaches are highlighted in the first section. The second section shifts the focus to the non-Cartesian framework and its potential advantages compared to Cartesian techniques. The third section explores the promising use of Compressed Sensing (CS) in fMRI. The discussion encompasses the theory behind CS and introduces a specific method, three-dimensional Spreading Projection Algorithm for Rapid K-space sampLING (3D-SPARKLING), which holds particular significance in this work as it is employed for the first time to acquire fMRI data.

This chapter draws inspiration from former Ph.D. works conducted in the team, specifically Chaithya GR [Cha23] and Redouane Jamil's [Jam22] manuscripts.

2.1 Accelerating fMRI acquisitions in the traditional Cartesian framework

In the Cartesian (i.e., sampling on the grid) framework, achieving a higher spatial resolution without sacrificing the temporal resolution or, conversely, enhancing the temporal resolution for a given spatial resolution requires fast sampling techniques. In fMRI, such techniques are primarily based on the so-called Echo Planar Imaging (EPI) methods: Instead of sampling the k-space line by line, EPI implements a zig-zag readout and, therefore, samples a whole plane of k-space in a given TR. By doing so, the aim was to speed up the acquisition by

ensuring a more efficient use of the TR. An EPI readout can be used with a GRE or SE pulse sequence. In the following, we focus on GRE-EPI.

Initially, EPI was employed in 2D acquisitions (Fig. 2.1), where MR image slices were excited (utilizing the slice selection gradient) and acquired individually, meaning the entire volume was obtained one single slice at a time. A k-space plane can be acquired using either a single-shot sampling involving a single readout that covers the entire plane or a segmented fashion where the entire plane is covered using multiple readouts. The second option is employed when aiming for very high spatial resolution, which means an extended readout length, which can pose challenges concerning T_2^* decay and the potential signal loss.

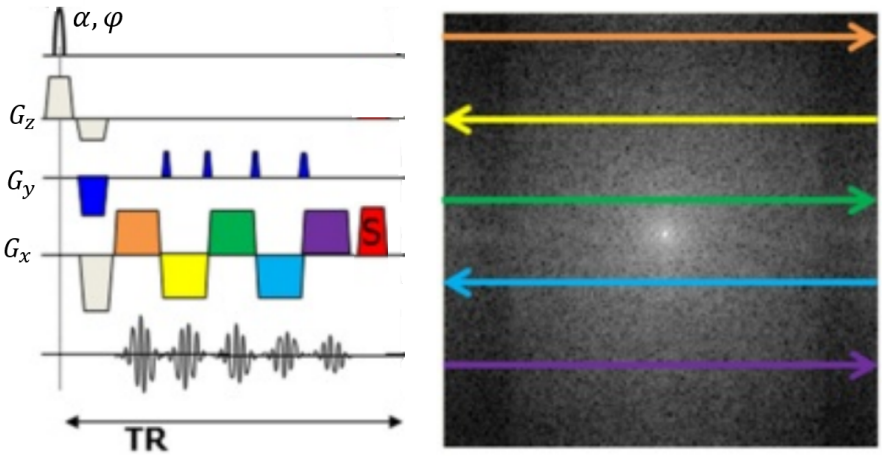

Figure 2.1: Simplified GRE 2D-EPI pulse sequence diagram. S refers to the spoiling gradient. (This figure is an adapted version of that shown in [BRR12]).

To further enhance the efficiency of 2D-EPI sampling, undersampling needs to be performed as well. Typically, rather than sampling all k-space lines, a fraction is acquired, like 1 out of 2 or 1 out of 4. The corresponding undersampling factor is denoted R. However, as previously noted, performing undersampling will result in aliasing artifacts (Fig. 1.5). Parallel imaging (PI) is typically used to tackle this challenge.

PI [Des+12; Cha+14a; Ham17] relies on two main practical principles: a) Acquiring the MR signal through different receive channels positioned around the brain, and b) employing adapted reconstruction algorithms that leverage the data redundancy ensured by different channels associated with complementary spatial sensitivity profiles to produce unaliased images from sub-sampled k-space.

MR acquisition using multi-channel coils In the context of employing multiple channels for MR signal reception, we refer to the hardware as receiver coil arrays. Each array captures the MR signal, and hence the MR image, according to a specific sensitivity profile that depends on its location, as shown in Fig. 2.2. These sensitivity profiles are called sensitivity or coil maps. Ideally, these individuals receive arrays that should be homogeneously distributed around the brain and cover the entire FOV. The final MR image, formed by combining those acquired by each individual receive coil, is typically defined as the sum-of-squares (SOS) of these images. Conversely, the individual MR images from each coil can be defined by multiplying the SOS image with the corresponding sensitivity profile. Alternative combination strategies that consider the noise distribution between these coils also exist but will not be discussed here. In Fig. 2.2, a full k-space acquisition is postulated as no aliasing artifacts are evident on the individual coil images. In such a case, the use of multi-receive arrays boosts the SNR (and, therefore, in the case of fMRI, the tSNR). To further leverage the use of receiver coil arrays associated with complementary spatial sensitivity profiles to undersample the k-space, it must be combined with specific reconstruction strategies. In fact, the term

parallel imaging more judiciously describes the reconstruction methods rather than the acquisition process, even though it requires the use of several receive channels.

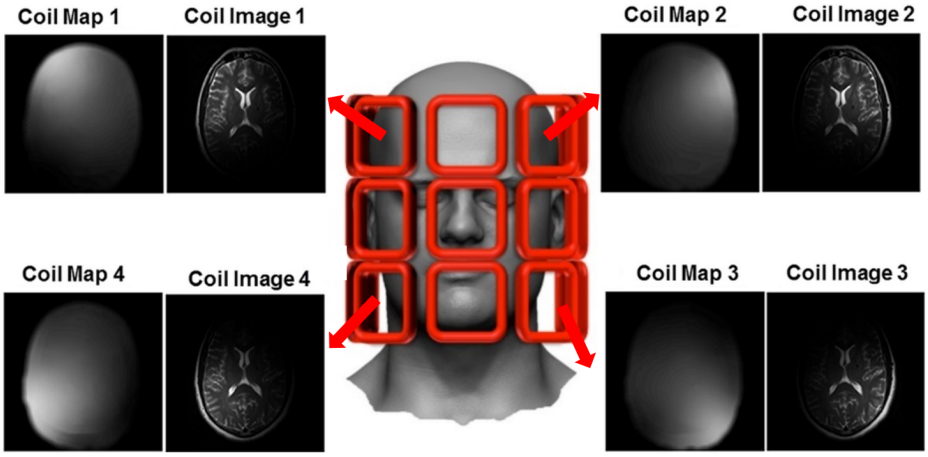

Figure 2.2: MR image acquisition using receiver coil arrays: Each array captures the MR signal and consequently the MR image, each adhering to a unique sensitivity profile determined by its location. (This figure is adapted from the mriquestions website, and [Des+12].)

PI image reconstruction techniques There are two main families of PI techniques to consider. The first pertains to methods that act in the image domain. We refer to this category as SENSitivity Encoding (SENSE) [Pru+99] and its variations. The second involves techniques that operate in the k-space domain. We refer to this category as GeneRalized Autocalibrating Partial Parallel Acquisition (GRAPPA) [Gri+02] and its variations. In the following, we will briefly explain how the two principled approaches work.

SENSE The SENSE algorithm formulates the MR image reconstruction problem from undersampled k-space data as a linear system incorporating sensitivity profiles. Let us suppose that $R = 2$, then, the intensity $F_j(x, y)$ of an aliased voxel (at the spatial location (x, y)) in the image obtained from the jth coil can be expressed as follows:

$$F_j(x, y) = A_j + B_j = I_A \times S_{A,j} + I_B \times S_{B,j} \tag{2.1}$$

I_A and I_B are the intensities of the unaliased voxels (located at (x, y_A) and (x, y_B)) in the MR image reconstructed by combining all individual single-coil images and $S_{A,j}$ and $S_{B,j}$ the corresponding sensitivity profile (located at (x, y_A) and (x, y_B)). The values of $F_j(x, y)$, $S_{A,j}$ and $S_{B,j}$ can be computed and the objective is to determine I_A and I_B. For L coils, we will have a rank-L system as illustrated in Fig. 2.3.

If we generalize this problem to an arbitrary R leading to n_p aliased pixels at the spatial position (x, y) in each of the 2D folded (aliased) individual images from each of the L receive channels, then we can write down:

$$\underbrace{\begin{pmatrix} F_1(x,y) \\ \vdots \\ F_{n_p}(x,y) \end{pmatrix}}_{\text{intensities of the folded voxels}} = \overbrace{\begin{pmatrix} S_1(x,y_1) \dots S_1(x,y_R) \\ \vdots \\ S_L(x,y_1) \dots S_L(x,y_R) \end{pmatrix}}^{\text{sensitivity profiles from } L \text{ coils}} \underbrace{\begin{pmatrix} I(x,y_1) \\ \vdots \\ I(x,y_R) \end{pmatrix}}_{\text{intensities of the unfolded voxels}} \tag{2.2}$$

In the conventional Cartesian framework on which we focus in this section, $n_p = R$. And as long as $L \geq R$, the system is overdetermined and thus admits a unique solution

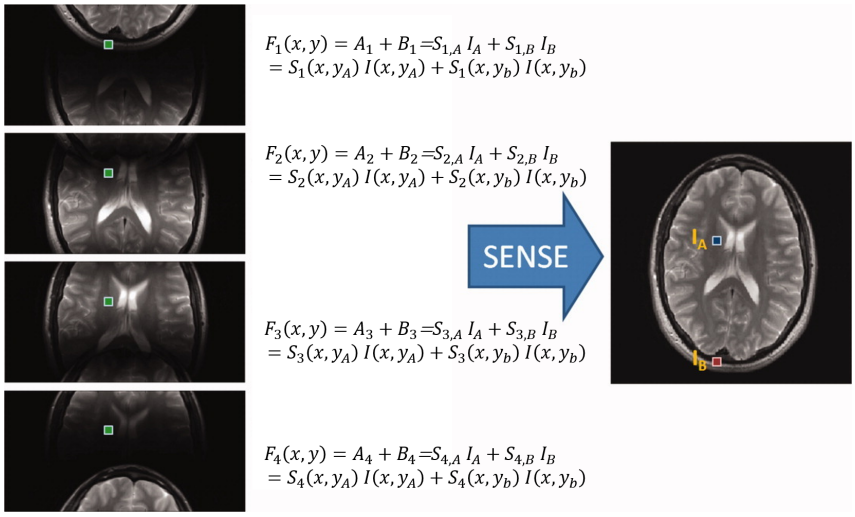

Figure 2.3: SENSE reconstruction frames the problem of MR image reconstruction from undersampled k-space data as a linear system that includes sensitivity profiles. (This figure is a modified version of that shown in [Des+12].)

$\mathbf{I} = \mathbf{UF}$, where $\mathbf{I}$ (respectively, $\mathbf{F}$) is the unfolded (respectively, folded) voxels values and $\mathbf{U} = (\mathbf{S}^H\mathbf{S})^{-1}\mathbf{S}^H$ the unfolding matrix. In practice, the different channels correlate with each other, and taking this into account, we define $\mathbf{U} = (\mathbf{S}^H\psi^{-1}\mathbf{S})^{-1}\mathbf{S}^H\psi^{-1}$, where ψ is the noise correlation matrix between the different coils. Rather than using matrix inversion, $\mathbf{U}$ can be computed using conjugate gradient descent.

GRAPPA GRAPPA relies on interpolating the missing data in the undersampled k-space information. More specifically, it operates on the premise that any k-space point can be expressed as a weighted sum of its neighboring points in the multi-coil undersampled k-space data. Therefore, the challenge for GRAPPA is determining this weighting kernel, also called GRAPPA kernel. This is achieved by estimating a calibration kernel (denoted W) from a fully sampled region around the central portion of k-space, referred to as the AutoCalibration Signal (ACS). The calibration kernel is then convolved with the undersampled k-space data acquired from each of the receive channels (denoted $S_{sub,j}, \forall j = 1, .., L$) to interpolate the missing data points and estimate the full k-space data from the ith coil (denoted as $S_{full,i}$). In Eq. (2.3), an example of this convolution is expressed when the k-space is undersampled along $\mathbf{k}_y$. i (respectively, j) is used to index the coil associated with the (full) estimated (respectively, undersampled) k-space data. The ranges of τ_x and τ_y depend on the size and shape of the kernel W.

$$S_{full,i}(k_x, ky + \Delta k_y) = \sum_{j=1}^{L} \sum_{\tau_x} \sum_{\tau_y} W((i,j,\tau_x,\tau_y) S_{sub,j}(k_x + \tau_x, k_y + \tau_y) \tag{2.3}$$

After performing this interpolation for all the coils and obtaining $S_{full,i}, \forall i = 1, ..., L$, the full dataset can be used to reconstruct an unfolded image.

Combining 2D-EPI with PI only permits undersampling the k-space in the $\mathbf{k}_x\mathbf{k}_y$ plane, not along $\mathbf{k}_z$, limiting its acceleration capacities. To achieve greater acceleration, EPI evolved into 3D-EPI and 2D simultaneous multi-slice (SMS)-EPI.

3D-EPI In 3D-EPI [Pos+10], an entire slab (covering the full volume or a portion of it) is excited and acquired, thus enabling undersampling both in the $\mathbf{k}_x\mathbf{k}_y$ plane and along $\mathbf{k}_z$, also called partition direction. The acceleration factor R, then, encompasses the acceleration performed both in the $\mathbf{k}_x\mathbf{k}_y$ plane and along $\mathbf{k}_z$. The different k-space planes are sampled consecutively one by one after each RF excitation, meaning that the sampling of two consecutive k-space planes is spaced by TR. The readout and phase encoding gradients

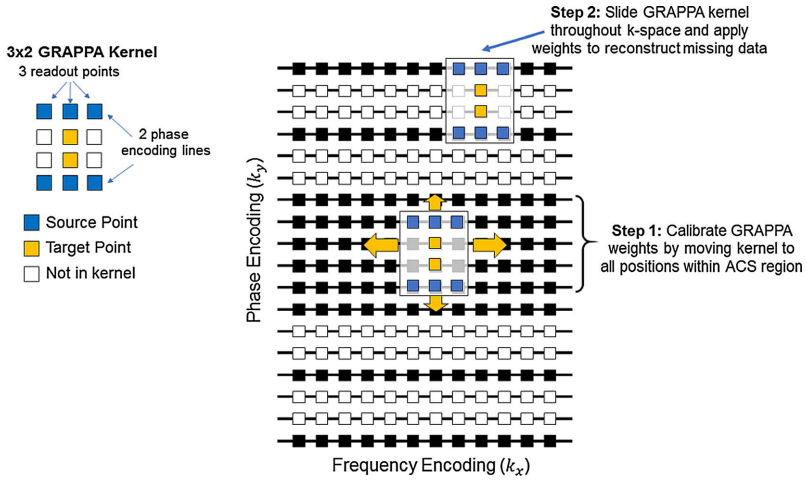

Figure 2.4: The GRAPPA reconstruction technique operates on the principle that the full k-space information from each coil can be effectively interpolated. This is achieved by utilizing an interpolation kernel, which is estimated from a fully sampled region, along with the undersampled k-space data obtained from each individual coil. (This figure is taken from [Ham17]).

implement the zig-zag over a k-space plane while the gradient over the partition direction (Fig. 2.5) moves along the $\mathbf{k}_z$ direction and therefore selects the different planes consecutively. When targeting very small voxel sizes, as is the case in layer fMRI, segmented 3D-EPI proves more efficient than 3D-EPI. In segmented 3D-EPI, a single k-space plane is acquired using multiple zig-zag patterns, which can also be interleaved. This approach enables the sampling of larger k-space matrices (due to the small voxel sizes) while keeping a TR and TE that are suitable for BOLD contrast. Additionally, 2D CAIPIRINHA [Bre+06] is implemented in-plane and across slices when using 3D-EPI (segmented or not), effectively undersampling k-space in a checkerboard fashion. Using 2D CAIPIRINHA with 3D-EPI proves advantageous for SNR. In fact, the act of undersampling k-space tends to degrade the SNR, as expressed hereafter: $SNR_R = \frac{SNR_{R=1}}{g\sqrt{R}}$. SNR_R denotes the SNR at the individual volume level for an undersampling factor R, and g represents the g-factor associated with the noise distribution. As R increases, SNR_R decreases. CAIPIRINHA effectively reduces g, thereby enhancing SNR_R.

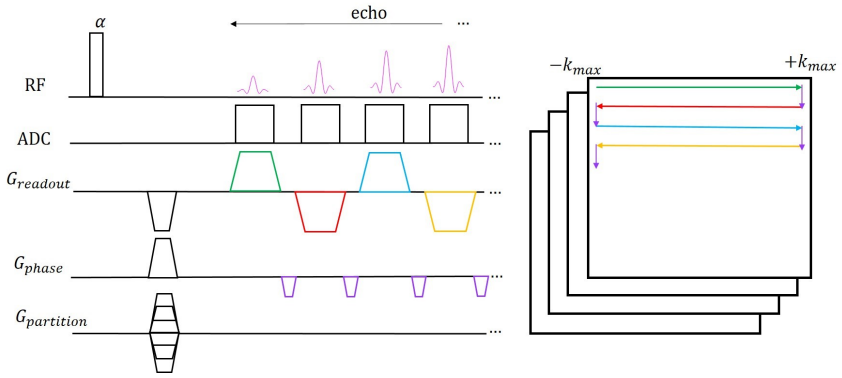

Figure 2.5: Non-selective GRE 3D-EPI pulse sequence diagram. (This figures is taken from [Jam22]).

2D SMS-EPI 2D SMS-EPI relies on the simultaneous excitation and acquisition of multiple slices at the same time [Moe+10]: Undersampling along the partition encoding direction becomes feasible through the use of simultaneous multi-slice selective pulses, as

indicated by the "SMS" in the name. This leads to an acceleration factor that depends on the number of simultaneously excited and acquired slices, referred to as the multiband (MB) factor, as well as the in-plane ($\mathbf{k}_x\mathbf{k}_y$) undersampling. However, the simultaneous acquisition of several slices can lead to spatial aliasing along the partition-encoding direction, resulting from the overlap of signals from different slices. Additionally, when slices are closely spaced, there is a risk of signal overlap from adjacent slices as well. Controlled Aliasing in Parallel Imaging Results IN Higher Acceleration (CAIPIRINHA) [Bre+05] is therefore used to mitigate this issue by using controlled aliasing in order to shift aliasing artifacts.

3D-EPI and 2D-SMS EPI have the same acceleration capabilities, meaning in the phase encoding direction and across slices and can be combined with the 3D extensions of SENSE and GRAPPA. However, 3D-EPI is less robust to physiological noise and motion than 2D SMS-EPI. Nevertheless, 2D SMS-EPI requires very high flip angles. Therefore, SAR becomes limiting in the case of 2D SMS-EPI.

EPI-based methods are regarded as fast sampling techniques and currently represent the established standard in fMRI. Combining them with PI is widely used today to achieve high resolutions. Additionally, using a Cartesian grid for k-space sampling allows straightforward implementation of reconstruction algorithms through a (uniform) Fast Fourier Transform (FFT). However it is worth noting that when compared to EPI's Cartesian gradient waveforms, non-Cartesian waveforms are able to cover broader regions in a shorter time. Furthermore, PI-based reconstructions can also be extended to include non-Cartesian readouts.

2.2 Accelerating fMRI acquisitions in the non-Cartesian framework

Non-Cartesian sampling patterns were introduced in MRI in general for a variety of reasons, which can be succinctly summarized as follows:

- Non-Cartesian readouts provide increased flexibility in the trajectories used to collect k-space data, influencing how the k-space is covered: They enable the exploration of broader regions within a shorter time frame than conventional Cartesian readouts. When combined with PI, non-Cartesian readouts can concurrently achieve speed and broader coverage. These features provide a dual advantage, enabling more flexible spatiotemporal resolution and the potential to improve it.

- Non-Cartesian trajectories typically exhibit a higher sampling rate in the central portion of k-space compared to their Cartesian counterparts. This characteristic makes them essentially more robust to motion and physiological noise, contributing to enhanced data quality.

One of the early non-Cartesian sampling patterns developed for MRI involved using radial readouts [Lau73b]. These radial readouts can be applied in 2D (Fig. 2.6**(a)**), or stacked (similar to the stacking of the EPI zig-zag pattern) across multiple planes to acquire 3D k-space data (Fig. 2.6**(b)**). Alternatively, they can be directly implemented in 3D, where each trajectory of the sampling pattern crosses the center of the k-space (Fig. 2.6**(c)**). Spiral readouts are also popular non-Cartesian techniques thanks to their efficient utilization of gradient capabilities, operating effectively at S_{max}. Like radial readouts, spirals can either be stacked [IN95] (Fig. 2.7**(b)**) or implemented fully in 3D using cones [GHN06], for example (Fig. 2.7**(c)**).

In fMRI, purely radial readouts are very rarely employed. However, the combination of radial readout concepts with EPI has been performed in techniques such as PROPELLER [KJR12] (Fig. 2.6**(d)**) and TURBINE [GMC22] (Fig. 2.6**(e)**). That being said, the most widely employed non-Cartesian readout in contemporary fMRI is the spiral-based readout [Glo12; Rie+21; Kas+22]. In this context, a new version, namely the Tilted Hexagonal (T-Hex) spiral [Eng+21; Bia+22] (Fig. 2.7**(d)**) technique, which samples spiral readouts on a tilted hexagonal grid, was recently introduced. This approach enables 3D imaging while ensuring a uniform coverage of the 3D k-space.

As the data points are no longer acquired on a Cartesian grid, the conventional uniform FFT is no longer applicable, necessitating the use of the Non-Uniform Fast Fourier Transform

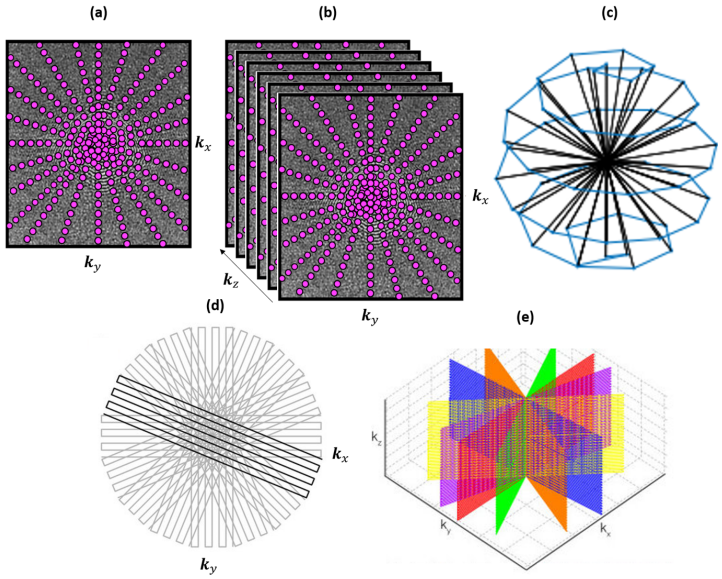

Figure 2.6: Radial sampling in **(a)** 2D, **(b)** stack-of-stars pattern in 2.5D, **(c)** full 3D radial sampling, **(d)** PROPELLER [KJR12], and **(e)** TURBINE [GMC22].

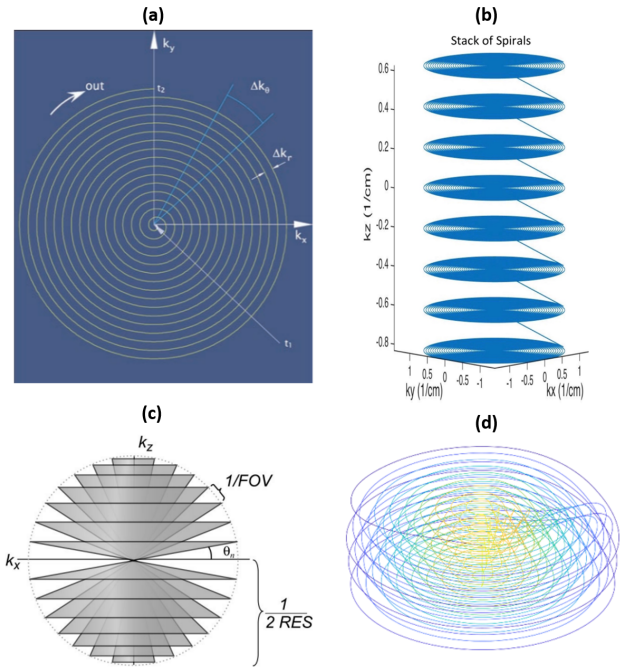

Figure 2.7: Spiral sampling in **(a)** 2D [FHM06], **(b)** stack-of-spirals pattern [SR17], **(c)** full 3D cone sampling [GHN06], **(d)** T-Hex spiral encoding scheme [Eng+21; Bia+22].

(NUFFT) for MR image reconstruction. The NUFFT operator facilitates the mapping between k-space points off the Cartesian grid and those on the grid. Two main techniques can be used for this end:

- Grid-driven technique: The missing on-the-grid k-space points can be interpolated from the neighboring off-the-grid measured k-space points. A large interpolation kernel ensures the inclusion of a sufficient number of off-the-grid measurements for interpolation. However, larger kernels may also result in significant overlaps, potentially introducing errors.

- Data-driven technique: The contribution of each off-the-grid measured k-space point is distributed to its neighboring missing on-the-grid k-space points, also using a kernel to define its neighborhood. Typically, in non-Cartesian sampling, the central portion of k-space is more densely sampled than the rest. This implies that the central part of k-space will have a higher representation in its neighboring on-the-grid k-space points. Density compensation should then be performed assigning weights to k-space regions in inverse proportion to their sampling density.

In short, on the one hand, the grid-driven approach estimates the missing on-the-grid samples based on their neighboring off-the-grid collected samples, and therefore, expresses the missing on-the-grid samples as a weighted sum of the neighboring off-the-grid collected samples. On the other hand, the data-driven approach, considers each off-the-grid collected sample and redistributes its contributions to the surrounding missing on-the-grid samples.

Non-Cartesian readouts can be combined with PI. Subsequently, reconstruction methods like Conjugate Gradient SENSE (CG SENSE) [Pru+01], non-Cartesian GRAPPA [GHJ03], or Iterative Self-consistent Parallel Imaging Reconstruction from Arbitrary (SPIRiT) [LP01] are employed.

Both radial and spiral readouts inherently incorporate variable density sampling (VDS) by favoring the sampling of the center of k-space over its periphery. This strategy is implicitly based on the notion that some data points may offer more pertinent information than others. It can be further combined with the fact that MR images/volumes are inherently compressible in some domains, such as the wavelets domain or total variation domain, to allow for higher undersampling of the k-space.

2.3 Compressed Sensing in fMRI

CS has found extensive application in MRI, with initial applications introduced in [LDP07; Lus+08]. However, its utilization in fMRI remains relatively uncommon. The foundation of CS lies in the assumption that MR images possess inherent sparsity or compressibility in an appropriate transform domain. Consequently, it becomes feasible to significantly undersample the k-space without compromising image quality. This is achieved through a pseudo-random sampling pattern combined with a nonlinear reconstruction method that enforces sparsity in a convenient domain, such as the wavelet domain.

2.3.1 Sparsity and nonlinear reconstructions

Let us consider $\mathbf{x} \in \mathbb{C}^N$, the complex MR image containing N voxels. If $\mathbf{x}$ has a sparse representation, then there exists $\Psi \in \mathbb{C}^{N \times K}$ a sparsifying basis (such as the wavelets transform) of K linear functions such that,

$$\mathbf{z} = \Psi\mathbf{x} \text{ where, } \mathbf{z} \text{ has some few non-zero coefficients.} \tag{2.4}$$

We can alternatively represent $\mathbf{x}$ as given in Eq. (2.5), where $\mathbf{y} \in \mathbb{C}^M$ represents the k-space data (NMR signal) that were collected according to the sampling pattern or mask Ω, over which the encoding operator $\mathbf{F}_\Omega$ is defined.

$$\mathbf{F}_\Omega^*\mathbf{y} = \mathbf{x} \iff \mathbf{y} = \mathbf{F}_\Omega\mathbf{x} \tag{2.5}$$

Combining Eq. (2.4) and Eq. (2.5), we obtain $\mathbf{y} = \mathbf{F}_\Omega\Psi^*\mathbf{z}$. In reality, $\mathbf{y}$ is noisy, leading to most coefficients in $\mathbf{z}$ being not strictly zero but very close to zero. We can estimate $\mathbf{x}$ by minimizing the problems in Eq. (2.7) (using the synthesis formulation) or Eq. (2.6) (using the analysis formulation). While the two formulations are equivalent when Ψ is a linear basis (i.e., $K = N$), the choice between them may depend on the algorithm used for iterative problem-solving, with one or the other being more convenient. Fast iterative algorithms such as Fast Iterative Soft Thresholding Algorithm (FISTA) [BT09] and Proximal Optimal Gradient Method (POGM) [THG18] are typically used along with the synthesis formulation. As the value of K increases (such as when using curvelets instead of wavelets), the sparsity

also increases, leading to improved image reconstruction quality. However, this improvement comes at a higher reconstruction cost in the synthesis formulation.

$$\begin{aligned} \hat{\boldsymbol{z}} &= \underset{\boldsymbol{z}\in\mathbb{C}^K}{\arg\min}\, \frac{1}{2}\left\|\boldsymbol{F}_\Omega \Psi^* \boldsymbol{z} - \boldsymbol{y}\right\|_2^2 + \lambda \left\|\boldsymbol{z}\right\|_1 \\ \hat{\boldsymbol{x}} &= \Psi^* \hat{\boldsymbol{z}} \end{aligned} \tag{2.6}$$

$$\hat{\boldsymbol{x}} = \underset{\boldsymbol{x}\in\mathbb{C}^N}{\arg\min}\, \frac{1}{2}\left\|\boldsymbol{F}_\Omega \boldsymbol{x} - \boldsymbol{y}\right\|_2^2 + \lambda \left\|\boldsymbol{\Psi x}\right\|_1 \tag{2.7}$$

In the context of PI, considering the synthesis formulation as an example, the problem transforms into: $\hat{\boldsymbol{x}} = \underset{\boldsymbol{x}\in\mathbb{C}^N}{\arg\min}\, \frac{1}{2}\sum_{\ell=1}^{L} \sigma_\ell^{-2} \left\|\boldsymbol{F}_\Omega \mathcal{S}_\ell \boldsymbol{x} - \boldsymbol{y}_\ell\right\|_2^2 + \lambda \left\|\boldsymbol{\Psi x}\right\|_1$, L being the number of receive channels, $\mathcal{S}_\ell$ the sensitivity profile of each of them, and σ_ℓ^2 is the corresponding noise variance.

If combined with non-Cartesian readouts, CS enables the optimal and isotropic undersampling of k-space in full 3D imaging. This concept inspired the development of optimization-driven CS methods like SPARKLING [Laz+19] and subsequently, 3D-SPARKLING [Laz+20; Cha+22].

2.3.2 3D-SPARKLING

Recently, the CS-based SPARKLING (Spreading Projection Algorithm for Rapid K-space sampLING) encoding scheme was introduced for 2D [Laz+19] and 3D [Laz+20; Cha+22] T_2^*-weighted MR anatomical imaging.

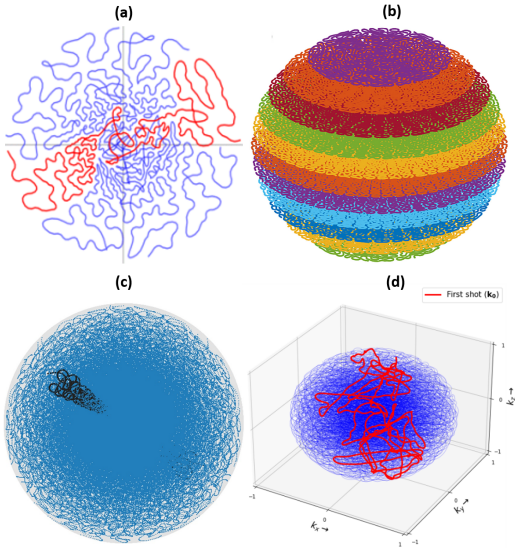

Figure 2.8: Sparkling sampling in **(a)** 2D, **(b)** spherical stack-of-sparkling pattern [Laz+20], **(c)** sub-optimal cone-filling 3D Sparkling [Laz+20], **(d)** full 3D-SPARKLING [Cha+22].

3D-SPARKLING [Cha+22] generates non-Cartesian segmented (also called multi-shots, i.e. multi-trajectories) pseudo-random sampling patterns that fit a non-uniform target sampling density. Compared to previous SPARKLING versions, the full 3D implementation optimizes the localization of trajectories in the whole 3D k-space.

3D-SPARKLING is well-suited for fMRI when compared to the older versions of SPARKLING (Fig. 2.9**(a)**, **(b)**, and **(c)**) for several reasons. Firstly, it is optimal for 3D imaging, which helps mitigate SAR issues, especially at high magnetic field strength, even though it leads to higher sensitivity to physiological noise. Secondly, the global optimization of the trajectories in 3D grants great flexibility when it comes to the target spatiotemporal

resolution. Lastly, in the 3D configuration, all shots sample the center of k-space, providing crucial benefits such as self-navigation, motion correction capabilities, and more flexible manipulation of the spatiotemporal resolution at the image reconstruction step.

In essence, the algorithm consists of two main steps: First, a gradient descent step (Fig. 2.9**(a)**) ensures, given an initialization and target sampling density, that the N_{shot} sampling pattern follows the target sampling density and is locally uniform. The target sampling density is typically chosen as a VDS where the center of k-space is densely sampled compared to its periphery. This design is motivated by the necessity to sample the low-resolution image corresponding to low frequencies fully and to undersample the high frequencies related to the details in the image domain, which can be recovered through sparsity constraints. Second, the shot-wise projection step (Fig. 2.9**(b)**) in the optimization algorithm ensures that each shot fits the hardware constraints (G_{max} and S_{max}) as well as the contrast affine constraint (same echo time for all shots). This process is iterated a number of times until a convergence criterion is met (e.g., distance to target distribution and shots compliance with G_{max} and S_{max}).

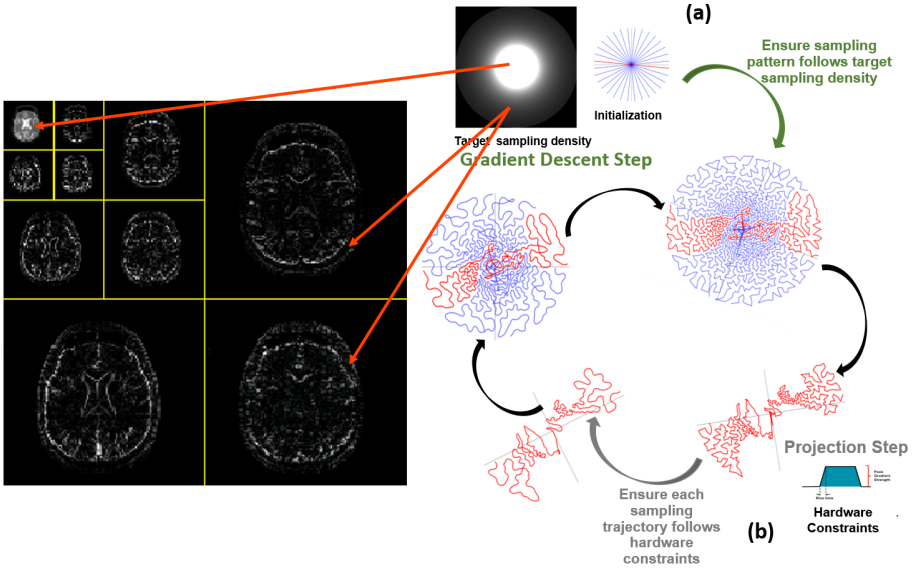

Figure 2.9: SPARKLING pattern generation algorithm: A projected gradient descent algorithm. **(a)** The gradient descent step ensures that, given an initialization and a target sampling density, the sampling pattern follows the target density and is locally uniform. **(b)** The projection step involves a shot-wise projection in the optimization algorithm, ensuring each shot adheres to hardware constraints (G_{max} and S_{max}) and contrast constraints (same echo time for all shots).

Theory

3D-SPARKLING implementation is detailed in [Cha+22] and is based on earlier works [Boy+16; Laz+19]. Hereafter, we briefly explain the theory underpinning the trajectories design. More details can be found in [Boy+16; Cha+17; Laz+19; Cha+22].

Let $\mathbf{K} = (\mathbf{k}_i)_{i=1}^{N_c}$ be a segmented 3D sampling pattern consisting of N_c shots and each shot has N_s sampling points. Each shot can be written in 3D as follows $\mathbf{k}_i(t) = (k_{i,x}(t), k_{i,y}(t), k_{i,z}(t))$. K-space trajectories in MRI are run using varying magnetic field gradients according to the following equation:

$$\mathbf{k}_i(t) = \frac{\gamma}{2\pi} \int_0^t \mathbf{G}_i(\tau) d\tau, \text{ where } \mathbf{G}_i(t) = (G_{i,x}(t), G_{i,y}(t), G_{i,z}(t)). \tag{2.8}$$

Let $K_{\max}$ define the boundaries of a 3D k-space domain such as $K_{\max} = K_{\max}^x = K_{\max}^y = K_{\max}^z$ for simplicity. 3D-SPARKLING shots are defined according to the following set of

constraints:

$$\mathcal{Q}_{\alpha,\beta}^{N_c} = \begin{Bmatrix} \forall i = 1, \dots, N_c, \quad \mathbf{k}_i \in \mathbb{R}^{3\times N_s}, \\ \mathbf{A}\mathbf{k}_i = \mathbf{v}, \\ \|\dot{\mathbf{k}}_i\|_{2,\infty} \leq \alpha, \quad \|\ddot{\mathbf{k}}_i\|_{2,\infty} \leq \beta, \end{Bmatrix} \tag{2.9}$$

where $\|\mathbf{c}\|_{2,\infty} = \sup_{0\leq n\leq N_s-1} \left(|c_x[n]|^2 + |c_y[n]|^2 + |c_z[n]|^2\right)^{1/2}$.
$\dot{\mathbf{k}}_i$ and $\ddot{\mathbf{k}}_i$ are the first and second-order time derivatives of the shot denoted $\mathbf{k}_i$.
$\alpha = \frac{1}{K_{\max}} \min\left(\frac{\gamma G_{\max}}{2\pi}, \frac{1}{FOV\cdot\delta t}\right)$ and $\beta = \frac{\gamma S_{\max}}{2\pi K_{\max}}$ with $G_{\max}$ and $S_{\max}$ the maximum gradient and slew rate constraints respectively. δt represents the dwell time, indicating the time interval between the sampling of two consecutive k-space points. $\mathbf{A}$ and $\mathbf{v}$ define the linear constraints that ensure that each shot crosses the center of k-space at the TE.

3D-SPARKLING trajectories are optimized to 1) match a target sampling density ρ and 2) optimally cover the k-space $\Omega = [-1, 1]^3$ in a locally uniform way according to the following formulation. Given a target sampling density $\rho : \Omega \to \mathbb{R}$ defined such as $\rho(x) \geq 0$ for all x and $\int \rho(x)\, dx = 1$, the sampling pattern $\mathbf{K} \in \Omega^p$ ($p = N_c \times N_s$) is generated by minimizing the problem defined by:

$$\widehat{\mathbf{K}} = \arg\min_{\mathbf{K}\in\mathcal{Q}_{\alpha,\beta}^{N_c}} F_p(\mathbf{K}) = \left[F_p^{\mathrm{a}}(\mathbf{K}) - F_p^{\mathrm{r}}(\mathbf{K})\right] \tag{2.10}$$

$$\text{with} \quad F_p^{\mathrm{a}}(\mathbf{K}) = \frac{1}{p}\sum_{i=1}^{p}\int_{\Omega} H(x - \mathbf{K}[i])\rho(x)\, dx$$

$$\text{and} \quad F_p^{\mathrm{r}}(\mathbf{K}) = \frac{1}{2p^2}\sum_{1\leq i,j\leq p} H(\mathbf{K}[i] - \mathbf{K}[j])\,.$$

F_p^{a} is an attraction term that guarantees 1) while F_p^{r} is a repulsion term that ensures 2) and $H(x) = \|x\|_2$. In this formulation, $p = N_c \times N_s$ denotes the total number of sampling points in $\mathbf{K}$ and $\mathcal{Q}_{\alpha,\beta}^{N_c}$ denotes the set of hardware and linear constraints defined earlier.

The pulse sequence

In practice, the implementation of 3D-SPARKLING for T_2^*-weighted 3D imaging involves utilizing an arbitrary gradients GRE sequence, as illustrated in Fig. 2.10. The In-Out (starting from one border of the k-space and progressing towards the center, finally sampling the second border) trajectories are executed through readout gradients along the three axes ($\mathbf{k}_x$, $\mathbf{k}_y$, $\mathbf{k}_z$). In fact, once the trajectories are generated, the corresponding gradient waveforms ($G_x(t)$, $G_y(t)$, $G_z(t)$) are computed as their time derivatives and given as input to the pulse sequence. Additionally, pre-phasing gradients are applied to position the initial k-space locations of each trajectory or shot, effectively transitioning from the center of the k-space to its periphery. A spoiling gradient is also applied after each shot.

In conclusion, this chapter has provided a comprehensive overview of selected state-of-the-art strategies and methodologies to accelerate fMRI acquisitions, encompassing traditional Cartesian, non-Cartesian, and less common (in fMRI) CS frameworks. Combining CS with non-Cartesian trajectories that are fully optimized in 3D k-space, as is the case with 3D-SPARKLING, provides increased flexibility in selecting the spatiotemporal resolution. Furthermore, the fact that all shots sample the k-space center proves instrumental for various applications in the broad context of fMRI. Hence, the pivotal role of 3D-SPARKLING in this work

When targeting high resolution in fMRI for large or full brain coverage, even with efficient undersampling techniques, BOLD sensitivity is significantly compromised due to smaller voxels (meaning there is less BOLD signal available voxel-wise), increased noise, and higher sensitivity to physiological noise. This is why moving to higher fields is utilized as a BOLD sensitivity booster in such a case. However, despite its advantages, it also comes with some inconveniences. This will be the focus of the next chapter's discussion.

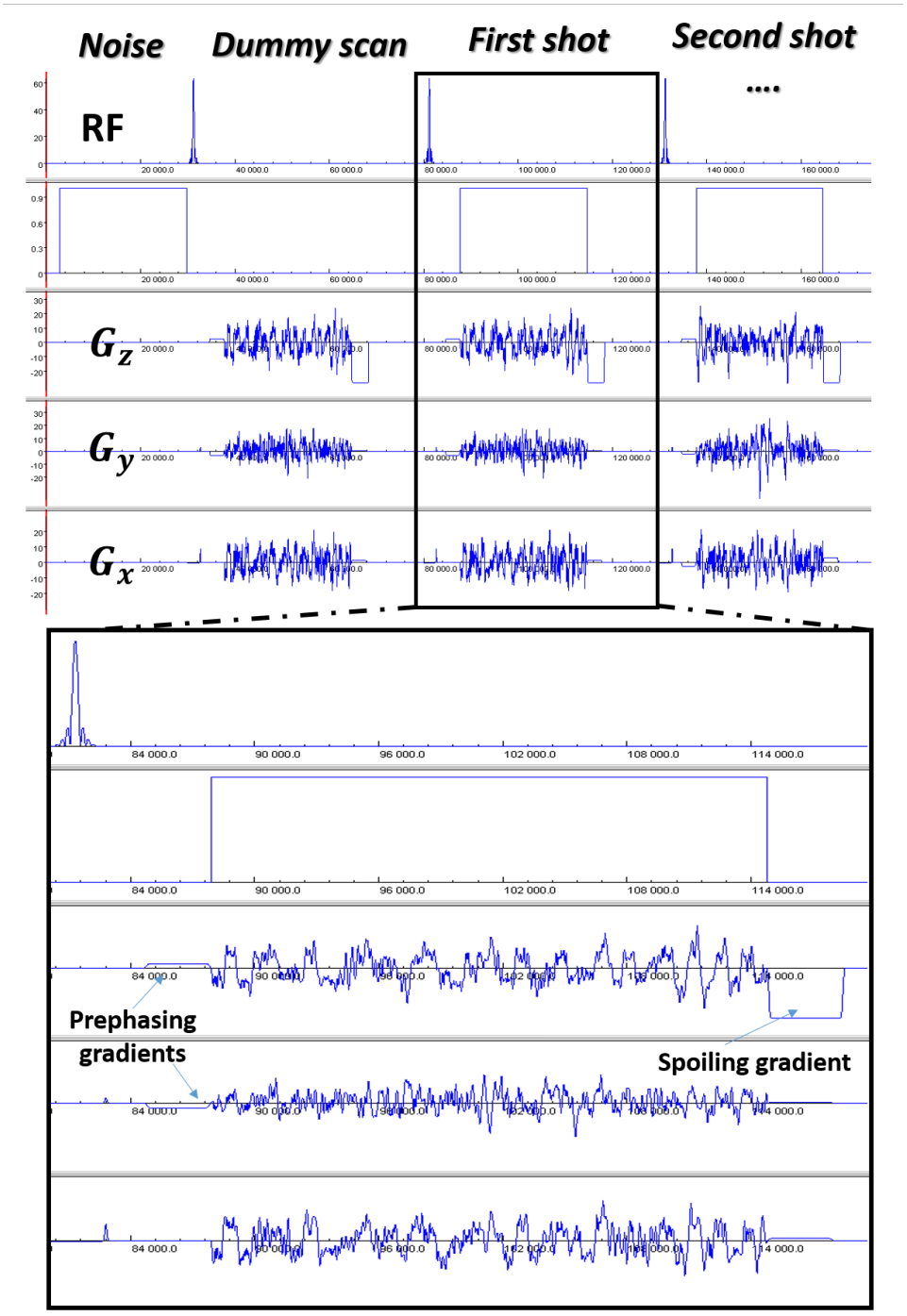

Figure 2.10: T_2^*-weighted 3D-SPARKLING arbitrary gradient GRE pulse sequence. The readouts are implemented using arbitrary gradients, and the sequence also incorporates noise and dummy scans. The user has the flexibility to choose the number of these scans

* * *
* *
*

Chapter 3

Ultra High Field (UHF) fMRI

In the previous chapter, we explored various strategies for accelerating fMRI acquisitions as a way to achieve high resolution without sacrificing brain coverage. We also identified 3D-SPARKLING as a potential asset to achieve high-resolution fMRI without compromising brain coverage. The conclusion briefly addressed the challenges of compromised BOLD sensitivity resulting from acceleration. This chapter discusses how leveraging high magnetic field strengths can effectively mitigate this issue and exposes the associated consequences. We focus on the challenge of $\mathbf{B}_0$ inhomogeneities and perturbations and discuss a specific technique that is crucial for the rest of this work to mitigate this issue.

3.1 Rationale for UHF fMRI

While BOLD fMRI stands out as a sensitive endogenous functional contrast method compared to other contrasts, its overall sensitivity remains limited, typically manifesting as some units of percentage of signal change ($\frac{\Delta S}{S_0} \approx TE\Delta R_2^*$ in case of a predominant T_2^* contrast). This diminished sensitivity becomes more apparent as spatial resolution is improved. Also, enhancing the temporal resolution by reducing the acquisition time or sampling the k-space faster leads to noisier data, degrading the method's sensitivity.

To enhance BOLD sensitivity, especially for applications that require either high spatial or high temporal resolution or both, higher magnetic fields (7T, and beyond) have been employed as signal boosters. The strength of the magnetic field stands out as a pivotal factor influencing BOLD sensitivity, with SNR and CNR exhibiting at least a linear augmentation as the field strength increases [Duy12; PSS16; Ste+22]. The SNR is known to depend on the magnetic field strength, as described by the relation $SNR \propto |\mathbf{B}_0|^\alpha$. In [PSS16], α was determined to be 1.65, while in [Ste+22], the authors reported α=1.94. From [Duy12], one can derive that CNR $\propto$ SNR $\frac{\Delta R_2^*}{R_2^*}$. If we consider that $\frac{\Delta R_2^*}{R_2^*} \propto |\mathbf{B}_0|$ and α=1.65, then CNR $\propto |\mathbf{B}_0|^{2.65}$. The precise quantification of the gain in SNR and CNR with an increase in magnetic field strength is ultimately contingent on various factors, including the design of the RF coils and the type of tissues being imaged. However, it is established that such dependencies (boosting effect of $|\mathbf{B}_0|$) exist. Enhancing the SNR and CNR, in turn, enhances the tSNR and temporal CNR (tCNR), which are crucial data quality factors in fMRI. Furthermore, higher fields offer enhanced BOLD specificity through a dual mechanism: 1) Enabling higher spatial resolution without a substantial loss of sensitivity, and 2) amplifying

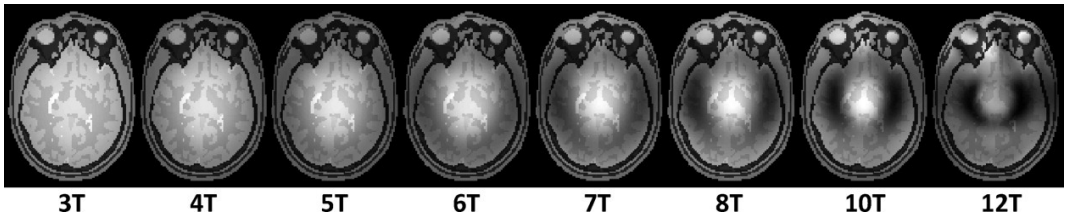

Figure 3.1: Simulated gradient-echo images, showing the extend of the $\mathbf{B}_1^+$ heterogeneities on image quality, as a function of field strength using a birdcage coil. (Figure taken from [Web11]).

the impact of extravascular contributions in BOLD signal over intravascular ones, resulting in improved specificity of the detected effect and reduced contamination from larger draining veins [Gat+97].

With the rise in magnetic field strength, there is a concurrent increase in the influence of its inhomogeneities and imperfections on image quality, often manifested as geometric distortions and signal loss. Additionally, when targeting higher spatial resolution, the dimensions of the sampling matrix and the duration of readouts expand. Consequently, following each excitation, $\mathbf{B}_0$ inhomogeneities and imperfections accumulate over a longer time, exacerbating their impact on the data even further. If uncorrected, $\mathbf{B}_0$ imperfections can cancel out the gain in sensitivity and specificity expected by moving to higher fields: Correcting off-resonance effects due to $\mathbf{B}_0$ inhomogeneities is, therefore, one way to secure the advantages of high fields without being subject to their disadvantages.

Issues related to $\mathbf{B}_1^+$ inhomogeneities (variations in the $\mathbf{B}_1^+$ transmit field strength leading to non-uniform excitation of spins within the imaging volume and signal loss in the image domain [Fig. 3.1]) and SAR limitations also become more pronounced at higher magnetic field strengths. To enhance the uniformity of magnetic spin excitation across the imaging volume, the Parallel Transmission (pTx) technique is utilized to optimize the design of RF pulses, aiming to minimize the heterogeneity of $\mathbf{B}_1^+$. RF design considerations also take into account the mitigation of specific SAR constraints. In [Jam+23], the authors demonstrate, at 7T, the benefit of implementing pTx through universal pulses (UP) [Gra+16] for tSNR enhancement in fMRI data. Nevertheless, at 7T, when employing GRE sequences, which do not require high flip angles, the signal loss due to $\mathbf{B}_1^+$ heterogeneities is not very severe. While these challenges are not addressed in detail within the scope of this work, interested readers are encouraged to explore the NeuroImage special issue entitled "Neuroimaging with Ultra-high Field MRI: Present and Future" for a more in-depth discussion.

3.2 $\mathbf{B}_0$ Field imperfections

Ideally, $\mathbf{B}_0$ is expected to be spatially homogeneous and constant over time. However, practical considerations introduce imperfections, leading to spatial inhomogeneities that may also vary over time. These inhomogeneities will locally alter the precession frequency of the affected spins (cf Section 1.1.2 in Chapter 1), consequently influencing how the recorded NMR signal is encoded. As a result, this can lead to inaccuracies in the image domain or even signal loss. The severity and nature of $\mathbf{B}_0$-related artifacts (signal loss, blurring, geometric distortions, etc) are also related to the encoding scheme and can be quite critical for some non-Cartesian schemes. In general, field imperfections, denoted $\Delta B_0(\mathbf{r}, t)$, depend both on space and time. In the following, we will decompose them into three terms: $g(\mathbf{r})$ is dependent on the spatial coordinates and corresponds to the static off-resonance term. $f(t)$ is time-varying and represents the dynamic field fluctuations. Finally, $\mathbf{B}_0$ imperfections lead to (first-order) errors in the effective encoding trajectories ($\delta\mathbf{k}$): These errors typically vary in time. Higher-order encoding errors can also be considered [Wil+11]. However, in what follows, we only take into account the three above mentioned terms.

3.2.1 Static $\mathbf{B}_0$ inhomogeneties

The static contribution of spatially varying magnetic field offsets arises mainly from the susceptibility differences at tissue-air interfaces and is, to some extent, routinely corrected in MRI in general. This issue is most prominent in brain MR images near the sinuses, buccal cavities, and ear canals. Static $\mathbf{B}_0$ inhomogeneities can cause geometric distortions, blurring, shading, and intense signal loss, ultimately exerting a negative impact on BOLD specificity and sensitivity [Dei+03]. They are usually minimized by means of shimming, which aims at homogenizing the spatial profile of the field by applying the opposite distribution of its spatial inhomogeneities. Shimming can be passive by placing magnetic objects near the ears, for example, or active by sending currents in the coils that produce a counter profile to the field inhomogeneities. Optimizing active shimming for brain MRI, especially at high fields (3T and beyond), is an active field of research [MA21; SW18]. However, shimming is never perfect, and residual $\mathbf{B}_0$ inhomogeneities must be accounted for using a ΔB_0 map during image reconstruction [SNF03; Fes+05a; Don20] using a more realistic signal model that includes this spatial inhomogeneities map (ΔB_0 map): Eq. (1.6) becomes Eq. (3.1). Preprocessing steps such as the TOPUP approach [ASA03; Smi+04] can also be applied in the case of EPI fMRI to correct further geometric ΔB_0 distortions. TOPUP employs data acquired in opposite phase-encoding directions to estimate distortion maps caused by field inhomogeneities. A summary of the primary causes, their impact on fMRI data, and the principal solution for static field inhomogeneities is provided in Table 3.1.

$$
\begin{aligned}
&S(t) = \int_{FOV} M(t=0,\mathbf{r}) e^{-2i\pi g(\mathbf{r})t} e^{-2i\pi \mathbf{k}(t)\cdot\mathbf{r}} d\mathbf{r} \\
&\text{where } \mathbf{k}(t) = [k_x(t), k_y(t), k_z(t)]^T (\mathrm{m}^{-1}),\ \mathbf{r} = [x, y, z] \\
&\text{and } g(\mathbf{r}) \text{ is the value of the } \Delta B_0 \text{ map (Hz) at the spatial position } \mathbf{r}
\end{aligned}
\tag{3.1}
$$

Table 3.1: A summary of the primary causes, effects, and solutions for static magnetic field inhomogeneities.

Static field inhomogeneities	
Causes	Differences in susceptibility at tissue air interfaces.
Effects	Geometric distortions $\Longrightarrow$ Loss in specificity. Blurring and shading and signal loss $\Longrightarrow$ Loss in sensitivity.
Solutions	Prospective methods: Shimming. Retrospective methods: Correction during image reconstruction using a ΔB_0 map. Preprocessing methods: TOPUP.

Static ΔB_0 mapping: A GRE sequence using multiple echo times (i.e., the signal is acquired for several echo times during a single TR) is typically used to estimate the ΔB_0 map. The phase ($\phi(\mathbf{r}, TE)$) of a complex MR image can be expressed as follows:

$$
\begin{aligned}
&\phi(\mathbf{r}, TE) = \phi_0 - \gamma \Delta B_0(\mathbf{r}, TE), \\
&\text{where } \phi_0 \text{ is an offset due to the permittivity, conductivity, and RF design}
\end{aligned}
\tag{3.2}
$$

If we consider, two different echo times, TE_1 and TE_2, then we can write:

$$
\Delta B_0(\mathbf{r}) = \frac{\phi(\mathbf{r}, TE_2) - \phi(\mathbf{r}, TE_1)}{\gamma(TE_2 - TE_1)} \tag{3.3}
$$

Consequently, a minimum of two echoes is required for estimating $\Delta B_0(\mathbf{r})$, although employing additional echoes, which extends the acquisition time of the GRE sequence, allows for a more refined estimation. Moreover, it is crucial to find a compromise between the spatial resolution of the field map and the time required for its acquisition.

3.2.2 Dynamic $\mathbf{B}_0$ fluctuations

Dynamic perturbations of the $\mathbf{B}_0$ field can stem from the system (instabilities in the gradient system such as temperature drifts, eddy currents, etc [Van+13]) or from the volunteer (e.g. breathing and heart rate).

- Eddy currents: The fast switching of the gradients generates, according to Faraday's law of induction, electrical currents in the conducting elements of the scanner. These so-called eddy currents generate unwanted time-varying field gradients and offsets in $\mathbf{B}_0$.

- Temperature drifts: The temperature influences the magnetic properties of the main magnet that generates $\mathbf{B}_0$ and the properties of other components within the scanner. FMRI experiments are demanding for the gradient system, particularly with the use of fast readouts like EPI or non-Cartesian techniques. This is executed by applying currents in the gradients, contributing to the heating of the system and its materials. Consequently, this leads to gradual drifts in $\mathbf{B}_0$.

- Physiological noise: The volunteer's motion, breathing, and heartbeat also produce small fluctuations in $\mathbf{B}_0$. These small fluctuations produce BOLD-like changes in the MR signal. Moreover, as voxel size diminishes, the challenge of motion artifacts becomes more pronounced.

Dynamic field perturbations are typically divided into a global zeroth order term ($f(t)$), first-order deviations from the nominal trajectories ($\delta\mathbf{k}$), and some higher-order cross terms [Kas+15; Bol+17]. As explained above, $\mathbf{B}_0$ imperfections affect the intensities of the MR images. Therefore, when they are dynamic and therefore time-varying, they constitute a potential confounding factor for fMRI in regions where a significant BOLD effect is sought: They may act as nuisance variables [MBB13] by causing intensity changes that are unrelated to the neuro-vascular coupling and degrade the tSNR. Similar to static field inhomogeneities, dynamic field fluctuations can be compensated prospectively during the acquisition or corrected retrospectively during image reconstruction using time-varying estimates [Don20] and including them into the signal model: Adding the first-order dynamic terms to Eq. (3.1), it becomes Eq. (3.4).

$$S(t) = \int_{FOV} M(t=0,\mathbf{r}) e^{-2i\pi(g(\mathbf{r})+f(t))t} e^{-2i\pi(\mathbf{k}(t)+\delta\mathbf{k}(t))\cdot\mathbf{r}} d\mathbf{r} \tag{3.4}$$

The systematic characterization and correction of the reproducible component of field fluctuations (typically induced by the system) can be achieved using the Impulse Response Function (IRF) of the system, also known as Gradient IRF (GIRF) [Van+13]. That said, monitoring the non-reproducible components during every experiment ensures a systematic observation of both non-reproducible and reproducible components.

Navigators are typically implemented into sequences to monitor dynamic field fluctuations [EF89]. However, navigators require alteration of the pulse sequences and sometimes lengthen the acquisition time. Some sampling techniques such as [KJR12; GMC22] have a distinct feature that allows estimating these fluctuations from the acquired k-space data itself: These techniques are called self-navigating. Physiological probes such as breathing belts can also be used to correct physiology-related field fluctuations during acquisition but only give an indirect measure of the induced field perturbations.

A method that uses NMR probes [De +08; BDP08; Bar+09] to monitor the field fluctuations has been proposed. Unlike navigators, using NMR probes does not require alteration of the pulse sequence. Compared to self-navigating techniques, it allows for field monitoring in real-time instead of having access only to average measurements of the temporal field fluctuations.

3.3 Field Camera

The system presented in [De +08; BDP08; Bar+09], uses transmit and receive probes that contain an NMR active product excited by applying a radio frequency (RF) pulse at its Larmor frequency. It later evolved into a field camera using doped Fluorine (^{19}F) NMR probes (Fig. 3.2) and was used for field monitoring with anatomical and functional MRI [Van+15; Bol+17; Sch+19]. Given the difference in Larmor frequency of doped Fluorine and Hydrogen, such probes enable monitoring the field concurrently with the imaging process in the case of proton MR imaging.

Figure 3.2: Skope Magnetic Resonance Imaging AG's field camera consisting of ^{19}F probes.

3.3.1 Theory

Let us consider a single probe. After being excited during a proton imaging MR pulse, an NMR signal is generated from its NMR-active product with a phase accrual in time ($\phi_p(t)$) as expressed in Eq.(3.5), where γ_p (respectively, γ) is the gyromagnetic ratio of ^{19}F (respectively, ^{1}H) and $\phi_{0,p}$ the initial phase of the probe.

$$\phi_p(t) = \frac{\gamma_p}{\gamma}\int_0^t B(\mathbf{r}_p, t')dt' + \phi_{0,p} \tag{3.5}$$

We can consider $B(\mathbf{r}, t)$ as a separable function in time and space and decompose it over N_b-function basis: $B(\mathbf{r}, t) = \sum_{i=1}^{N_b} c_i(t)b_i(\mathbf{r})$, where $c_i(t)$ and $b_i(\mathbf{r})$ are respectively the dynamic and spatial coefficients. Therefore, we can rewrite:

$$\begin{aligned}\phi_p(t) &= \frac{\gamma_p}{\gamma}\sum_{i=1}^{N_b}\int_0^t c_i(t')b_i(\mathbf{r}_p)dt' + \phi_{0,p} = \frac{\gamma_p}{\gamma}\sum_{i=1}^{N_b}\int_0^t c_i(t')dt'b_i(\mathbf{r}_p) + \phi_{0,p}\\ \phi_p(t) &= \frac{\gamma_p}{\gamma}\sum_{i=1}^{N_b} k_i(t)b_i(\mathbf{r}_p) + \phi_{0,p}, \text{ where } k_i(t) = \int_0^t c_i(t')dt'\end{aligned} \tag{3.6}$$

We can write this in matrix form, as $\bar{\phi}(t) = \mathbf{P}\bar{\mathbf{k}}(t) + \bar{\phi}_0$, where $\mathbf{P}$ represents the spatial basis and $\bar{\mathbf{k}}(t)$ the corresponding phase coefficients.

$$\bar{\phi}(t) = \begin{pmatrix}\phi_1(t)\\ \phi_2(t)\\ \vdots\\ \phi_{N_p}(t)\end{pmatrix} \tag{3.7}$$

$$\mathbf{P} = \frac{\gamma_p}{\gamma}\begin{pmatrix} b_1(\mathbf{r}_1) & b_2(\mathbf{r}_1) & \cdots & b_{N_b}(\mathbf{r}_1)\\ b_1(\mathbf{r}_2) & b_2(\mathbf{r}_2) & \cdots & b_{N_b}(\mathbf{r}_2)\\ \vdots & \vdots & \ddots & \vdots\\ b_1(\mathbf{r}_{N_p}) & b_2(\mathbf{r}_{N_p}) & \cdots & b_{N_b}(\mathbf{r}_{N_p})\end{pmatrix} \tag{3.8}$$

$$\bar{\mathbf{k}}(t) = \begin{pmatrix} k_1(t) \\ k_2(t) \\ \vdots \\ k_{N_b}(t) \end{pmatrix} \tag{3.9}$$

$$\bar{\phi}_0 = \begin{pmatrix} \phi_{0,1} \\ \phi_{0,2} \\ \vdots \\ \phi_{0,N_p} \end{pmatrix} \tag{3.10}$$

Therefore $\bar{\mathbf{k}}(t) = \mathbf{P}^+(\bar{\phi}(t) - \bar{\phi}_0)$ such that $\mathbf{P}^+ = (\mathbf{P}^T\mathbf{P})^{-1}\mathbf{P}^T$ is the pseudo-inverse of $\mathbf{P}$. If $N_p >> N_b$ (i.e., if the spatial positions $\mathbf{r}_p, p \in [1, N_p]$ of the probes are known, through a calibration scan for instance), this linear system is overdetermined and admits a unique solution. The spatial spherical harmonics basis (cf Table 3.2) is convenient since it represents a mathematically efficient way to define functions over a spherical surface. Stopping at the first order of the spherical harmonics terms and ignoring $\frac{\gamma_p}{\gamma}$ and $\bar{\phi}_0$, we can write $\phi(\mathbf{r}, t) = k_0(t) + k_1(t)x + k_2(t)y + k_3(t)z$, where $k_0(t) = f(t)$ and $[k_1, k_2, k_3] = \mathbf{k} + \delta\mathbf{k}$. Consequently, by monitoring the phases of the probes, the field camera enables the estimation of the field fluctuations and deviations from the nominal trajectories.

Order	Spherical harmonics terms
0	x
1	y
1	z
1	$z^2 - (x^2 + y^2)$
2	xz
2	yz
2	$x^2 - y^2$
2	$2xy$
3	$3yx^2 - y^3$
3	xyz
3	$5yz^2 - y(x^2 + y^2 + z^2)$
3	$2z^3 - 3z(x^2 + y^2)$
3	x $5xz^2 - x(x^2 + y^2 + z^2)$
3	x $z(x^2 - y^2)$
3	x $x^3 - 3xy^2$

Table 3.2: Terms of the spherical harmonics basis up to the third order

In conclusion, this chapter focused on the rationale for adopting UHF in fMRI, with a specific emphasis on mitigating some of its inconveniences by addressing $\mathbf{B}_0$ field imperfections. In connection with the previous chapter, 3D-SPARKLING at UHF, coupled with additional $\mathbf{B}_0$ imperfections correction, holds considerable promise for fMRI. However, it is essential to note that the correction of $\mathbf{B}_0$ perturbations, while valuable, constitutes only a partial solution for motion-related artifacts. Moving forward, dedicated solutions aimed at comprehensive motion correction are imperative to improve the robustness of UHF fMRI.

* * *
* *
*

Part II

Methodological Developments

Chapter 4

Experimental setup for non-Cartesian CS-based 3D-SPARKLING high spatial resolution fMRI

4.1 Context

The overall goal of this work is to achieve high spatio-temporal resolution whole-brain BOLD fMRI by taking advantage of 3D-SPARKLING and its unique features that combine CS theories and non-Cartesian sampling through the judicious global and isotropic optimization of the trajectories, each crossing the center of k-space, in 3D. These features are expected to offer benefits in 3D imaging, providing flexibility in spatiotemporal resolution achievable.

In the realm of fMRI, CS-based approaches are rarely employed. In fact, the application of CS to dynamic MR imaging, such as fMRI, should optimally enforce sparsity both in space and time. However, sparsity in the time domain is difficult to achieve in fMRI applications as the recorded fMRI signal is not quasi-periodic in contrast to the heartbeat in cardiac cine imaging, for instance. Hence, finding a sparsifying basis for the BOLD signal, such as activelets [Kha+11], has been a research topic in itself. This is why the application of CS in fMRI [Cha+13; Han+15; Fan+16; Zon+14] remains limited. Additionally, what sets apart the general direction of this work is the fact that 3D-SPARKLING has never been used in fMRI before: In contrast to EPI-based methods or commonly used non-Cartesian methods such as spiral-based readouts, SPARKLING is a relatively recent technique initially introduced for 2D imaging [Laz+19] in 2019 and later extended to full 3D imaging [Cha+22] in 2022 and was mainly investigated for anatomical imaging. Moreover, we choose to use it to collect whole-brain acquisitions at a rather high spatial resolution ($1mm^3$). As the first

validation step, 3D-SPARKLING will be used in a scan-and-repeat mode without enforcing any kind of sparsity in time.

This chapter aims to provide a comprehensive yet concise overview of the full experimental setup we opted for regarding the use of 3D-SPARKLING for collecting high spatial resolution fMRI *in vivo*. We start by describing the stimulation paradigm, how the data was collected, and specify the pulse sequence parameterization. We then report the strategies employed to reconstruct the functional MR volumes from the acquired k-space data and their implementation. We also provide insight into the preprocessing pipeline and statistical analysis steps.

4.2 Experimental design

Data was collected during resting-state and task-based fMRI experiments, as shown in Fig. 4.1. The volunteers were asked to look at a fixation cross for 5 minutes during each resting-state run. Task-based fMRI data was acquired using a classical retinotopic mapping experimental paradigm with a 32s-period rotating wedge. We denote this rotation period as $P_{\text{cyc}} = 32$. A full retinotopic mapping experiment/run encompasses two consecutive sessions: A clockwise and a counter-clockwise rotation. Each session lasted 4 minutes and 48 seconds, accounting for $n_{\text{cyc}} = 9$ rotation cycles. The code of the stimulation can be found in[1].

Reliability is an issue in fMRI studies: In [BM10], the authors claim that fMRI studies' reproducibility can be characterized with intra-class correlation coefficients (ICC) values ranging from 0.33 to 0.66. This is due to several uncontrolled variables, such as thermal and physiological noises, evolution in cognitive strategies, and their overlap with non-task-related cognitive processes. Therefore, the choice of the retinotopic mapping paradigm emanated from two main factors: First, a higher tSNR (and tCNR) available in the visual cortex, and second, the fact that passive viewing is less prone to variability or errors in task performance [BM10]. By doing so, we aim to mitigate the impact of 1) thermal noise and 2) changes in cognitive strategies.

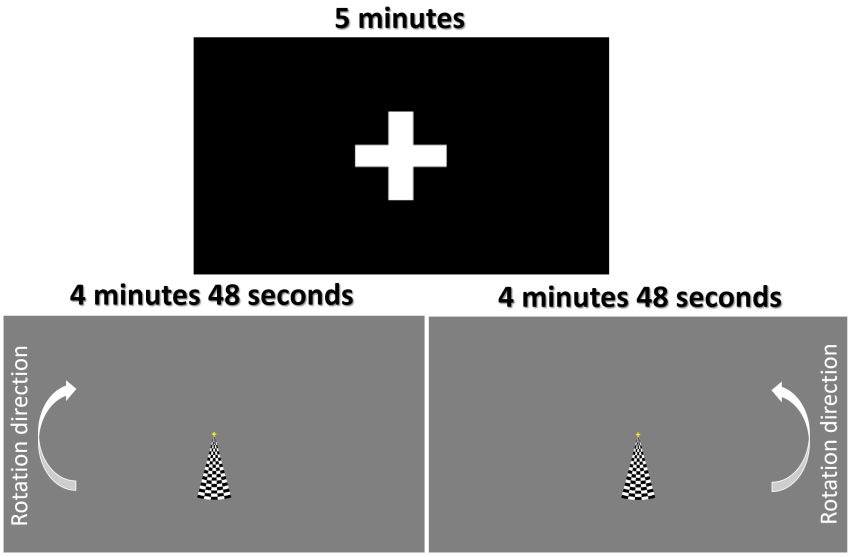

Figure 4.1: For each participant, resting-state and retinotopic mapping fMRI data was collected. A full retinotopic mapping experiment encompasses a clockwise and a counter-clockwise session.

[1] https://github.com/hbp-brain-charting/public_protocols

4.3 Data acquisition and sequence parameters

Functional data was collected at a 1-mm isotropic and 2.4s spatio-temporal resolution using T_2^*-weighted multi-repetition 3D-SPARKLING whole-brain acquisitions. The FOV chosen was (192×192×128)mm^3 and TE/TR$_{shot}$=20/50ms. One resting-state (125 scans or repetitions) and a full retinotopic mapping (2 consecutive sessions, 120 scans each) experiments were carried out for each participant.

The specific 3D-SPARKLING encoding used pattern consisted of $N_{shot} = 48$ shots generated to match the target sampling density that yielded the trajectories (Fig 4.2) with the best point spread function (PSF) in terms of full width at half maximum (FWHM) and maximum-to-side lobe ratio. The best-identified cutoff C and decay D parameters of the target density $\pi_{C,D}$ were set respectively to $C = 0.25$ and $D = 2$ in (Eq.(4.1)) to separate out the sampling regimes in the low and high frequencies as follows:

$$\pi_{C,D}(x) = \begin{cases} \kappa & |x| < C \\ \kappa \left(\frac{C}{|x|}\right)^D & |x| > C \end{cases} \tag{4.1}$$

where κ is a normalizing constant.

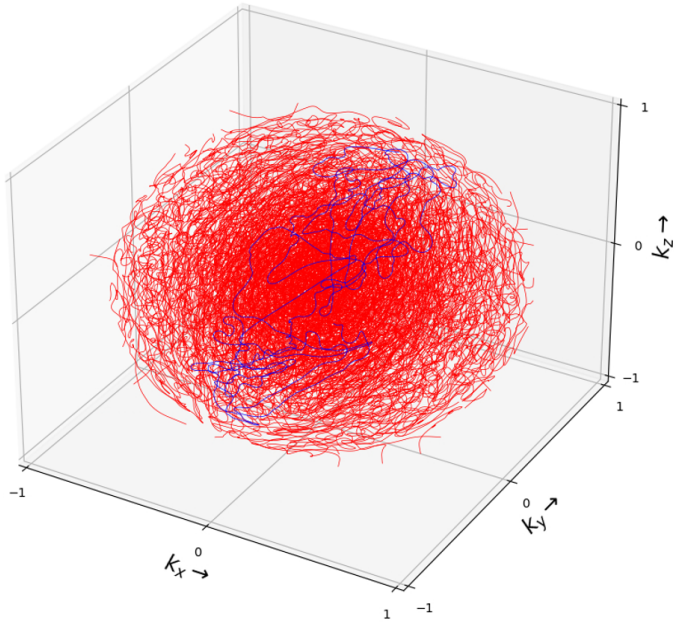

Figure 4.2: 3D-SPARKLING sampling scheme for fMRI. The sampling scheme is segmented into 48 readouts plotted in red except for one plotted in blue for the sake of visualization.

Additionally, a distinct 3D GRE sequence with three consecutive echoes was used to estimate both an external field map and external coil sensitivity maps. In order to have a reasonable acquisition time, the above-mentioned sequence was run for a spatial resolution of 3mm^3.

4.4 Functional MR volumes reconstruction and preprocessing

4.4.1 Single volume reconstruction

Extended signal model

Let T_{obs} be the duration of each of the N_{shot} shots, and let's recall that each of them samples the center of k-space at the echo time (TE). Therefore, during the s-th shot, the NMR signal $\mu_\ell^s(t)$ collected by the ℓ-th coil for each $t \in [TE - \frac{T_{obs}}{2}, TE + \frac{T_{obs}}{2}]$ (in s) can be modeled by

the extended signal model as follows:

$$\mu_\ell^s(t) = e^{-2\imath\pi t \Delta B_{0,dyn}^s} \int_{\text{FOV}} \bar{x}_\ell(\boldsymbol{r}) e^{-2\imath\pi\left[\Delta B_{0,stat}(\boldsymbol{r})t + \tilde{\boldsymbol{k}}^s(t)\cdot\boldsymbol{r}\right]} \, \mathrm{d}\boldsymbol{r} \tag{4.2}$$

where $\bar{x}_\ell(\boldsymbol{r}) = \zeta_\ell(\boldsymbol{r})x(\boldsymbol{r})$ is the image x multiplied by the sensitivity profile of the ℓ-th coil ζ_ℓ at the spatial position $\boldsymbol{r}$. Note that $\Delta B_{0,stat}(\boldsymbol{r})$ (in Hz) denotes the static inhomogeneities of the magnetic field in space whereas $\Delta B_{0,dyn}^s$ (in Hz) and $\tilde{\boldsymbol{k}}^s = \boldsymbol{k}^s + \delta\boldsymbol{k}^s$ (in m^{-1}) denote respectively its zeroth order dynamic fluctuation and the measured trajectory which deviates the prescribed one ($\boldsymbol{k}^s$) due to first order fluctuation $\delta\boldsymbol{k}^s$. $\Delta B_{0,dyn}^s$ is slowly varying and considered constant during a shot.

In Eq. (4.2), the term $\Delta B_{0,stat}(\boldsymbol{r})t$ depends both on the image domain and k-space, making the integral mathematically involved and incompatible with the usual (non-uniform) Fourier transform model.

Linear approximation of the non-Fourier model

According to Eq. (4.2), the discretized adjoint transform can be written as follows:

$$\forall \ell = 1, ..., L,\ \bar{x}_\ell(\boldsymbol{r_n}) = \sum_{t_m=m}^{M} e^{2\imath\pi t_m \Delta B_{0,dyn}^s} \mu_\ell^s(t_m) e^{2\imath\pi\left[\Delta B_{0,stat}(\boldsymbol{r_n})t_m + \tilde{\boldsymbol{k}}^s(t_m)\cdot\boldsymbol{r_n}\right]} \tag{4.3}$$

The mixed term $e^{2\imath\pi\Delta B_{0,stat}(\boldsymbol{r_n})t_m} = \sum_{p=1}^{P} b_{m,p}c_{p,n}$ can be split in a P-rank linear decomposition using an SVD to recover a sum of P (non-uniform) Fourier transform as written in Eq.(4.4). The details of the implementation are explained in the supplementary materials of [Dav+22] and follow the methods in [Fes+05b]

$$\forall \ell = 1, ..., L,\ \bar{x}_\ell(\boldsymbol{r}_n) = \sum_{p=1}^{P} c_{p,n} \sum_{t_m=m}^{M} b_{m,p} \underbrace{e^{2\imath\pi\Delta B_{0,dyn}^s t_m} \mu_\ell^s(t_m)}_{\widetilde{\mu}_\ell^s(t_m)} e^{2\imath\pi\tilde{\boldsymbol{k}}^s(t_m)\cdot\boldsymbol{r}_n} \tag{4.4}$$

Since the term related to $\Delta B_{0,dyn}^s$ is outside the integral in Eq. (4.2), the zeroth order dynamic fluctuations can be corrected by simply demodulating each $\mu_\ell^s(t)$ with the corresponding $e^{2\imath\pi t\Delta B_{0,dyn}^s}$ to obtain $\widetilde{\mu}_\ell^s(t)$. As Eq. (4.4) holds for all frequencies $\tilde{\boldsymbol{k}}^s$ and locations $\boldsymbol{r}_n$ across the N_{shot} readouts, we can summarize the perturbed acquisition in Eq. (4.5), as a sum of adjoint non-uniform Fourier transforms $\mathcal{F}_{\widetilde{\Omega}}$, yielding a coil-specific image $\bar{\boldsymbol{x}}_\ell$ from the measured frequencies locations $\widetilde{\Omega}$ and associated corrected values ($\widetilde{\boldsymbol{\mu}}_\ell = [\widetilde{\mu}_\ell^s]_{1\le s\le N_{shot}}$):

$$\forall \ell = 1, ..., L,\ \bar{\boldsymbol{x}}_\ell = \sum_{p=1}^{P} \boldsymbol{c}_p \odot \boldsymbol{\mathcal{F}}_{\widetilde{\Omega}}^*(\boldsymbol{b}_p \odot \widetilde{\boldsymbol{\mu}}_\ell) = \widetilde{\boldsymbol{\mathcal{F}}}_{P,\widetilde{\Omega}}^*(\tilde{\boldsymbol{\mu}}_\ell), \tag{4.5}$$

where $\odot$ denotes the element-wise product.

CS-based multi-coil reconstruction formulation

Let $\boldsymbol{x}_j \in \mathbb{C}^N$ (N is the number of voxels in each volume) be one single MR volume, the CS-based multi-coil reconstruction solves the problem in Eq. (4.6) where $\bar{\boldsymbol{y}}_{j,\ell} = \bar{\boldsymbol{\mu}}_{j,\ell} + \boldsymbol{n}_{j,\ell}$ is the k-space data, associated with the set of sampled frequencies points $\bar{\Omega}_j = \bar{\Omega} = [\bar{\boldsymbol{k}}_1, \ldots, \bar{\boldsymbol{k}}_{N_{shot}}]$ relative to the j-th volume. Here, $\boldsymbol{n}_{j,\ell}$ is an additive zero-mean white Gaussian noise of σ_ℓ^2 variance and $\bar{\boldsymbol{y}}_{j,\ell} \in \mathbb{C}^M$. M is the number of k-space measurements collected by each coil.

$$\hat{\boldsymbol{x}}_j = \underset{\boldsymbol{x}_j \in \mathbb{C}^N}{\arg\min} \frac{1}{2} \sum_{\ell=1}^{L} \sigma_\ell^{-2} \left\| \widetilde{\boldsymbol{\mathcal{F}}}_{P,\bar{\Omega}} \mathcal{S}_\ell \boldsymbol{x}_j - \bar{\boldsymbol{y}}_{j,\ell} \right\|_2^2 + \lambda g(\boldsymbol{\Psi}\boldsymbol{x}_j). \tag{4.6}$$

$$\bar{\boldsymbol{y}}_{j,\ell} = \begin{cases} \widetilde{\boldsymbol{y}}_{j,\ell} = \widetilde{\boldsymbol{\mu}}_{j,\ell} + \boldsymbol{n}_{j,\ell} \text{ if o-}th \text{ order field fluctuations are taken into account} \\ \boldsymbol{y}_{j,\ell} = \boldsymbol{\mu}_{j,\ell} + \boldsymbol{n}_{j,\ell} \text{ otherwise,} \end{cases} \tag{4.7}$$

and

$$\bar{\Omega} = \begin{cases} \widetilde{\Omega} = [\widetilde{\boldsymbol{k}}_1, \ldots, \widetilde{\boldsymbol{k}}_{N_{shot}}] \text{ if first-order field fluctuations are taken into account} \\ \Omega = [\boldsymbol{k}_1, \ldots, \boldsymbol{k}_{N_{shot}}] \text{ otherwise} \end{cases} \tag{4.8}$$

$\mathcal{S}_\ell$ denotes the sensitivity profile[2] of the ℓ-th coil and $\widetilde{\boldsymbol{\mathcal{F}}}_{P,\bar{\Omega}}$ the *linearized over P interpolators* off-resonance corrected[3] Fourier operator. $\boldsymbol{\Psi}$ is the sym8 wavelet sparsifying basis, g is chosen as the ℓ_1-norm, and the other reconstruction parameters were set to $L = 32, P = 30, \lambda = 10^{-8}$.

4.4.2 Implementation of a full fMRI session reconstruction

Each volume ($\boldsymbol{x}_j \in \mathbb{C}^N, j = 1, .., N_t$) is reconstructed independently of the others using a `Python` implementation of the minimization problem in Eq.(4.6) which relies on the method published in [El +18] and the `pysap-mri`[4] plugin [Gue+20] of the `pySAP` package [Far+20] and performs the optimization using the proximal optimized gradient method (POGM) algorithm [THG18].

The reconstruction of each full-time series was run on the Jean Zay[5] cluster where every five volumes were parallelized over a single Nvidia V100 GPU, allowing the reconstruction of a full times series/fMRI session in a few hours (3 to 8 depending on the number of GPUs available).

4.4.3 General preprocessing pipeline

Motion correction and co-registration of the functional and the anatomical (i.e., T_1-weighted) volumes was performed using `SPM12`[6]. Unless explicitly stated, no spatial smoothing was applied to the volumes in order to keep the advantages of the native 1-mm isotropic spatial resolution.

4.5 Statistical analysis of the task-based fMRI data

4.5.1 Design matrix for capturing task-related BOLD signal fluctuations

For each participant, the sequence of task-related fMRI volumes was analyzed using a two-session first-level general linear model (GLM) that is summarized through a design matrix $\mathbf{X} \in \mathbb{R}^{2N_{\text{vol}} \times Q}$ with $N_{\text{vol}} = 120$ scans per session and Q defines the number of regressors as detailed hereafter. The objective was to estimate the parameters of interest $\boldsymbol{\beta} = (\beta_i)_{i=1}^V \in \mathbb{R}^{Q \times V}$ in V voxels from the observed BOLD fMRI time series $\mathbf{Y} = (\mathbf{y}_i)_{i=1}^V \in \mathbb{R}^{2N_{\text{vol}} \times V}$, in the classical massively univariate linear model: $\mathbf{Y} = \mathbf{X}\boldsymbol{\beta} + \mathbf{N}$, where $\mathbf{N} = (\nu_i)_{i=1}^V \in \mathbb{R}^{2N_{\text{vol}} \times V}$ stands for the voxelwise additive serially correlated Gaussian noise term.

Due to the repetition of the task over two consecutive sessions, matrix $\mathbf{X}$ has a block-diagonal structure:

$$\mathbf{X} = \begin{pmatrix} \mathbf{X}_1 & \mathbf{0}_{N_{\text{vol}},Q/2} \\ \mathbf{0}_{N_{\text{vol}},Q/2} & \mathbf{X}_2 \end{pmatrix},$$

where the non-zero diagonal blocks $\mathbf{X}_1$ and $\mathbf{X}_2$ are respectively associated with the experimental paradigm that is carried out during the first and second sessions, namely the clockwise

[2] Raw data of the first echo from the multi-echo GRE sequence mentioned above was used to compute the sensitivity maps. Extrapolation in the k-space was performed to match the sensitivity maps to the fMRI volumes spatial resolution and FOV.

[3] The 3 echoes were used to obtain an accurate estimate of the ΔB_0 field map. The latter was extrapolated in the image domain to fit the spatial resolution and 3D FOV of the 3D-SPARKLING fMRI scans.

[4] https://github.com/CEA$_C OSMIC/pysap - mri$

[5] A French national HPC cluster under the authority of the Ministry of Research and Higher Education: http://www.idris.fr/eng/jean-zay/index.html

[6] https://www.fil.ion.ucl.ac.uk/spm/doc/biblio/

and counter-clockwise rotating wedges. Each block $\mathbf{X}_s$ is composed of $Q/2 = 10$ regressors defined as follows:

$$\mathbf{X}_s = \begin{pmatrix} \mathbf{x}_{s,1}^{\text{task}} & \mathbf{x}_{s,2}^{\text{task}} & \mathbf{x}_{s,3}^{\text{mot}} & \dots & \mathbf{x}_{s,8}^{\text{mot}} & \mathbf{x}_{s,9}^{\text{pol}} & \mathbf{x}_{s,10}^{\text{bas}} \end{pmatrix} \in \mathbb{R}^{N_{\text{vol}} \times Q/2}, \tag{4.9}$$

where two paradigm-related parametric and continuous regressors $\mathbf{x}_{s,1}$ and $\mathbf{x}_{s,2}$ serve to capture the BOLD fluctuations elicited by the stimulus presentation. For the clockwise session ($s = 1$), we used

$$\begin{cases} x_{1,1}^{\text{task}}(t) &= \cos\Big(-\frac{\pi}{2} - \frac{2n_{\text{cyc}}\, t\, \pi}{N_{\text{vol}}}\Big) = -\sin\Big(\frac{2n_{\text{cyc}}\, t\, \pi}{N_{\text{vol}}}\Big) \\ x_{1,2}^{\text{task}}(t) &= \sin\Big(-\frac{\pi}{2} - \frac{2n_{\text{cyc}}\, t\, \pi}{N_{\text{vol}}}\Big) = -\cos\Big(\frac{2n_{\text{cyc}}\, t\, \pi}{N_{\text{vol}}}\Big) \end{cases} \tag{4.10}$$

where $n_{\text{cyc}} = N_{\text{vol}} \times \text{TR}/P_{\text{cyc}} = 9$, while for the counter-clockwise session ($s = 2$) we define the first regressor turning in the opposite direction:

$$\begin{cases} x_{2,1}^{\text{task}}(t) &= \cos\Big(-\frac{\pi}{2} + \frac{2n_{\text{cyc}}\, t\, \pi}{N_{\text{vol}}}\Big) = -x_{1,1}^{\text{task}}(t) \\ x_{2,2}^{\text{task}}(t) &= \sin\Big(-\frac{\pi}{2} + \frac{2n_{\text{cyc}}\, t\, \pi}{N_{\text{vol}}}\Big) = x_{1,2}^{\text{task}}(t) \end{cases}. \tag{4.11}$$

Next, 6 session-specific motion-related regressors $(\mathbf{x}_{s,3}^{\text{mot}}, \dots, \mathbf{x}_{s,8}^{\text{mot}})$, three for rotations and three for translations, were estimated using `SPM12` while a simple polynomial regressor $x_{s,9}^{\text{pol}}(t) = t$ was fitted to capture the linear trend on top of the mean signal modeled by $x_{s,10}^{\text{bas}}(t) = 1, \forall t$.

The parameter estimates $\widehat{\boldsymbol{\beta}} = (\widehat{\beta}_i)_{i=1}^{V}$ were estimated in the maximum likelihood sense using the `Nilearn`[7] package, which implements a prewhitening procedure based on a first-order autoregressive noise model for $\mathbf{N}$. Massive univariate analysis was thus carried out to obtain parameter estimates $\widehat{\boldsymbol{\beta}}$ within the brain mask composed of V voxels where V varies between 1,449 299 and 1,649 380 across participants (approximately one-fourth of the 3D FOV).

Statistical analysis of the retinotopic mapping data

Firstly, a Fisher test was constructed to estimate the global effect of interest associated with the task-related regressors, namely the reduced model encoded by $\mathbf{X}_0 = (\mathbf{x}_{1,1}^{\text{task}}, \mathbf{x}_{1,2}^{\text{task}}, \mathbf{x}_{2,1}^{\text{task}}, \mathbf{x}_{2,2}^{\text{task}}) \in \mathbb{R}^{2N_{\text{vol}} \times 4}$. The corresponding null hypothesis reads $H_{0,EOI} : \mathbf{C}^T\boldsymbol{\beta} = 0$ where $\mathbf{C}^T \in \{0,1\}^{4\times Q}$ is a contrast matrix given by:

$$\mathbf{C}^T = \begin{pmatrix} \overbrace{1}^{\mathbf{x}_{1,1}^{\text{task}}} & \overbrace{0}^{\mathbf{x}_{1,2}^{\text{task}}} & \dots & \dots & \overbrace{0}^{\mathbf{x}_{2,1}^{\text{task}}} & \overbrace{0}^{\mathbf{x}_{2,2}^{\text{task}}} & \dots & \dots & 0 \\ 0 & 1 & 0 & \dots & 0 & 0 & \dots & \dots & 0 \\ 0 & 0 & \dots & \dots & 1 & 0 & \dots & \dots & 0 \\ 0 & 0 & \dots & \dots & 0 & 1 & 0 & \dots & 0 \end{pmatrix}. \tag{4.12}$$

The degrees of freedom of the F_{ν_1,ν_2}-test are given by $\nu_1 = rank(\mathbf{X}) - rank(\mathbf{X}_0) = 16$ and $\nu_2 = 2N_{\text{vol}} - rank(\mathbf{X}) = 220$. In practice, $\widehat{\boldsymbol{\beta}}$ was used in the computation of the residual sums of squares:

$$\text{RSS} = \|\mathbf{Y} - \mathbf{X}\widehat{\boldsymbol{\beta}}\|_2^2 \quad \text{and} \quad \text{RSS}_0 = \|\mathbf{Y} - \mathbf{X}_0\widehat{\boldsymbol{\beta}}_0\|_2^2 \tag{4.13}$$

where $\widehat{\boldsymbol{\beta}}_0 = (\widehat{\beta}_{0,i})_{i=1}^{V}$ with $\widehat{\beta}_{0,i} = (\widehat{\beta}_{1,i}, \widehat{\beta}_{2,i}, \widehat{\beta}_{11,i}, \widehat{\beta}_{12,i})^T$.

These results were then used to form the Fisher statistics $F_{\nu_1,\nu_2} = \frac{\text{RSS}_0 - \text{RSS}}{\text{RSS}}$. The resulting whole-brain statistical F_{ν_1,ν_2}-map was thresholded for chosen statistical control levels.

[7] https://nilearn.github.io/stable/index.html

The individual F-maps have been used as statistical masks for further analysis of retinotopic mapping at the subject level as detailed hereafter. Secondly, in order to derive the retinotopic maps, we also formed the Student-t tests that are based on the following elementary null hypotheses:

$$\begin{cases} H_{0,1}: & \beta_{1,i} = 0 \quad \forall i = 1:V, \\ H_{0,2}: & \beta_{2,i} = 0 \quad \forall i = 1:V, \\ H_{0,3}: & \beta_{11,i} = 0 \quad \forall i = 1:V, \\ H_{0,4}: & \beta_{12,i} = 0 \quad \forall i = 1:V. \end{cases}$$

$H_{0,1}$ and $H_{0,2}$ are related to the first session while $H_{0,3}$ and $H_{0,4}$ represent the second.

We computed the corresponding z-score maps $\mathbf{z} = (z_{j,i})_{j=1:4,i=1:V}$ from which we formed the voxelwise estimates of the signal phase in a session-specific manner as follows:

$$\begin{cases} \phi_{Clock,i} & = & \arctan\left(\frac{-z_{1,i}}{-z_{2,i}}\right) & \forall i = 1:V, \\ \phi_{CClock,i} & = & \arctan\left(\frac{-z_{3,i}}{z_{4,i}}\right) & \forall i = 1:V, \end{cases}$$

where $\phi_{Clock,i}$ and $\phi_{CClock,i}$ respectively stand for the phase estimates associated with the clockwise and counter-clockwise sessions. Then, after compensating for the recorded BOLD response delay ($d_{h,i} = \frac{\phi_{Clock,i}+\phi_{CClock,i}}{2} \quad \forall i = 1:V$) due to the hemodynamic delay in $\phi_{Clock,i}$ and $\phi_{CClock,i} \quad \forall i = 1:V$, we derived the overall retinotopic phase estimate as follows:

$$\phi_i = \frac{\phi_{Clock,i} - \phi_{CClock,i}}{2} \quad \forall i = 1:V. \tag{4.14}$$

4.6 Conclusion

In this chapter, we presented the full experimental pipeline we put in place to acquire high spatial resolution 3D-SPARKLING fMRI data. This pipeline will be useful for the next two chapters.

In chapter 5, we first evaluate 3D-SPARKLING against the state-of-the-art 3D-EPI on resting-state and task-based fMRI acquisitions in a cohort of 6 healthy volunteers. Starting from k-space data collection, through preprocessing and all the way to statistical analysis, we meticulously ensure that the data sets acquired using 3D-SPARKLING and 3D-EPI are harmonized.

Later, in chapter 6, we investigate the benefit of correcting additionally to static magnetic field inhomogeneities, the dynamic field perturbations in 3D-SPARKLING fMRI data on BOLD sensitivity in a different cohort of 3 healthy participants. Only 3D-SPARKLING data was acquired for this purpose, and the impact on image quality, tSNR, and the detection of evoked brain activity, of the contribution of each of the field terms mentioned in 4.4.1 was assessed.

* * *
* *
*

Chapter 5

Evaluation of 3D-SPARKLING fMRI against the state-of-the-art 3D-EPI

5.1 Context

After outlining a comprehensive description of the pipeline we opted for to collect 1mm^3 whole-brain BOLD fMRI data using CS-based non-Cartesian 3D-SPARKLING, our current focus is on its viability as an fMRI acquisition strategy.

Whole brain fMRI has been primarily performed at 3 Tesla (3T) at a usual spatial resolution of 2 to 3 mm^3 isotropic and a temporal resolution of 2-3s using 2D EPI. This has recently changed with significant progress in two areas, namely the rise of ultra-high magnetic fields (UHF, 7T and beyond) and the possibility of accelerating data acquisition. Both improvements offer the opportunity to reach higher spatio-temporal resolution [Pol+10; Lin+13; VYL21; BHF21; Urg21].

Significant efforts have been pushed forward to develop and implement more efficient encoding techniques and their corresponding image reconstruction methods in order to accelerate data acquisition without sacrificing the 3D FOV through under-sampling the

k-space. However, the latter degrades both the SNR [AVT14] and tSNR as the two indices are linearly linked in the thermal noise regime [TRW11]. As the tSNR is a proxy of the temporal stability in fMRI, significant efforts have been deployed to mitigate this issue either by moving to stronger magnetic fields (7T and beyond) or by using advanced coil designs or both [PSS16].

As seen in Chapter 2, under-sampling the k-space in the Cartesian framework was made possible through the progress of PI [Pru06; Des+12; Cha+14a; Ham17] and the corresponding reconstruction methods such as SENSE [Pru+99] or GRAPPA [Gri+02]. These developments helped improve the spatio-temporal resolution in whole brain fMRI: By using multi-band excitation pulses, 2D SMS-EPI [Lar+01; Moe+10] is able to acquire several slices using a single shot. 3D-EPI [Pos+10] has the same acceleration capabilities as 2D SMS-EPI, enabling acceleration in-plane and along the partition encoding direction. However, 3D-EPI requires lower flip angles and provides a better SNR. Nevertheless, 3D-EPI is more sensitive to physiological noise than 2D SMS-EPI. In [Le +19], the authors report comparable performances between 3D-EPI and 2D SMS-EPI. That being said, the high SAR associated with 2D SMS-EPI strategy constitutes a limitation for *in vivo* applications at UHF. Furthermore, CAIPIRINHA for multi-slice imaging [Bre+05] and 2D CAIPIRINHA [Bre+06] for 3D acquisitions can be applied to improve the g-factor map [Rob+08; Bre+09] which quantifies, among other things, the effect of the undersampling pattern on the noise spatial distribution in the parallel imaging setting.

Despite offering shorter scan times, PI-based accelerated Cartesian strategies remain limited due to the suboptimal gradient waveforms they use. This has motivated the development of non-Cartesian encoding patterns such as radial and spiral as a way to further enhance the sampling efficiency by enabling a denser coverage of the low frequencies and an optimal use of the gradient power. In addition to a faster coverage of the k-space, non-Cartesian strategies yield fewer (but more complex) coherent under-sampling artifacts. This feature, combined with the difficulty of accurately regridding non-Cartesian samples into a Cartesian grid, has led to a shift in reconstruction methods: NUFFT gained ground over the FFT and new iterative reconstruction algorithms such as CG SENSE [Pru+01] or SPIRiT [LP01] have been implemented. Spiral-based acquisition schemes are, today, the most used non-Cartesian alternatives for high-resolution fMRI [Glo12; Rie+21; Kas+22].

Even though a more efficient traversal of the k-space was the main motivation behind their development, non-Cartesian methods naturally implement variable density sampling (VDS), thereby implicitly capitalizing on the idea that some data points bring more knowledge than others. However, given the deterministic character of their trajectories, they do not fully exploit an important notion that emerged recently: MR images are inherently sparse or compressible in a well-chosen transform domain like wavelets, for instance.

Following the later idea and in the context of further shortening the acquisition time, compressed sensing was first introduced in the MRI field [LDP07] in an attempt to reach higher acceleration factors and, therefore, better image resolution without extending the scan time. CS can be optimally combined with multi-coil acquisition [CAT16] and allows us to accurately reconstruct images from highly under-sampled measurements using three complementary ingredients: VDS, locally uniform coverage of k-space, and nonlinear sparsity-promoting reconstruction methods. Successful applications of CS-MRI implement VDS where the central portion of k-space is oversampled compared to its periphery [Puy+12; Cha+14b].

In this chapter, we investigate the use of a finely tuned version of the CS-based 3D-SPARKLING for BOLD fMRI. We compare it to state-of-the-art Cartesian 3D-EPI during both a retinotopic mapping paradigm and resting-state acquisitions at $1mm^3$ (isotropic spatial resolution) and a temporal resolution (volumetric TR) of 2.4s for whole-brain fMRI at 7T. 3D-SPARKLING was used in a scan-and-repeat mode. This study involves six healthy volunteers, and both acquisition sequences were run on each individual in a balanced order across subjects. The performances of both acquisition techniques are compared to one another in regard to tSNR, sensitivity to the BOLD effect, and spatial specificity.

5.2 Materials and methods

5.2.1 General setup

Data was collected at 7T MRI (7T Siemens Magnetom scanner, Erlangen, Germany) from seven healthy volunteers (3 females, 4 males) aged between 20 and 40 years old with normal-to-corrected vision, and using a 1Tx-32Rx head coil (Nova Medical, Willimgton, CO, USA). Data from only 6 volunteers (1 male excluded) was actually involved in this work as the last volunteer felt asleep during the experiment. The experimental protocol was approved by the national ethics committee (Comité de Protection des Personnes) under the protocol identifier CPP 100048 (CPP Sud Méditerranée 4 number 180913, IDRCB:2018-A011761-53). All participants gave their written informed consent.

In each participant, the same fMRI data were acquired using 3D-EPI and 3D-SPARKLING consecutively. The order in which 3D-EPI and 3D-SPARKLING sequences were run was balanced across individuals as shown in Fig 5.1. For technical reasons, resting-state fMRI data was collected for only five volunteers out of the six in order to evaluate the tSNR, whereas retinotopic mapping fMRI experiments were conducted for all volunteers (cf Section 4.2). Resting-state data was always collected before task-based (retinotopic mapping) fMRI in order to avoid any contamination in the visual network due to task performance.

	Resting-State		***Retinotopic Mapping***			
	5 minutes	*5 minutes*	*4 minutes 48 seconds*	*4 minutes 48 seconds*	*4 minutes 48 seconds*	*4 minutes 48 seconds*
V#1			**3D-SPARKLING Clockwise**	**3D-SPARKLING Counter-clockwise**	**3D-EPI Clockwise**	**3D-EPI Counter-clockwise**
V#2	**3D-EPI**	**3D-SPARKLING**	**3D-EPI Clockwise**	**3D-EPI Counter-clockwise**	**3D-SPARKLING Clockwise**	**3D-SPARKLING Counter-clockwise**
V#3	**3D-SPARKLING**	**3D-EPI**	**3D-SPARKLING Clockwise**	**3D-SPARKLING Counter-clockwise**	**3D-EPI Clockwise**	**3D-EPI Counter-clockwise**
V#4	**3D-EPI**	**3D-SPARKLING**	**3D-EPI Clockwise**	**3D-EPI Counter-clockwise**	**3D-SPARKLING Clockwise**	**3D-SPARKLING Counter-clockwise**
V#5	**3D-SPARKLING**	**3D-EPI**	**3D-SPARKLING Clockwise**	**3D-SPARKLING Counter-clockwise**	**3D-EPI Clockwise**	**3D-EPI Counter-clockwise**
V#6	**3D-EPI**	**3D-SPARKLING**	**3D-EPI Clockwise**	**3D-EPI Counter-clockwise**	**3D-SPARKLING Clockwise**	**3D-SPARKLING Counter-clockwise**

Figure 5.1: Time course of the resting-state and task-based fMRI sessions. From subject V#2 to V#6, resting-state fMRI data was systematically collected prior to retinotopic mapping data. The order in which 3D-EPI and 3D-SPARKLING were run was balanced across individuals.

5.2.2 Streamlining and harmonizing data acquisition and processing for 3D-EPI and 3D-SPARKLING

Great care was given to matching the sequence parameters between 3D-EPI and 3D-SPARKLING as shown in Table 5.1: The same spatio-temporal resolution, brain coverage, and TE/TR_{shot} were used. The readouts of both sequences had very close observation times: 26.33ms for 3D-EPI and 26.88ms for 3D-SPARKLING, and both were acquired in the same native oblique transverse orientation. Additionally, the two 3D gradients recalled echo (GRE) sequences involved a gradient spoiling as well as an RF spoiling.

3D-EPI readouts were accelerated along the phase encoding direction and the partition encoding direction by a factor of 4 and 2, respectively. Partial Fourier (6/8) was also applied along both phase encoding directions. CAIPIRINHA 2D [Bre+06] reconstruction was applied to the 3D-EPI data. A 15s-calibration sequence was run at the beginning of each 3D-EPI sequence (be it single or multi-repetition) to estimate coil sensitivity maps for 3D-EPI data. An additional single-repetition 3D-EPI acquisition in the opposite A-P encoding direction

was then performed to correct 3D-EPI functional data for ΔB_0 distortions using the so-called TOPUP approach [ASA03; Smi+04].

Table 5.1: Specifications of the different pulse sequences: 3D-SPARKLING and 3D-EPI were used to acquire the fMRI data at 1mm^3 and 2.4s-TR_v (volumetric TR) resolution. The native orientation was kept the same for the acquisitions associated with both sequences: Oblique transverse orientation. The GRE sequence used for external field maps had 3 echoes. An additional single-repetition 3D-EPI in A-P encoding was acquired for ΔB_0 correction on 3D-EPI. The MP2RAGE sequence was used to acquire an anatomical T_1w scan.

	3D-SPARKLING	3D-EPI	3D GRE	3D-EPI	MP2RAGE
TE(ms)	20	20	1.8, 3.06, 5.10	20	3.29
Unitary TR(ms) - TR_{shot}	50	50	20	50	5000
Volumetric TR(s) - TR_v	2.4	2.4	58	2.4	347
Spatial resolution (mm)	1	1	3	1	1
FOV(mm)	(192,192,128)	(192,192,128)	(192,192,132)	(192,192,128)	(192,192,128)
Number of repetitions	120 125	120 125	1	1	1
Encoding direction		P-A	P-A	A-P	R-L

The 3D-EPI volumes were reconstructed independently from each other using a calibrated multi-coil reconstruction, which involves the 15s-calibration sensitivity maps mentioned in the section above. The reconstruction is implemented using the vendor's ICE software. Since navigators were implemented into the 3D-EPI sequence, the 3D-EPI volumes were corrected for zeroth order dynamic magnetic field fluctuations. The 3D-SPARKLING volumes were also reconstructed independently from each other according to the implementation explained in Section 4.4 in Chapter 4. Only the static term of magnetic field imperfections was taken into account by means of the multi-echo 3D GRE acquisition. The dynamic field perturbations were not corrected in 3D-SPARKLING data at this point.

Functional data realignment and co-registration with the T_1-weighted anatomical scan were performed similarly for 3D-SPARKLING and 3D-EPI fMRI volumes, as explained in Subsection 4.4.3 in Chapter 4. Additionally, 3D-EPI data was corrected for off-resonance artifacts using the additional single-repetition A-P acquisition, and the TOPUP approach available in `FSL`[1].

5.2.3 Metrics used for quality assessment

Resting-state fMRI mean images (i.e., volumes), computed as the mean over the volumetric (3D) time series, were visually inspected on an individual basis to evaluate image quality, while the whole scan sequences were used to compute the tSNR metric, allowing us to make a comparison between the 3D-EPI and 3D-SPARKLING encoding schemes for each subject.

Complementary to that, retinotopic mapping fMRI data was used to produce activation maps from the F-maps mentioned in Subsection 4.5.1 in Chapter 4 according to three different thresholding strategies where the null hypothesis $H_{0,EOI}$ (cf Subsection 4.5.1 in Chapter 4) was rejected if the p-value p met at least one of the following criteria:

(i): $p < 0.05$ with false discovery rate (FDR) correction [BY01];

(ii): $p < 0.001$ without correcting for multiple comparisons;

(iii): $p < 0.05$ without correcting for multiple comparisons and with a minimum cluster size of 5 voxels.

[1] https://fsl.fmrib.ox.ac.uk/fsl/fslwiki/topup

In addition to strategies (i) and (ii), which were applied to all participants, alternative (iii) has also been used in participant V#5 for whom the global effect of interest was weak and the tSNR low. Furthermore, given the high spatial resolution and the whole brain analysis, the false discovery rate correction was too restrictive for the majority of the volunteers.

We then conducted both qualitative and quantitative assessments at the subject level through a series of metrics, respectively referenced as q- and Q-metric in the following in order to compare the statistical performances of 3D-EPI and 3D-SPARKLING in terms of sensitivity and specificity. First, the consistency of activation maps between the two acquisition techniques was evaluated according to the following qualitative (q) and quantitative (Q) criteria:

1) `qCons1`: **Consistency of activation maps**. The z-score maps derived from the global effects of interest (cf. $H_{0,EOI}$) were visually assessed and compared subject-wise.

2) `QCons1`: **Spatial overlap of the statistically significant activation maps**. Binarized activation masks were first generated from the respective 3D-EPI and 3D-SPARKLING above-mentioned z-score maps, with z-scores higher (respectively, lower) than 3.09 (corresponding to $p = 0.001$) set to the value of 1 (respectively, 0). Then the Dice index [Dic45] or $F1$-score was used to measure the overlap between these 3D-EPI and 3D-SPARKLING activation masks, a value closer to 1 (respectively, 0) indicating a strong (respectively, weak) overlap or consistency between activation patterns.

Second, an evaluation of the sensitivity to the BOLD contrast was conducted on the basis of complementary criteria:

3) `QSens1`: **Number of activated voxels overall and in the gray matter**. These figures were computed from the global effect of interest statistical maps (z-scores) after applying a threshold at $p < 0.001$ without multiple comparisons correction in both 3D-EPI and 3D-SPARKLING data sets and compared one another in each participant.

4) `qSens1`: **Significance of the activation patterns**. The activation patterns derived from the data collected from two volunteers (V#3 and V#4) were displayed on the same slices and visually compared. These two volunteers were selected to specifically showcase the session order effect, namely, what is the impact of running 3D-SPARKLING or 3D-EPI prior to the other sequence, respectively.

5) `QSens2`: **Statistical comparison of the distributions of the significant effects of interest**. A Kolmogorov-Smirnov (KS) test [Fra51] was performed between the distributions of the statistically significant z-scores located in the gray matter and associated either with 3D-EPI or 3D-SPARKLING retinotopic fMRI data and denoted respectively $P_{EPI}(z)$ and $P_{SPARK}(z)$. The goal was to assess what distribution had a heavier tail (i.e. was more shifted to the right).

Third, an evaluation of the spatial specificity was carried out according to the following metric:

6) `QSpe1`: **Percentage of activations in the brain tissues**. For each participant, we compared the percentages of activated voxels in gray and white matter (GM and WM, respectively) as well as in the cerebrospinal fluid (CSF), defined as $\frac{\#\text{activated voxels in tissue}}{\#\text{all activated voxels}}$, for both encoding schemes after carrying out the tissue segmentation on the anatomical T_1-weighted image and the co-registration of the mean fMRI images with the anatomical scan using `SPM12`. This software actually yielded the tissue probability masks for gray and white matter and the CSF.

7) `QSpe2`: **Prevalence of true positives vs false positives**. The total number of activated voxels retrieved after thresholding the z-scores at $p < 0.05$ with FDR correction is reported for all participants and compared with the figures corresponding to `QSens1`.

Finally, the accuracy of the BOLD phase maps was assessed qualitatively according to the following criterion:

8) `qAccu1`: **Accuracy of retinotopic mapping**. The volumetric statistical phase maps $\boldsymbol{\phi} = (\phi_i)_{i=1:V}$ (cf. Eq. (4.14)) and their projection onto the pial cortical surface were visually assessed for two volunteers (V#3 and V#4). The projection was performed using `vol_to_surf` from `Nilearn`, and the meshes corresponding to the pial, inflated, sulcus, and white matter surfaces were computed using `FreeSurfer 7`.

The order of these metrics matters. It has been carefully chosen to progressively demonstrate the benefits associated with 3D-SPARKLING. For the quantitative criteria denoted `QCons1`, `QSens1`, `QSens2`, `QSpe1`, the statistically significant activations were defined by thresholding the z-scores at 3.09 (corresponding to a p-value of 0.001).

5.3 Results

5.3.1 Image quality and temporal SNR

Fig 5.3 demonstrates on an individual basis the superior image quality yielded by 3D-EPI: Fine-grained anatomical details are lost in 3D-SPARKLING mean fMRI images. Moreover, the between-tissue contrast of 3D-EPI images is clearer compared to that of the 3D-SPARKLING. The two encoding schemes are actually differently affected by the signal loss: 3D-SPARKLING appears less impacted in the frontal lobes (blue arrows) but more severely degraded around the ventricles (orange arrows). Geometric distortions are also differently influencing the 3D-EPI and 3D-SPARKLING images and are mostly visible in the sagittal views. These discrepancies arise from the well-known differences between Cartesian and non-Cartesian imaging in terms of robustness to static and dynamic B_0 field inhomogeneities, which affect their point spread function (PSF) and, therefore, their effective spatial resolution differently. Consequently, even after accounting for the impact of the partial Fourier (6/8) applied to 3D-EPI on the PSF, the effective resolution of 3D-SPARKLING fMRI images is lower than that of 3D-EPI images.

The temporal stability of the fMRI signal is usually evaluated through the tSNR. Fig 5.4 shows tSNR maps derived from 3D-EPI and 3D-SPARKLING resting-state fMRI data and collected in five volunteers as previously mentioned. The tSNR values are higher on 3D-SPARKLING data, which suggests improved temporal stability and potentially a better sensitivity to the BOLD contrast, a feature that will be further analyzed hereafter. It is, however, important to keep in mind that a direct comparison between the tSNR yielded by the unbiased linear reconstruction applied to the k-space data collected by 3D-EPI and that yielded by the CS-based reconstruction applied to the k-space data collected by 3D-SPARKLING is limited as the latter induces some bias and therefore a reduced variance. However, as a moderate amount of ℓ_1 regularization was used, the impact was limited.

5.3.2 Consistency of activation maps between the two encoding schemes

Fig 5.5 compares the significant global effects of interest estimated from the retinotopic fMRI data collected using 3D-EPI and 3D-SPARKLING. It shows that the activation patterns are well localized in the visual cortex (cf `qCons1`).

Compared to the other participants, V#5 elicits less activated voxels: $p < 0.001$ was too conservative to extract a significant activation pattern for both techniques. Due to this, we slightly relaxed the threshold to $\alpha = 0.05$ to gain insight into functional activity, notably in 3D-SPARKLING. At this level of significance, the activation pattern associated with 3D-EPI data remains meaningless. This is likely a consequence of the lower tSNR observed in V#5, notably in the visual cortex as shown in Fig 5.4. Globally, the statistically significant activation patterns are relatively consistent across encoding schemes. This qualitative observation is supported by Table 5.2 which reports the F1-score (i.e. Dice index) values computed between the statistically significant activation patterns derived from 3D-SPARKLING and 3D-EPI retinotopic fMRI data (`QCons1`): As these values range

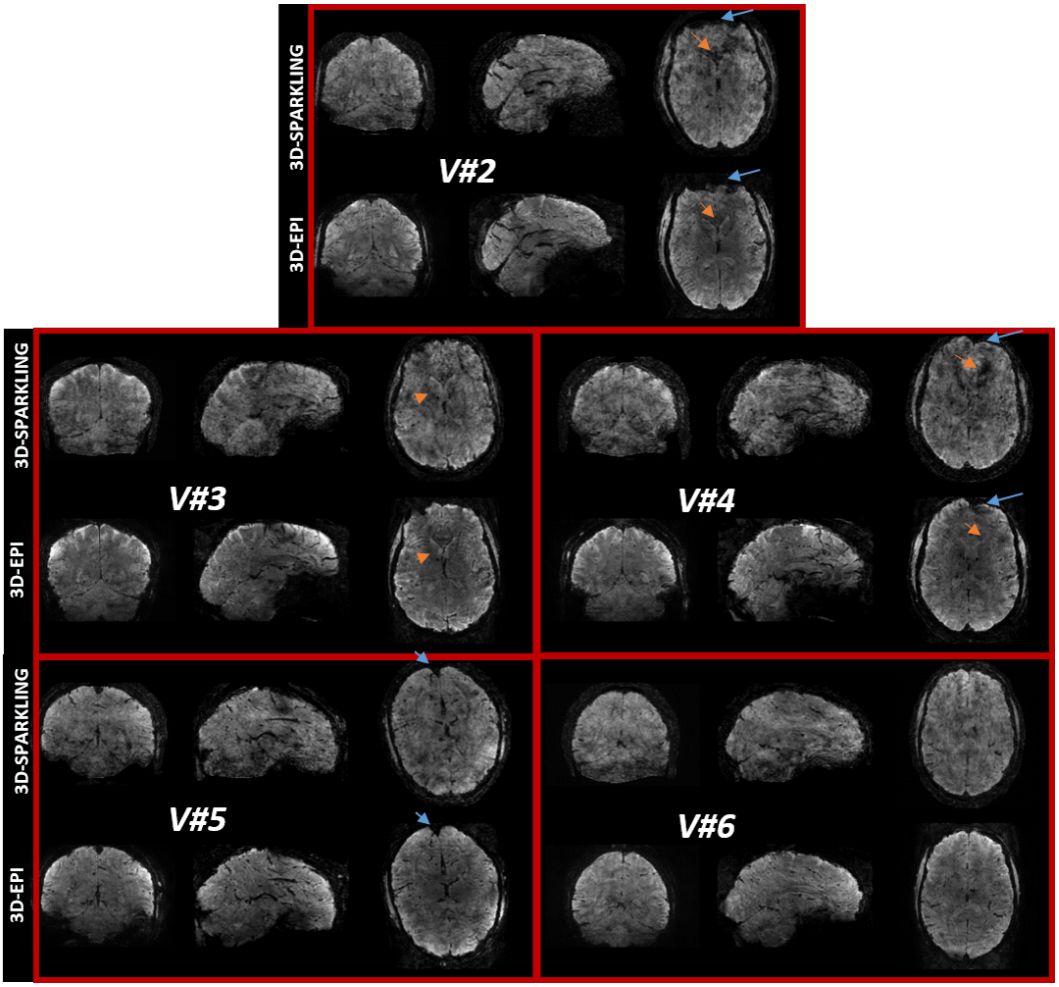

Figure 5.3: Subject-wise comparison of the mean images derived from 3D-EPI and 3D-SPARKLING resting-state fMRI data. Anatomical details that are lost in 3D-SPARKLING data are well recovered in 3D-EPI data. The overall contrast between tissues is clearer using the 3D-EPI encoding scheme. Signal loss and geometric distortions affect data collected using the two acquisition techniques differently. The blue and orange arrows point to brain areas where 3D-SPARKLING is respectively less and more affected by signal loss than 3D-EPI. The overall mean image quality of 3D-EPI data is superior to that of 3D-SPARKLING in all participants.

between 0.82 and 0.99 across participants, this showcases that the spatial supports of these activation patterns are very consistent and cover the same brain areas. This simple yet meaningful sanity check between fMRI data collected using the two competing encoding schemes allowed us to look further into their potential differences as related to effect size i.e., height of activation peaks and recovery of retinotopic maps. Indeed, the activation maps in Fig 5.5 suggest that:

(i): 3D-SPARKLING outperforms 3D-EPI in V#1-V#3 and V#5.

(ii): 3D-EPI outperforms 3D-SPARKLING in V#4.

(iii): Both techniques perform similarly in V#6.

As 3D-SPARKLING (respectively, 3D-EPI) is run first for the volunteers indexed by odd numbers (respectively, even numbers, cf. Fig 5.1), these observations suggest that the differences in terms of effect size may not solely result from the difference in the sampling techniques but also be partly driven by the order of execution of the runs. In order to gain

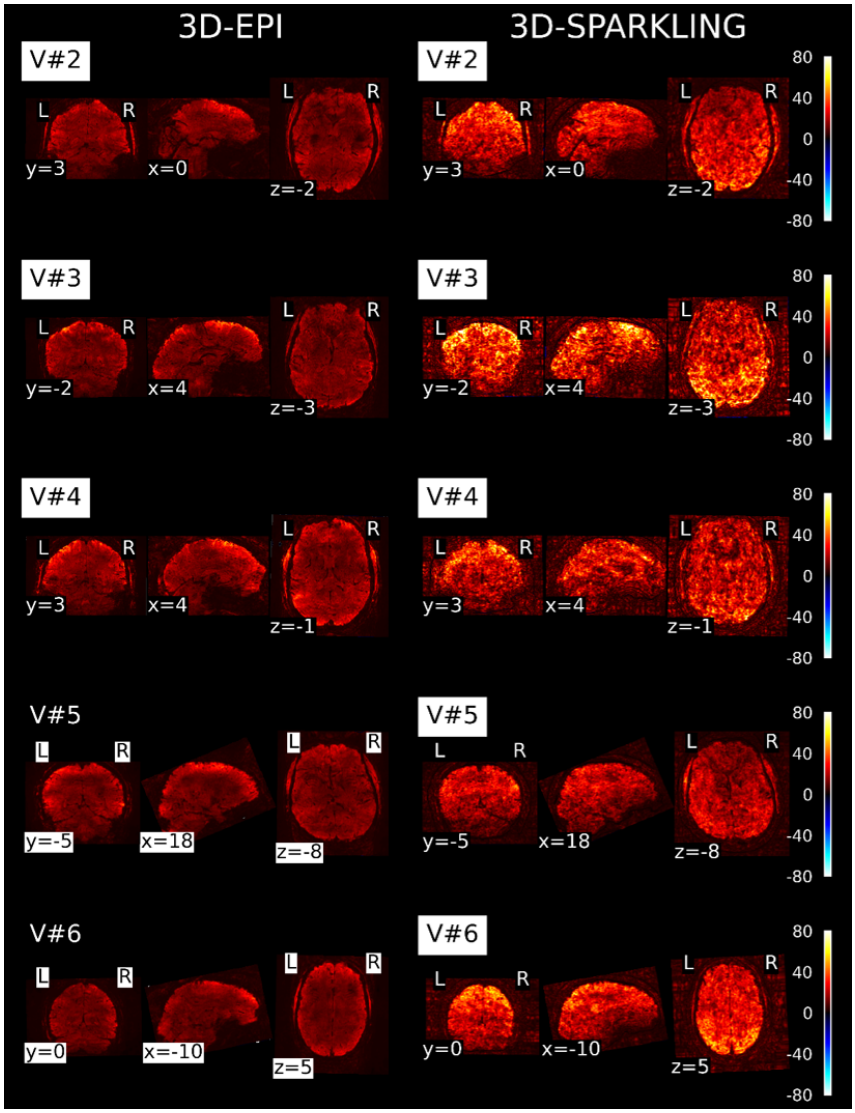

Figure 5.4: Comparison of the tSNR maps derived from 3D-SPARKLING and 3D-EPI resting-state fMRI data. 3D-SPARKLING data reveals a higher tSNR in comparison with 3D-EPI data. V#5 has a lower tSNR on average than the other participants, notably in the visual cortex and the posterior part of the brain.

more insight into the impact of the encoding scheme versus the order of acquisition, the sensitivity to the BOLD effect was studied and compared between the two methods.

Table 5.2: Comparison of the $F1$-scores computed between the activation patterns (thresholded z-score maps associated with the global effects of interest) derived from 3D-EPI and 3D-SPARKLING retinotopic fMRI data for the 6 volunteers.

Volunteer	F1-score
V#1	0.834
V#2	0.925
V#3	0.819
V#4	0.820
V#5	0.987
V#6	0.933

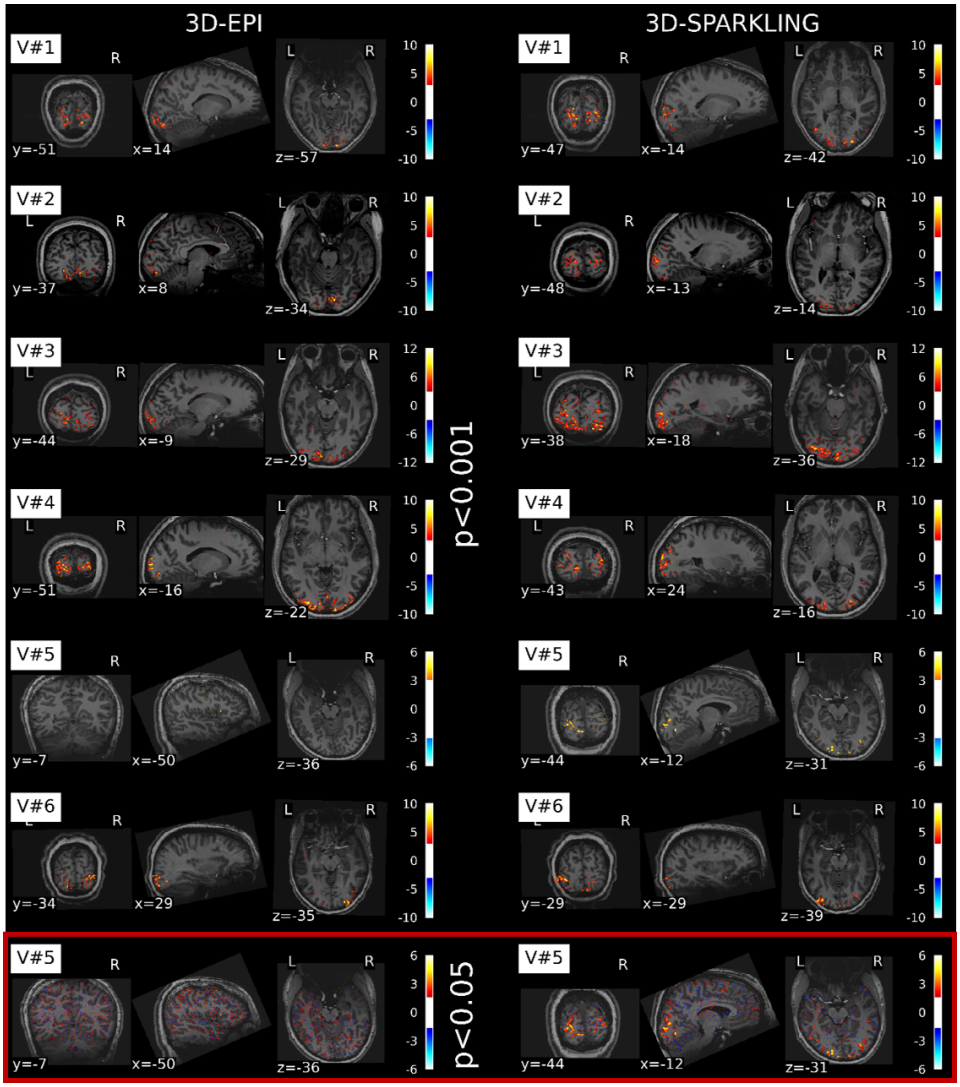

Figure 5.5: Z-score maps derived from the global effects of interest. From top to bottom: Activation maps displayed for the 6 participants and the two acquisition techniques. The six first rows show the activation maps yielded after thresholding the z-scores over the whole brain for $p < 0.001$ without applying any correction for multiple comparisons. The seventh row shows the activation map obtained after thresholding the z-scores over the whole brain for $p < 0.05$ with a minimum cluster size of 5 voxels for the fifth participant. Row-wise, the color bars are unchanged but differ from one volunteer to another. The slices were chosen according to the largest spatial extent of the activation patterns.

5.3.3 Sensitivity to the BOLD effect elicited by task performance

Table 5.3 reports the number of activated voxels within the whole brain and in the gray matter for 3D-EPI and 3D-SPARKLING data (QSens1): The total number of voxels activated is larger in 3D-EPI data for five participants out of six, however, this number can be biased by false positives and it is far more problematic as no correction for multiple comparisons was performed. It is then more interesting to examine the number of activated voxels in the gray matter: The figures in Table 5.3 show that more voxels in the gray matter were systematically activated in the data collected first. This can be explained by a stimulus presentation effect also called the repetition suppression effect [HSD00; Hen+02].

Such an observation supports the hypothesis that the higher sensitivity to the BOLD effect is partly driven by the order of execution of the sequences, however, the number of

Table 5.3: Comparison of the number of activated voxels (statistically significant at $p < 0.001$ without correcting for multiple comparisons) overall and in gray matter (GM) for 3D-EPI and 3D-SPARKLING data in the 6 volunteers. The lowest numbers are retrieved in V#5.

Volunteer	Total number of activated voxels		Number of activated voxels in GM	
	EPI	SPARK	EPI	SPARK
V#1	**7362**	6661	4736	**4863**
V#2	**8423**	5246	**5528**	3949
V#3	9010	**24410**	6040	**15263**
V#4	**11779**	4847	**8350**	3101
V#5	**3222**	2606	1952	**2265**
V#6	**6437**	4350	**4198**	2815

activated voxels in gray matter only partially reflects the sensitivity to the BOLD effect. A more global insight can be obtained by examining the activation maps and their potential differences in terms of peak heights using both qualitative and quantitative metrics.

These activation maps were produced by thresholding the z-scores over the whole brain for $p < 0.001$ (uncorrected for multiple comparisons). Despite the difference in significance, the activation patterns fit the gray matter quite well for both 3D-EPI and 3D-SPARKLING.

To do this, we show in Fig 5.6 the same axial slices of activation maps for volunteers V#3 and V#4 (`qSens1`): A higher statistical significance (or effect size) is observed for 3D-SPARKLING data in V#3 while the opposite statement holds in V#4 with more significant activations for 3D-EPI data. This confirms that the data collected first (i.e. 3D-SPARKLING in V#3, 3D-EPI in V#4) elicits more evoked brain activity.

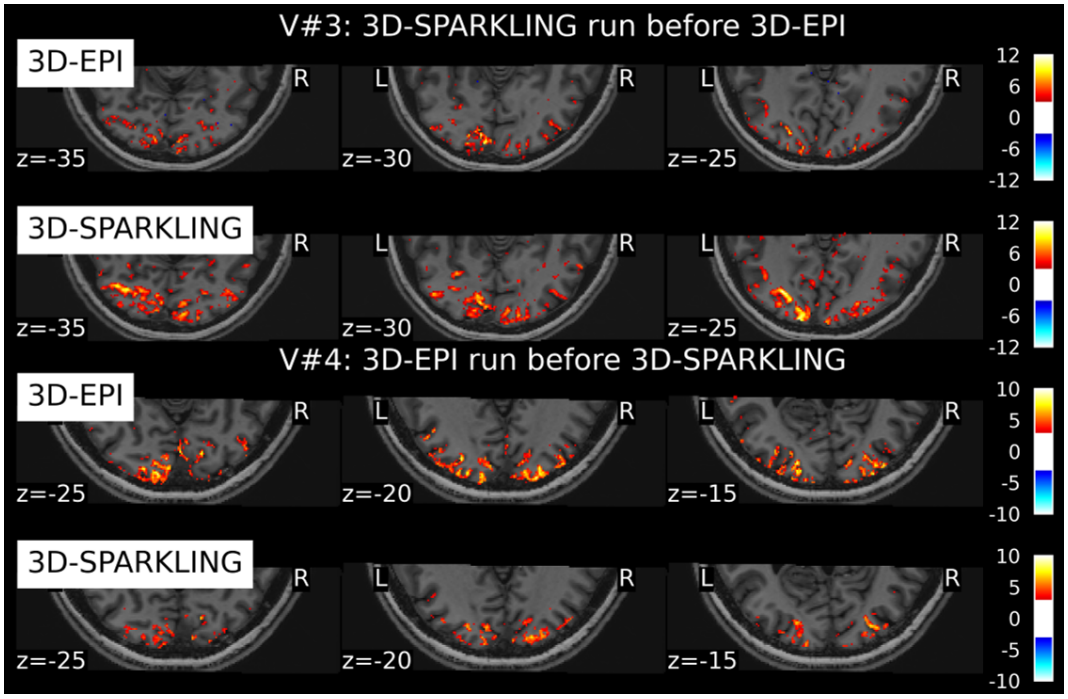

Figure 5.6: Three axial slices showing the impact of the order of sequence execution on the statistical sensitivity and activation patterns similarity between the two encoding schemes in V#3 and V#4. The sequence run first elicits more activation.

Optimally from a statistical perspective, if we had a larger cohort, a two-way repeated measures analysis of variance (ANOVA) could have been performed voxelwise in order to disentangle the contribution of the order of sequence execution from that of the encoding scheme to the sensitivity to the BOLD effect. However, since we only collected fMRI data in

six volunteers, we proceeded differently by first constructing for each subject the distribution of the statistically significant z-scores in the gray matter associated with 3D-EPI and 3D-SPARKLING retinotopic data, and then by testing the statistical difference between these two ensuing distributions using a Kolmogorov-Smirnov test (cf. `QSens2`). As we pulled the z-scores across voxels, this within-subject test is no longer spatially localized. However, it is a good indicator to use when deciding which encoding scheme elicits more evoked activity during task performance. Hence, in each individual we considered the following null hypothesis (H_0: $P_{EPI}(z) = P_{SPARK}(z)$, $\forall z \geq 3.09$) and eventually rejected it for all participants (p-values ranging between 10^{-6} and 10^{-70}) as shown in Table 5.4. In the latter we actually reported the unilateral (i.e. one-sided) p-values of the KS test we carried out subjectwise.

Table 5.4: Table summarizing the p-values and D-statistics of a Kolmogorov-Smirnov test between the distributions of the statistically significant z-scores within the gray matter extracted from 3D-EPI and 3D-SPARKLING retinotopic fMRI data: We used the following null hypothesis H_0: $P_{EPI}(z) = P_{SPARK}(z)$, $\forall z \geq 3.09$ and separately in one-sided tests the two alternative hypotheses
H_{Alt}^{Right}: $\exists\, z \geq 3.09 \,|\, P_{SPARK}(z) > P_{EPI}(z)$ and H_{Alt}^{Left}: $\exists\, z \geq 3.09 \,|\, P_{SPARK}(z) < P_{EPI}(z)$.

Volunteer	H_{Alt}^{Right}		H_{Alt}^{Left}	
	D-statistic	p-value	D-statistic	p-value
V#1	0.18	$\mathbf{10^{-70}}$	0.0	1.0
V#2	0.06	$\mathbf{10^{-9}}$	0.005	0.84
V#3	0.07	$\mathbf{10^{-23}}$	0.001	0.98
V#4	0.015	0.3489	0.053	$\mathbf{10^{-6}}$
V#5	0.29	$\mathbf{10^{-79}}$	0.0004	0.99
V#6	0.12	$\mathbf{10^{-24}}$	0.0	1.0

In five volunteers out of six, the distribution of activations elicited during 3D-SPARKLING retinotopic fMRI acquisitions is significantly shifted to the right (i.e., higher z-scores) compared to the similar distribution associated with 3D-EPI retinotopic fMRI data. The opposite effect is only retrieved in V#4. Therefore, irrespective of the order of sequence execution, the 3D-SPARKLING encoding scheme and its associated preprocessing pipeline yield a higher statistical sensitivity to detect evoked brain activity in the gray matter compared to the 3D-EPI acquisition technique.

5.3.4 Spatial specificity of activation maps on retinotopic fMRI data

In order to compare the two encoding methods according to the spatial specificity criterion `QSpe1`, the percentages of activated voxels within the GM, WM, CSF, and other tissues were extracted in each individual. Table 5.5 reports the main findings and shows that 3D-SPARKLING induces a higher percentage of activated voxels in the gray matter than 3D-EPI. The mean gap between the two encoding methods is quite large (71% for 3D-SPARKLING vs 64.5% for 3D-EPI). A similar analysis conducted in the white matter shows a marginal difference between 3D-SPARKLING (22% of activated voxels) and 3D-EPI (21%).

Although these average differences are quite small, they hide a large variability across individuals (V#2 vs. V#5 for 3D-EPI, V#2 vs. V#6 for 3D-SPARKLING) and even across encoding methods in the same participant (e.g., V#5).

Additionally, the percentage of activated voxels in the CSF and other tissues is on average twice (respectively, 20 times) higher for 3D-EPI than for 3D-SPARKLING, namely 12.27% (respectively, 2.15%) for 3D-EPI as compared to 6.68% (respectively, 0.11%) for 3D-SPARKLING.

These observations reveal first an increased average specificity of activations in gray matter using 3D-SPARKLING. This finding actually holds in 4 participants out of 6, including V#2 for whom 3D-EPI data were collected first.

Second, the fact that both encoding schemes yielded a fairly large mean percentage of activations in the white matter suggests a mismatch in the co-registration between the mean fMRI image and the anatomical scan on an individual basis. The higher mean percentage of activations in the white matter using 3D-SPARKLING data can be explained by the fact that the images are more blurry and the borders between white and gray matter less sharp.

Third, the larger amount of unexpected activations in the CSF and other tissues using 3D-EPI is questionable. As we demonstrated that this encoding scheme is associated with improved image quality, it is unlikely that this is due to an intrinsic lack of specificity. Instead, we suspect that the differences in addressing magnetic field inhomogeneities (TOPUP for 3D-EPI vs. our own correction/reconstruction pipeline for 3D-SPARKLING) might induce co-registration mismatches, especially in the frontal cortex, as pointed out by the yellow arrows in Fig 5.7. Such an explanation is consistent with the observations in Fig 5.3 where 3D-EPI is more impacted by signal loss in the frontal regions than 3D-SPARKLING. Of course, correcting the statistical tests for multiple comparisons might eradicate these false positives, but in that case, the statistical approach would fully hide the outlined intrinsic differences between the two encoding methods.

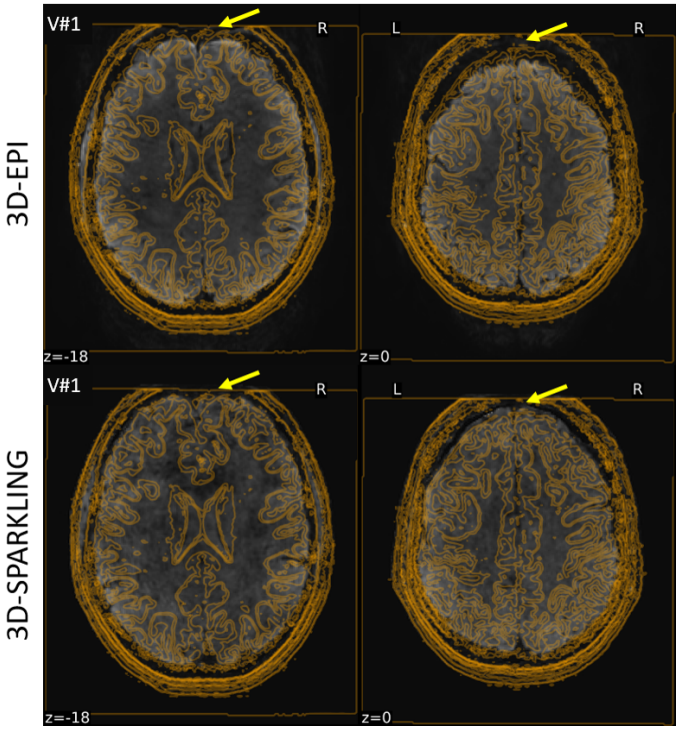

Figure 5.7: The contour edges of the T_1-w anatomical scan overlaid on the mean fMRI images acquired using 3D-EPI and 3D-SPARKLING encoding schemes in V#1 during the retinotopic experiment. The yellow arrows point to regions where the difference of mismatch between the functional and anatomical scans is visible.

To further bring evidence that 3D-SPARKLING has intrinsically a better spatial specificity than 3D-EPI and that the higher mean percentage of activated voxels in gray matter is not merely a result of a mismatch in co-registration, Table 5.6 reports the number of activated voxels after thresholding the z-scores over the whole brain at a statistical threshold of $p < 0.05$ with FDR correction (`QSpe2`). The figures in Table 5.6 are in agreement with the numbers of activated voxels in GM at $p < 0.001$ without correcting for multiple comparisons as originally reported in Table 5.3: In fact, we systematically found more activated voxels in the data collected first. This first demonstrates that the larger number of activated voxels yielded by 3D-EPI for five volunteers out of six when no correction for multiple comparisons is applied (cf. second column of Table 5.3) is merely biased by false positives. Second, it suggests that the data collected using 3D-SPARKLING yields functional maps that contain

fewer false positives and more true positives at a given level of control in comparison with 3D-EPI, hence an improved spatial specificity.

Table 5.5: Percentage of activated voxels in gray matter (%GM), white matter (%WM), cerebrospinal fluid (%CSF) and other tissues with regards to the total number of activated voxels for 3D-EPI and 3D-SPARKLING denoted respectively EPI and SPARK in each participant. Significant p-values were thresholded at 0.001 uncorrected for multiple comparisons. The higher the better (in bold font) in the % GM column, the lower the better (in bold font) in others.

Volunteer	%GM		%WM		%CSF		%other tissues	
	EPI	SPARK	EPI	SPARK	EPI	SPARK	EPI	SPARK
V#1	64.33	**73.01**	20.71	**18.75**	11.06	**8.05**	3.9	**0.19**
V#2	65.63	**75.28**	**15.26**	17.55	18.34	**7.05**	0.77	**0.12**
V#3	60.04	**62.53**	**16.27**	26.49	16.13	**10.84**	7.56	**0.14**
V#4	**70.90**	63.98	**15.84**	28.57	13.08	**7.37**	0.18	**0.08**
V#5	60.58	**86.57**	30.94	**10.09**	8.27	**3.34**	0.25	**0**
V#6	**65.12**	64.71	**27.97**	31.77	6.7	**3.4**	0.21	**0.12**
Average	64.43	**71.01**	**21.17**	22.2	12.26	**6.68**	2.15	**0.1**

Table 5.6: Total number of activated voxels for 3D-EPI and 3D-SPARKLING data in the 6 volunteers. These figures were retrieved by thresholding the z-scores over the whole brain at a p-value of 0.05 after FDR correction for multiple comparisons.

Volunteer	Total number of activated voxels at p<0.05 after FDR correction	
	3D-EPI	3D-SPARKLING
V#1	3197	**4535**
V#2	**2853**	1708
V#3	4891	**25193**
V#4	**9392**	3235
V#5	4	**660**
V#6	**2722**	2253

5.3.5 Accuracy of the retinotopic phase maps

To go one step further in examining the quality of the collected retinotopic fMRI data, we estimated the retinotopic phase maps (cf. Eq. (4.14)) from 3D-SPARKLING and 3D-EPI raw fMRI data (i.e. spatially unsmoothed). In Fig 5.8 we visualize these maps on selected axial views to check their consistency as well as their closeness to prior knowledge on the projection of the retina (represented by a colored disk in Fig 5.8) onto the visual cortex. As V#3 and V#4 were the most compliant volunteers during the whole fMRI experiment (no motion, results not shown), and as such, data reliability is enhanced, and hence, a stronger evoked activity was elicited, leading to more accurate retinotopic maps.

More precisely, 3D-SPARKLING data yields a higher quality phase map in V#3 (cf. top of Fig 5.8) with a smoother color-coded (i.e. directional) gradient. In contrast, 3D-EPI data produced a more spatially extended and accurate phase map in V#4 (cf. bottom of Fig 5.8), reflecting again the order of sequence execution. As the visual fields in the retina are actually mirrored in the visual cortex, this means that the two visual hemifields project respectively onto the contra-lateral hemisphere in the visual cortex [Wad+02; War+02]. For this particular reason, it is easier to visualize the projection of retinotopic maps on the cortical pial (`qAccu1`), as illustrated in Fig 5.9 for both raw (i.e. unsmoothed) and spatially smoothed (using a Gaussian kernel with a full width at half maximum (FWHM) of 2mm). fMRI data collected in V#3 and V#4. This 2-mm isotropic smoothing was applied during preprocessing prior to re-running a GLM analysis subjectwise.

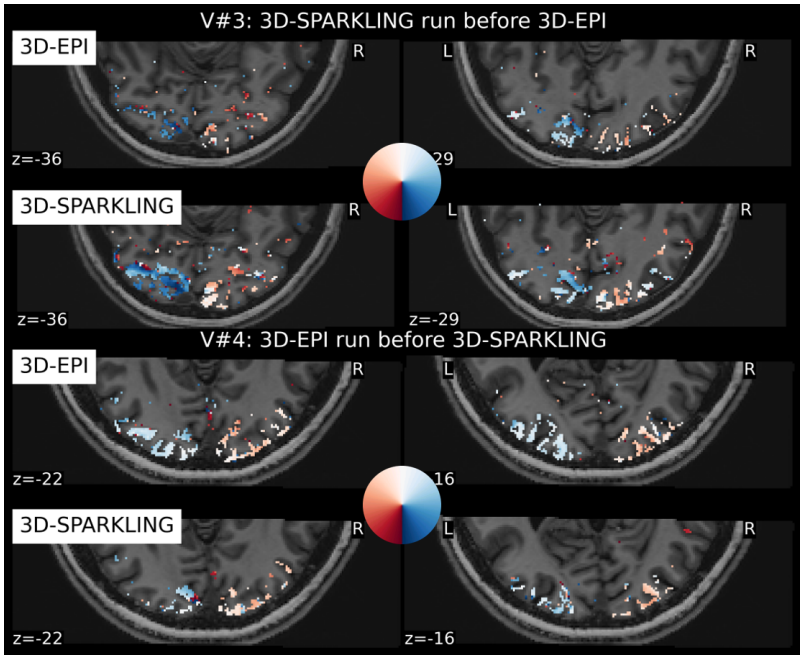

Figure 5.8: BOLD phase maps computed for participants V#3 and V#4. The BOLD phase maps agree with how the retina is supposed to be projected onto the visual cortex for both techniques.

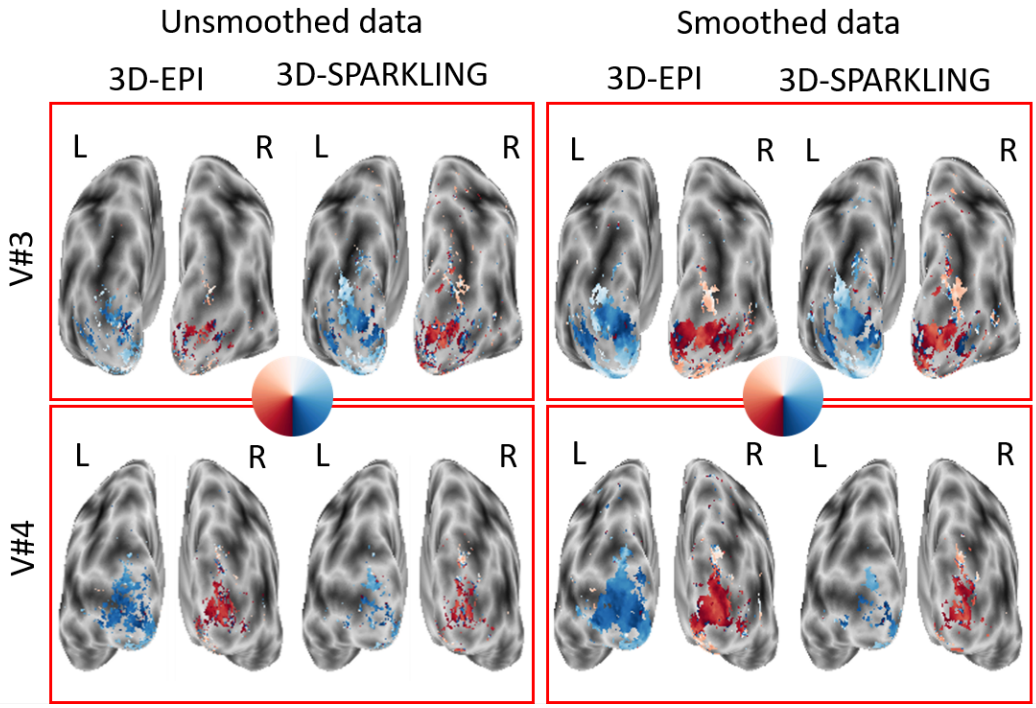

Figure 5.9: Projection of the BOLD phase maps on the pial surface visualized on the inflated surface for participants V#3 (3D-SPARKLING run first) and V#4 (3D-EPI run first). 3D-SPARKLING yields improved projected BOLD phase maps for V#3 in comparison with 3D-EPI both on raw and spatially smoothed data. Opposite results were found in favor of 3D-EPI in V#4, notably on spatially smoothed data.

The projected phase maps computed from the raw data illustrate once again the session effect as 3D-SPARKLING (resp., 3D-EPI) yields a larger effect for V#3 (resp., V#4). The data collected first yields a size effect that is large enough to retrieve an appreciable retinotopic organization. In contrast, the effect size is smaller in the data collected second. It allows, however, for a moderate recognition of the retinotopic organization. In addition to this, the results are overall consistent along the dorsal pathway: The blue (resp., red) color in the right (resp., left) hemifield projects to the left (resp., right) visual cortex.

The spatial smoothing at the preprocessing stage boosted the effect size and allowed us to retrieve more spatially extended phase maps, both for 3D-SPARKLING and 3D-EPI encoding schemes. Clearly, spatial smoothing was more beneficial to 3D-EPI than 3D-SPARKLING fMRI data : Smoothing has a greater impact on 3D-EPI data than on 3D-SPARKLING data in V#4. Nonetheless, this additional preprocessing step alters the intrinsic statistical sensitivity and specificity and is not entirely justified when only conducting within-subject statistical analyses.

5.4 Discussion

This study seeks to evaluate the feasibility of 3D-SPARKLING as a non-Cartesian encoding scheme for high-resolution fMRI, specifically its sensitivity to the BOLD effect as well as its spatial specificity. The performance of 3D-SPARKLING was assessed on 6 volunteers and compared to the state-of-the-art Cartesian 3D-EPI encoding pattern at the same spatio-temporal resolution (1mm isotropic, 2.4s) at 7T. Image quality and tSNR metrics computed from resting-state data, as well as outcomes from within-subject statistical analysis performed on retinotopic data, were compared in each volunteer across the two acquisition methods.

5.4.1 Main findings

First, regarding the resting-state fMRI data we show that 3D-EPI produces an improved image quality as compared to 3D-SPARKLING. On the other hand, 3D-SPARKLING yields higher tSNR in all participants over the whole brain but notably in the occipital lobe. On task-related fMRI data, across participants, we checked the validity of the retinotopic experiment, i.e. its ability to elicit evoked brain activity in the visual cortex at 7T for the set of acquisition parameters we considered, notably the spatio-temporal resolution and the two encoding schemes (`qCons1` and `QCons1`). Despite the moderate quality of the BOLD phase maps yielded by the collected data, it is possible to retrieve a moderately reliable mapping of the visual areas on the cortical surface (`qAccu1`). Second, according to the criterion `QSens2`, we demonstrated that 3D-SPARKLING has an increased sensitivity to the BOLD effect in gray matter. Third, based on criteria `QSpe1` and `QSpe2`, we proved that 3D-SPARKLING has an improved spatial specificity.

5.4.2 Challenges related to comparing competing acquisition strategies in a few volunteers

In this study, we compared fMRI activation patterns from two data sets that were acquired using concurrent encoding schemes and image reconstruction strategies. Although we tried with due diligence to harmonize the experimental setup between both acquisition techniques by keeping very similar readout times, the same echo and repetition times, the same number of shots, and very close fMRI preprocessing pipeline (except for field distortion correction), we still encountered the limitations of comparing data sets that were acquired at different time points, notably due to the presence of confounding factors such as between-run subject's motion. Additionally, the different image reconstruction strategies used for 3D-EPI and 3D-SPARKLING data are entirely justified by the different acquisition techniques. On one hand, 2D CAIPIRINHA [Bre+06] was implemented within the 8-fold accelerated 3D-EPI sequence together with 6/8-fold partial Fourier. On the other hand, compressed sensing reconstruction with sparsity promoting prior in the wavelet domain [El +18] was used on 3D-SPARKLING data.

Following a linear reconstruction and in the thermal noise regime, the Gaussianity of the residual noise is generally judged as a realistic assumption. Such a claim may not be as straightforward following a nonlinear CS reconstruction. As the GLM framework supposes the Gaussianity of the residuals, it is then essential that both reconstructions do not bias the noise distribution. The Gaussianity assumption remains realistic in our case, as well as illustrated by the experiment presented in Appendix A.

With that in mind, Table 5.2 demonstrates that the shapes of the activation patterns elicited by the two encoding schemes are close to each other. Additionally, we paid attention to balancing the number of participants scanned first with 3D-EPI and 3D-SPARKLING acquisition strategy to mitigate any potential loss in effect size due to the well-known repetition suppression effect. We, therefore, think that despite some noticeable differences this comparative study remains valid and insightful.

That being said, we believe that the readout time, the unitary repetition time as well as the number of shots were mostly optimal for 3D-EPI and not for 3D-SPARKLING: Using either more shots by reducing the unitary TR or a longer readout time allowing us to collect more k-space data points can be implemented in 3D-SPARKLING and would be beneficial as it could improve image quality, higher tSNR and provides increased sensitivity and accuracy for retinotopic mapping. We however, decided not to implement such suggested changes either by using a shorter unitary TR with a larger number of shots or a longer readout time (which implies slightly mismatched TE values) for 3D-SPARKLING in order to avoid different T_2^* contrasts between 3D-SPARKLING and 3D-EPI.

Hence for the sake of a fair comparison, we gave priority to choosing the same acquisition parameters for the two encoding schemes over using the most efficient parameters for 3D-SPARKLING.

5.4.3 Challenges of high spatial resolution whole brain retinotopic mapping fMRI

In this work, we compared the activation and retinotopic maps derived from 3D-EPI and 3D-SPARKLING data: Our findings suggest that 3D-SPARKLING data has an improved sensitivity to the BOLD effect compared to 3D-EPI. This is likely due to the higher tSNR observed in such data which could be explained by the expected larger PSF and hence effective voxel size of 3D-SPARKLING data compared to 3D-EPI. A larger voxel size helps in aggregating more signals and, therefore, enhances the sensitivity at the cost of spatial specificity. We have demonstrated, however, that the spatial specificity of the data collected with 3D-SPARKLING is not severely impacted.

Furthermore, it is worth noticing that the reported unsmoothed retinotopic maps, whether obtained from 3D-EPI or 3D-SPARKLING data, are not as reliable as those usually reported in the literature. This is a direct consequence of the high resolution employed. In fact, the existing literature on retinotopic mapping is scarce concerning high-resolution fMRI experiments as most studies are performed at a resolution around 3mm^3 [Hen+12; Pra+21].

Interestingly, in [Hof+08], the authors collected 1.1mm isotropic retinotopic fMRI data over 25 slices at 3T and 7T in a volumetric TR of 2s. Although this spatial resolution is close to ours, the retinotopic maps they obtained at 7T were more accurate and consistent with the state of the art than ours. It is a challenge to adequately explain this discrepancy as they used a significantly different experimental setup: 1) a different coil geometry, 2) a 2D imaging protocol with differing parameters and 3) a lower acceleration factor in parallel imaging. It is, however, interesting to note that they smoothed the projected phase maps using a Gaussian filter with a FWHM of 4mm. Applying the same strategy in Fig 5.9 but with a smaller FWHM of 2mm, we recovered consistent and improved phase values. We marginally used this smoothing strategy as it is detrimental to the native spatial resolution. The mediocre quality of the retinotopic maps retrieved from unsmoothed data tells us that this isotropic millimetric resolution remains challenging for a 10-minute high-resolution whole brain fMRI retinotopy at 7T. However, given the variations of cortical thickness across lobes, choosing this resolution is a decent target to carefully analyze the spatial specificity of activation in gray matter.

Recent trends in high-resolution fMRI based either on 3D spiral encoding schemes [Kas+22] or on hybrid radial-EPI (TURBINE) k-space coverage [GMC22] report enhanced evoked brain activity in the visual cortex as compared to ours obtained with both 3D-SPARKLING and 3D-EPI. Again, analyzing these differences is challenging as the authors employ a different set of parameters. Furthermore, we note that they rarely performed a direct comparison with the standard state-of-the-art (2D-SMS EPI or 3D-EPI) and/ or did not fully cover the brain. It is actually worth mentioning that when a high isotropic resolution is targeted, the 3D FOV very rarely covers the whole brain as otherwise higher acceleration factors are required which translates into a lower tSNR in 3D. Our results prove, however, that despite being challenging, our experimental setup is interesting and informative.

5.4.4 How does sensitivity to ΔB_0 inhomogeneities in non-Cartesian fMRI impact image quality and spatial specificity of detecting the BOLD effect?

The lower image quality observed on 3D-SPARKLING data in Fig 5.3 results from a higher sensitivity to static and dynamic magnetic field inhomogeneities due to the random nature of the trajectories which led to the accumulation of differently oriented ΔB_0 artifacts whereas, for 3D-EPI, the same readout is repeated across the k-space planes. Consequently, $\mathbf{B}_0$ inhomogeneities in 3D-SPARKLING acquisitions yield severe blurring and signal loss, in contrast to the main geometric distortions in 3D-EPI images due to off-resonance effects. More generally, this sensitivity to $\mathbf{B}_0$ imperfections is more prominent for some non-Cartesian encoding schemes. In regards to the dynamic fluctuations of the magnetic field, [Eng+21] showed on a T-Hex spiral-out encoding scheme that image quality was admissible in spiral imaging only when a full signal model was used for image reconstruction, i.e. when distortions related to both static and dynamic $\mathbf{B}_0$ inhomogeneities were corrected. In this work, even though we tried to minimize the impact of static magnetic field inhomogeneities on 3D-SPARKLING data by correcting them retrospectively during image reconstruction, this correction was imperfect as a separately acquired ΔB_0 field map was used for this purpose. Hence, any inconsistency between 3D-SPARKLING fMRI data and ΔB_0 field map acquisitions (due to significant subject's motion, for instance, as in V#6) may significantly lower the impact of this correction. Moreover, we did not correct 3D-SPARKLING data from dynamic magnetic field fluctuations, whereas a zeroth order correction was applied to 3D-EPI data.

As explained in Section "Image Quality and temporal SNR," this high sensitivity to $\mathbf{B}_0$ imperfections affects the PSF of the acquisition and in turn, can degrade the effective spatial resolution of 3D-SPARKLING data and, consequently, their spatial specificity. Nevertheless, this needs to be balanced with the PSF of the BOLD effect itself. In this respect, we noted that neither 3D-EPI nor 3D-SPARKLING have an actual spatial resolution of 1mm^3. Beyond the sensitivity to $\mathbf{B}_0$ fluctuations, other sources of degradation, such as the partial Fourier acceleration technique used in 3D-EPI or the strength of wavelet-based regularization implemented in the 3D-SPARKLING image reconstruction pipeline, may play a significant role. Confronting 3D-SPARKLING's poor image quality observed in Fig 5.3 with its relatively good spatial specificity (64%-87% of activated voxels localized in gray matter) suggests that the PSF of the detected BOLD effect was not strongly affected. This could be partly explained by the fact that the spatial resolution we chose is slightly higher or very close to the theoretical BOLD PSF: In [Shm+07], using fMRI data collected at a $1 \times 1 \times 3\text{mm}^3$ resolution, the authors showed that the BOLD PSF is less than 2mm in the primary visual cortex of the human brain. Later on, [FDP21] used $0.9 \times 0.9 \times 1.0\text{mm}^3$ fMRI data to estimate the BOLD PSF in the secondary visual cortex (V2) in the human brain. These authors reported that the BOLD PSF ranges between 0.83mm at the level of the WM/GM interface and 1.78mm at the border between the GM and CSF. As shown in Table 5.5, the relative percentage of activations retrieved in gray matter was higher in 3D-SPARKLING compared to 3D-EPI, and lower in the CSF and other tissues. This reflects a stronger spatial specificity or fewer false positives in 3D SPARKLING data. Concomitantly, the significant KS tests reported in

Table 5.4 brought evidence that higher z-scores were obtained when using 3D-SPARKLING as an encoding scheme, suggesting a larger number of true positives.

Taken together, these results prove that despite lower image quality, 3D-SPARKLING better preserves the temporal properties of the BOLD signal compared to 3D-EPI and may become even more competitive in the future with a full signal model, including correction for dynamic magnetic field inhomogeneities for image reconstruction.

5.5 Conclusion and perspectives

In this chapter, 3D-SPARKLING was used for the first time to conduct whole brain fMRI acquisitions at 1mm^3 and for a temporal resolution of 2.4s. We also performed an exhaustive subjectwise (because six volunteers were enough to perform robust group analysis) comparison between 3D-SPARKLING and state-of-the-art 3D-EPI based on image quality, tSNR, sensitivity to the BOLD effect as well as spatial specificity following both qualitative and quantitative criteria. The results revealed that 3D-SPARKLING yields a higher tSNR, an improved sensitivity to the BOLD contrast, and better spatial specificity than 3D-EPI. However, we observed that 3D-SPARKLING is penalized by its high sensitivity to $\mathbf{B}_0$ field imperfections, and the simple correction of the static term gives limited improvements. It is worth noticing that similarly to 3D-EPI, both [Kas+22] and [GMC22] perform dynamic field fluctuation corrections in non-Cartesian imaging during image reconstruction. To do so, they used either external estimates from a field camera or their sequence in a self-navigating manner. Our next goal is to investigate how this type of correction positively affects 3D-SPARKLING fMRI data.

In the next chapter, we will study the impact of static and dynamic magnetic perturbations on 3D-SPARKLING fMRI and how their correction improves image quality, tSNR and BOLD sensitivity. External measurements from a field camera will be used.

* * *
* *
*

Chapter 6

Impact of B_0 field imperfections correction on BOLD sensitivity in 3D-SPARKLING fMRI data

6.1 Context

In the previous chapter, for the first time, 3D-SPARKLING was evaluated for high spatial resolution (1mm^3) retinotopic mapping BOLD fMRI by systematically comparing its performances with those of 3D-EPI in terms of image quality, tSNR, BOLD sensitivity, and accuracy of the estimated retinotopic maps. 3D-SPARKLING proved competitive compared to 3D-EPI when it comes to detecting evoked brain activity. However, the image quality yielded by 3D-EPI was superior to that of 3D-SPARKLING. This can be explained by several factors, including:

- The ℓ_1-regularized reconstruction introduces some blurring in the image domain.
- The PSF of the sampling pattern.
- Sensitivity to motion.
- Sensitivity to $\mathbf{B}_0$ imperfections.

We believe that sensitivity to motion and magnetic field imperfections has the most significant impact.

In the following, our emphasis will be on the degrading impact of $\mathbf{B}_0$ imperfections on 3D-SPARKLING data. While we did correct the static term during 3D-SPARKLING's data reconstruction for Chapter A, the remaining uncorrected dynamic perturbations continue to influence the results. In this chapter, we aim to address this issue by implementing an experimental protocol in which we collect measurements of the field perturbations concurrently to the imaging process and correct them during the reconstruction step. Additionally, we will study the impact of both static and dynamic field perturbations on 3D-SPARKLING fMRI data with a specific focus on image quality, tSNR, and BOLD sensitivity.

Static and dynamic $\mathbf{B}_0$ field imperfections are detrimental to fMRI applications in general, especially at ultra-high magnetic fields, as they degrade the sensitivity to the BOLD contrast and the tSNR [TRW11]. The static contribution of spatially varying magnetic field offsets arises mainly from the susceptibility differences at tissue-air interfaces and is, to some extent, routinely corrected in MRI in general. In brain MRI, this issue is most prominent near the sinuses, buccal cavity, and ear canals. Static magnetic field inhomogeneities can cause geometric distortions, blurring, shading as well as strong signal loss.

Dynamic field fluctuations, which vary over time, pose an important challenge for fMRI. These fluctuations can act as nuisance variables [MBB13] and can induce intensity changes unrelated to neurovascular coupling, potentially affecting the robustness of the statistical analysis applied to fMRI data. They also degrade the tSNR. Prospective compensation or retrospective correction of dynamic field fluctuations is possible during image acquisition using internal estimates or external measurements of these fluctuations [Don20].

External measurements of static and dynamic $\mathbf{B}_0$ fluctuations can be used to correct 3D-SPARKLING fMRI data. For instance, the Skope field camera can be employed for this purpose. However, the T_2 relaxation time of its probes is around 45ms at 7T, implying that a relatively long TR_{probe} is needed to eliminate residual transverse magnetization between the consecutive shots and achieve a proper steady-state at the level of the probes. Using only RF spoiling, the field camera requires a constraining minimum TR_{probe} of roughly 110ms. Such a situation is particularly challenging for 3D fMRI applications as all shots are, ideally, monitored in real-time using $TR_{probe} = TR_{shot} \leq$50ms.

In [Sch+19], the authors managed to use this system to acquire realistic 3D-EPI fMRI data with a short TR_{shot} and a long TR_{probe}: They assumed repeatable readouts between the shots, skipped monitoring some shots and interpolated the missing NMR probe data. A similar strategy was used in [Kas+22] where the same system was used to correct up-to-the-first-order dynamic field fluctuations in single-shot high-resolution spiral fMRI data: Field fluctuations were recorded for every third shot using a $TR_{probe} = 270$ms and a $TR_{shot} = 90$ms. Such strategies are impractical for 3D-SPARKLING applications given the pseudo-random nature of the sampling pattern, i.e., the large variability across shots and, thus, the impossibility of interpolating NMR probe data across shots.

In this chapter, we alleviate this issue using an external spoiling gradient and adapting the experimental protocol to enable the use of Skope's Clip-on field Camera with $TR_{probe} = TR_{shot} = 50$ms challenging its long TR_{probe} constraint and evaluate it for 1mm^3 3D-SPARKLING retinotopic mapping and resting-state fMRI acquisitions. We demonstrate the feasibility of our experimental protocol and study the impact of static and dynamic B_0 field imperfections correction during image reconstruction in terms of image quality, tSNR, sensitivity to the BOLD contrast, and quality of the retinotopic maps. To the best of our knowledge, it is the first time such a thorough comparison has been performed using the Skope Clip-on field Camera for fMRI data at 7T and non-Fourier MR image reconstruction.

6.2 Materials and methods

6.2.1 General setup

The study was conducted at 7T MRI (7T Magnetom investigational device, Siemens Healthineers, Erlangen, Germany) on three healthy volunteers (1 female, 2 males) aged between 20

and 40 years old with normal-to-corrected vision using a 1Tx-32Rx head coil (Nova Medical, Willmington, CO, USA). The experimental protocol was approved by the national ethics committee (Comité de Protection des Personnes) under the protocol identifier CPP 100048 (CPP Sud Méditerranée 4 number 180913, IDRCB:2018-A011761-53). All participants gave their written informed consent.

Retinotopic mapping and resting-state data (cf Section 4.2 in Chapter 4) with normal breathing (NB) was collected from the three participants. Additional data with forced breathing (FB) and while performing a hand-to-chin movement (HC) was collected at resting-state from one volunteer.

Concurrently and for each acquired 3D-SPARKLING fMRI volume, 16 NMR probes from the field Camera, Cranberries edition (Skope Magnetic Resonance Technologies AG, Zurich, Switzerland) were used to monitor and record, in real-time the zeroth order field fluctuations over the acquisition window $k_0 = [k_{0,1}, \dots, k_{0,N_{shot}}] \backsimeq [2\pi t \Delta B_{0,dyn,1}, \dots, 2\pi t \Delta B_{0,dyn,N_{shot}}]$ and measure the trajectories played by the MR system $\tilde{\boldsymbol{k}} = [\widetilde{\boldsymbol{k}}_1, \dots, \widetilde{\boldsymbol{k}}_{N_{shot}}]$ for a $TR_{probe} = TR_{shot} = 50$ms. $\forall i \in [1, N_{shot}]$, $k_{0,i}$ provides a more temporally-resolved measurement than $\Delta B_{0,dyn,i}$ and relates to slow variation sources such as thermal drifts and breathing as well as faster fluctuations due to the gradient dynamics for example. The residual magnetization resulting from the use of such a short TR_{probe} was destroyed using the strongest spoiling gradient (47$0$mT*ms/m) implementable within a 50ms-TR_{shot} 3D-SPARKLING sequence.

6.2.2 Reconstruction strategy

The fMRI volumes were reconstructed independently from each other by minimizing the problem in Eq. (4.6) where the static and up-to-the-first-order dynamic field perturbations are corrected by means of the static field map acquired using the multi-echo GRE sequence mentioned in Section 4.3 in Chapter 4 and the field camera measurements mentioned above. Additionally, the Siemens scanner applies an eddy current phase compensation upon reception of the raw k-space data $\boldsymbol{y}_{j,\ell} = \boldsymbol{\mu}_{j,\ell} + \boldsymbol{n}_{j,\ell}$. The field camera does not perform such a correction. Applying the zeroth order dynamic correction on $\boldsymbol{y}_{j,\ell}$ directly using $k_0 = [k_{0,1} \dots k_{0,Nshot}]$ without taking into account this additional step means that eddy currents phase compensation will be applied twice. To avoid this, we cancel the correction applied by the scanner by demodulating the k-space data by a simulated phase of the eddy current compensation before correcting the zeroth order field term.

6.2.3 Evaluation metrics

The mean images computed from the resting-state time series were used to inspect the impact of $\mathbf{B}_0$ perturbations correction on image quality qualitatively. In order to gain a deeper insight into the impact of each field term, six distinct reconstruction strategies accounting for different combinations of field terms were used (Table 6.1):

(a) `No correction`: None of the field terms were taken into account.

(b) $\Delta B_{0,dyn}$: Only the zeroth order dynamic contribution was accounted for by the correcting the data itself.

(c) $\Delta B_{0,dyn}$ & $\delta\mathbf{k}$: The zeroth and first-order dynamic field fluctuations were corrected.

(d) $\Delta B_{0,stat}$: Only the static inhomogeneities were corrected.

(e) $\Delta B_{0,stat}$ & $\Delta B_{0,dyn}$: Static inhomogeneities and zeroth order dynamic fluctuations were corrected.

(f) $\Delta B_{0,stat}$ & $\Delta B_{0,dyn}$ & $\delta\mathbf{k}$: Static and up-to-the-first-order dynamic contributions were included in the signal model for reconstruction.

The resting-state fMRI scans were reconstructed using strategies (a)-(f) was and further used to compute the tSNR maps in order to rank the impact of each contribution both visually on the image quality and quantitatively.

Table 6.1: Table summarizing the different reconstruction strategies and the impact on the reconstruction algorithm with respect to the terms included in the signal model and reconstruction time. The primary factor contributing to the significant increase in reconstruction time is the static term, necessitating the use of the non-Fourier operator.

	Static contribution: $\Delta B_{0,stat}$		Dynamic contributions: $\Delta B_{0,dyn}$ and $\delta\boldsymbol{k}$				
	Encoding operator		K-space data		Trajectories		Reconstruction time per volume
	Fourier	non-Fourier ($\widetilde{\boldsymbol{\mathcal{F}}}_P$)	Uncorrected ($\boldsymbol{y}$)	Corrected ($\widetilde{\boldsymbol{y}}$)	Prescribed ($\boldsymbol{\Omega}$)	Measured ($\widetilde{\boldsymbol{\Omega}}$)	
(a)	×		×		×		∼15min
(b)	×			×	×		∼15min
(c)	×			×		×	∼15min
(d)		×	×		×		∼3h
(e)		×		×	×		∼3h
(f)		×		×		×	∼3h

In order to gain insight on the differences between the three volunteers and several physiological noise scenarios, the power spectra of the recorded $\Delta B_{0,dyn}$ measurements were computed over the whole resting-state fMRI acquisition at an individual level and visualized for specific frequency intervals.

To go one step further and investigate the influence of B_0 imperfections correction on the statistical performances when detecting evoked brain activity, the retinotopic mapping fMRI data was used to estimate activation maps by computing z-score maps after thresholding F-statistic maps (cf Section 4.5.1 in Chapter 4) over the entire brain for two different strategies:

(i) $p < 0.001$ without correcting for multiple comparisons

(ii) $p < 0.05$ with false discovery rate (FDR) control [BY01].

The impact on the sensitivity to the BOLD effect, as well as the prevalence of true versus false positives, was assessed, at the subject level according to the following qualitative (q) and quantitative (Q) criteria:

1) `qActiv1`: The statistically significant z-score maps obtained from the fMRI volumes reconstructed with strategies (a) and (f) and thresholded according to strategies (i)-(ii) were compared one another subjectwise.

2) `QActiv1`: The Number of activated voxels (defined using thresholding strategies (i)-(ii)) and maximum z-score values were compared at the subject level once the fMRI volumes were reconstructed using strategies (a) and (f).

Finally, the impact on the quality of the BOLD phase maps was evaluated according to the following criterion:

3) `qPhase1`: The volumetric BOLD phase map derived from the fMRI scans reconstructed using strategies (a) and (f) were compared subjectwise. Furthermore, the BOLD phase maps corresponding to V#1 were projected onto the cortical surface for both hemispheres and visually assessed.

6.3 Results

6.3.1 Achieving steady state signal of the NMR probes

Figure 6.1 depicts $S_{raw}(t = 0)$ (the raw signal measured by the field camera before any estimation of field fluctuations) for the first 96 consecutive shots of the multi-repetition 3D-SPARKLING sequence used to acquire *in vivo* fMRI data without/with the application of an external spoiling gradient through the 3D-SPARKLING sequence and using a $TR_{shot} = TR_{probe} = 50$ms. The data plotted in this figure is acquired in vitro (phantom data) and comes from a single probe. It illustrates the temporal evolution of the ^{19}F NMR signal in the absence of participant-induced perturbations: Stimulated echoes due to the very short TR_{probe} prevent steady-state at the level of the probes in the absence of a spoiling

gradient(blue trace) whereas an external 470mT*ms/m spoiling gradient overcomes this issue (orange trace). Therefore, It becomes possible to use the field monitoring system in this alternative setting to challenge its long TR_{probe} constraint by simply applying an external spoiling gradient that is strong enough to eradicate the residual transverse magnetization.

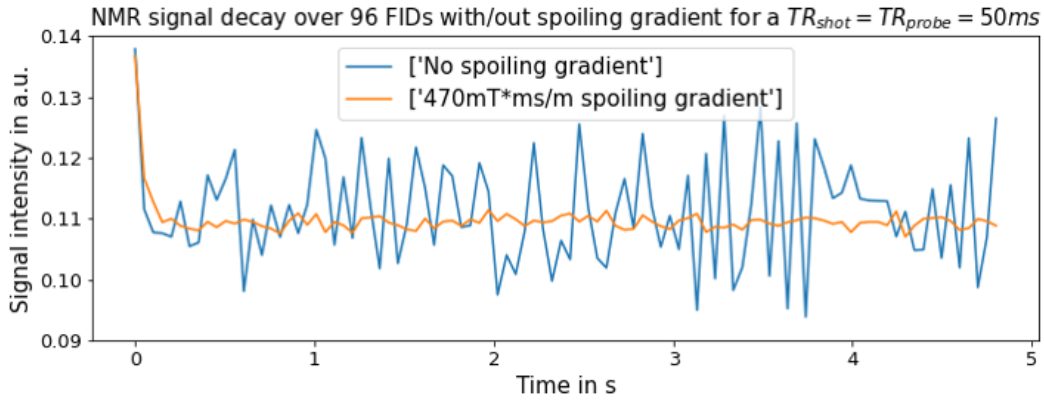

Figure 6.1: Example of the NMR signal decay from one probe of the field camera over 96 FIDs with/out an external spoiling gradient for a $TR_{shot} = TR_{probe} = 50$ms: Stimulated echoes prevent steady-state in the absence of an external spoiling gradient, whereas a 470mT*ms/m spoiling gradient ensures a steady-state at the level of the probes.

However, according to the signal equation at steady state, even at the Ernst angle, using a smaller TR induces a lower NMR signal and, therefore, a degraded SNR at the level of the probes. The following subsections will demonstrate that even with a degraded SNR, the field camera manages to estimate field fluctuations that are accurate enough to yield beneficial correction for fMRI data.

6.3.2 Enhanced image quality

Figure 6.2 shows a comparison of the mean images computed from the resting-state fMRI data collected in volunteer #1 (V#1) and reconstructed according to the strategies (a) to (f) mentioned in Section 6.2.3. It is noteworthy that the image quality associated with strategy (a) is very degraded. Additionally, the figure demonstrates that the overall T_2^* contrast is significantly enhanced when correction of both static and dynamic fluctuations of the magnetic field is performed: The blue arrows illustrate how the correction of either the dynamic or static contribution alone (strategy (c) or (d)) resulted in partial improvement whereas correcting both terms (strategy (f)) induced a more significant enhancement. Moreover, the lost signal in strategy (a) is now recovered, and anatomical details are more finely reconstructed, as depicted by the orange and green arrows, respectively. Again, it is worth noting that strategies (b)-(e) yield limited improvement when compared to strategy (f), suggesting that none of the field terms has a negligible influence on image quality.
Figure 6.3(A) displays a subjectwise comparison between the mean images from the resting-state sequence of fMRI scans reconstructed without and with static and up-to-the-first-order dynamic field terms correction: The gain in image quality is systematic across the three volunteers and for three physiological movement scenarios namely NB, FB and HC.

6.3.3 Increased tSNR

Figure 6.3(B) qualitatively depicts the boost in tSNR obtained when correcting static and up-to-the-first-order dynamic field terms: A notable increase is observed across the three volunteers for the normal breathing scenario, notably in the anterior and posterior cortex and, along the edges of the brain suggesting that subtle head movement-induced field fluctuations related to breathing were compensated. V#2, however, yielded slightly superior tSNR maps compared to the two other participants. This is likely due to the fact that they had less

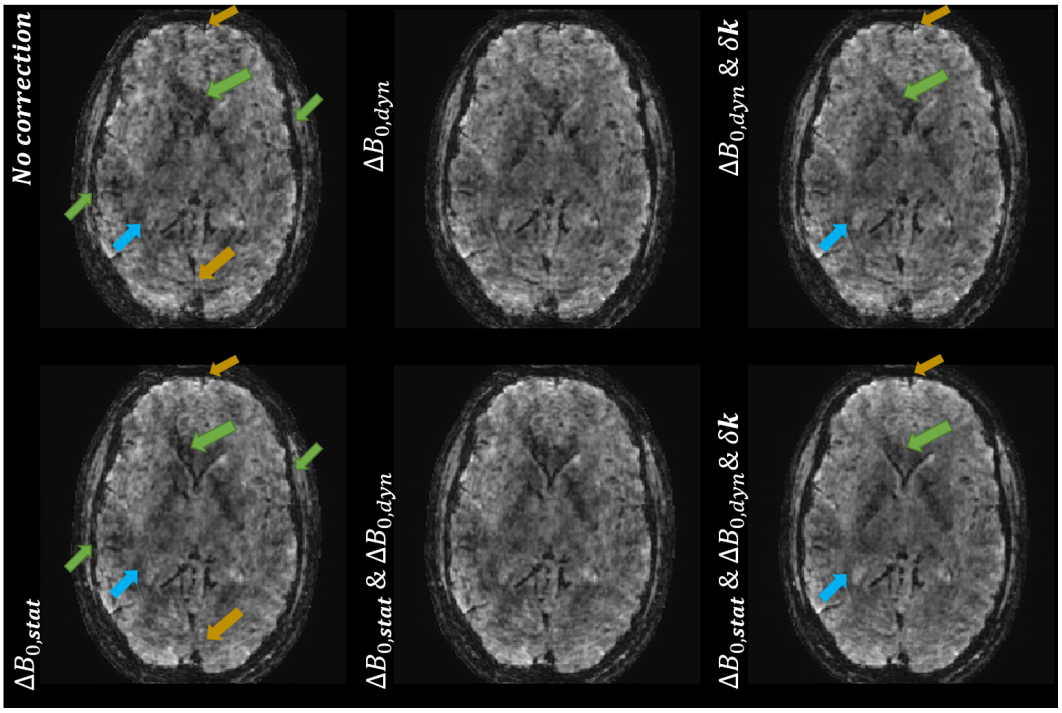

Figure 6.2: Comparison of the mean image of resting-state fMRI scans collected from V#1 reconstructed using strategies (a) to (f). From left to right, the top row (resp., bottom row) depicts the mean images yielded by the images reconstructed using strategies (a) to (c) (resp., (d) to (f)). The overall contrast is enhanced, the lost signal is better recovered, and anatomical details are better reconstructed, as illustrated by the blue, orange, and green arrows, respectively.

energetic breathing fluctuations, as demonstrated in Fig. B-1(A) (in Appendix B.1) where the power spectra of the breathing-induced field fluctuations during the NB scenario are shown for each subject. Despite a discernible increase in tSNR in the data collected in V#3 during forced breathing and when performing the hand-to-chin movement, we did not recover levels that are comparable with the normal breathing scenario. This is likely due to the involvement of additional large-amplitude head movements that we are currently unable to correct using our current protocol (cf Fig. B-2 in Appendix B.2).

These qualitative findings are quantitatively supported by Table 6.2: It reports the relative gain in % of median tSNR computed over the brain mask when correcting the different field terms during image reconstruction. Although the increase is systematic across volunteers and scenarios, the relative gain for V#2 is approximately one-half (resp, one-third) lower than for the two other volunteers when strategies (b) and (c) (resp., strategies (e) and (f)) are used. Otherwise, the relative gain in median tSNR reaches a plateau around 30% at maximum. The limited improvement in the tSNR maps corresponding to the FB and HC scenarios (Figure 6.3(B)) highlights the limits of the correction in extreme cases.

6.3.4 Increased sensitivity to the BOLD contrast

Figure 6.4 illustrates a subjectwise comparison of the statistically significant activation patterns thresholded using alternatives (i) and (ii) and yielded by the uncorrected (strategy (a)) and fully corrected (strategy (f)) data (`qActiv1`) on selected axial slices.

First, a larger effect size is associated with $\mathbf{B}_0$ imperfections correction for both statistical thresholding strategies. This is reproducible across the three volunteers but most visible in V#1 where, in addition to an increased statistical significance, the activation pattern seems to better delineate the gray matter in the visual cortex, suggesting a finer fit to the cortical surface.

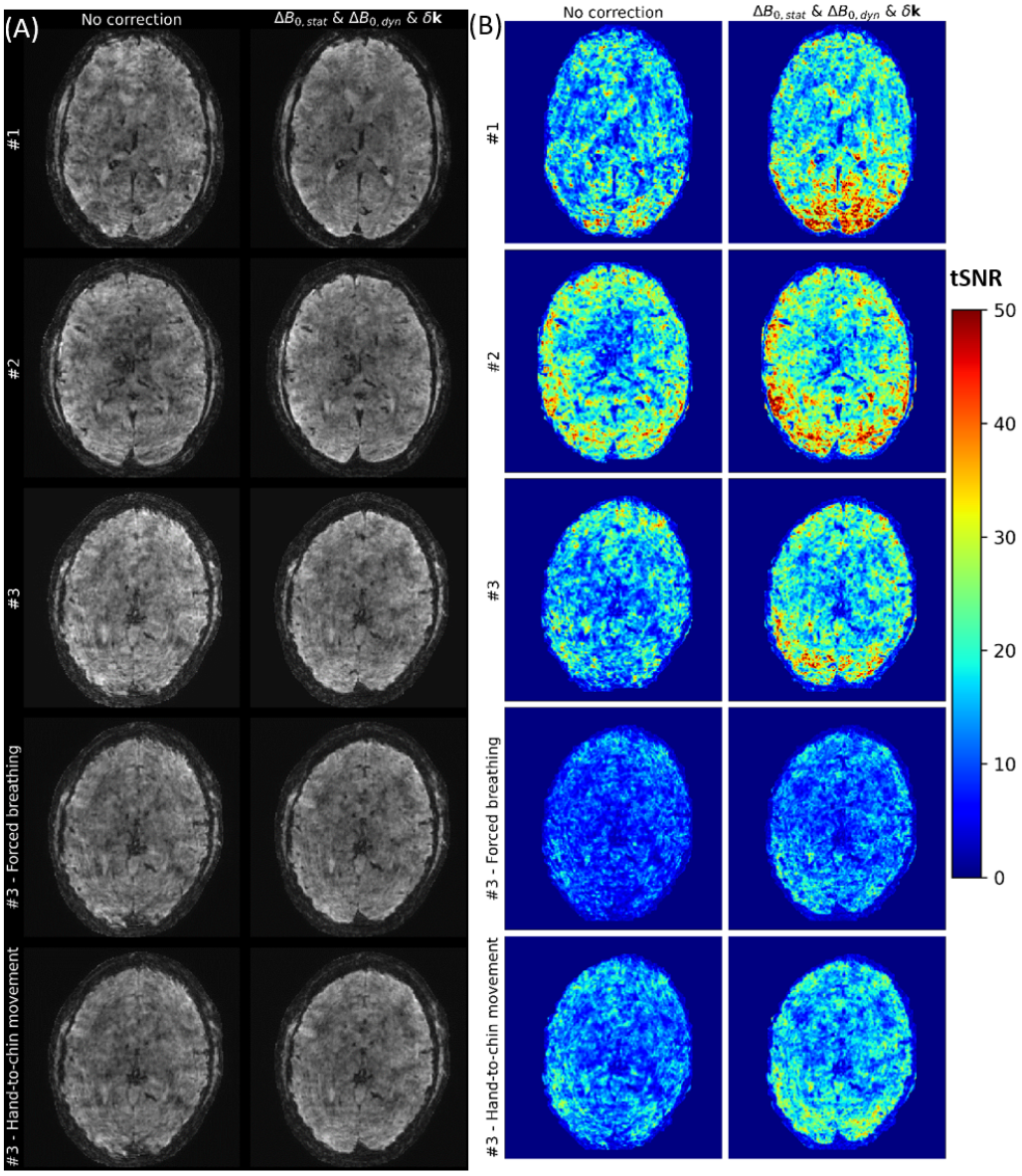

Figure 6.3: Comparison of the (A) mean images and (B) tSNR maps yielded by the resting-state fMRI scans sequence collected in the three volunteers and using the different physiological movement scenarios reconstructed using strategies (a) and (f). The improved image quality when strategy (f) is used is reproducible across volunteers.

Table 6.2: Gain in % of median tSNR in corrected data (strategies (b) to (f)) relative to the native tSNR (uncorrected data, i.e., strategy (a)) computed over the brain mask. The highest figures (in bold) are retrieved when strategy (f) is used.

	Gain in % of median tSNR					
Terms correctedVolunteer	#1 NB	#2 NB	#3 NB	Average NB	#3 FB	#3 HC
(b) $\Delta B_{0,dyn}$	+20	+11	+22	+18	+24	+24
(c) $\Delta B_{0,dyn}$ & δ**k**	+26	+13	+23	+21	+27	+26
(d) $\Delta B_{0,stat}$	+5	+6	+4	+5	+5	+5
(e) $\Delta B_{0,stat}$ & $\Delta B_{0,dyn}$	+28	+18	**+29**	+25	+32	+31
(f) $\Delta B_{0,stat}$ & $\Delta B_{0,dyn}$ & δ**k**	**+34**	**+20**	**+29**	**+28**	**+34**	**+33**

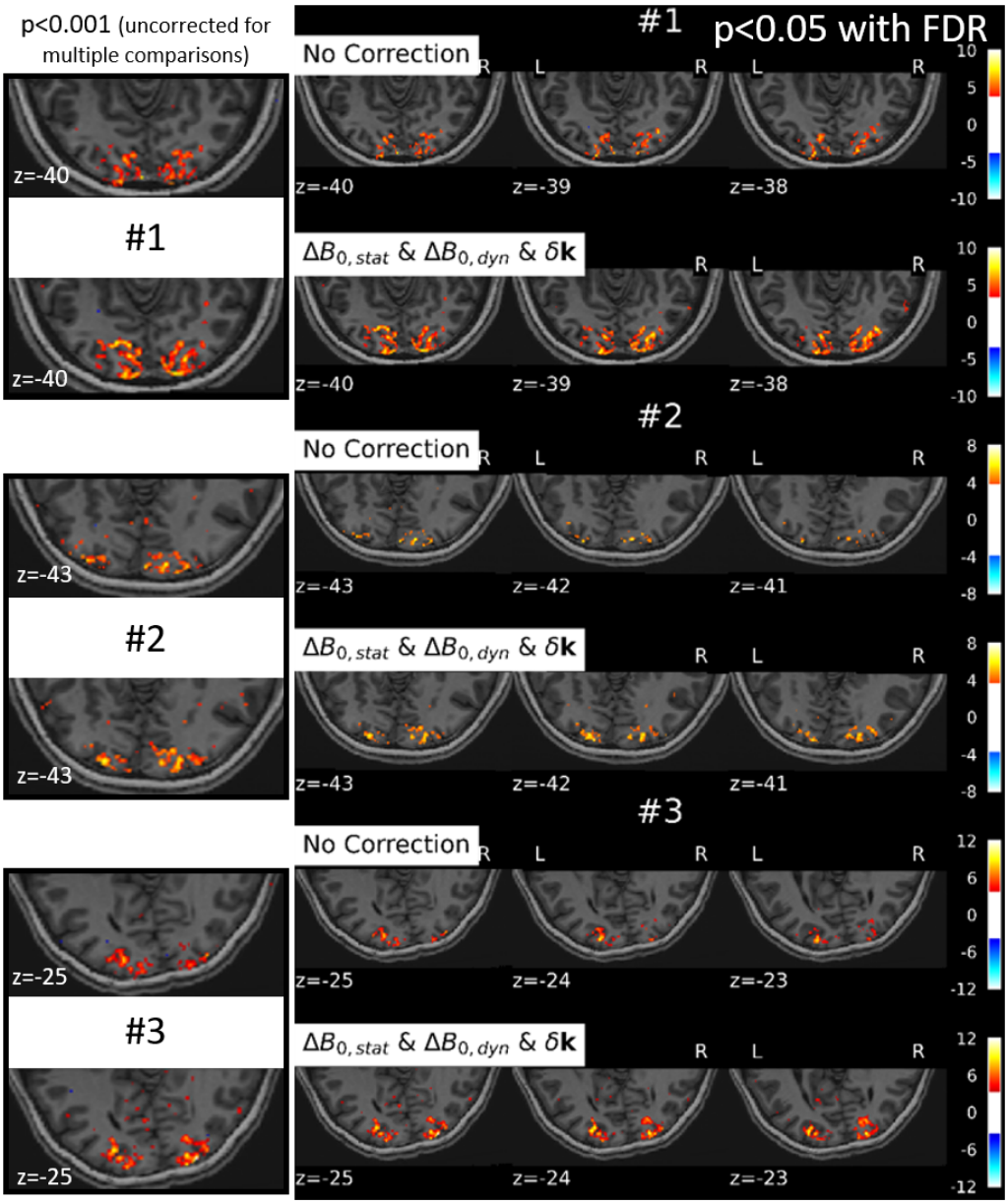

Figure 6.4: Comparison of the activation maps at the subject level for V#1-V#3 yielded by the retinotopic data reconstructed without and with static and up-to-the-first order field terms correction. The activation maps on the left (resp., right) panel were produced by thresholding the z-score maps corresponding to the global effects of interests using a p-value of 0.001 without multiple comparisons correction (resp., 0.05 with FDR control).

Second, comparing the results at two statistical control levels (i)-(ii), we observed a smaller discrepancy between the activation maps obtained when static and up-to-the-first-order dynamic field terms are corrected. This suggests that at a given false positive rate the sensitivity to the BOLD contrast is increased and that the results are not merely biased by false positives.
These qualitative findings are supported by the figures reported in Table 6.3, which summarizes the systematic gain in the number of activated voxels and maximum z-score values when B_0 field imperfections are corrected (strategy (f)): The number of activated voxels extracted using the thresholding alternative (i) (resp, (ii)) is on average 43.3% ± 17.2% (resp, 159,3% ± 38.6%) larger. The greater boost in effect size when an FDR control is applied suggests

once again a higher prevalence of true positives over false positives in the corrected fMRI scans. The reported figures are consistent between the first and third participants. V#2, however, reveals fewer activated voxels, notably after applying FDR control. This is likely due to larger head movement amplitudes as shown in Fig. B-3 in Appendix B.3 where the time course of motion regressors of the translation over the z-axis are depicted.

Table 6.3: Number of activated voxels and the maximum z-score values extracted from task-based fMRI volumes with/out correcting magnetic field imperfections. The activated voxels are defined using two distinct statistical significance levels: a p-value of 0.001 without multiple comparisons correction and a p-value of 0.05 with FDR control. The highest figures (in bold) are obtained when strategy (f) -Full Correction- is used. V#2 reveals the lowest statistical significance.

Volunteer	#Activated voxels $p < 0.001$ uncorrected for multiple comparisons		#Activated voxels $p < 0.05$ with FDR correction		Maximum z-score value	
	No correction	Full Correction	No correction	Full Correction	No correction	Full Correction
#1	6456	**9506**	3253	**7722**	8.02	**9.95**
#2	4367	**7405**	1059	**2204**	6.75	**7.59**
#3	8529	**10823**	2503	**7745**	10.83	**12.08**
Average	6450.67	**9244.67**	2271.67	**5890.34**	8.54	**9.87**

6.3.5 More accurate BOLD phase maps

Figure 6.5 depicts the BOLD phase maps derived from uncorrected and corrected fMRI volumes on selected axial views. Firstly, we noticed a larger spatial extent of the BOLD phase maps when $\mathbf{B}_0$ field imperfections are corrected. Second, the maps shown are in better agreement with prior knowledge about the visual field projection onto the occipital cortex. A zoomed-in example is shown for V#1 as she/he was the most compliant volunteer: We clearly observe that the two visual hemifields project onto the contra-lateral hemispheres in the occipital cortex, a well-known mirroring feature of the primary visual cortex. Furthermore, and without ambiguity, the top (resp., bottom) parts of the visual field project onto the bottom (resp. top) parts of the occipital cortex. In comparison, the BOLD phase map yielded by the uncorrected data seems noisy and matches the expected gradient only partially.

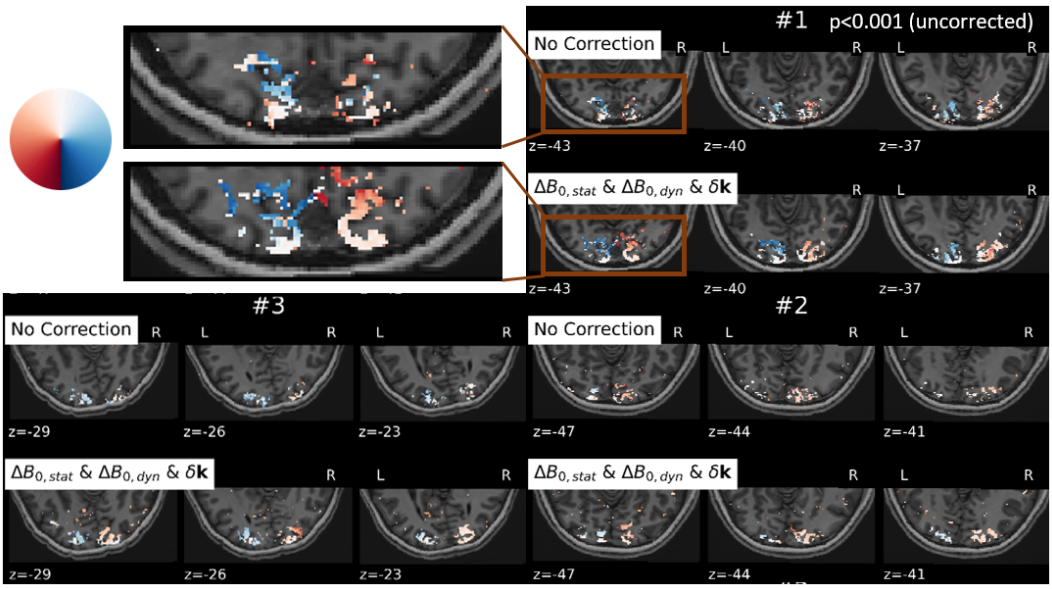

Figure 6.5: Comparison of the BOLD phase maps over an ROI defined using the thresholding alternative (i) yielded by retinotopic fMRI scans reconstructed without and with static and up-to-the-first order dynamic field terms correction.

To gain a better insight, the BOLD phase maps ought to be projected on the cortical surface as shown in Figure 6.6(A) (`qPhase1`). In the first column, we observe significantly enhanced BOLD phase maps when magnetic field imperfections are corrected: A poor retinotopic organization is retrieved when no field term is corrected, whereas an improved one can be inferred when they are. Furthermore, estimating the BOLD phase maps using an ROI defined using a p-value of 0.05 with FDR control (alternative (ii)) has a considerable demeaning effect on the phase maps yielded by the uncorrected fMRI volumes. However, the degradation is almost imperceptible on BOLD phase maps obtained from the corrected fMRI volumes.

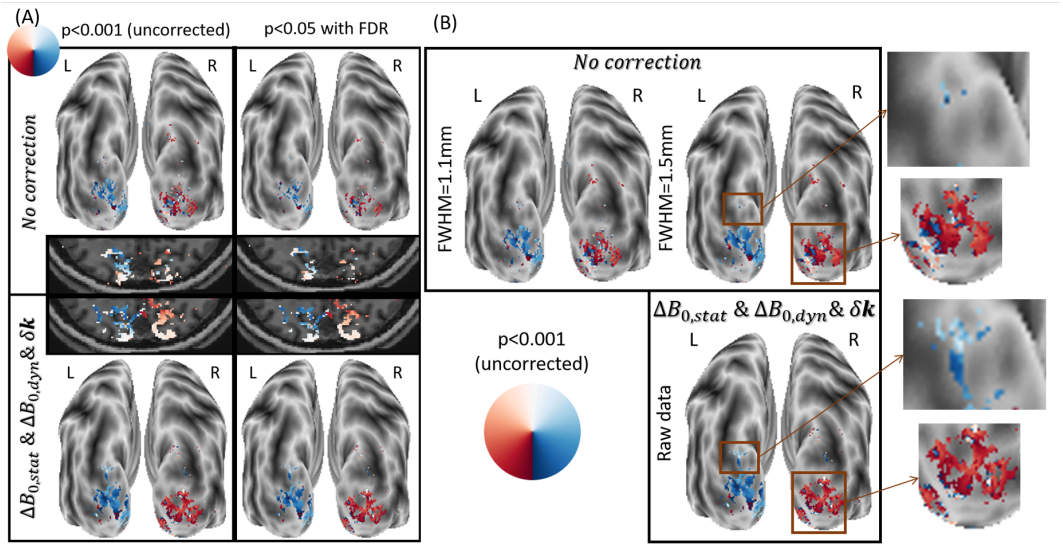

Figure 6.6: (A) BOLD phase maps yielded by the data collected from V#1 and reconstructed without/with B_0 field imperfections correction and their projections on the cortical surface. (B) Projected BOLD phase maps yielded by the data collected from V#1 and yielded by the smoothed (using a Gaussian kernel with FWHM=1.1mm and FWHM=1.5mm) B_0-uncorrected data and the raw B_0-corrected data.

Additionally, we compared in Figure 6.6(B) the BOLD phase maps derived from raw corrected (strategy(f)) and smoothed uncorrected (strategy(a)) fMRI volumes. Two distinct isotropic 3D Gaussian kernels (FWHM=1.1mm and FWHM=1.5mm) were used to smooth the raw fMRI volumes before performing a GLM analysis. FWHM=1.1mm was tested because all else being equal, it corresponds to an increase in tSNR of about 33%, which roughly corresponds to the maximum gain in tSNR we claim is possible to achieve using our protocol. Firstly, we observed that the smoothed uncorrected volumes yield BOLD phase maps with lower quality than the raw corrected scans. Secondly, we noticed that smoothing the images at FWHM=1.5mm does not recover the lost signal, whereas correcting $\mathbf{B}_0$ field imperfections does (zoomed-in region in the left hemisphere). Furthermore, while it is true that we recover more spatially extended BOLD phase maps on the right hemisphere when smoothing the images, this map remains less spatially specific than in the raw corrected volumes. We conclude that the increase in median tSNR observed when correcting B_0 imperfections yields an increase in sensitivity that exceeds the expected improvement if we choose to degrade the spatial resolution to increase the tSNR.

6.4 Discussion

In this work, the impact of static magnetic field inhomogeneities and their dynamic fluctuations retrospective correction on fMRI volumes has been assessed.

6.4.1 Main findings

Through the application of a suitable external spoiling gradient, we have first demonstrated that it is possible to use the field camera outside its standard experimental setting, which requires a quite long TR_{probe} with respect to the TR_{shot} in fMRI, and accurately estimate up-to-the-first-order dynamic field fluctuations. Second, on resting-state fMRI data, we have proved that $\mathbf{B}_0$ field imperfections correction has a hugely beneficial impact on 3D-SPARKLING image quality as well as tSNR: Up to 30% increase in median tSNR was quantified.
Finally, a rather exhaustive evaluation of the impact on the fMRI volumes demonstrated a significant improvement in the sensitivity and quality of the BOLD phase maps.

6.4.2 Improved tSNR and detection of evoked brain activations

Our findings provide qualitative and quantitative evidence of a systematic gain in tSNR on average, as demonstrated by using resting-state fMRI data. This is generally in accordance with previous studies. In [Bol+17], the same field camera was used to correct field fluctuations in 2D-EPI fMRI acquisitions at 3T. The authors note that the increase in tSNR is most notable in the occipital lobe, consistent with Figure 6.3(B). Furthermore, they demonstrate that the gain in tSNR is mainly due to the correction of hardware-related fluctuations. At 7T and in 3D acquisitions, physiological fluctuations impact the signal more severely: In [Sch+19], the authors observed up to 14.3% (resp., 35.6%) relative gain in the mean tSNR over the brain when performing forced breathing (resp., hand-to-chin movement) for 1mm^3 3D-EPI fMRI (20 repetitions) data at 7T. Upon comparison with 2mm^3 fMRI data, they showed that the gain in tSNR is more significant at higher spatial resolution, i.e., 1mm^3. The differences in the reported numbers arise from the experimental conditions (2D vs 3D, 3T vs 7T, number of repetitions, volunteer's movement).
To the best of our knowledge, no existing study in the literature using a field camera pushed the comparison up to the statistical analysis. The increase in sensitivity associated with B_0 field imperfections correction we observed remains notable at stricter statistical thresholding levels as demonstrated by criteria `QActiv1`: The recovery of lost signal plays a major role in retrieving true positives. The enhanced image quality is also expected to yield better spatial specificity as blurring is extremely reduced. Such a claim is supported by the projections of the retinotopic maps onto the cortical surface for V#1.

The BOLD phase maps obtained from the corrected volumes were not merely better than those produced by the uncorrected ones, but their quality also exceeded that of those yielded by smoothing (using either FWHM=1.1mm or FWHM=1.5mm) uncorrected volumes: In fact, when $\mathbf{B}_0$ field imperfections correction is performed, confounding factors due to the participant's physiological movement and the system's instabilities and drifts are eliminated prior to preprocessing and statistical analysis whilst larger voxel sizes only help in aggregating more signal within a voxel without effectively minimizing the effects of such confounding factors.

6.4.3 Is it relevant to go beyond first-order dynamic field fluctuations correction?

It is worth noting that our protocol is feasible and has proved without ambiguity that static and up-to-the-first-order dynamic magnetic field imperfections correction is beneficial for 3D-SPARKLING fMRI statistical analysis by illustrating the gain in image quality, tSNR, and accuracy of the retinotopic mapping. Nevertheless, it is essential to keep in mind that data collected from 16 probes was used to estimate four unknown terms for each time point t, namely one zeroth-order term ($k_0(t)$) and three terms translating the first-order field fluctuations ($\delta\mathbf{k}(t) = (\delta k_x(t), \delta k_y(t), \delta k_z(t))$). This means that the lower SNR of the probes expected from using a shorter TR_{probe} is compensated with data redundancy.
A further step would be to correct the higher-order field terms [Wil+11] during MR image reconstruction. However, it involves an additional and heavy computational burden during image reconstruction, especially in the non-Cartesian setting. Depending on the encoding

scheme, it would be necessary to consider the higher order terms [Eng+21] or not [Van+15; Kas+22]. In our case, the compromise between the possible benefit and computational load of such a strategy could be further investigated. Furthermore, additional investigation will be required to prove that the SNR at the levels of the probes remains high enough to estimate higher-order terms accurately as well.

6.4.4 Limitations

In the literature, several Cartesian and non-Cartesian methods[Pos+10; Sch+19; Gra+17; Kas+22] seem to yield improved image quality compared to that reported in this work. However, it is actually challenging to perform relevant and fair comparisons as different experimental setups are used in the competing studies [Pos+10; Sch+19; Gra+17; Kas+22] in terms of brain coverage, number of shots, 2D vs. 3D acquisitions, etc. In Chapter 5, we performed an extensive comparison in fMRI between 3D-EPI and 3D-SPARKLING for similar acquisition parameters. The dynamic field fluctuations were not corrected in 3D-SPARKLING fMRI volumes, and we found a poorer image quality as compared to 3D-EPI. We explained this by the fact that 3D-SPARKLING is more sensitive to the acquisition's imperfections than 3D-EPI. However, we demonstrated that despite a poorer image quality, the sensitivity/specificity statistical trade-off for the detection of evoked brain activity based on the BOLD contrast is, on average, over six volunteers, similar for both techniques (3D-SPARKLING vs. 3D-EPI). With the addition of dynamic field perturbations correction, in the chapter, we believe that we further improve the image quality for 3D-SPARKLING.
As demonstrated by our findings on resting-state fMRI data collected for the FB and HC scenarios, the fact that head movements are not corrected hinders the efficiency of the correction performed for the most extreme cases. In contrast, in typical cases of involuntary moderate movement such as for V#2, the findings showcase undeniable benefits. In [Hae+15], the authors present an experimental protocol for using the field camera for motion monitoring in anatomical imaging. Such a solution should work for fMRI as well. However, it is beyond the scope of this work.
In this work, we resort to external measurements of the dynamic field fluctuations, overlooking the fact that each shot crosses the center of the k-space in 3D-SPARKLING. In fact, such a feature enables self-navigation and the estimation of an average zeroth-order dynamic term $\Delta B_{0,dyn}$ per shot, similar to the solution proposed for TURBINE in [Gra+17]. Nevertheless, such estimates may not be as accurate as the field camera measurements. In any case, it would be interesting to implement such a strategy and to compare its estimates with external measurements.
Furthermore, we consider that the static and dynamic field terms evolve independently from each other since such an approximation is easy to implement and remains accurate enough. Nevertheless, it does not reflect the MR physics of the experiment faithfully. In fact, a truthful model would consider static and dynamic magnetic imperfections as evolving jointly: A ΔB_0 map would be estimated for each volume in this case analogously to what is proposed in [Dym+18; Has+22]. As demonstrated in [Dav+22], it would actually be possible to estimate a volume-wise ΔB_0 map from 3D-SPARKLING data. Such a solution would also avoid any possible inconsistencies between an external ΔB_0 map and the fMRI volumes in case of patient movement for instance. However, the pipeline in [Dav+22] was conceptualized for anatomical scans and would need further tuning for fMRI data since, to date, it does not produce good estimates of ΔB_0 maps from highly accelerated fMRI data.

6.5 Conclusion and perspectives

In this chapter, we demonstrated a systematic and significant benefit in image quality, tSNR, and in terms of effect size and accuracy of the brain activity detection and localization when adopting magnetic field monitoring: In fact, using retinotopic fMRI data, we have noted an increase in sensitivity, notably at a stricter statistical control level, and more accurate BOLD phase maps. This study was conducted using a field camera in an alternative setting challenging its TR_{probe} constraint to monitor up-to-the-first-order dynamic magnetic

field fluctuations. However, as the trajectories cross the center of k-space at each TR_{shot}, 3D-SPARKLING could also be used as a self-navigating encoding scheme as described in the subsection 6.4.4. More importantly, such a feature also offers more flexibility when it comes to choosing the spatiotemporal resolution of the fMRI sequence of volumes a posteriori during the reconstruction step. For example, using a sliding window [KJR12] approach where k-space data is shared between consecutive scans at the image reconstruction step can help improve the current temporal resolution without significantly impacting the spatial resolution, the coverage, and the tSNR. The next and final goal of this thesis is to explore the possibility of retrospectively enhancing the temporal resolution through a sliding-window approach specifically within the context of SPARKLING acquisitions, in an effort to uncover its viability, capabilities, and limitations.

In the next chapter, we conduct a simulation study to assess to what extent such an approach is able to detect fast oscillations in BOLD responses and disentangle physiological noise-induced fluctuations from neural activity by artificially improving the temporal resolution.

* * *
* *
*

Chapter 7

Sliding-window reconstruction for improved temporal resolution in SPARKLING fMRI

7.1 Context

In the context of this thesis, we wanted to achieve high spatiotemporal resolution of whole-brain fMRI using 3D-SPARKLING. We started by validating 3D-SPARKLING as a viable technique to collect fMRI data in the above-mentioned context of spatial resolution (1mm^3) and brain coverage using an acceptable temporal resolution (2.4s) by performing a comparison with 3D-EPI in a systematic subjectwise manner and according to an exhaustive list of qualitative and quantitative criteria. Having observed a higher sensitivity to magnetic field perturbations in 3D-SPARKLING data, we set up an experimental protocol to correct static and dynamic field perturbations in 3D-SPARKLING data and demonstrated the benefit of magnetic field perturbations monitoring and correction in terms of image quality, tSNR, and BOLD sensitivity. In this final stage, we pay attention to improving the temporal resolution using one of the intrinsic properties of SPARKLING (each trajectory samples the center of k-space) as a generic case of 3D-SPARKLING to retrospectively enhance the temporal resolution without decreasing the brain coverage or degrading the spatial resolution.

Historically and despite some precursor interest and works [Sav+95; Ban02] that tried to investigate the limits of temporal resolution in BOLD fMRI, the temporal dimension received less attention than the spatial one, as fMRI was primarily used as a brain mapping tool. Furthermore, as an indirect measure of neural activity, BOLD effect [Oga+90] has slower dynamics than the neural activity itself, partly due to the data acquisition process and partly due to the sluggishness of the HRF [Fri+95]. Hence, methodological developments (fMRI acquisition and reconstruction methods) were essentially directed toward enhancing

spatial specificity and optimizing the paradigm designs (block or slow event-based designs, jittering, etc.) compensated for the lack of temporal precision. However, while the slowness of BOLD with regard to neural events is widely acknowledged, its inherent temporal resolution remains ambiguous. Moreover, the precise HRF model (profile and temporal precision) is still an ongoing research topic [Ciu+03; STC13; Che+21b]. In recent years, more efforts have been made to enhance the temporal resolution in fMRI primarily because of a growing interest in the high-frequency components of BOLD [Lew+16; Che+21a; PL21]. This trend is not confined solely to task-based fMRI, where the nature of the task can modulate the observed frequencies. It actually extends to resting-state fMRI, where new findings suggest that the traditional 0.1Hz upper bound [Fra05; Dam+06] is very restrictive [RCB13; CG15]. Furthermore, achieving a higher temporal resolution is expected to help better understand rapid naturalistic high-level cognitive processes such as sleep, language, awareness, fast decision-making, etc. More generally, complex cognitive functions can be studied in more ecologically valid setups using free-form stimulation, for instance, that mimics real-world scenarios better than highly controlled paradigms. Additionally, high temporal resolution is essential to eliminate physiological artifacts related to breathing or heartbeat [Jah+19; Huo19].

Most current attempts achieve high temporal resolution at the expense of either diminished brain coverage [Rai+21; Rai+23] or a loss in spatial resolution [Ley+21; Bia+22]. The assumption of repeatability combined with data reshuffling either in k-space [Fra+23] or the image domain [Nag+22; Sch+23] have also been used to enhance temporal resolution as well as sharing data between different consecutive frames [Gao+96; KJR12; Yun+13; Yun+19]. Methods that rely on data sharing or reshuffling alter the autocorrelation structure of the fMRI signal. While most studies [Yun+13; Yun+19; Nag+22; Sch+23; Fra+23] investigating these methods acknowledge the induced autocorrelation issue, the authors either claim that it is not significant or leave its characterization and potential correction for subsequent investigations.

In this context, we re-investigate the sliding-window approach introduced in [KJR12] for fMRI, where the native k-space data acquired is rearranged into overlapping blocks during reconstruction time. In SPARKLING, each trajectory crosses the center of the k-space allowing for a continuous update of the contrast along the entire acquisition time. Additionally, the pseudo-random nature of the sampling pattern ensures that each trajectory covers distinct k-space regions, resulting in a broad spectrum of frequencies being sampled during each TR_{shot}. These features can be optimally combined with the sliding-window approach. We demonstrate the ability of the sliding-window image reconstruction approach, when applied to SPARKLING fMRI data without additional autocorrelation correction, to detect oscillations beyond the traditionally accepted 0.1Hz threshold and to disentangle physiology from neural activity in simulations of 2D BOLD fMRI using SPARKLING [Laz+19; Cha+22] in a scan-and-repeat mode.

7.2 Materials and methods

7.2.1 Synthesis of realistic artificial fMRI data

To explore the potential benefit of the sliding-window approach when applied to SPARKLING fMRI data, a simulation study where the ground truth is controlled was conducted. This study serves as a demonstration designed to showcase to which extent it is possible to detect high-frequency oscillations in BOLD and disentangle physiological noise, such as breathing, from neural activity using a sliding-window reconstruction. To maintain computational simplicity and a clear demonstration, BOLD fMRI data was simulated in 2D using 2D-SPARKLING and the following pipeline (Fig. 7.1), partially implemented using modules from [CVC24]:

(A) Highly temporally-resolved simulated neural activity: Two types of neural events were convolved with the Glover HRF to produce the ground truth or reference for slow and fast BOLD responses at a temporal resolution of 0.1s and for a total

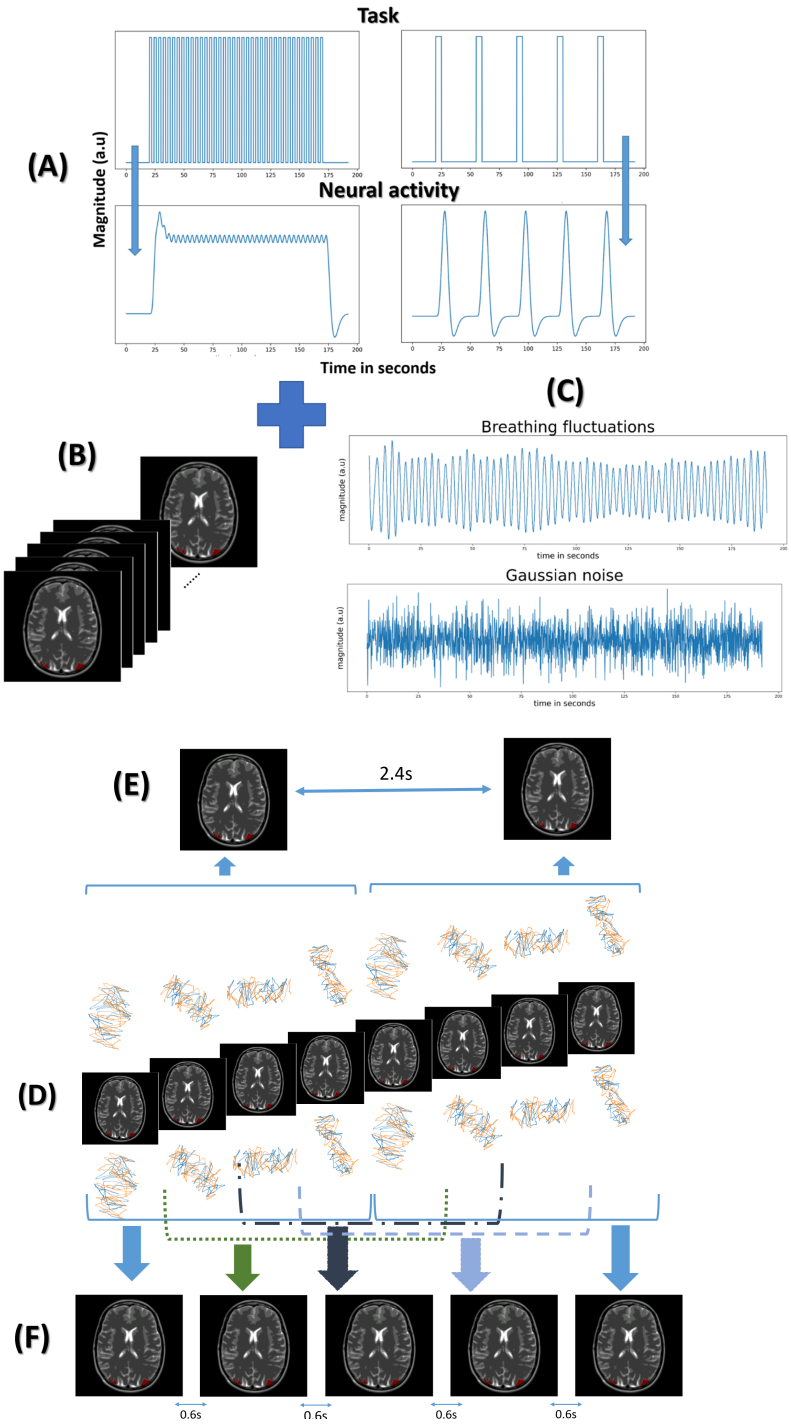

Figure 7.1: fMRI Simulation pipeline: Highly temporally-resolved **(A)** simulated neural activity, **(B)** reference of 2D fMRI frames (The maximum intensity change due to **(A)** is defined as 5% of the baseline magnitude) and **(C)** physiological and thermal noises. **(D)** Retrospective k-space sampling: SPARKLING sampling pattern is used in a scan-and-repeat mode. **(E)** Sequential and **(F)** Sliding-window fMRI image reconstruction at TR_{native} and TR_{eff} respectively.

duration of 192s. The neural events (tasks) are defined as on/off blocks with varying duration (T_{on}/T_{off}) as shown in Fig. 7.2.

– Slow BOLD responses are emulated using T_{on}/T_{off}=5/30s illustrating a simple

block design paradigm that exhibits some transient phases despite inducing a low-frequency content response. It can be executed experimentally using an audio, visual, or motor task.

– Four sub-types of fast BOLD responses were emulated using T_{on}=T_{off}=2s (respectively, 1.2s,1s,0.8s) corresponding to BOLD oscillations at 0.25Hz (respectively, 0.416Hz, 0.5Hz, 0.625Hz). These portray instances of incrementally increasing frequencies of stimulus-induced and controlled BOLD oscillations. An experimental implementation can be accomplished through a flickering checkerboard with a luminance that oscillates around the frequency of interest following the paradigm proposed in [Lew+16].

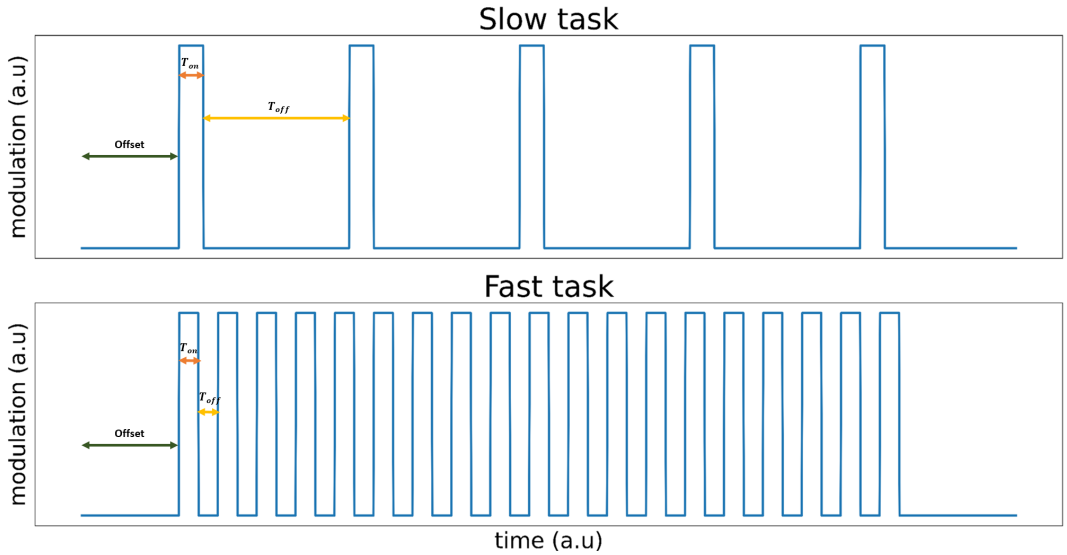

Figure 7.2: Schematic view of the tasks used to generate slow and fast BOLD responses.

(B) Highly temporally-resolved ground truth of 2D fMRI frames: The BOLD responses in **(A)** are used to modulate the magnitude of the pixels of a chosen region of interest (ROI) in a sequence of a 2D (1mm^2 and (192×192)mm^2 FOV) numerical brain phantom [Gue+12]. The ROI comprises 137 pixels in the visual cortex (red ROI in Fig 7.2 **(B)**) and was defined manually.

(C) Highly temporally-resolved physiological and thermal noises: Gaussian noise and/or breathing fluctuations that occur around 0.3Hz are emulated over all voxels in the 2D sequence of frames defined in **(B)**. A given SNR is chosen and translated directly into the tSNR (numerical phantom). The maximum intensity change due to breathing fluctuations is defined as 0.2% of the baseline magnitude.

(D) Retrospective k-space sampling: The k-space data is synthesized by sampling each 2D frame using two consecutive shots (from a complete sampling pattern of N_{shot} shots), meaning at a pace of 0.1s since each shot corresponds to $TR_{shot} = 50ms$. Therefore, every $\frac{N_{shot}}{2}$-period spaced reference frames are sampled using the same trajectories[1].

(E) Sequential fMRI image reconstruction at the native TR (TR_{native}) The k-space data generated in **(D)** is gathered to form N_{shot}-shot blocks. Then, each N_{shot}-shot block of k-space data is used to reconstruct a single frame using a simple zero-filled adjoint. We opted for a zero-filled adjoint reconstruction because of the substantial number of shots used in our 2D acquisitions which ensures good image quality even

[1]As an illustrative example, when considering N_{shot}=48, it implies that the trajectories for sampling the first, 24th, 48th frames, and so on, are identical.

without resorting to a CS-based reconstruction. Moreover, the adjoint method is faster than a CS-based reconstruction. Additionally, it helps minimize the introduction of nonlinearities to the signal caused by the CS reconstruction, particularly when combined with the sliding-window approach at this stage of the demonstration.

(F) Sliding-window fMRI image reconstruction at the effective TR (TR_{eff}): A sliding-window approach of width and stride of N_{shot} and $\frac{N_{shot}}{4}$ shots, respectively, is used to reconstruct consecutive frames from overlapping k-space data. A simple zero-filled adjoint is also used.

7.2.2 Evaluation metrics

To study the ability to detect high-frequency oscillations in BOLD, two cases of (TR_{native}, TR_{eff}) were considered, namely (2.4s, 0.6s) and (1.2s, 0.3s) corresponding to N_{shot}=48 and 24, respectively. This was done to study any potential interaction between the TR_{native} and using SPARKLING in a scan-and-repeat mode. Such a large number of shots (and therefore TR_{native}) is not necessary for a single MRI slice and reflects more of a 3D acquisition setup. Here, however, we chose to proceed in 2D for the sake of simplicity, computational efficiency, and demonstration. Only BOLD oscillations that occur at 0.25Hz were studied when using TR_{native}=2.4s and TR_{eff}=0.6s, whereas, four cases of progressively increasing frequencies (0.25Hz, 0.416Hz, 0.5Hz, 0.625Hz) were explored when using TR_{native}=1.2s and TR_{eff}=0.3s. An effective temporal resolution of 0.6s and 0.3s enables sampling oscillations up to 0.833Hz and 1.2666Hz, respectively. Therefore, the selected values of TR_{eff} are sufficient for the detection of the frequencies that were simulated in the BOLD signal. The ability to detect high-frequency oscillations was then assessed qualitatively for an infinite SNR and an SNR=100 (leading to a (maximal *in vivo*) realistic tSNR according to [TRW11]) by visualizing the time courses of the BOLD responses as well as their power spectra. To achieve this and tackle the increasing difficulty of distinguishing BOLD oscillations within thermal noise as their frequencies increase (resulting in lower magnitudes), a spatial average of the pixel-wise BOLD response is computed within the earlier mentioned ROI.

- TR_{native}=1.2s, TR_{eff}=0.3s, 0.416 Hz-oscillating BOLD response, SNR=100: 5 different occurrences of the simulation were generated (a total of 3185 images were reconstructed using the sliding-window approach) and the BOLD responses were also averaged across those occurrences, and

- TR_{native}=1.2s, TR_{eff}=0.3s, 0.5 Hz-oscillating BOLD response, SNR=100: 20 different occurrences of the simulation were generated (a total of 12740 images were reconstructed using the sliding-window approach), and the BOLD responses were also averaged across those occurrences.

While only signal fluctuations due to breathing will be captured using TR_{eff}=0.6s, TR_{eff}=0.3s, ensure that both signal fluctuations due to breathing and heartbeat are captured. However, here, we only consider breathing. Therefore, the ability to disentangle physiological noise from neural activity was investigated for a single case, namely, TR_{native}=2.4s and TR_{eff}=0.6s. Neural activity was emulated using a slow-dynamic BOLD response, and realistic breathing fluctuations occurring around 0.3Hz were added. The time courses of the BOLD responses and their power spectra in a single activated pixel were visualized.

7.3 Results

7.3.1 Ability to detect high-frequency oscillations in the BOLD response

Fig. 7.3 demonstrates that it is possible to track BOLD fluctuations that occur at 0.25Hz for an SNR=100 by using the sliding-window approach to reduce a TR_{native}=2.4s down to TR_{eff}=0.6s. However, the zoomed-in ROI in Fig. 7.3 **(C)** demonstrates how the sliding-window approach brings in an artifactual frequency around 0.416Hz corresponding

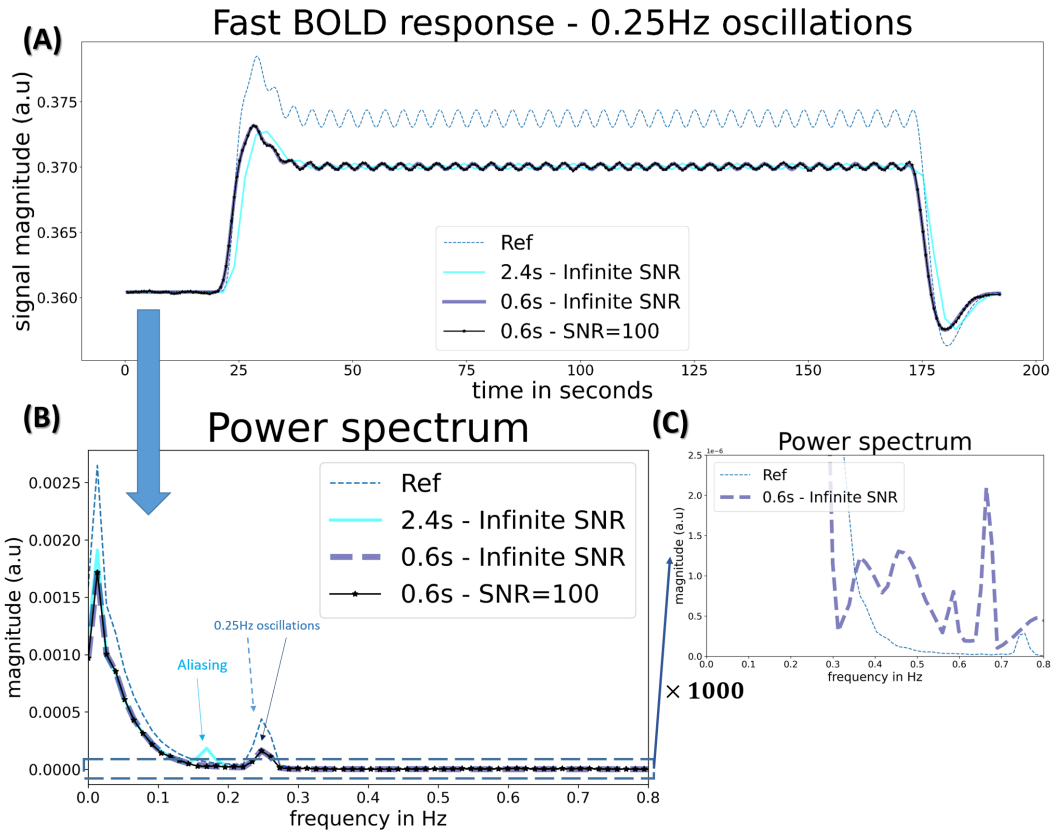

Figure 7.3: (A) Time courses (averaged over the ROI and one occurrence of the simulation), and corresponding (B) full-scale and (C) zoomed-in power spectra of a reference fast BOLD response vs. those estimated from simulation data (assuming an infinite SNR and SNR=100) and using a sequential (resp., sliding-window) reconstruction at a $TR_{native} = 2.4s$ (resp., $TR_{eff} = 0.6s$).

to $\frac{1}{TR_{native}} = \frac{1}{2.4}$. While the amplitude of such an artifactual frequency is very limited, it remains susceptible of interacting with BOLD oscillations in the same frequency interval and, potentially impeding the efficacy of their detection, notably when those higher-frequency BOLD oscillations are also characterized by small amplitudes. Opting for TR_{native}=1.2s shifts this artifactual frequency around 0.833Hz ($\frac{1}{TR_{native}} = \frac{1}{1.2}$), hence providing more flexibility in the range of easily detectable frequencies.

Fig. 7.4 shows three scenarios of fast BOLD responses (oscillations occurring at 0.25Hz, 0.416Hz, and 0.5Hz) for an infinite SNR. It is worth noting that as the oscillations frequency increases, their amplitudes are highly attenuated. This trend is consistently observed, including in the reference plot, and is due to the convolution with the Glover HRF. Secondly, while the time courses obtained with TR_{eff}=0.3s are more temporally resolved for 0.25Hz and 0.416Hz than those obtained with TR_{native}=1.2s, the latter still proves sufficient for detecting these oscillations, 0.416Hz being the detectable limit. The 0.5Hz oscillations, however, remain undetectable with TR_{native}=1.2s but becomes discernible with TR_{eff}=0.3s.

These observations are further backed by Fig. 7.5 **(A)**. Oscillations that occur at 0.5Hz and 0.625Hz are aliased in the TR_{native}=1.2s-reconstructed data (since this TR_{native} provides up to 0.416Hz frequency resolution) but become detectable in TR_{eff}=0.3s-reconstructed data despite being exponentially attenuated as the frequency increases. Fig. 7.5 **(B)** confirms the existence of an artifactual frequency around 0.833Hz. Studying the more realistic case of SNR=100 in Fig. 7.6, we observed that a single occurrence of the simulation is sufficient to detect 0.25Hz oscillations from the thermal noise. However, 5 occurrences (respectively, at least 20 occurrences) are required to identify 0.416Hz (respectively, 0.5Hz) oscillations in the BOLD signal. This number is expected to be significantly larger for 0.625Hz.

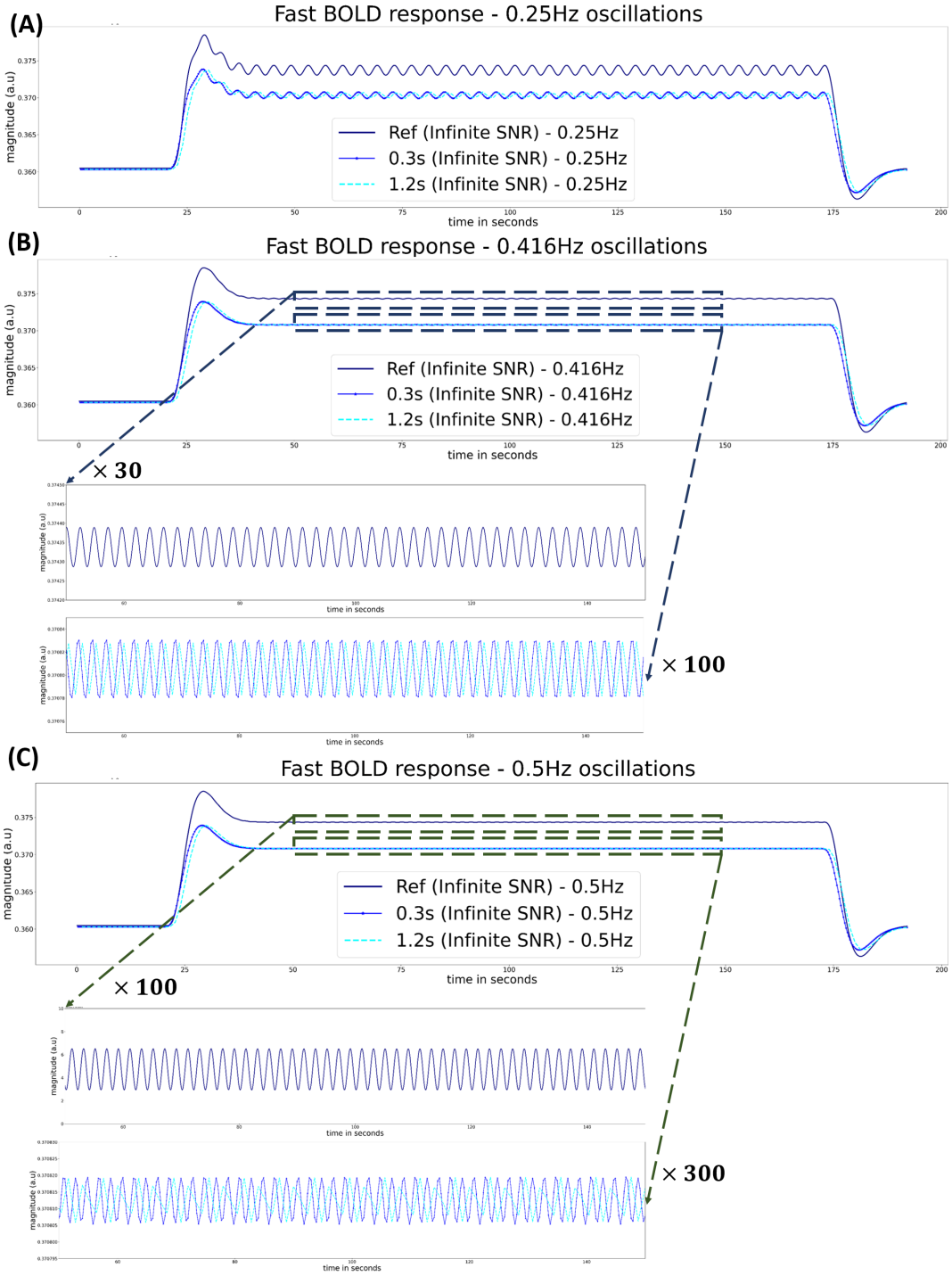

Figure 7.4: Time courses of the reference BOLD response vs. those estimated from simulation data (assuming an infinite SNR) using a sequential (resp., sliding-window) reconstruction at a $TR_{native} = 1.2s$ (resp., $TR_{eff} = 0.3s$). Three scenarios are illustrated, namely **(A)** 0.25Hz- **(B)** 0.416Hz- and **(C)** 0.5Hz-oscillating BOLD responses (averaged over the ROI and, respectively, 1, 5, and 20 occurrences of the simulation). As the temporal dynamics become faster, the sliding-window approach becomes more relevant as it allows for a better temporal segmentation of the signal.

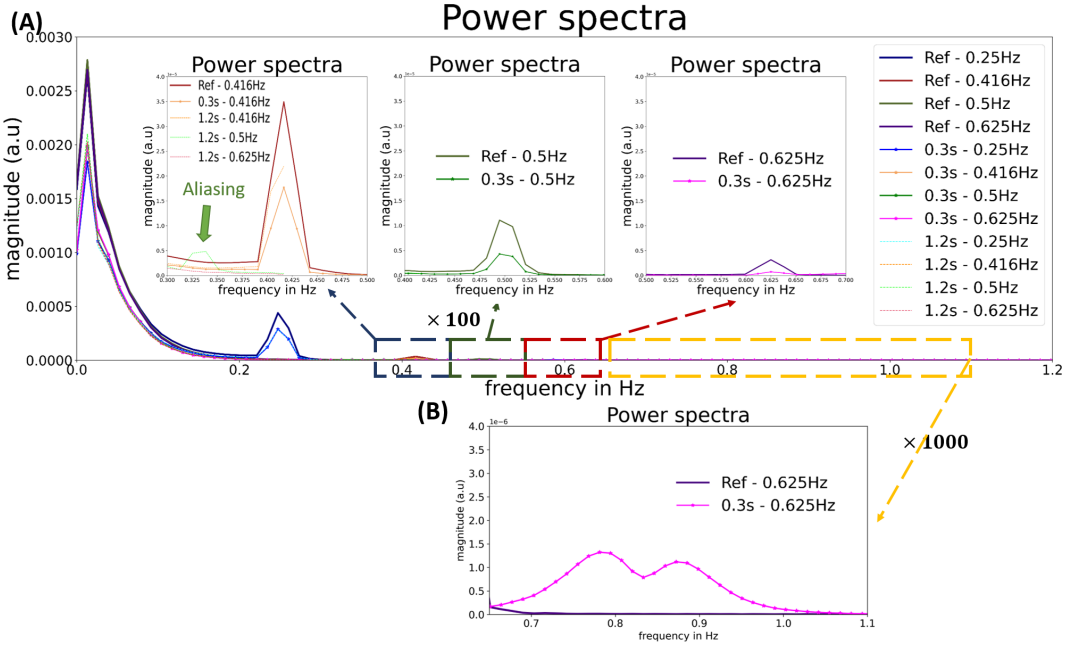

Figure 7.5: **(A)** Power spectra of the reference BOLD response vs. those estimated from simulation data (assuming an infinite SNR) and using a sequential (resp., sliding-window) reconstruction at a $TR_{native} = 1.2s$ (resp., $TR_{eff} = 0.3s$). Four scenarios are illustrated, namely, 0.25Hz-, 0.416Hz-, 0.5Hz-, and 0.625Hz-oscillating BOLD responses. **(B)** Zoomed-in [0.65Hz, 1.1Hz] interval illustrating an artifactual frequency due to the use of the sliding-window approach.

7.3.2 Ability to disentangle physiological noise from neural activity

The time courses of the reconstructed BOLD responses for TR_{native}=2.4s and TR_{eff}=0.6s at infinite SNR shown in Fig. 7.7 illustrate how choosing a TR_{eff}=0.6s enables a better definition of the transient phases. Furthermore and most importantly, Fig. 7.7 shows that it's possible to effectively resolve and separate physiological noise from neural activity using the sliding-window technique. Such a feature is useful as it would decrease spurious correlations due to physiological noise in both task-based and resting-state fMRI data. A TR_{eff}=0.3s (dividing the TR_{native}=2.4s by 8) is enough to be able to disentangle heartbeat from neural activity. Achieving a TR_{eff}=0.3s instead of 0.6s starting from a TR_{native}=2.4s is straight forward by choosing a stride = $\frac{TR_{native}}{8}$

7.4 Discussion

This chapter investigated the benefits of a sliding-window reconstruction in SPARKLING fMRI data through a 2D simulation study where the inputs and ground-truths were controlled. As far as we know, we are the first to conduct such a study with controlled inputs and simulation data to thoroughly identify the capabilities and limits of this method.

7.4.1 Main findings

We demonstrated that a sliding-window reconstruction method allows for tracking BOLD oscillations above 0.1Hz and disentangling physiological noise from neural activity at realistic SNR/tSNR in 2D.

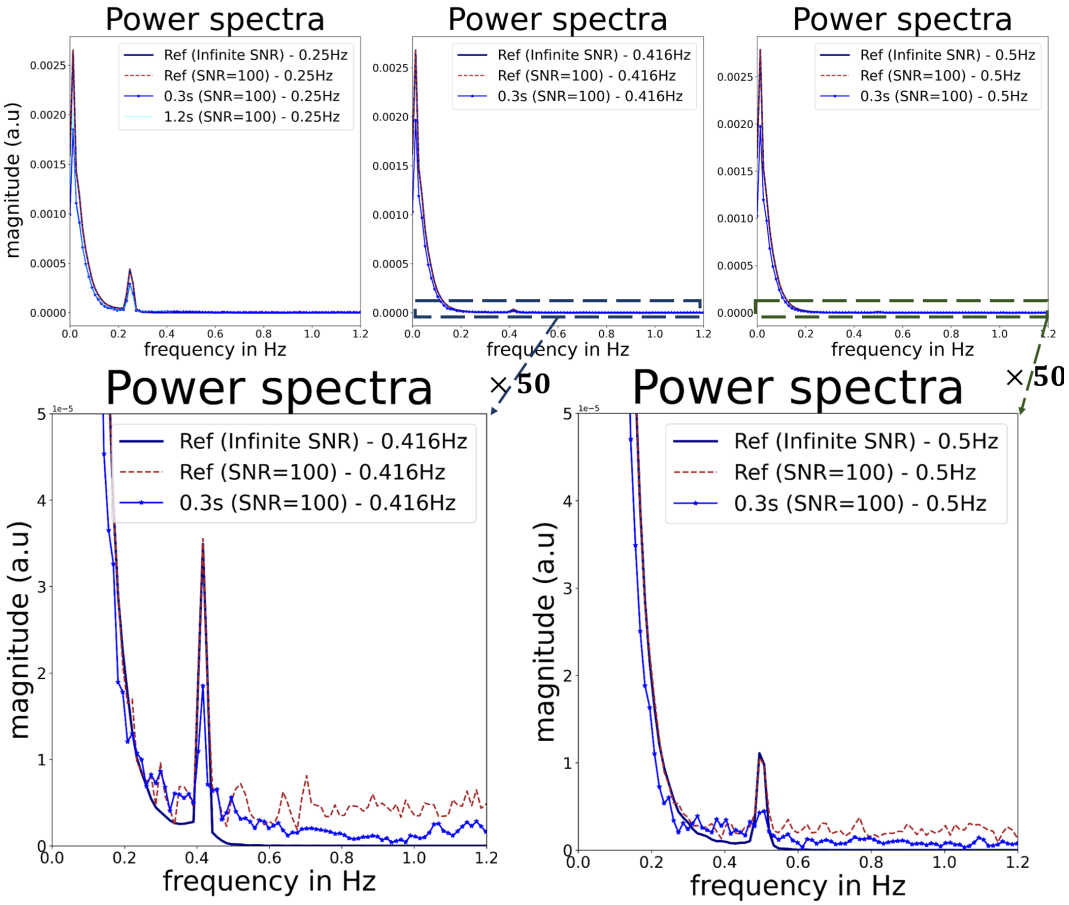

Figure 7.6: Power spectra of the reference BOLD response vs. those estimated from simulation data (assuming SNR=100) and using a sequential (resp., sliding-window) reconstruction at a $TR_{native} = 1.2s$ (resp., $TR_{eff} = 0.3s$). Three scenarios are illustrated, namely, 0.25Hz-, 0.416Hz-, 0.5Hz-oscillating BOLD responses. The cases of oscillations occurring at 0.416Hz and 0.5Hz are zoomed-in.

7.4.2 Barriers for detecting high-frequency oscillations in BOLD response

As neural events become faster, the convolution with the conventional HRF model [Fri+95] is expected to produce highly attenuated oscillations in the BOLD response that can be easily drowned in thermal noise. Therefore, the noise barrier becomes more limiting due to the exponential decrease in the amplitudes of these oscillations. Accumulating multiple repetitions and averaging through them can help better identify these oscillations. However, depending on the amplitudes of these oscillations, and given that a higher SNR/tSNR (beyond 100) is hardly achievable, longer scan times and/or a larger number of repetitions may still be needed. Moving to higher fields (e.g., 11.7T) is also an alternative to ensure higher sensitivity to these BOLD oscillations. In [Lew+16], the authors demonstrated that fast BOLD oscillations detected *in vivo* have higher amplitudes than those expected theoretically. Thus, the noise barrier for detecting such oscillations *in vivo* should be less constraining than the theoretical one.

Our findings also suggest that, as long as SPARKLING is used in a scan-and-repeat mode, TR_{native} and therefore N_{shot} should be chosen carefully. In fact, the presence of artifactual frequencies due to the periodic cycling of the sampling pattern when using the sliding-window approach can also hinder the efficacy of identification of BOLD oscillations that occur around $\frac{1}{TR_{native}}$ if they are characterized by amplitudes of the same order of magnitude (or lower) than those of the artifactual frequencies. However, this constraint can also be relaxed if

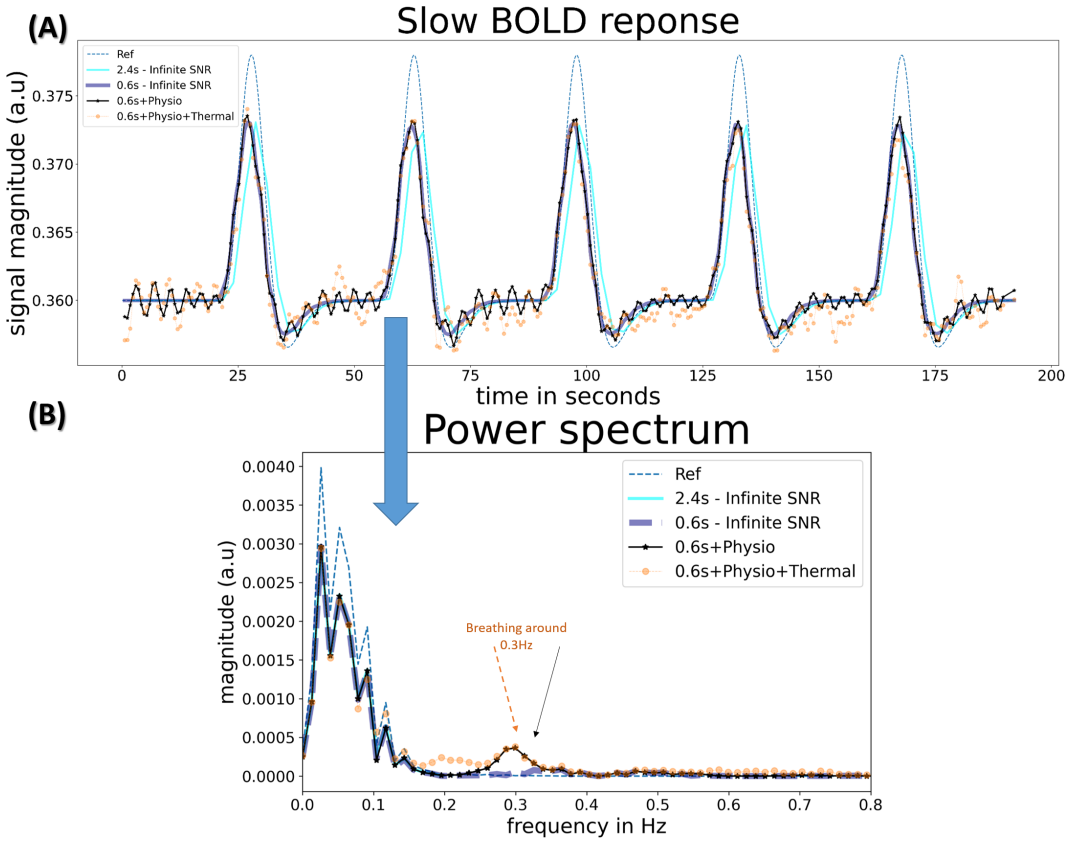

Figure 7.7: **(A)** Time courses in a single activated voxel, and **(B)** corresponding power spectra of a reference slow BOLD response vs. those estimated from simulated data (assuming an infinite SNR and accounting for physiological and/or thermal noises [SNR=100]) using a sequential (resp., sliding-window) reconstruction at a $TR_{native} = 2.4s$ (resp., $TR_{eff} = 0.6s$).

the BOLD oscillation amplitude is effectively larger *in vivo* compared to the theory. One of the alternatives used in this work to partially alleviate this issue is to reduce TR_{native} by reducing N_{shot}, ensuring a larger range of easily detectable BOLD frequencies. However, such a strategy (i.e., reducing N_{shot}) would impact the effective spatial resolution. To avoid this, using faster gradients [Fei+23] can be an alternative to ensure a reduced TR_{native} without changing N_{shot}. Finally, considering a continuously changing sampling pattern throughout the acquisition (i.e., extended 3D-SPARKLING into 4D, where the sampling patterns change from one volume to the next) is expected to solve this issue as it avoids any cycling period when using the sliding-window reconstruction. However, it is also expected to bring new challenges, such as maintaining the same PSF during the acquisition process.

7.4.3 Extension to 3D imaging and perspectives

While the sliding-window strategy can be extended straightforwardly in its implementation to accommodate 3D imaging, the effective spatial resolution and SNR/tSNR will most certainly differ from the 2D case studied in this chapter. Nevertheless, even after accounting for these potential variations and how they impact the constraints of detecting high-frequency BOLD oscillations, extending the sliding-window strategy into 3D is likely to open a new door to whole-brain high spatiotemporal resolution fMRI: Contrary to most current attempts to achieve high temporal resolution, extending the sliding-window to 3D imaging would allow acquiring high temporal resolution fMRI data without sacrificing brain coverage [Lew+16; Rai+21; Rai+23] or compromising spatial resolution [Ley+21; Bia+22]. Such a feature is valuable for resting-state fMRI or new cognitive neuroscience studies about naturalistic high-level cognitive processes where the brain regions involved in the task are not fully identified

yet. That is why it is crucial to start by validating the findings of this 2D simulation study through *in vivo* experiments in 3D fMRI. Subsequently, this will pave the way to explore new research avenues. Furthermore, extending the sliding-window approach in 3D should be ideally accompanied by a 4D-SPARKLING implementation where instead of being used in a scan-and-repeat mode, as explained earlier. Nevertheless, implementing this at the current stage poses challenges, particularly in maintaining a consistent PSF across all consecutive volumes, as stated earlier.

The gain in temporal resolution through the sliding-window approach can be instrumental in revisiting the HRF model as well. The example of the BOLD response shown in Fig. 7.7 can actually be used for such an endeavor. Furthermore, re-exploring topics such as the existence of the initial dip and its dependence on the brain region or task performed would be possible. In a recent study [Nag+22], the HiHi fMRI method was applied to 2D (EPI) imaging, aiming to improve the temporal resolution by reshuffling the data in the image domain. The data collected and analyzed by the authors revealed the presence of the initial dip only in the visual response, while it was absent in the motor one. In a broader sense, refining the delimitation of the HRF holds high significance not only to advance fundamental neuroscience (gain a deeper understanding of the underlying BOLD mechanism, for instance) but also for the clinical applications where differences in the HRF profiles can serve as biomarkers for some neuro-degenerative pathologies.

The fact that we are able to separate physiological noise from neural-induced fluctuations with the sliding-window approach is also expected to yield an accurate estimation of the neural-induced intensity fluctuations in fMRI data. Coupled with the systematically enhanced temporal resolution achieved through refined sampling at a short effective TR (TR_{eff}), this is expected to produce finer profiles of these fluctuations, thanks to the increased number of effective sampling points. Ultimately, in task-based fMRI, this is expected to contribute to higher statistical power during the analysis step. This reasoning is not limited to tasks that induce fast BOLD responses but also encompasses those that induce slow BOLD responses. Additionally, once the physiological fluctuations are extracted from the neural activity, we can either filter them out and/or include them as additional regressors in the GLM, further improving the robustness of the analysis. A recent paper [RMS22], applied the sliding-window approach to radial EPI BOLD fMRI acquisitions for a T_{on}=T_{off}=20s block-design visual paradigm, despite the fact that the paradigm the authors used was very slow. The authors demonstrated higher sensitivity and specificity with this method for detecting evoked brain activity compared to a classical sequential reconstruction. Nevertheless, when overlapping k-space data across consecutive reconstructed MR volumes, the sliding-window approach induces additional autocorrelation in the reconstructed fMRI signal. This can have drawbacks, particularly contingent on the degree and structure of autocorrelation induced and whether it can be corrected using standard autoregressive models or not. This particular aspect still needs to be carefully characterized. A first preliminary test of the viability and behavior of the sliding-window approach on *in vivo* 3D-SPARKLING fMRI data was performed using the already collected retinotopic mapping data. The results and limitations that emerge for *in vivo* conditions such as motion are discussed in Appendix C.

7.5 Conclusion

This simulation-based work demonstrates that a sliding-window reconstruction method allows for the tracking of BOLD oscillations beyond 0.1Hz and disentangles physiological noise from neural activity at realistic SNR/tSNR in 2D. The simulations were conducted in 2D for the sake of computational efficiency and reduced computational load, as conducting them directly in 3D would have been time-consuming and resource-intensive. The implementation of such a strategy can be extended to 3D imaging in a straightforward manner and applied to sampling strategies other than 3D-SPARKLING. Furthermore, the findings uncovered in this chapter are expected to hold for other sampling techniques. That being said, it is crucial to validate the sliding-window approach for *in vivo* 3D SPARKLING fMRI to corroborate the findings from the simulations. Indeed, within an *in vivo* framework, various challenges

emerge, with motion being a notable factor that can hinder the effectiveness of the method, particularly when it accumulates over consecutive volumes due to shared k-space data.

* * *
* *
*

Chapter 8

General conclusions and perspectives

During this thesis, 3D-SPARKLING was employed for the first time in fMRI. It was evaluated against the state-of-the-art 3D-EPI according to an exhaustive list of qualitative and quantitative criteria on a cohort of six healthy volunteers. After observing higher sensitivity to static and dynamic magnetic field imperfections in 3D-SPARKLING data, we established an experimental protocol to correct them. The benefits of this correction were quantified in terms of image quality, tSNR, and BOLD sensitivity over a cohort of three healthy participants. Finally, we explored the potential benefit of the sliding-window image reconstruction approach when applied to SPARKLING fMRI data. A simulation study was conducted and demonstrated the possibility of detecting high-frequency oscillations in BOLD and separating physiological noise from neural activity.

8.1 Contributions and limitations

The initial endeavor of this Ph.D. work was to evaluate 3D-SPARKLING, in a scan-and-repeat mode, as a viable encoding scheme for high spatial resolution (1mm^3) whole-brain fMRI. The temporal resolution was 2.4s. This evaluation involved a comparison with the state-of-the-art 3D-EPI in resting-state and retinotopic mapping experiments conducted on a cohort of six healthy volunteers. A subjectwise analysis revealed that 3D-SPARKLING performed competitively with 3D-EPI in detecting evoked brain activations. However, we observed that 3D-SPARKLING was more penalized by $\mathbf{B}_0$ imperfections than 3D-EPI, leading to degraded image quality. To address this issue, we implemented an experimental protocol utilizing a field camera to monitor magnetic field fluctuations. These external measurements, along with a static ΔB_0 map, were then used to correct both static and dynamic $\mathbf{B}_0$ imperfections during MR image reconstruction. The results demonstrated clear benefits regarding image quality, tSNR, and BOLD sensitivity. Nevertheless, incorporating the static term in the reconstruction problem turned it into a non-Fourier model, extending the reconstruction time. To mitigate this challenge, we opted for a parallel implementation on a supercomputer, significantly speeding it up. However, it is worth noting that accessibility to such powerful supercomputing resources remains a limitation. Moreover, while our protocol is expected to correct breathing-induced field fluctuations effectively, it currently does not address head movement, representing a remaining limitation. Finally, we studied the capabilities and

limitations of employing a sliding-window reconstruction technique in combination with the SPARKLING encoding scheme for fMRI to retrospectively enhance temporal resolution during image reconstruction and detect rapid oscillations in BOLD responses. This was performed through a simulation study where the ground truth is controlled. This study serves as a demonstration to showcase to which extent it is possible to detect high-frequency oscillations in the BOLD signal and disentangle physiological noise, such as breathing, from neural activity using a sliding-window reconstruction. To maintain computational simplicity and clear demonstration, BOLD fMRI simulation data was generated in 2D using 2D-SPARKLING. The corresponding implementation can be extended quite straightforwardly for 3D fMRI, enabling high spatiotemporal resolution for large brain coverage while keeping a sufficient SNR. However, the findings of the 2D simulations need to be further validated *in vivo* and in 3D, where additional challenges, such as motion (that would be accumulated over several consecutive volumes due to the sharing of data), can hinder the efficacy of the method.

8.2 Perspectives

Beyond 3D-SPARKLING

In this work, 3D-SPARKLING [Cha+22] was used for the first time to acquire fMRI data. A recent implementation introduced an updated version of SPARKLING, named MORE-SPARKLING [Cha+23], specifically designed to minimize static off-resonance effects. However, an assessment of its effectiveness in mitigating $\mathbf{B}_0$ imperfections in highly accelerated acquisitions, such as within the fMRI framework, is yet to be conducted. Moreover, 3D-SPARKLING was used in a scan-and-repeat mode. However, it can be further extended into 4D, where the sampling pattern changes from one volume to the next. This would enforce, in addition to the sparsity in space, temporal sparsity as well. In that case, 'low rank plus sparse' image reconstruction methods or local low-rank denoising techniques [Com+23] could also be instrumental in obtaining high-quality fMRI images. A more distant (and still highly theoretical) rationale would entail refining the 4D k-space sampling pattern according to the task at hand and collecting the spatial frequencies over time that effectively capture the most crucial BOLD information.

Speeding up the non-Fourier reconstruction

In this work, the reconstruction of each full-time series was run on the Jean Zay cluster where every five volumes were parallelized over a single Nvidia V100 GPU, allowing the reconstruction of the full time series in a few hours (3 to 8 depending on the number of GPUs available). On more accessible hardware, the reconstruction time is longer:

1. A local cluster with 4 GPU nodes would enable the reconstruction of one fMRI time series in about one day.

2. On a standard machine that has a Quadro RTX 8000 GPU and Intel Xeon Silver 4214 CPU @2.20GHz (12 cores and 24 threads) and using a simple embarrassingly parallel pipeline by launching six reconstructions at once using joblib[1], the reconstruction time is of about 4 days.

Following the recent in-house developments [2] and further optimizing the NUFFT operator implementation[3] in 3D can help to reduce the reconstruction time in the future. Furthermore, the reconstruction algorithm currently has many GPU/CPU transfers due to the lack of GPU implementation of the wavelet transform. If the latter was available, such transfers would be significantly reduced, hence the reconstruction time would be much shorter. These issues will be handled in the near future. Furthermore, deep learning-assisted implementations [Dav+23]

[1] https://joblib.readthedocs.io/en/stable/
[2] https://github.com/mind-inria/mri-nufft
[3] https://github.com/flatironinstitute/cufinufft

can be utilized to reduce the reconstruction time when static magnetic field inhomogeneities correction is involved.

Dynamic (4D) $\mathbf{B}_0$ imperfections monitoring and motion correction

In this work, we demonstrated the benefit of correcting $\mathbf{B}_0$ imperfections in 3D-SPARKLING fMRI data. While we simplify the model by treating static and dynamic field terms as evolving independently, an easily implementable and sufficiently accurate approximation, it deviates from the true MR physics. A more faithful representation would involve considering static and dynamic magnetic field imperfections as evolving jointly, i.e., a ΔB_0 map would be estimated for each volume. While we can imagine using 3D-SPARKLING in a self-navigating fashion for this purpose, the currently available method [Dav+22] does not return accurate estimates for highly accelerated 3D-SPARKLING fMRI acquisition. An alternative approach involves leveraging the Skope field camera system to estimate a very low-resolution dynamic ΔB_0 map. Indeed, the measurements obtained from the 16 probes can be employed in a source detection approach, resembling methods used in EEG or MEG, to have a very coarse spatial estimate of the field inhomogeneities and their temporal evolution over the imaging FOV, leading to a series of very low-resolution ΔB_0 maps. These very low-resolution maps could then be utilized to update the static ΔB_0 map acquired using a moderate spatial resolution multi-echo GRE sequence.

In addition, head movements should also be accounted for. Following a similar approach as suggested in [Gra+17], 3D-SPARKLING can be independently used to estimate motion parameters and correct the k-space data at the reconstruction step. It is worth noting, however, that this entails estimating motion parameters for each block of shots and applying them collectively to each block rather than on a shotwise basis. Methods that rely on orbital navigators, as proposed in [URP23], can be integrated into 3D-SPARKLING to enable shotwise motion estimation with minimal impact on acquisition time. Initially, a retrospective correction based on these estimations should be implemented. Subsequently, a prospective solution for 3D-SPARKLING can be envisioned.

Evaluation of the sliding-window approach with *in vivo* 3D-SPARKLING data

The 2D simulations conducted demonstrated that it is possible to significantly enhance temporal resolution in SPARKLING fMRI data through sliding-window reconstruction. The corresponding implementation can be extended quite straightforwardly for 3D fMRI, enabling high spatiotemporal resolution for large brain coverage while keeping a sufficient SNR. However, the findings of the simulations need to be further validated *in vivo* and in 3D. In fact, *in vivo* settings introduce additional challenges, such as motion (that would be accumulated over several consecutive volumes due to the sharing of data), which can hinder the efficacy of the method. Moreover, induced signal autocorrelation due to the sliding-window reconstruction technique should be considered in the statistical analysis. Once initial validation is conducted, and signal autocorrelation correction measures are implemented, this method can be extended to address more complex neuroscience inquiries, such as new cognitive neuroscience studies that delve into naturalistic high-level cognitive processes or better characterize the HRF.

3D-SPARKLING fMRI at 11.7T

At 11.7T, 3D-SPARKLING fMRI is expected to benefit from increased tSNR and tCNR. However, addressing $\mathbf{B}_0$ imperfections presents a more challenging task, and the correction pipeline we have established (or a potentially improved version) is expected to be crucial. Furthermore, while $\mathbf{B}_1^+$ heterogeneities were not serious at 7T, they will need to be addressed at 11.7T, necessitating a parallel transmission (pTx) implementation of 3D-SPARKLING using universal pulses [Gra+16], for instance.

Overall, SPARKLING stands out as a promising technique for fMRI. The fact that it samples the center of k-space with each shot opens up a wide range of possibilities for manipulations at the reconstruction step. The most critical among these is the retrospective

enhancement of temporal resolution, which can be instrumental in addressing diverse fundamental and clinical questions in neuroscience, such as the characterization of the temporal profile of the HRF and its spatial and task dependencies or more adequate spatiotemporal resolution for resting-state and high-level cognitive task fMRI.

* * *
* *
*

)

Appendices

Appendix A

Evaluation of 3D-SPARKLING fMRI against the state-of-the-art 3D-EPI

This is the appendix related to Chapter 5.

Nonlinear CS-based reconstructions can induce bias, and depending on the level of regularization, they may not guarantee the Gaussianity of the noise, which is an essential hypothesis as the GLM analysis is grounded on the Gaussianity of the residuals. In this work, the same regularization parameter (and, therefore, the same reconstruction algorithm) was used for all consecutive volumes. This means that any potential bias caused by nonlinear regularized reconstruction would be constant across all fMRI scans. Such a tendency would be captured by the baseline regressor in the design matrix, and the residual error distribution would remain centered. Additionally, as we used a moderate amount of ℓ_1 regularization, we showcase in the following that this does not strongly affect the Gaussianity hypothesis on the residuals of the GLM.

First, we compared the impact of three different reconstruction strategies on the statistical analysis, namely, the effect (β coefficients) captured by the baseline regressor (Figure A-1) and residual errors (Figure A-2) of the GLM-fitted 3D-SPARKLING fMRI time series collected in V#3. These three different strategies were chosen in order to disentangle the effect of nonlinear reconstruction due to sparse regularization from that of the regularization itself on top of the 3D SPARKLING encoding scheme:

a: The nonlinear regularized reconstruction using a ℓ_1-norm regularization in the wavelet domain ($\lambda = 10^{-8}$).

b: The linear regularized reconstruction using a squared ℓ_2-norm regularization in the wavelet domain (the regularization parameter $\lambda = 10^{-8}$). The wavelet basis chosen is `Sym8`, which is an orthogonal basis; therefore, even though the squared ℓ_2-norm is applied to the wavelet coefficients, the reconstruction remains linear.

c: The zero-filled adjoint Fourier reconstruction (no regularization, i.e. $\lambda = 0$).

Second, and specifically regarding the distributions of the residuals, we compared the results associated with 3D-SPARKLING to those associated with 3D-EPI and corresponding to the same volunteer (V#3).

Figure A-1**(A)** shows the maps of the voxel-wise difference of the β coefficients derived from the baseline regressor in the GLM and associated with 3D-SPARKLING data reconstructed using (a) to (c): After computing the β coefficient maps associated with the baseline regressor and each reconstruction strategy ((a) to (c)), the voxel-wise differences between these maps were computed, namely, $\beta_{\ell_1} - \beta_{\ell_2}$, $\beta_{\ell_1} - \beta_{noregu}$ and $\beta_{\ell_2} - \beta_{noregu}$. There are visible differences between the 3 maps. As we assume that reconstruction strategy (c) yields no bias as it's not regularized, these results suggest that the bias induced by the nonlinearity ($\beta_{\ell_1} - \beta_{\ell_2}$) is actually lower than that induced by the regularization ($\beta_{\ell_1} - \beta_{noregu}$ or $\beta_{\ell_2} - \beta_{noregu}$). In Figure A-1**(B)**, the histograms of these voxel-wise differences in β coefficients are plotted and confirm the above observations: As the distribution of these differences is narrower or

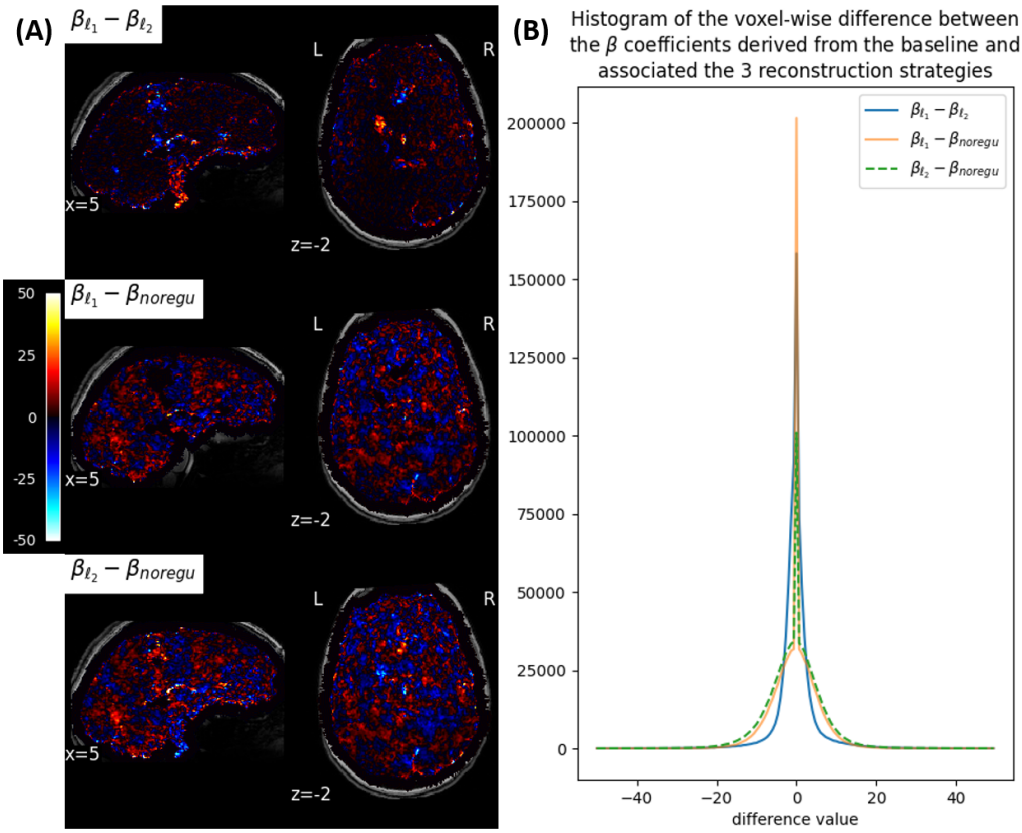

Figure A-1: **(A)**: Maps of the voxel-wise difference between the β coefficients derived from the baseline regressor in GLM analysis and associated with 3D-SPARKLING data reconstructed using (a) to (c) in V#3. **(B)**: Histograms of these maps.

tighter between the two regularized (linear versus nonlinear) reconstruction strategies as compared to the differences between the regularized and unregularized strategies, most of the bias is due to the regularization itself and not to its nonlinear aspect.

Figure A-2**(A)** shows the residual error maps associated with 3D-SPARKLING (reconstructed using (a)-(c) strategies) and 3D-EPI fMRI volumes. These maps were produced by averaging the temporal residual errors over the time dimension to obtain a global summary. The residual error seems centered around zero for the four datasets. Additionally, reconstruction strategy (c) results in more lost signal than (a) and (b) as the residuals reach higher values. Figure A-2**(B)** shows the histograms of the temporal residual error of the GLM-fitted fMRI volumes: Firstly, we spatially averaged the residual errors over the brain mask, then computed the temporal histograms[1]. The results associated with the four scenarios, namely the data acquired with 3D-SPARKLING and reconstructed using strategies (a)-(c) and those acquired with 3D-EPI, are reasonably similar. Despite small differences between the histograms associated with the reconstruction strategies (a)-(c), the distributions are centered around zero. Furthermore, the histograms associated with 3D-SPARKLING and reconstruction strategy (a) and those associated with 3D-EPI are quite similar and are spread alike around zero. Additionally, to obtain an objective measure of the similarity between these histograms and evaluate how tenable the hypothesis of the Gaussianity of the residuals is, a Kolmogorov-Smirnov (KS) test was performed between:

(i) The histograms associated with 3D-SPARKLING data and reconstruction strategies (a) and (b), respectively.

[1]The number of samples in the histograms is given by the number of scans.

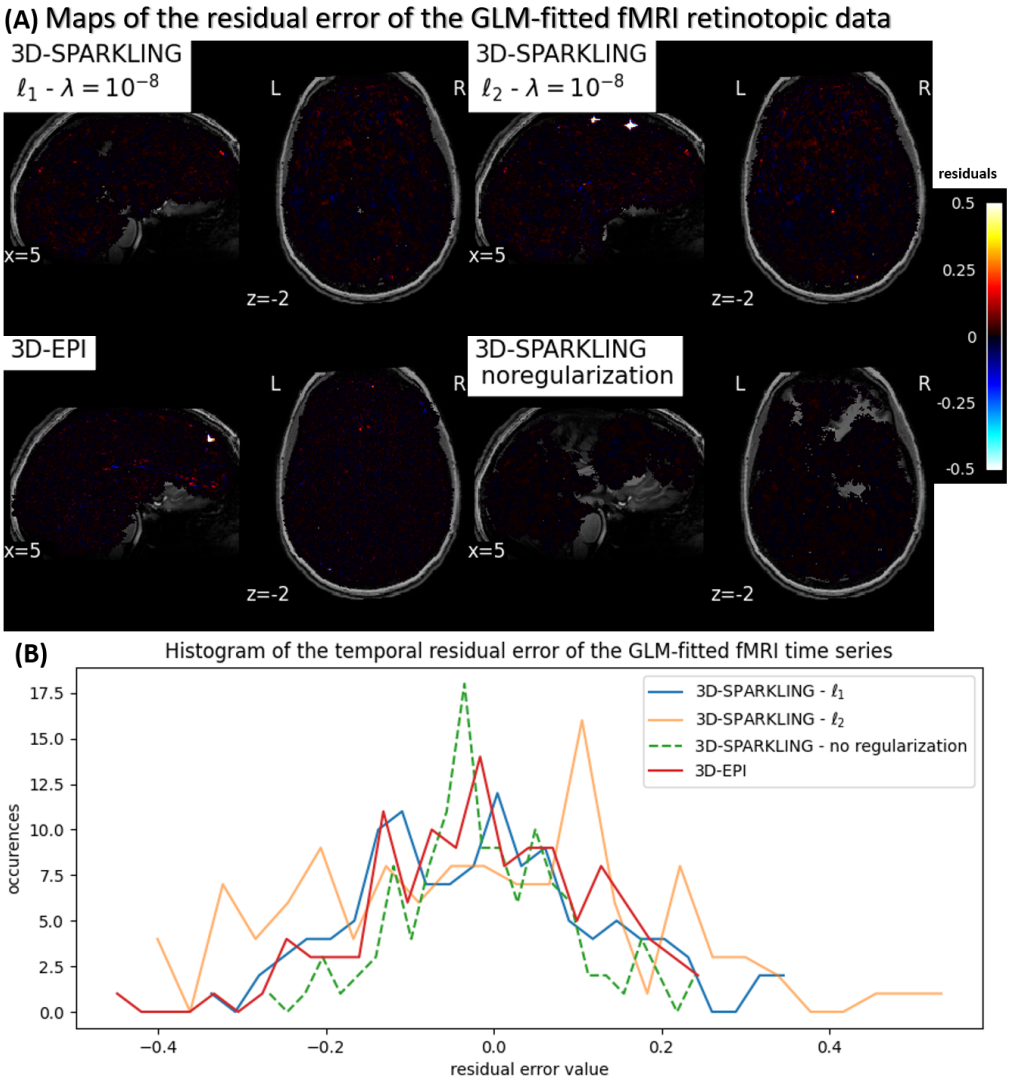

Figure A-2: **(A)** Maps and **(B)** temporal histograms of the residual error of the GLM-fitted retinotopic fMRI data associated with 3D-SPARKLING (reconstructed with strategies (a)-(c)) and 3D-EPI and collected in V#3.

(ii) The histograms associated with 3D-SPARKLING data and reconstruction strategies (a) and (c), respectively.

(iii) The histograms associated with 3D-SPARKLING data and reconstructed using (a) and those associated with 3D-EPI.

The null hypothesis (H_0) used is that the two distributions are identical, and the p-values were 0.18, 0.1, and 0.9 for (i), (ii), and (iii), respectively. This means that H_0 cannot be rejected and, therefore, that the distributions are significantly similar. We conclude that the hypothesis of Gaussianity remains tenable for 3D-SPARKLING data reconstructed with a CS-based reconstruction. This could be explained by the fact that the level of regularization performed was set to a reasonably good but low value.

Appendix B

Impact of B_0 field imperfections correction on BOLD sensitivity in 3D-SPARKLING fMRI data

These are the appendices related to Chapter 6.

B.1 Power spectra of physiological noise-induced field perturbations

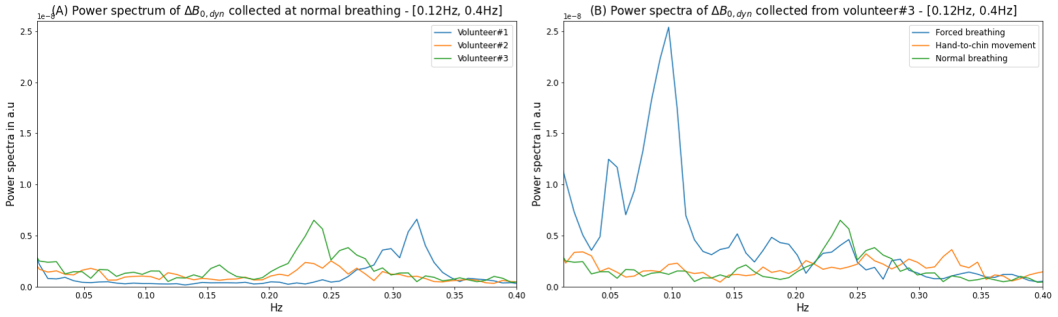

Figure B-1: (A) Power spectra of the $\Delta B_{0,dyn}$ term monitored during resting-state fMRI for the 3 volunteers and (B) for the volunteer#3 at the different physiological noise scenarios. Only the range [0.12Hz, 0.4Hz] is displayed to observe the fluctuations due to breathing.

B.2 Time course of motion regressors of the translation over the z-axis (estimated with SPM12) for volunteer#3 and the three physiological noise scenarios.

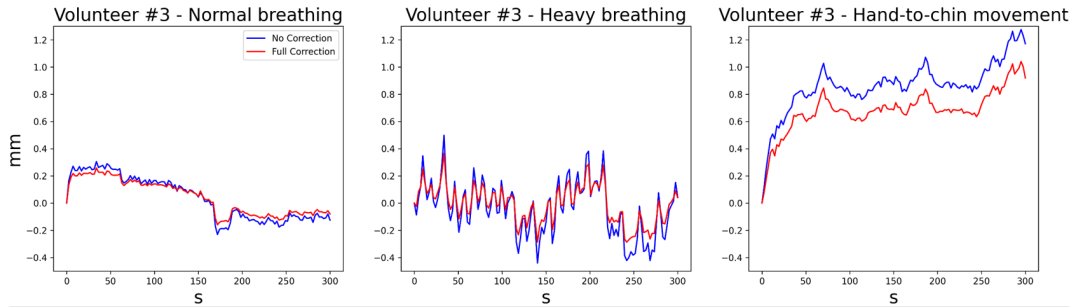

Figure B-2: Time course of motion regressors of the translation over the z-axis (estimated with SPM12) for volunteer#3 and the three physiological noise scenarios.

B.3 Time course of motion regressors of the translation over the z-axis (estimated with SPM12) for the three volunteers and the clockwise as well as the counter-clockwise time series data

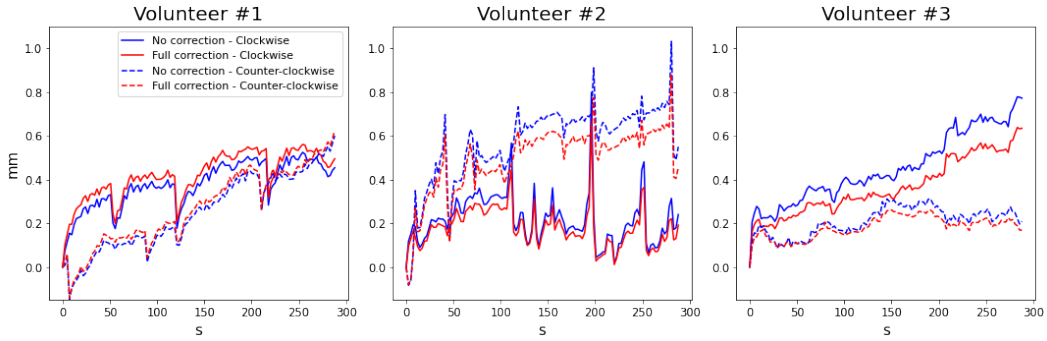

Figure B-3: Time course of motion regressors of the translation over the z-axis (estimated with SPM12) for the three volunteers and the clockwise as well as the counter-clockwise time series data.

B.4 Prescribed versus measured trajectories

In Fig. B-4, we show three randomly chosen shots out of the 48 shots used in a volumetric TR (the 5th, 16th, and 27th shots). The prescribed (theoretical) trajectories are plotted in blue, whereas those measured during the 20th repetition of the resting-state fMRI scans acquired from V#1 are drawn in black. The 20th repetition is taken as an example. The results are similar across all repetitions. We observe a good agreement between the prescribed trajectories and the actual ones. This is confirmed when looking more closely at the 16th shot in Fig. B-4(B) over the three axes: The k-space locations were normalized between -0.5 and 0.5. We quantified the maximum error in k-space location, on this resting-state data set, as 1% relative to k_{max}. Therefore, the zeroth order captures most of the dynamic field perturbations. Only residual perturbations are captured by the first and higher-order terms. Our results show that the first-order term (errors along the trajectories) has a less significant impact on the tSNR (and therefore on the temporal variance) than the zeroth-order. However, the impact on image quality shows that even such minor discrepancies between the prescribed trajectories and those actually played by the system can impact image quality.

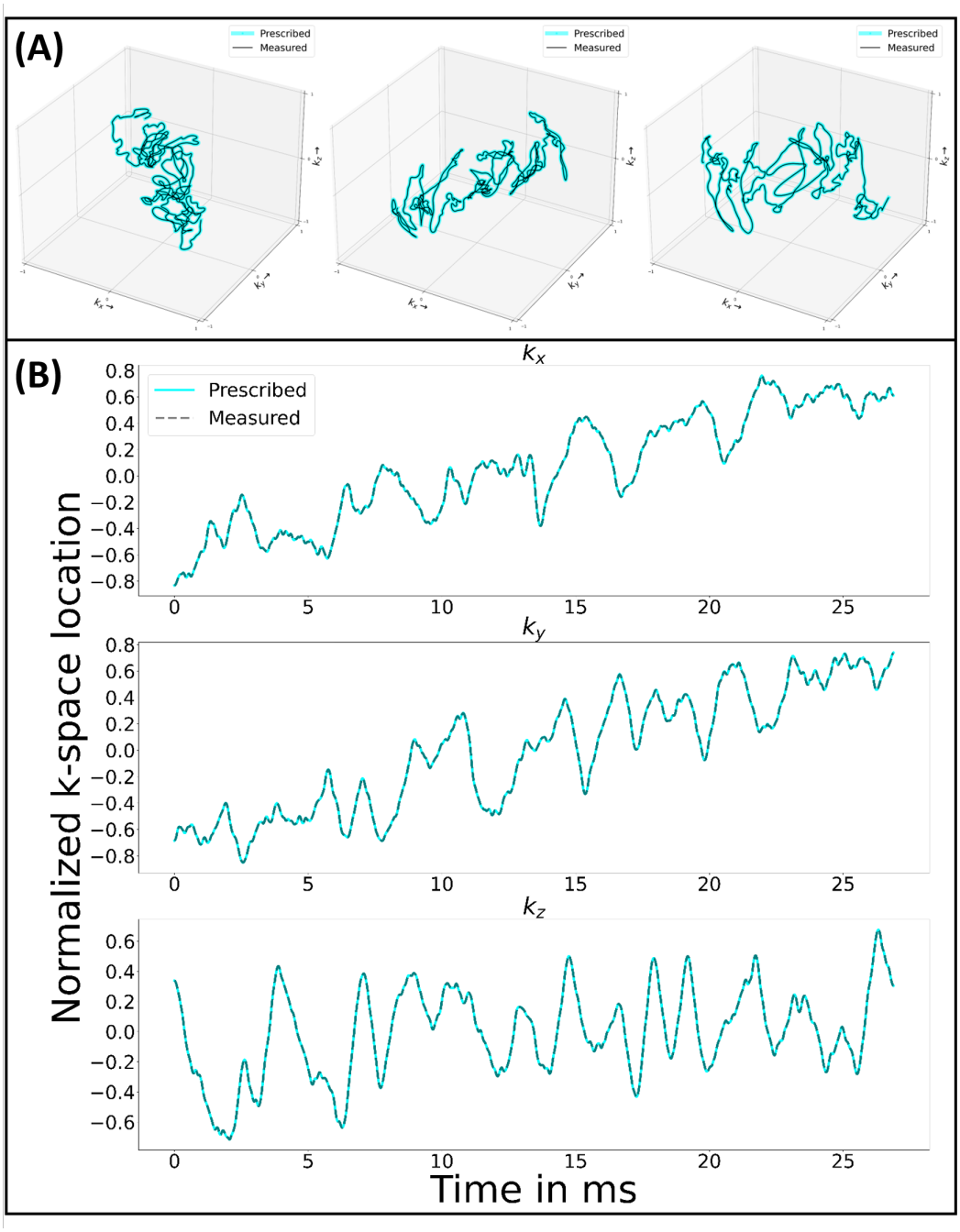

Figure B-4: Prescribed versus measured trajectories: Three randomly chosen prescribed shots (in blue) and plotted against the corresponding measured trajectories (in black) (A) in 3D and (B) along each of the three axes.

Appendix C

Preliminary *in vivo* validation of the sliding-window image reconstruction technique for 3D-SPARKLING fMRI data

Following the findings in Chapter 7, this appendix provides an initial investigation of the sliding-window reconstruction's behavior when extended to 3D-SPARKLING fMRI and the *in vivo* setting without accounting for the induced autocorrelation in the fMRI signal due to the sliding-window reconstruction. For this purpose, we leverage the retinotopic mapping fMRI data (participants V#1 and V#2) previously collected for Chapter 6 and the associated $\mathbf{B}_0$-corrected reconstruction pipeline: Static and up-to-the-first-order magnetic field perturbations were corrected. As a reminder, this dataset is acquired for a spatial resolution of $1mm^3$ and a temporal resolution (referred to in the sliding-window reconstruction context as TR_{native}) of 2.4s. Each full retinotopic experiment encompasses a clockwise and a counter-clockwise rotation. We apply the mentioned $\mathbf{B}_0$-corrected reconstruction pipeline twice: Firstly, using the traditional sequential reconstruction resulting in a temporal resolution that is equal to TR_{native} and secondly, using the sliding-window reconstruction, yielding an effective temporal resolution of $TR_{eff} = \frac{TR_{native}}{4}$ =0.6s or $TR_{eff} = \frac{TR_{native}}{8}$ =0.3s. The statistical analysis performed follows what is explained in Chapter 4. Then, the activation maps were estimated by computing z-score maps derived from the global effects of interest after thresholding F-statistic maps (cf Section 4.5.1 in Chapter 4) over the entire brain for $p < 0.001$ without correcting for multiple comparisons. Afterwards, we proceed to a qualitative comparison between the activation maps obtained from the data reconstructed using sequential and sliding-window reconstruction.

C.1 Increased BOLD sensitivity

Fig. C-1 shows the activation maps obtained from the 3D-SPARKLING retinotopic fMRI data collected from participant V#1 and reconstructed using a simple sequential (TR_{native}=2.4s) and a sliding-window (TR_{eff}=0.6s) reconstruction. We note that the activation patterns exhibit greater spatial extent and that statistically significant z-score values are higher when applying the sliding-window approach. For V#1, identified in Chapter 6 as the best volunteer, the sliding-window reconstruction approach does not induce artifactual activations in unexpected regions. In fact, Fig. C-2 shows (yellow arrows) that the activated voxels that have been recovered through the sliding-window approach are very relevant. For V#1, the sliding-window approach enhances the BOLD sensitivity even though the retinotopic mapping paradigm induces very slow BOLD responses. This is in accordance with what was observed in [RMS22], where the authors demonstrate a higher sensitivity associated with the sliding-window reconstruction combined with a radial EPI encoding scheme using a block-design (T_{on}=T_{off}=20s) paradigm. Furthermore, considering this specific case of TR_{eff}=0.6s and V#1, the sliding-window approach does induce false positives even though

the potential additional signal correlation induced by the sliding-window technique was not corrected.

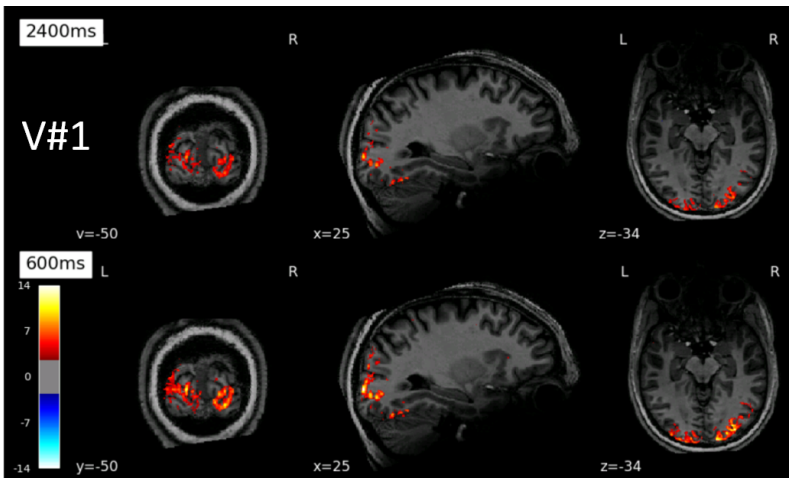

Figure C-1: Activation maps displayed for participant V#1 and the two reconstruction approaches, namely the sequential (yielding a temporal resolution of 2.4s, **Top**) and sliding-window technique (yielding an effective temporal resolution of 0.6s, **Bottom**). The color bar is unchanged for both reconstruction techniques.

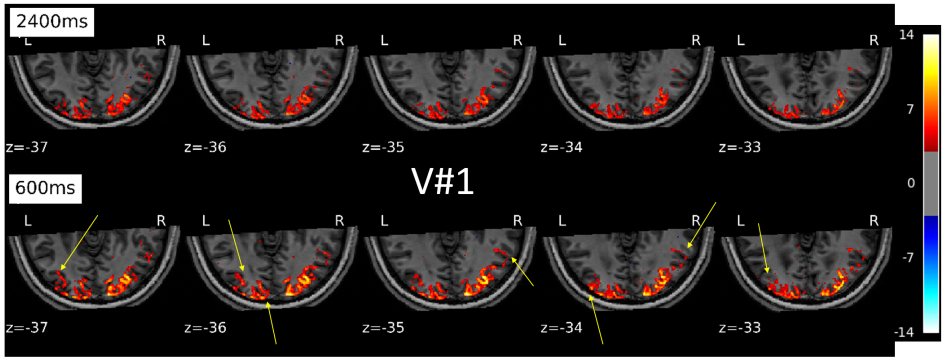

Figure C-2: Five axial slices showing, for V#1, the activations recovered (yellow arrows) when using the sliding window (yielding an effective temporal resolution of 0.6s, **Bottom**) vs. sequential (yielding a temporal resolution of 2.4s, **Top**) image reconstruction. The color bar is unchanged for both reconstruction techniques.

C.2 Sliding-window induced signal autocorrelation and motion propagation

Fig. C-3 shows the limits, for V#1, of the sliding-window approach as the TR_{eff} decreases, and therefore the overlap between the k-space data used to reconstruct consecutive scans increases. This results in a higher induced signal correlation that becomes significant and can no longer be disregarded. In fact, even though the sensitivity continues to increase in the visual cortex (Fig. C-2 vs. Fig. C-3, yellow arrows in the axial slice z=-34), false positives appear, especially around the brain edges. This specific location of false positives is known to be related to the patient's movement. In fact, in addition to the added signal autocorrelation, the sliding-window approach also propagates and accumulates the influence of motion (not assessed in Chapter 7) over several scans. This problem is even more visible for V#2 (Fig. C-4), where the false positives appear already for TR_{eff}=0.6s. If we compare the motion of V#1 and V#2 (cf Fig. C-5), we observe that V#2 moved more. We can, therefore, expect large head movement and increased physiological noise originating from breathing, for instance, to hinder the efficacy of the sliding-window approach. Retrospective

or prospective motion correction can be implemented as a solution. Furthermore, estimating the autocorrelation induced by the sliding-window reconstruction can be performed using tools such as SPM, AFNI, FSL, etc, and assuming a specific autoregressive (AR) or autoregressive-moving-average (ARMA) model. These models can then be used in the prewhitening step. However, one should carefully choose the toolbox as their performances and the models they use vary [Ols+19]. For instance, AFNI uses a voxel-wise ARMA(1,1) modeling, while SPM considers a global autocorrelation that follows a simple AR(1) model. Moreover, these models are not guaranteed to be realistic in the case of a sliding-window reconstruction. Furthermore, deriving the autocorrelation model analytically is not trivial because of the nonlinearity induced by the NUFFT operator. These aspects remain, for now, beyond the scope of this work and will be tackled in the future.

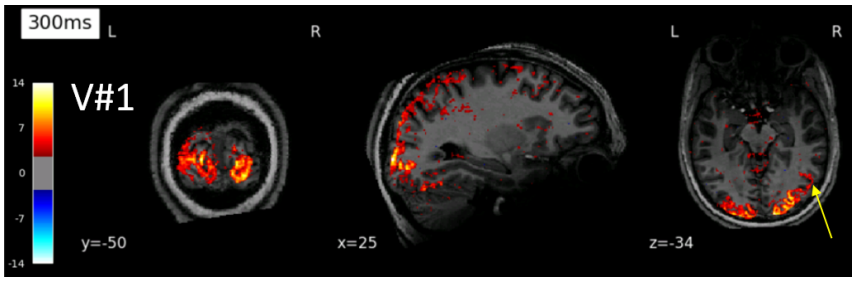

Figure C-3: Activation maps obtained from participant V#1 and reconstructed using sliding-window technique yielding an effective temporal resolution of 0.3s.

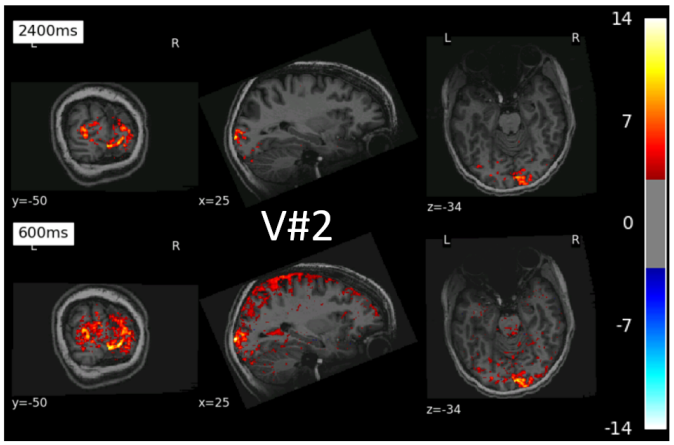

Figure C-4: Activation maps displayed for participant V#2 and the two reconstruction approaches, namely the sequential (yielding a temporal resolution of 2.4s, Top) and sliding-window technique (yielding an effective temporal resolution of 0.6s, Bottom). The color bar is unchanged for both reconstruction techniques.

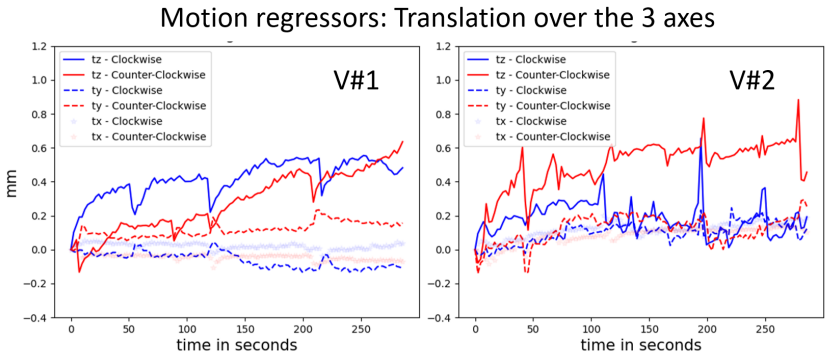

Figure C-5: Time course of motion regressors of the translation over the three axes (estimated with SPM12 from the clockwise and counter-clockwise datasets) for V#1 and V#2.

Funding

This Ph.D. received CFR funding from the Le Commissariat à l'Energie Atomique et aux Energies Alternatives (CEA).
This work was granted access to the HPC resources of TGCC in France under the allocation 2019-GCH0424 made by GENCI.
This work has received financial support from Leducq Foundation (Large Equipement de Recherche et Plateformes Technologiques program).

* * *
* *
*

List of Figures

List of Tables

Bibliography

[Abr61] A. Abragam. "The principles of nuclear magnetism". In: *Oxford University Press* (1961) (page 16).

[ASA03] J. L. R. Andersson, S. Skare and J. Ashburner. "How to correct susceptibility distortions in spin-echo echo-planar images: application to diffusion tensor imaging". In: *NeuroImage* 20.2 (2003), pp. 870–888 (pages 45, 62).

[AVT14] S. Aja-Fernández, G. Vegas-Sánchez-Ferrero and A. Tristán-Vega. "Noise estimation in parallel MRI: GRAPPA and SENSE". In: *Magnetic Resonance in Medicine* 32 (2014), pp. 281–290 (page 60).

[Ban+92] P. A. Bandettini, E. C. Wong, R. S. Hinks, R. S. Tikofsky and J. S. Hyde. "Time course EPI of human brain function during task activation." In: *Magnetic Resonance in Medicine* 25.2 (1992), pp. 390–397 (pages 1, 5).

[Ban02] P. A. Bandettini. "The spatial, temporal, and interpretive limits of functional MRI". In: *Neuropsychopharmacology: The Fifth Generation of Progress: An Official Publication of the American College of Neuropsychopharmacology* (2002) (page 91).

[Bar+09] C. Barmet, N. De Zanche, B. Wilm and K. Pruessmann. "A Transmit/Receive System for Magnetic Field Monitoring of In Vivo MRI". In: *Magnetic Resonance in Medicine* 62.1 (2009), pp. 269–276 (pages 46, 47).

[Bat+23] S. Bates, S. Dumoulin, P. Folkers, E. Formisano, R. Goebel, A. Haghnejad, R. Helmich, D. Klomp, A. van der Kolk, Y. Li, A. Nederveen, D. Norris, N. Petridou, S. Roell, T. Scheenen, M. Schoonheim, I. Voogt and A. Webb. "A vision of 14 T MR for fundamental and clinical science". In: *Magnetic Resonance Materials in Physics, Biology and Medicine* 36.2 (2023), pp. 211–225 (pages 2, 7, 21).

[BDP08] C. Barmet, N. De Zanche and K. Pruessmann. "Spatiotemporal Magnetic Field Monitoring for MR. Magnetic Resonance in Medicine". In: *Magnetic Resonance in Medicine* 60.1 (2008), pp. 187–197 (pages 46, 47).

[BHF21] P. Bandettini, L. Huber and E. Finn. "Challenges and opportunities of mesoscopic brain mapping with fMRI". In: *Current Opinion in Behavioral Sciences* 40 (Aug. 2021), pp. 189–200 (pages 26, 59).

[Bia+22] S. Bianchi, M. Engel, J. Heinzle, S. Frassle, K. E. Stephan and K. P. Pruessmann. "T-Hex spirals for whole-brain fMRI at 5 frames per second: Image quality and BOLD sensitivity". In: *ISMRM Annual Meeting*. 2022 (pages 36, 37, 92, 100).

[Blo46] F. Bloch. "Nuclear Induction". In: *Physical Review* 70 (7-8 Oct. 1946), pp. 460–474 (page 16).

[BM10] C. M. Bennett and M. B. Miller. "How reliable are the results from functional magnetic resonance imaging?" In: *Annals of The New York Academy Of Sciences* 1191 (2010), pp. 133–155 (page 52).

[Bol+17] S. Bollmann, L. Kasper, S. J. Vannesjo, A. O. Diaconescu, B. E. Dietrich, S. Gross, K. E. Stephan and K. P. Pruessmann. "Analysis and Correction of Field Fluctuations in fMRI Data Using Field Monitoring". In: *NeuroImage* 154 (2017), pp. 92–105 (pages 46, 47, 87).

[Boy+16] C. Boyer, N. Chauffert, P. Ciuciu, J. Kahn and P. Weiss. "On the generation of sampling schemes for MRI". In: *SIAM Journal on Imaging Sciences* 9.4 (2016), pp. 2039–2072 (page 40).

[Bre+05] F. A. Breuer, M. Blaimer, R. M. Heidemann, M. F. Mueller, M. A. Griswold and P. M. Jakob. "Controlled Aliasing in Parallel Imaging Results in Higher Acceleration (CAIPIRINHA) for Multi-Slice Imaging". In: *Magnetic Resonance in Medicine* 53.3 (2005), pp. 684–91 (pages 36, 60).

[Bre+06] F. A. Breuer, M. Blaimer, M. F. Mueller, N. Seiberlich, R. M. Heidemann, M. A. Griswold and P. M. Jakob. "Controlled Aliasing in Volumetric Parallel Imaging (2D CAIPIRINHA)". In: *Magnetic Resonance in Medicine* 55.3 (2006), pp. 549–556 (pages 35, 60, 61, 73).

[Bre+09] F. A. Breuer, S. A. R. Kannengiesser, M. Blaimer, N. Seiberlich, P. M. Jakob and M. A. Griswold. "General Formulation for Quantitative G-factor Calculation in GRAPPA Reconstructions". In: *Magnetic Resonance in Medicine* 62.3 (2009), pp. 739–746 (page 60).

[BRR12] J. Biglands, A. Radjenovic and J. Ridgway. "Cardiovascular magnetic resonance physics for clinicians: Part II". In: *Journal of Cardiovascular Magnetic Resonance* 14 (Sept. 2012) (page 32).

[BT09] A. Beck and M. Teboulle. "A Fast Iterative Shrinkage-Thresholding Algorithm for Linear Inverse Problems". In: *SIAM Journal on Imaging Sciences* 2.1 (2009), pp. 183–202 (page 38).

[BUF07] K. Block, M. Uecker and J. Frahm. "Undersampled radial MRI with multiple coils. Iterative image reconstruction using a total variation constraint". In: *Magnetic Resonance in Medicine* 57 (June 2007), pp. 1086–98 (pages 2, 6).

[BY01] Y. Benjamini and D. Yekutieli. "The Control of the False Discovery Rate in Multiple Testing Under Dependency". In: *The Annals of Statistics* 29.4 (2001) (pages 62, 80).

[CAT16] I. Y. Chun, B. Adcock and T. Talavage. "Efficient Compressed Sensing SENSE pMRI Reconstruction With Joint Sparsity Promotion". In: *IEEE Transactions on Medical Imaging* 35.1 (2016) (page 60).

[CG15] J. E. Chen and G. H. Glover. "BOLD fractional contribution to resting-state functional connectivity above 0.1 Hz". In: *NeuroImage* 107 (2015), pp. 207–218 (page 92).

[Cha+13] C. Chavarrias, J. F. P. J. Abascal, P. Montesinos and M. Desco. "How Does Compressed Sensing Affect Activation Maps in Rat fMRI?" In: *XIII Mediterranean Conference on Medical and Biological Engineering and Computing* 41 (2013) (page 51).

[Cha+14a] L. Chaari, P. Ciuciu, S. Mériaux and J.-C. Pesquet. "Spatio-temporal wavelet regularization for parallel MRI reconstruction: application to functional MRI". In: *MAGMA* 27.6 (Dec. 2014), pp. 509–529 (pages 32, 60).

[Cha+14b] N. Chauffert, P. Ciuciu, J. Kahn and P. Weiss. "Variable density sampling with continuous trajectories. Application to MRI". In: *SIAM Journal on Imaging Sciences* 7.4 (2014), pp. 1962–1992 (pages 2, 6, 60).

[Cha+17] N. Chauffert, P. Ciuciu, J. Kahn and P. Weiss. "A projection method on measures sets". In: *Constructive Approximation* 45.1 (2017), pp. 83–111 (page 40).

[Cha+22] G. R. Chaithya, P. Weiss, A. Massire, A. Vignaud and P. Ciuciu. "Optimizing full 3D SPARKLING trajectories for high-resolution Magnetic Resonance imaging". In: *IEEE Transactions on Medical Imaging* 41.8 (2022), pp. 2105–2117 (pages 2, 6, 39, 40, 51, 92, 104).

[Cha+23] G. R. Chaithya, G. Daval-Frérot, A. Massire, A. Vignaud and P. Ciuciu. "Improving spreading projection algorithm for rapid k-space sampling trajectories through minimized off-resonance effects and gridding of low frequencies". In: *Magnetic Resonance in Medicine* 90 (May 2023) (page 104).

[Cha23] G. R. Chaithya. "Designing and learning non-Cartesian k-space sampling trajectories for accelerated 3D MRI". PhD thesis. 2023 (page 31).

[Che+21a] J. E. Chen, G. H. Glover, N. E. Fultz, B. R. Rosen, J. R. Polimeni and L. D. Lewis. "Investigating mechanisms of fast BOLD responses: The effects of stimulus intensity and of spatial heterogeneity of hemodynamics". In: *NeuroImage* 245 (2021), p. 100288 (page 92).

[Che+21b] H. Cherkaoui, T. Moreau, A. Halimi, C. Leroy and P. Ciuciu. "Multivariate semi-blind deconvolution of fMRI time series". In: *NeuroImage* 241 (July 2021), p. 118418 (page 92).

[Ciu+03] P. Ciuciu, J.-B. Poline, G. Marrelec, J. Idier, C. Pallier and H. Benali. "Unsupervised robust non-parametric estimation of the hemodynamic response function for any fMRI experiment." In: *IEEE Transactions on Medical Imaging* 22 (2003), pp. 1235–1251 (pages 25, 92).

[Com+23] P.-A. Comby, **Z. Amor**, A. Vignaud and P. Ciuciu. "Denoising of fMRI volumes using local low rank methods". In: *20th IEEE International Symposium on Biomedical Imaging (ISBI)*. Cartagena de Indias, Colombia, 2023 (pages 11, 104).

[CVC24] P.-A. Comby, A. Vignaud and P. Ciuciu. "SNAKE-fMRI: A modular fMRI simulator from the space-time domain to k-space data and back". In: *ISMRM Annual Meeting, (in press)*. Singapore, 2024 (page 92).

[Dam+06] J. S. Damoiseaux, S. A. R. B. Rombouts, F. Barkhof, P. Scheltens, C. J. Stam, S. M. Smith and C. F. Beckmann. "Consistent resting-state networks across healthy subjects". In: *PNAS* 103.37 (2006), pp. 13848–13853 (page 92).

[Dav+22] G. Daval-Frérot, A. Massire, B. Mailhe, M. Nadar, A. Vignaud and P. Ciuciu. "Iterative static field map estimation for off-resonance correction in non-Cartesian susceptibility weighted imaging". In: *Magnetic Resonance in Medicine* 88.4 (2022), pp. 1592–1607 (pages 54, 88, 105).

[Dav+23] G. Daval-Frérot, A. Massire, B. Mailhé, M. Nadar, B. Bapst, A. Luciani, A. Vignaud and P. Ciuciu. "Deep learning-assisted model-based off-resonance correction for non-Cartesian SWI". In: *Magnetic Resonance in Medicine* 90 (June 2023) (page 104).

[De +08] N. De Zanche, C. Barmet, J. Nordmeyer-Massner and K. Pruessmann. "NMR Probes for Measuring Magnetic Fields and Field Dynamics in MR Systems". In: *Magnetic Resonance in Medicine* 60.1 (2008), pp. 176–186 (pages 46, 47).

[Dei+03] R. Deichmann, J. Gottfried, C. Hutton and R. Turner. "Optimised EPI for fMRI studies of orbitofrontal cortex". In: *NeuroImage* 19 (July 2003), pp. 430–41 (page 45).

[Des+12] A. . Deshmane, V. Gulani, M. A. Griswold and N. Seiberlich. "Parallel MR Imaging". In: *Journal of Magnetic Resonance Imaging* 36.1 (2012), pp. 55–72 (pages 20, 32–34, 60).

[Dic45] L. R. Dice. "Measures of the Amount of Ecologic Association Between Species". In: *Ecology* 26.3 (1945), pp. 297–302 (page 63).

[Don20] M. Doneva. "Mathematical Models for Magnetic Resonance Imaging Reconstruction". In: *IEEE Signal Processing Magazine* 37.1 (2020), pp. 24–32 (pages 45, 46, 78).

[Duy12] J. Duyn. "The future of ultra-high field MRI and fMRI for study of the human brain." In: *NeuroImage* 62.2 (2012), pp. 1241–1248 (page 43).

[Dym+18] B. Dymerska, B. Poser, M. Barth, S. Trattnig and S. Robinson. "A method for the dynamic correction of B0-related distortions in single-echo EPI at 7 T". In: *NeuroImage* 168 (2018), pp. 312–331 (page 88).

[EF89] R. Ehman and J. Felmlee. "Adaptive Technique for High-Definition MR Imaging of Moving Structures". In: *Radiology* 173.1 (1989), pp. 255–263 (page 46).

[El +18] L. El Gueddari, C. Lazarus, H. Carrié, A. Vignaud and P. Ciuciu. "Self-calibrating nonlinear reconstruction algorithms for variable density sampling and parallel reception MRI". In: *IEEE 10th Sensor Array and Multichannel Signal Processing Workshop (SAM)*. 2018 (pages 55, 73).

[Eng+21] M. Engel, L. Kasper, B. Wilm, B. Dietrich, L. Vionnet, F. Hennel, J. Reber and K. P. Pruessmann. "T-Hex: Tilted hexagonal grids for rapid 3D imaging". In: *Magnetic Resonance in Medicine* 85.5 (2021), pp. 2507–2523 (pages 36, 37, 75, 88).

[Fan+16] Z. Fang, N. V. Le, M. Choy and J. H. Lee. "High Spatial Resolution Compressed Sensing (HSPARSE)Functional MRI". In: *Magnetic Resonance in Medicine* 76.2 (2016), pp. 440–455 (page 51).

[Far+20] S. Farrens, A. Grigis, L. El Gueddari, Z. Ramzi, G. R. Chaithya, B. Starck S.and Sarthou, H. Cherkaoui, P. Ciuciu and J.-L. Starck. "PySAP: Python Sparse Data Analysis Package for Multidisciplinary Image Processing". In: *Astronomy and Computing* 32 (2020) (page 55).

[FDP21] A. Fracasso, S. O. Dumoulin and N. Petridou. "Point-spread function of the BOLD response across columns and cortical depth in human extra-striate cortex". In: *Neurobiology* 202 (2021), p. 102034 (page 75).

[Fei+23] D. Feinberg, A. Beckett, A. Vu, J. Stockmann, L. Huber, S. Ma, S. Ahn, K. Setsompop, X. Cao, S. Park, C. Liu, L. Wald, J. Polimeni, A. Mareyam, B. Gruber, R. Stirnberg, C. Liao, E. Yacoub, M. Davids and P. Dietz. "Next-generation MRI scanner designed for ultra-high-resolution human brain imaging at 7 Tesla". In: *Nature Methods* 20 (Nov. 2023), pp. 1–10 (pages 21, 100).

[Fen+14] L. Feng, R. Grimm, K. Block, H. Chandarana, S. Kim, J. Xu, L. Axel, D. Sodickson and R. Otazo. "Golden-Angle Radial Sparse Parallel MRI: Combination of Compressed Sensing, Parallel Imaging, and Golden-Angle Radial Sampling for Fast and Flexible Dynamic Volumetric MRI". In: *Magnetic Resonance in Medicine* 72 (2014) (pages 2, 6).

[Fes+05a] J. A. Fessler, S. Lee, V. T. Olafsson, H. R. Shi and D. Noll. "Toeplitz-Based Iterative Image Reconstruction for MRI With Correction for Magnetic Field Inhomogeneity". In: *IEEE Transactions On Signal Processing* 53.9 (2005), pp. 3393–3402 (page 45).

[Fes+05b] J. A. Fessler, S. Lee, V. T. Olafsson, H. R. Shi and D. C. Noll. "Toeplitz-Based Iterative Image Reconstruction for MRI With Correction for Magnetic Field Inhomogeneity". In: *IEEE Transactions On Signal Processing* 53.9 (2005), pp. 3393–3402 (page 54).

[FHM06] S. Faro, V. Haughton and F. Mohamed. *Functional MRI: Basic principles and clinical applications*. Jan. 2006, pp. 1–533 (pages 16, 37).

[Fil16] M. Filippi. *fMRI Techniques and Protocols*. Jan. 2016 (page 16).

[FR86] P. T. Fox and M. E. Raichle. "Focal physiological uncoupling of cerebral blood flow and oxidative metabolism during somatosensory stimulation in human subjects". In: *PNAS* 83 (1986), pp. 1140–4 (page 24).

[Fra+23] B. Franceschiello, S. Rumac, T. Hilbert, M. Nau, M. Dziadosz, G. Degano, C. W. Roy, A. Gaglianese, G. Petri, J. Yerly, M. Stuber, T. Kober, R. B. van Heeswijk, M. M. Murray and E. Fornari. "Hi-Fi fMRI: High-resolution, fast-sampled and sub-second whole-brain functional MRI at 3T in humans". In: *Preprint. bioRxive* (2023) (page 92).

[Fra05] P. Fransson. "Spontaneous Low-Frequency BOLD SignalFluctuations: An fMRI Investigation of theResting-State Default Mode of BrainFunction Hypothesis". In: *Human Brain Mapping* 26 (2005), pp. 15–29 (page 92).

[Fra51] J. Frank J. Massey. "The Kolmogorov-Smirnov Test for Goodness of Fit". In: *Journal of the American Statistical Association* 46.253 (1951), pp. 68–178 (page 63).

[Fri+95] K. J. Friston, A. P. Holmes, J. B. Poline, P. J. Grasby, S. C. Williams, R. S. Frackowiak and R. Turner. "Analysis of fMRI Time-Series Revisited". In: *NeuroImage* 2.1 (1995), pp. 45–53 (pages 25, 91, 99).

[Gao+96] J.-H. Gao, J. Xiong, S. Laia, E. M. Haacke, M. G. Woldorff, J. Li and P. T. Fox. "Improving the temporal resolution of functional MR imaging using keyhole techniques". In: *Magnetic Resonance in Medicine* 35.6 (1996), pp. 854–860 (page 92).

[Gat+97] J. S. Gati, R. S. Menon, K. Ugurbil and B. K. Rutt. "Experimental Determination of the BOLD Field Strength Dependence in Vessels and Tissue". In: *Magnetic Resonance in Medicine* 38.2 (1997), pp. 296–302 (page 44).

[GHJ03] M. A. Griswold, R. M. Heidemann and P. M. Jakob. "Direct parallel imaging reconstruction of radially sampled data using GRAPPA with relative shifts". In: *ISMRM Annual Meeting*. 2003 (page 38).

[GHN06] P. T. Gurney, B. A. Hargreaves and D. G. Nishimura. "Design and analysis of a practical 3D cones trajectory". In: *Magnetic Resonance in Medicine* 55.3 (2006), pp. 575–582 (pages 36, 37).

[Glo12] G. H. Glover. "Spiral imaging in fMRI". In: *NeuroImage* 62.2 (2012), pp. 706–12 (pages 2, 6, 36, 60).

[GMC22] N. N. Graedel, K. L. Miller and M. Chiew. "Ultrahigh Resolution fMRI at 7T Using Radial-Cartesian TURBINE Sampling". In: *Magnetic Resonance in Medicine* 88.5 (2022), pp. 2058–2073 (pages 8, 36, 37, 46, 75, 76).

[Gra+16] V. Gras, A. Vignaud, A. Amadon, D. Le Bihan and N. Boulant. "Universal pulses: A new concept for calibration-free parallel transmission". In: *Magnetic Resonance in Medicine* 77 (Feb. 2016) (pages 44, 105).

[Gra+17] N. N. Graedel, J. A. McNab, M. Chiew and K. L. Miller. "Motion Correction for Functional MRI With Three-Dimensional Hybrid Radial-Cartesian EPI". In: *Magnetic Resonance in Medicine* 78.2 (2017), pp. 527–540 (pages 88, 105).

[Gri+02] M. A. Griswold, P. M. Jakob, R. M. Heidemann, M. Nittka, V. Jellus, J. Wang, B. Kiefer and A. Haase. "Generalized Autocalibrating Partially ParallelAcquisitions (GRAPPA)". In: *Magnetic Resonance in Medicine* 47.6 (2002), pp. 1202–1210 (pages 33, 60).

[Gue+12] M. Guerquin-Kern, L. Lejeune, K. P. Pruessmann and M. Unser. "Realistic Analytical Phantoms for Parallel Magnetic Resonance Imaging". In: *IEEE Transactions on Medical Imaging* 31.3 (2012), pp. 626–636 (page 94).

[Gue+20] L. Gueddari, C. Gr, Z. Ramzi, S. Farrens, S. Starck, A. Grigis, J.-L. Starck and P. Ciuciu. "PySAP-MRI: A Python package for MR image reconstruction". In: *ISMRM workshop on Data Sampling and Image Reconstruction*. 2020 (page 55).

[Hae+15] M. Haeberlin, L. Kasper, C. Barmet, D. Brunner, B. Dietrich, S. Gross, B. Wilm, S. Kozerke and K. Pruessmann. "Real-time motion correction using gradient tones and head-mounted NMR field probes". In: *Magnetic Resonance in Medicine* 74.3 (2015), pp. 647–660 (page 88).

[Ham17] J. Hamilton. "Recent advances in parallel imaging for MRI". In: *Progress in Nuclear Magnetic Resonance Spectroscopy* 101 (2017), pp. 71–95 (pages 32, 35, 60).

[Han+15] P. K. Han, S. Park, S. Kim and J. C. Ye. "Compressed Sensing for fMRI: Feasibility Study on the Acceleration of Non-EPI fMRI at 9.4T". In: *BioMed Research International* (2015) (page 51).

[Has+22] M. Haskell, A. Lahiri, J.-F. Nielsen, J. Fessler and D. Noll. "FieldMapNet MRI: Learning-based mapping from single echo time BOLD fMRI data to fieldmaps with model-based reconstruction". In: *ISMRM Annual Meeting* (2022) (page 88).

[Hen+02] R. Henson, T. Shallice, M. L. Gorno-Tempini and R. Dolan. "Face repetition effects in implicit and explicit memory tests as measured by fMRI". In: *Cereb Cortex* 12 (2002), pp. 187–86 (page 67).

[Hen+12] L. Henriksson, J. Karvonen, N. Salminen-Vaparanta, H. Railo and S. Vanni. "Retinotopic Maps, Spatial Tuning, and Locations of Human Visual Areas in Surface Coordinates Characterized with Multifocal and Blocked fMRI Designs". In: *PLoS ONE* 7.5 (2012), e36859 (page 74).

[Hof+08] M. B. Hoffmann, J. Stadler, M. Kanowski and O. Speck. "Retinotopic mapping of the human visual cortex at a magnetic field strength of 7T". In: *Clinical Neurophysiology* 120.1 (2008), pp. 108–16 (page 74).

[HSD00] R. Henson, T. Shallice and R. Dolan. "Neuroimaging evidence for dissociable forms of repetition priming". In: *Science* 287.5456 (2000), pp. 1269–72 (page 67).

[Huo19] N. Huotari. "Sampling Rate Effects on Resting State fMRI Metrics". In: *Frontiers in Neuroscience* 13 (2019), p. 279 (page 92).

[IN95] P. Irarrazabal and D. G. Nishimura. "Fast three dimensional magnetic resonance imaging". In: *Magnetic Resonance in Medicine* 33.5 (1995), pp. 656–662 (page 36).

[Jah+19] H. Jahanian, S. Holdsworth, T. Christen, H. Wu, K. Zhu, A. B. Kerr, M. J. Middione, R. F. Dougherty, M. Moseley and G. Zaharchuk. "Advantages of short repetition time resting-state functional MRI enabled by simultaneous multi-slice imaging". In: *Journal of Neuroscience Methods* 311 (2019), pp. 122–132 (page 92).

[Jam+23] R. Jamil, A. Massire, F. Mauconduit, V. Gras, M. Naudin, R. Guillevin, E. Pracht, T. Stöcker, N. Boulant and R. Stirnberg. "PASTeUR package extension to slab-selective excitations and 3D-EPI for plug-and-play parallel transmit at 7 Tesla". In: *ISMRM Annual Meeting*. 2023 (page 44).

[Jam22] R. Jamil. "Development of a high spatial resolution functional MRI sequence at ultra-high field". PhD thesis. 2022 (pages 31, 35).

[Kas+15] L. Kasper, S. Bollmann, S. Vannesjo, S. Gross, M. Haeberlin, B. Dietrich and K. Pruessmann. "Monitoring, Analysis, and Correction of Megnetic Field Fluctuations in Echo Planar Imaging Time Series". In: *Magnetic Resonance in Medicine* 74.2 (2015), pp. 396–409 (page 46).

[Kas+18] S. Kashyap, D. Ivanov, M. Havlicek, S. Sengupta, B. Poser and K. Uludag. "Resolving laminar activation in human V1 using ultra-high spatial resolution fMRI at 7T". In: *Scientific Reports* 8 (Nov. 2018) (page 26).

[Kas+22] L. Kasper, M. Engel, J. Heinzle, M. Mueller-Schrader, N. N. Graedel, J. Reber, T. Schmid, C. Barmet, B. J. Wilm, K. E. Stephan and K. P. Pruessmann. "Advances in spiral fMRI: A high-resolution study with single-shot acquisition". In: *NeuroImage* 246 (2022), p. 118738 (pages 8, 36, 60, 75, 76, 78, 88).

[Kha+11] I. Khalidov, J. Fadili, F. Lazeyras, D. Van De Ville and M. Unser. "Activelets: Wavelets for sparse representation of hemodynamic responses". In: *Signal Processing* 91 (2011), pp. 2810–2821 (page 51).

[KJR12] M. Krämer, T. H. Jochimsen and J. R. Reichenbach. "Functional magnetic resonance imaging using PROPELLER-EPI". In: *Magnetic Resonance in Medicine* 68.1 (2012), pp. 140–51 (pages 36, 37, 46, 89, 92).

[Kwo+92] K. K. Kwong, J. W. Belliveau, D. A. Chesler, I. E. Goldberg, R. M. Weisskoff, B. P. Poncelet, D. N. Kennedy, B. E. Hoppel, M. S. Cohen and R. Turner. "Dynamic magnetic-resonance-imaging of human brain activity during primary sensory stimulation." In: *PNAS* 89.12 (1992), pp. 5675–5679 (pages 1, 5).

[Lar+01] D. Larkman, J. Hajnal, A. Herlihy, G. Coutts, I. Young and G. Ehnholm. "Use of multicoil arrays for separation of signal from multiple slices simultaneously excited". In: *Journal of Magnetic Resonance Imaging* 13.2 (2001), pp. 313–317 (page 60).

[Lau73a] P. C. Lauterbur. "Principles of Magnetic Resonance Imaging A Signal Processing Perspective". In: *Nature* (1973) (pages 18, 19).

[Lau73b] P. C. Lauterbur. "Image Formation by Induced Local Interactions: Examples Employing Nuclear Magnetic Resonance". In: *Nature* 242 (1973), pp. 190–191 (page 36).

[Laz+19] C. Lazarus, P. Weiss, N. Chauffert, F. Mauconduit, L. El Gueddari, I. Destrieux C.and Zemmoura, A. Vignaud and P. Ciuciu. "SPARKLING: variable-density k-space filling curves for accelerated T2*-weighted MRI". In: *Magnetic Resonance in Medicine* 81.6 (2019), pp. 3643–3661 (pages 2, 6, 39, 40, 51, 92).

[Laz+20] C. Lazarus, P. Weiss, L. El Gueddari, F. Mauconduit, A. Massire, M. Ripart, A. Vignaud and P. Ciuciu. "3D variable-density SPARKLING trajectories for high-resolution T2*-weighted magnetic resonance imaging". In: *NMR in Biomedicine* 33.9 (2020), e4349 (pages 2, 6, 39).

[LDP07] M. Lustig, D. Donoho and J. M. Pauly. "Sparse MRI: The application of compressed sensing for rapid MR imaging". In: *Magnetic Resonance in Medicine* 58.6 (2007), pp. 1182–1195 (pages 2, 6, 38, 60).

[Le +19] C. Le Ster, A. Moreno, F. Mauconduit, V. Gras, R. Stirnberg, B. A. Poser, A. Vignaud, E. Eger, S. Dehaene, F. Meyniel and N. Boulant. "Comparison of SMS-EPI and 3D-EPI at 7T in an fMRI localizer study with matched spatiotemporal resolution and homogenized excitation profiles". In: *PLoS ONE* 14.11 (2019), e0225286 (page 60).

[Lew+16] L. D. Lewis, K. Setsompop, B. R. Rosen and J. R. Polimeni. "Fast fMRI can detect oscillatory neural activity in humans". In: *PNAS* 113.43 (2016), E6679–E6685 (pages 25, 92, 94, 99, 100).

[Ley+21] A. P. Leynes, N. L. Damestani, D. J. Lythgoe, A. B. Solana, B. Fernandez, B. Burns, S. C. R. Williams, F. Zelaya, P. E. Larson and F. Wiesinger. "Extreme Looping Star: Quiet fMRI at high spatiotemporal resolution". In: *ISMRM Annual Meeting*. 2021 (pages 92, 100).

[Lin+13] F.-H. Lin, T. Witzel, T. Raij, J. Ahveninen, K. Wen-Kai Tsai, Y.-H. Chu, W.-T. Chang, A. Nummenmaa, J. R. Polimeni, W.-J. Kuo, J.-C. Hsieh, B. R. Rosen and J. W. Belliveau. "fMRI hemodynamics accurately reflects neuronal timing in the human brain measured by MEG". In: *NeuroImage* 78 (2013), pp. 372–384 (page 59).

[LL00] Z.-P. Liang and P. C. Lauterbur. "Principles of Magnetic Resonance Imaging A Signal Processing Perspective". In: *IEEE Press, New York* (2000) (page 18).

[LP01] M. Lustig and J. M. Pauly. "SPIRiT: Iterative Self-consistent Parallel Imaging Reconstruction from Arbitrary k-Space". In: *Magnetic Resonance in Medicine* 64.2 (2001), pp. 457–471 (pages 38, 60).

[LSS12] M. Lee, C. Smyser and J. Shimony. "Resting-State fMRI: A Review of Methods and Clinical Applications". In: *American journal of neuroradiology* 34 (Aug. 2012) (page 28).

[Lus+08] M. Lustig, D. L. Donoho, J. M. Santos and J. M. Pauly. "Compressed Sensing MRI". In: *IEEE Signal Processing Magazine* 25.2 (2008), pp. 72–82 (pages 2, 6, 38).

[MA21] B. P. Meneses and A. Amadon. "A fieldmap-driven few-channel shim coil design for MRI of the human brain". In: *Physics in Medicine and Biology* 66.1 (2021) (page 45).

[MBB13] K. Murphy, R. M. Birn and P. A. Bandettini. "Resting-state fMRI Confounds and Cleanup". In: *NeuroImage* 80.15 (2013), pp. 349–359 (pages 46, 78).

[MM77] P. Mansfield and A. A. Maudsley. "Medical imaging by NMR". In: *The British journal of radiology* (1977) (pages 18, 19).

[Moe+10] S. Moeller, E. Yacoub, C. Olman, E. Auerbach and J. H. N. Strupp. "Multiband multislice GE-EPI at 7 tesla, with 16-fold acceleration using partial parallel imaging with application to high spatial and temporal whole-brain fMRI". In: *Magnetic Resonance in Medicine* 63.5 (2010), pp. 1144–1153 (pages 2, 6, 35, 60).

[Nag+22] Z. Nagy, C. Hutton, G. David, N. Hinterholzer, R. Deichmann, N. Weiskopf and S. Vannesjo. "HiHi fMRI: a data-reordering method for measuring the hemodynamic response of the brain with high temporal resolution and high SNR". In: *Cerebral cortex* 33 (2022) (pages 92, 101).

[Naz+20] U. Nazar Hussain, M. Khan, M. I. Lali, K. Javed, I. Ashraf, J. Tariq, H. Ali and A. Din. "A Unified Design of ACO and Skewness based Brain Tumor Segmentation and Classification from MRI Scans". In: *Control Engineering and Applied Informatics* 22 (June 2020), pp. 1–15 (page 23).

[Oga+90] S. Ogawa, T. M. Lee, A. R. Kay and D. W. Tank. "Brain magnetic resonance imaging with contrast dependent on blood oxygenation". In: *PNAS* 87.24 (1990), pp. 9868–9872 (pages 1, 5, 24, 91).

[Oga+92] S. Ogawa, D. W. Tank, R. Menon, J. M. Ellermann, S. G. Kim, H. Merkle and K. Ugurbil. "Intrinsic signal changes accompanying sensory stimulation—functional brain mapping with magnetic resonance-imaging." In: *PNAS* 89.13 (1992), pp. 5951–5955 (pages 1, 5).

[Ols+19] W. Olszowy, J. Aston, C. Rua and G. Williams. "Accurate autocorrelation modeling substantially improves fMRI reliability". In: *Nature Communications* (2019) (pages 28, 119).

[PL21] J. R. Polimeni and L. D. Lewis. "Imaging faster neural dynamics with fast fMRI: a need for updated models of the hemodynamic response". In: *Progress in neurobiology* 207 (2021), p. 102174 (pages 25, 92).

[Pol+10] J. R. Polimeni, B. Fischl, D. N. Greve and L. L. Wald. "Laminar analysis of 7 T BOLD using an imposed spatial activation pattern in human V1". In: *NeuroImage* 52.4 (2010), pp. 1334–1346 (page 59).

[Pos+10] B. Poser, P. Koopmans, T. Witzel, L. Wald and M. Barth. "Three dimensional echo-planar imaging at 7 Tesla". In: *NeuroImage* 51 (Feb. 2010), pp. 261–6 (pages 2, 6, 34, 60, 88).

[Pra+21] G. T. Prabhakaran, K. O. Al-Nosairy, C. Tempelmann, H. Thieme and M. B. Hoffmann. "Mapping Visual Field Defects With fMRI – Impact of Approach and Experimental Conditions". In: *Frontiers in Neuroscience* 15 (2021), p. 745886 (page 74).

[Pru+01] K. P. Pruessmann, M. Weiger, P. Börnert and P. Boesiger. "Advances in sensitivity encoding with arbitrary k-space trajectories". In: *Magnetic Resonance in Medicine* 46.4 (2001), pp. 638–651 (pages 38, 60).

[Pru+99] K. P. Pruessmann, M. Weiger, M. B. Scheidegger and P. Boesiger. "SENSE: Sensitivity encoding for fast MRI". In: *Magnetic Resonance in Medicine* 42 (1999), pp. 952–962 (pages 33, 60).

[Pru06] K. P. Pruessmann. "Encoding and Reconstruction in Parallel MRI". In: *NMR in Biomedicine* 19.3 (2006), pp. 288–99 (page 60).

[PSS16] R. Pohmann, O. Speck and K. Scheffler. "Signal-to-Noise Ratio and MR Tissue Parameters in Human Brain Imaging at 3, 7, and 9.4 Tesla Using Current Receive Coil Arrays". In: *Magnetic Resonance in Medicine* 75.2 (2016), pp. 801–809 (pages 29, 43, 60).

[PTP46] E. M. Purcell, H. C. Torrey and R. V. Pound. "Resonance Absorption by Nuclear Magnetic Moments in a Solid". In: *Physical Review* 69 (1-2 Jan. 1946), pp. 37–38 (page 16).

[Pui+21] T. Puiseux, A. Sewonu, M. Ramiro, S. Mendez and N. Franck. "Numerical simulation of time-resolved 3D phase-contrast magnetic resonance imaging". In: *PLOS ONE* 16 (Mar. 2021), e0248816 (page 22).

[Puy+12] G. Puy, J. P. Marques, R. Gruetter, J.-P. Thiran, D. Van De Ville, P. Vandergheynst and Y. Wiaux. "Spread Spectrum Magnetic Resonance Imaging". In: *IEEE Transactions on Medical Imaging* 31.3 (2012), pp. 586–598 (page 60).

[Que+23] L. Quettier, G. Aubert, A. Amadon, J. Belorgey, C. Berriaud, C. Bonnelye, N. Boulant, P. Bredy, G. Dilasser, O. Dubois, G. Gilgrass, V. Gras, Q. Guihard, V. Jannot, F. Juster, H. Lannou, F. Lepretre, C. Lerman, C. Le Ster, F. Mauconduit, F. Molinié, F. Nunio, L. Scola, A. Sinanna, R. Touzery, P. Védrine and A. Vignaux. "Progress Toward Medical Use of the Iseult Whole Body 11.7 T MRI: First Images". In: *IEEE Transactions on Applied Superconductivity* 33.5 (2023), pp. 1–7 (pages 2, 7, 21).

[Rab+38] I. I. Rabi, J. R. Zacharias, S. Millman and P. Kusch. "A New Method of Measuring Nuclear Magnetic Moment". In: *Physical Review* 53 (4 Feb. 1938), pp. 318–318 (page 16).

[Rai+21] L. Raimondo, T. Knapen, l. A. Oliveira, X. Yu, S. O. Dumoulin, W. van der Zwaag and J. C. Siero. "A line through the brain: implementation of human line-scanning at 7T for ultra-high spatiotemporal resolution fMRI". In: *Journal of Cerebral Blood Flow and Metabolism* 41.11 (2021), pp. 2831–2843 (pages 92, 100).

[Rai+23] L. Raimondo, N. Priovoulos, C. Passarinho, J. Heij, T. Knapen, S. O. Dumoulin, J. C. Siero and W. van der Zwaag. "Robust high spatio-temporal line-scanning fMRI in humans at 7T using multi-echo readouts, denoising and prospective motion correction". In: *Journal of Neuroscience methods* 384 (2023), p. 109746 (pages 92, 100).

[RB23] H. Ratiney and O. Beuf. *Les enjeux de l'IRM - Techniques et methodes quantitatives pour la sante*. 2023 (pages 16, 25).

[RCB13] B. Rasim, F. B. Christian and M. Barth. "An investigation of RSN frequency spectra using ultra-fast generalized inverse imaging". In: *Frontiers in Human Neuroscience* 7.156 (2013) (page 92).

[Rid10] J. P. Ridgway. "Cardiovascular magnetic resonance physics for clinicians: part I". In: *Journal of Cardiovascular Magnetic Resonance* 71 (2010) (page 17).

[Rie+21] B. Riemenschneider, B. Akin, P. LeVan and J. Hennig. "Trading off spatio-temporal properties in 3D high-speed fMRI using interleaved stack-of-spirals trajectories". In: *Magnetic Resonance in Medicine* 86.2 (2021), pp. 777–790 (pages 36, 60).

[RMS22] C. A. Rettenmeier, D. Maziero and V. A. Stenger. "Three Dimensional Radial Echo Planar Imaging for Functional MRI". In: *Magnetic Resonance in Medicine* 87.1 (2022), pp. 193–206 (pages 101, 117).

[Rob+08] P. M. Robson, A. K. Grant, A. J. Madhuranthakam, R. Lattanzi, D. K. Sodickson and C. A. McKenzie. "Comprehensive Quantification of Signal-to-Noise Ratio and g-Factor for Image-Based and k-Space-Based Parallel Imaging Reconstructions". In: *Magnetic Resonance in Medicine* 60.4 (2008), pp. 895–907 (page 60).

[Rob+93] T. Robert, J. Peter, W. Han, K. K. Ken, L. B. Denis, A. Z. Thomas and S. B. Robert. "Functional mapping of the human visual cortex at 4 and 1.5 tesla using deoxygenation contrast EPI". In: *Magnetic Resonance in Medicine* 29.2 (1993), pp. 277–9 (page 26).

[Sav+95] R. L. Savoy, P. A. Bandettini, K. M. O'Craven, K. K. Kwong, T. L. Davis, J. R. Baker, R. M. Weisskoff and R. B. R. "Pushing the temporal resolution of fMRI: Studies of very brief visual stimuli, onset variability and asynchrony, and stimulus-correlated changes in noise". In: *Program of SMR presented at 3d Annual Meeting* (1995) (page 91).

[Sch+19] J. Schwarz, R. Stirnberg, P. Ehses and T. Stocker. "Correction of Physiological Field Fluctuations in High- and Low-resolution 3D-EPI Acquisitions at 7 Tesla". In: *ISMRM Annual Metting* (2019) (pages 47, 78, 87, 88).

[Sch+23] T. Schmidt, S. Vannesjo, S. Sommer and Z. Nagy. "fMRI with whole-brain coverage, 75-ms temporal resolution and high SNR by combining HiHi reshuffling and multiband imaging". In: *Magnetic Resonance Imaging* 103 (June 2023) (page 92).

[Sha+19] D. Sharoh, T. van Mourik, L. Bains, K. Segaert, K. Weber, P. Hagoort and D. Norris. "Laminar specific fMRI reveals directed interactions in distributed networks during language processing". In: *PNAS* 116 (2019), p. 201907858 (page 26).

[Shm+07] A. Shmuel, E. Yacoub, D. Chaimow, N. K. Logothetis and K. Ugurbil. "Spatio-Temporal Point-Spread Function of Functional MRI Signal in Human Gray Matter". In: *NeuroImage* 35.2 (2007), pp. 539–552 (page 75).

[Smi+04] S. M. Smith, M. Jenkinson, M. W. Woolrich, C. F. Beckmann, T. E. J. Behrens, H. Johansen-Berg, P. R. Bannister, M. De Luca, I. Drobnjak, D. E. Flitney, R. K. Niazy, J. Saunders, J. Vickers, Y. Zhang, N. De Stefano, J. M. Brady and P. M. Matthews. "Advances in functional and structural MR image analysis and implementation as FSL". In: *NeuroImage* 23 (2004), S208–S219 (pages 45, 62).

[SNF03] B. Sutton, D. Noll and J. Fessler. "Fast, Iterative Image Reconstruction for MRI in the Presence of Field Inhomogeneities". In: *IEEE Transactions on Medical Imaging* 22.2 (2003), pp. 178–188 (page 45).

[SR17] V. A. Stenger and C. Rettenmeier. "Blipped Stack of Spirals for Fast Volumetric Functional MRI". In: *ISMRM Annual Meeting*. 2017 (page 37).

[STC13] B. Solveig, V. Thomas and P. Ciuciu. "Group-level impacts of within- and between-subject hemodynamic variability in fMRI". In: *NeuroImage* 82 (2013), pp. 433–448 (pages 25, 92).

[Ste+22] C. Ster, A. Grant, P.-F. Van de Moortele, A. Monreal-Madrigal, G. Adriany, A. Vignaud, F. Mauconduit, C. Rabrait, B. Poser, K. Ugurbil and N. Boulant. "Magnetic field strength dependent SNR gain at the center of a spherical phantom and up to 11.7T". In: *Magnetic Resonance in Medicine* 88 (July 2022) (pages 29, 43).

[SW18] J. P. Stockmann and L. L. Wald. "In vivo B0 field shimming methods for MRI at 7 T". In: *NeuroImage* 168 (2018), pp. 71–87 (page 45).

[THG18] A. B. Taylor, J. M. Hendrickx and F. Glineur. "Exact worst-case convergence rates of the proximal gradient method for composite convex minimization". In: *Journal of Optimization Theory and Applications* 178.2 (2018), pp. 455–476 (pages 38, 55).

[TRW11] C. P. Triantafyllou, J. R. and L. L. Wald. "Physiological noise and signal-to-noise ratio in fMRI with multi-channel array coils". In: *NeuroImage* 55 (2011), pp. 597–606 (pages 29, 60, 78, 95).

[Uğu21] K. Uğurbil. "Ultrahigh field and ultrahigh resolution fMRI". In: *Current Opinion in Biomedical Engineering* 18 (Apr. 2021), p. 100288 (page 26).

[UMU09] K. Uludağ, B. Müller-Bierl and K. Uğurbil. "An integrative model for neuronal activity-induced signal changes for gradient and spin echo functional imaging". In: *NeuroImage* 48 (2009), pp. 150–165 (page 27).

[Urg21] K. Urgurbil. "Ultrahigh field and ultrahigh resolution fMRI". In: *Current Opinion in Biomedical Engineering* 18 (2021) (page 59).

[URP23] T. Ulrich, M. Riedel and K. Pruessmann. "Prospective Head Motion Correction Using Orbital K-Space Navigators and a Linear Perturbation Model". In: *ISMRM Annual Meeting*. 2023 (page 105).

[UUB15] K. Uludağ, K. Ugurbil and L. Berliner, eds. *fMRI: from nuclear spins to brain functions*. English. Biological Magnetic Resonance. Germany: Springer Verlag, 2015 (pages 16, 24).

[Van+13] S. J. Vannesjo, M. Haeberlin, L. Kasper, M. Pavan, B. J. Wilm, C. Barmet and K. P. Pruessmann. "Gradient System Characterization by Impulse Response Measurements with a Dynamic Field Camera". In: *Magnetic Resonance in Medicine* 69.2 (2013), pp. 583–593 (page 46).

[Van+15] S. J. Vannesjo, B. J. Wilm, Y. Duerst, S. Gross, D. O. Brunner, B. E. Dietrich, T. Schmid, C. Barmet and P. K. P. "Retrospective Correction of Physiological Field Fluctuations in High-field Brain MRI Using Concurrent Field Monitoring". In: *Magnetic Resonance in Medicine* 73.5 (2015), pp. 1833–1843 (pages 47, 88).

[Ved+14] P. Vedrine, G. Aubert, J. Belorgey, C. Berriaud, A. Bourquard, P. Bredy, A. Donati, O. Dubois, F. Elefant, G. Gilgrass, F. P. Juster, H. Lannou, F. Molinié, M. Nusbaum, F. Nunio, A. Payn, L. Quettier, T. Schild, L. Scola and A. Sinanna. "Manufacturing of the Iseult/INUMAC Whole Body 11.7 T MRI Magnet". In: *IEEE Transactions on Applied Superconductivity* 24.3 (2014), pp. 1–6 (pages 2, 7, 21).

[Viz+22] L. Vizioli, S. Moeller, A. Grant, N. Tavaf, L. Dowdle, A. Sadeghi-Tarakameh, Y. Eryaman, J. Radder, R. Lagore and P. V. D. Moortele. "Ultra-high resolution human functional imaging using 10.5 Tesla". In: *High Field ISMRM Workshop*. 2022 (page 26).

[VYL21] L. Vizioli, E. Yacoub and L. D. Lewis. "How pushing the spatiotemporal resolution of fMRI can advance neuroscience". In: *Progress in Neurobiology* 207 (2021), p. 102184 (page 59).

[Wad+02] A. R. Wade, A. A. Brewer, J. W. Rieger and B. A. Wandell. "Functional measurements of human ventral occipital cortex: retinotopy and colour". In: *Philosphical Transactions of the Royal Society of London* 357 (2002), pp. 963–973 (page 71).

[War+02] J. Warnking, M. Dojat, A. Guerin-Dugue, C. Delon-Martin, S. Olympieff, N. Richard, A. Chehikian and C. Segebarth. "fMRI Retinotopic Mapping—Step by Step". In: *NeuroImage* 17 (2002), pp. 1668–1683 (page 71).

[Web11] A. Webb. "Dielectric Materials in Magnetic Resonance". In: *Concepts in Magnetic Resonance Part A* 38A (July 2011), pp. 148–184 (page 44).

[Wil+11] B. Wilm, C. Barmet, M. Pavan and K. Pruessmann. "Higher Order Reconstruction for MRI in the Presence of Spatio-temporal Field Perturbations". In: *Magnetic Resonance in Medicine* 65.4 (2011), pp. 1690–1701 (pages 44, 87).

[Yun+13] S. D. Yun, M. Reske, K. Vahedipour, T. Warbrick and N. J. Shah. "Parallel imaging acceleration of EPIK for reduced image distortions in fMRI". In: *NeuroImage* 73 (2013), pp. 135–43 (page 92).

[Yun+19] S. D. Yun, R. Weidner, W. P. H. and N. J. Shah. "Evaluating the Utility of EPIK in a Finger Tapping fMRI Experiment using BOLD Detection and Effective Connectivity". In: *Scientific Reports* 9 (2019), p. 10978 (page 92).

[Z A+22a] **Z. Amor**, G. R. Chaithya, G. Daval-Frérot, B. Thirion, F. Mauconduit, P. Ciuciu and A. Vignaud. "3D-SPARKLING for functional MRI: A pilot study for retinotopic mapping at 7T". In: *OHBM*. Glasgow, Scotland, UK, 2022 (page 11).

[Z A+22b] **Z. Amor**, G. R. Chaithya, G. Daval-Frérot, B. Thirion, F. Mauconduit, C. Mirkes, P. Ciuciu and A. Vignaud. "Prospects of non-Cartesian 3D-SPARKLING encoding for functional MRI: A preliminary case study for retinotopic mapping". In: *ISMRM Annual Meeting*. London, UK, 2022 (page 11).

[Z A+22c] **Z. Amor**, G. R. Chaithya, C. Le Ster, G. Daval-Frérot, N. Boulant, F. Mauconduit, C. Mirkes, P. Ciuciu and A. Vignaud. "B_0 field distortions monitoring and correction for 3D non-Cartesian fMRI acquisitions using a field camera: Application to 3D-SPARKLING at 7T". In: *ISMRM Annual Meeting*. London, UK, 2022 (page 11).

[Z A+23a] **Z. Amor**, C. Le Ster, G. R. Chaithya, G. Daval-Frérot, B. Thirion, N. Boulant, F. Mauconduit, C. Mirkes, P. Ciuciu and A. Vignaud. "Impact of ΔB_0 imperfections correction on BOLD sensitivity in 3D-SPARKING fMRI data". In: *ISMRM Annual Meeting*. Toronto, ON, Canada, 2023 (page 11).

[Z A+23b] **Z. Amor**, C. Le Ster, P.-A. Comby, A. Vignaud and P. Ciuciu. "Non-Cartesian non-Fourier fMRI imaging for high-resolution retinotopic mapping at 7 Tesla". In: *9th IEEE International Workshop on Computational Adavnces in Multi-Sensor Adaptive Processing (CAMSAP)*. Los Suenos, Costa Rica, 2023 (page 11).

[Z A+24a] **Z. Amor**, P. Ciuciu, G. Chaithya, G. Daval-Frérot, F. Mauconduit, B. Thirion and A. Vignaud. "Non-Cartesian 3D-SPARKLING vs Cartesian 3D-EPI encoding schemes for functional Magnetic Resonance Imaging at 7 Tesla". In: *PLoS One, Accepted* (2024) (page 11).

[Z A+24b] **Z. Amor**, P.-A. Comby, P. Ciuciu and A. Vignaud. "Achieving high temporal resolution using a sliding-window approach for SPARKLING fMRI data: A simulation study". In: *ISMRM Annual Meeting, (in press)*. Singapore, 2024 (page 11).

[Z A+24c] **Z. Amor**, C. Le Ster, G. Chaithya, G. Daval-Frérot, N. Boulant, F. Mauconduit, B. Thirion, P. Ciuciu and A. Vignaud. "Impact of B_0 field imperfections correction on BOLD sensitivity in 3D-SPARKLING fMRI data". In: *Magnetic Resonance in Medicine* 91.4 (2024), pp. 1434–1448 (page 11).

[Zon+14] X. Zong, J. Lee, A. J. Poplawsky, S. Kim and J. C. Ye. "Compressed sensing fMRI using gradient-recalled echo and EPI sequences". In: *NeuroImage* 92 (2014), pp. 312–321 (page 51).